NASA Contractor Report 179555
MTI 87TR36

Space Power Demonstrator Engine

Phase I Final Report

Alec T. Brown
Mechanical Technology Incorporated
Latham, New York

May 1987

Prepared for
Lewis Research Center
Under Contract NAS3-23883

NASA

National Aeronautics and
Space Administration

1. Report No. NASA CR-179555	2. Government Accession No.	3. Recipient's Catalog No.
4. Title and Subtitle SPACE POWER DEMONSTRATOR ENGINE PHASE I FINAL REPORT		5. Report Date May 1987
		6. Performing Organization Code
7. Author(s) Alec T. Brown, Project Manager		8. Performing Organization Report No. MTI87TR36
		10. Work Unit No. 506-41-31
9. Performing Organization Name and Address MECHANICAL TECHNOLOGY INCORPORATED 968 Albany-Shaker Road Latham, NY 12110		11. Contract or Grant No. NAS3-23883
12. Sponsoring Agency Name and Address NATIONAL AERONAUTICS AND SPACE ADMINISTRATION Washington, DC 20546		13. Type of Report and Period Covered Contractor Report
		14. Sponsoring Agency Code

15. Supplementary Notes

Donald L. Alger, Project Manager
Stirling Engine Project Office
NASA/Lewis Research Center
Cleveland, OH 44135

16. Abstract

This report documents the design, analysis, and preliminary test results for a 25kWe Free-Piston Stirling Engine with integral linear alternators. The project is being conducted by Mechanical Technology Incorporated under the direction of NASA/Lewis Research Center as part of the SP-100 Nuclear Space Power Systems Program.

The engine/alternator system is designed to demonstrate the following performance:

- 25kWe output at a specific weight less than 8 kg/kW
- 25% efficiency at a temperature ratio of 2.0
- Low vibration (amplitude less than .003 inches)
- Internal gas bearings (no wear, no external pump)
- Heater temperature/cooler temperature ∼630°K/315°K

The design approach to minimize vibration is a two-module engine (12.5kWe per module) in a linearly-opposed configuration with a common expansion space. The low specific weight is obtained at high helium pressure (150 Bar) and high frequency (105 Hz) and by using high magnetic strength (Samarium Cobalt) alternator magnets.

Engine checkout testing began in June 1985; 16 months following initiation of the engine and test cell design. Hydrotest and consequent engine testing to date has been intentionally limited to half pressure, and electrical power output is within 15-20% of design predictions at these conditions. Vibration is negligible and engine operation is balanced and stable. High pressure and high power testing will be conducted during the next fiscal year.

17. Key Words (Suggested by Author(s)) Stirling Engine, Space Power, Opposed Pistons, Linear Alternators, Gas Bearings, Heat Engine	18. Distribution Statement UNCLASSIFIED until May 1992		
19. Security Classif. (of this report) UNCLASSIFIED	20. Security Classif. (of this page) UNCLASSIFIED	21. No. of pages	22. Price*

MTI87TR36

SPACE POWER DEMONSTRATOR ENGINE

PHASE I FINAL REPORT

Contract No. NAS3-23883

Covering the Period

February 1984 Through September 1985

Prepared For:

NASA/LEWIS RESEARCH CENTER

21000 Brookpark Road

Cleveland, OH 44135

Prepared By:

MECHANICAL TECHNOLOGY INCORPORATED

968 Albany-Shaker Road

Latham, NY 12110

May 1987

TABLE OF CONTENTS

TABLE OF CONTENTS cont'd

TABLE OF CONTENTS cont'd

LIST OF FIGURES

LIST OF TABLES

PAGE X INTENTIONALLY BLANK

ACKNOWLEDGEMENTS

The following personnel were responsible for the various technical areas listed:

PROGRAM/PROJECT MANAGEMENT	G. Dochat, A. Brown
TECHNICAL OVERVIEW	N. Vitale
MECHANICAL DESIGN	G. Yarr
ALTERNATOR DESIGN, ANALYSIS, AND FABRICATION	S. Bhate, S. Fallek, M. Frantsov
ENGINE ANALYSIS	M. Dhar (Thermodynamics, Dynamics, System Stability) D. Jones (Bearings and Ports) A. Brown (Stress)
MANUFACTURING ENGINEERING	G. Antonelli
INSTRUMENTATION AND ELECTRICAL SYSTEMS	H. Short, T. Russell, R. Lacy
DEVELOPMENT ENGINEERING AND MECHANICAL SYSTEMS	J. Rauch, M. Messaros
TECHNICAL EDITING, TYPING, AND REPORT COORDINATION	D. Clark

PRECEDING PAGE BLANK NOT FILMED

NOMENCLATURE

C_{D1}, C_{D2} = Damping coefficient for displacer 1, displacer 2

C_g = Tuning capacitance

C_{P1}, C_{P2} = Damping coefficient for piston 1, piston 2

K_{D1}, K_{D2} = Spring rate of gas spring for displacer 1, displacer 2

K_{P1}, K_{P2} = Spring rate of gas spring for piston 1, piston 2

L_{g1}, L_{g2} = Coil inductance of alternator 1, 2

M_{D1}, M_{D2} = Mass of displacer 1, displacer 2

M_{P1}, M_{P2} = Mass of piston 1, piston 2

PHID = Phase angle of displacer relative to pistons

P_{C1}, P_{C2} = Pressure amplitude of compression space 1, 2

P_e = Pressure amplitude - expansion space

P_M = Mean pressure

P_{mech} = Mechanical power

P_{TH} = Thermodynamic power

R_{g1}, R_{g2} = Coil resistance of alternator 1, 2

R_L = Load resistance

T_C = Average outer surface temperature of cooler tubes

T_H = Average outer surface temperature of heater tubes

V_{gen1}, V_{gen2} = Generated voltage of alternator 1, 2

V_L = Load voltage

X_C = Displacement amplitude - casing

X_D = Displacer half-stroke

X_{D1}, X_{D2} = Displacement amplitude of displacer 1, displacer 2

X_P = Piston half-stroke

X_{P1}, X_{P2} = Displacement amplitude of piston 1, piston 2

1.0 SUMMARY AND CONCLUSIONS

1.1 Introduction

The U.S. Government is evaluating power requirements for future space applications. As power requirements increase, solar or nuclear dynamic systems become increasingly attractive. Free-Piston Stirling Engines (FPSE's) have the potential to provide high reliability, long life, and efficient operation at reasonable hot-side temperatures. Therefore, they are excellent candidates for the dynamic power conversion module of a space-based, power-generating system. FPSE's, while extremely promising, are at an early stage of technological development. They have not yet demonstrated all the attributes necessary for a space power system.

To address the present FPSE state-of-the-art technology, Mechanical Technology Incorporated (MTI) was selected to demonstrate the major feasibility issues in a Space Power Demonstrator Engine (SPDE). The initial contract (NAS3-23883) was awarded in February 1984 and was to continue through September 1985. The program has since been extended to continue technology development of FPSE's for space power.

1.2 SPDE Program Objectives

The objective of the SPDE program is to design, build, and demonstrate, with actual hardware, the key technology issues that would permit selection of the FPSE generator as the space power conversion system. The key technology issues that were to be demonstrated within this program include:

- 25kW electrical power output;
- 25% system efficiency (heat into the head/electric power out);
- 8 kg/kW (17.6 lb/kW);
- $T_H/T_C = 2.0$;
- $T_H = 630°K$, $T_C = 315°K$;
- Internal gas bearings; and,
- Dynamic balance (less than 0.003-in vibration along any axis).

A major aspect of the demonstrator system involves operation of the system at a design temperature ratio of 2.0 but at reduced absolute heater and cooler temperatures. This results in significant schedule and cost benefits while meeting all the objectives without sacrificing any critical system thermodynamic parameters.

1.3 SPDE Design Summary

The space power demonstrator system consists of two major elements: the 25kW power module and the external heat source/cooling system and electric load. The power module consists of two identical 12.5kW submodules in an opposed in-line configuration (heater head to heater head). One submodule is shown in Figure 1-1. Each submodule is an engine/alternator consisting of a linear FPSE and a linear permanent-magnet alternator. These submodules are sealed within and connected together by a high-strength steel pressure vessel.

The FPSE's are standard spring-to-ground, virtual rod displacer engines that operate in a thermal oscillator mode with helium as the working fluid. The engine heater and cooler are annular tube-in-shell units, with the engine working fluid passing through the tubes. The regenerator is an annular-stacked screen, sandwiched between the heater and cooler.

The permanent-magnet alternator is a moving magnet design in which the magnets are carried on a lightweight, non-magnetic non-conducting cylindrical carrier. The magnet carrier operates between an inner and outer laminated Hyperco stator. The output coils of both submodules are connected in series.

The power module will require external heating and cooling systems in order to test at the desired temperature ratio of 2.0. Thermal power is supplied to the module by pumping a hot (670°K) molten salt heat transfer fluid through the shell of each tube-in-shell heater unit. Similarly, thermal power is dissipated from the module by an open water loop that circulates water through the shell of each tube-in-shell cooler. The electrical output of the module is rectified to DC and dissipated through a 25kW resistance unit.

The module is designed for steady-state operation at the design points and, as such, has no control system. Variations in power are accomplished through chang-

FIGURE 1-1

SPDE ENGINE CONFIGURATION

(1/2 of Power Module)
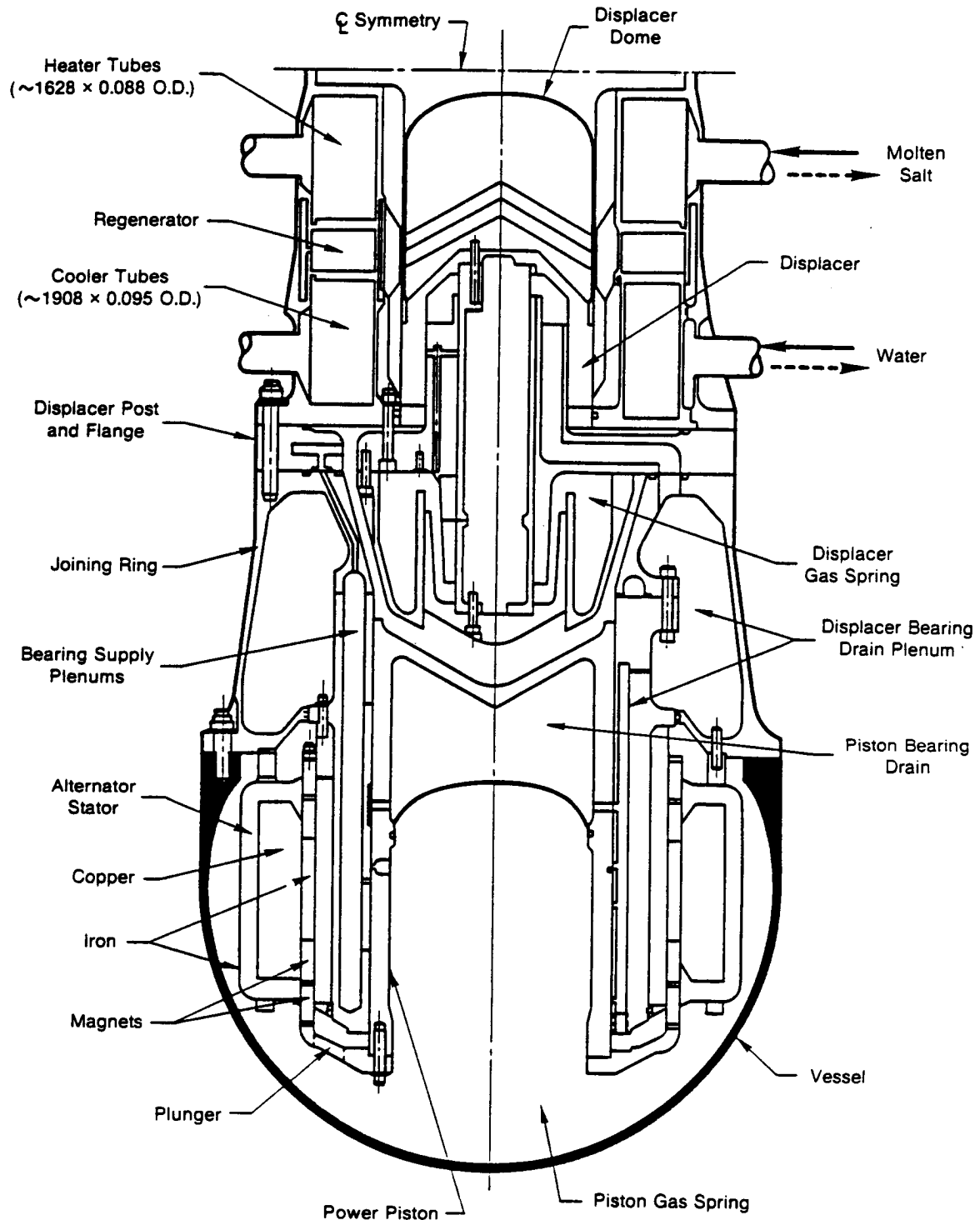
841631

es in temperature of the external heating/cooling systems. The selected SPDE operating point is presented in Table 1-1.

The predicted design performance of the SPDE is 25kWe power output at a system efficiency of 25% with a temperature ratio of 2.0. The opposed configuration will result in a dynamically-balanced system with less than 3 mils of vibration. The unit weight is projected to less than 8 kg/kW.

1.4 Developmental Test Results

Initial motoring tests indicated that the displacer-to-piston phase angle was lower than expected. Minor modifications were made first to the displacer gas spring, and second to the power piston mass to obtain the desired phase angle.

The initial hot low-pressure run of the engine was performed on June 15, 1985. During the first hot run of the assembled SPDE, the engine was motored via the alternators as the head temperature was increased. The engine was self-sustaining at 428°K. Temperature was increased toward the design temperature of 630°K. Initial data was taken from overhead displays which indicated that the electric power achieved was over 4kWe net output during this initial hot test.

The focus on subsequent low power testing was to achieve close to the predicted power at the low pressure test conditions and to correct problems associated with the data acquisition system. Testing in August-September 1985 produced excellent power (6.5kW) with reasonable accuracy of the instrumentation. Test results of the SPDE versus a predicted low pressure point is summarized in Table 1-2. Figure 1-2 shows the various temperature ratios that were obtained as a function of displacer amplitude. Figure 1-3 presents the electrical power output as a function of displacer amplitude.

1.5 Test Measurements Versus Goals

● Performance (25kWe - 25% Efficiency - TH/TC = 2.0) - As of September 1985, the SPDE has not yet been tested at full operating pressure; however, testing at half design pressure indicates that the engine is providing power close to predictions and expectations are that the engine will have the capability to provide full power at full design conditions. The engine has operated at a temperature ratio

TABLE 1-1

ENGINE DESIGN POINT OPERATING CHARACTERISTICS

- Frequency   105 Hz

- Mean Pressure   150 Bar

- Heater Wall Temperature   630°K

- Cooler Wall Temperature   315°K

- Displacer Stroke Amplitude (XD)   8.97 mm

- Piston Stroke Amplitude (XP)   10.16 mm

- Phase Angle XD Relative to XP   65°

- Compression Space Pressure Amplitude   14.38 Bar

TABLE 1-2

TEST RESULTS AT 75 BAR

	PREDICTED	DEMONSTRATED
Electric Power Output	6.7kWe	6.5kWe
P	75 Bar	75 Bar
XD	7.81mm	8.23mm
XP	10.16mm	8.65mm
Frequency	70.75 Hz	73.30 Hz
TH/TC	2.0	2.0
ϕD	75.6	81.0

FIGURE 1-2

SPDE ENGINE TEST RESULTS

TEMPERATURE RATIO OBTAINED AT VARIOUS DISPLACER AMPLITUDES

851944
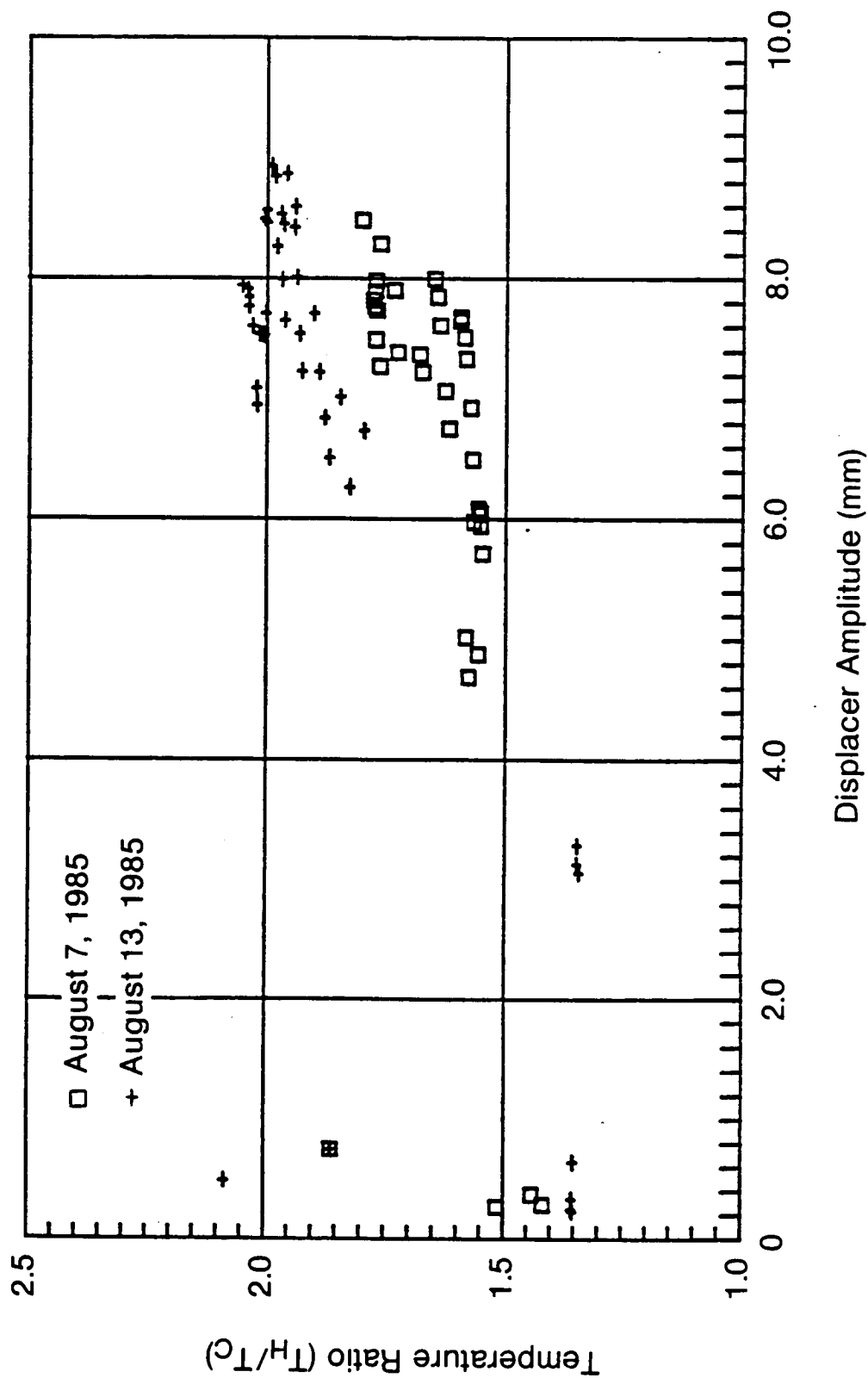
FIGURE 1-3

SPDE ENGINE TEST RESULTS

POWER AS A FUNCTION OF DISPLACER AMPLITUDE

851945
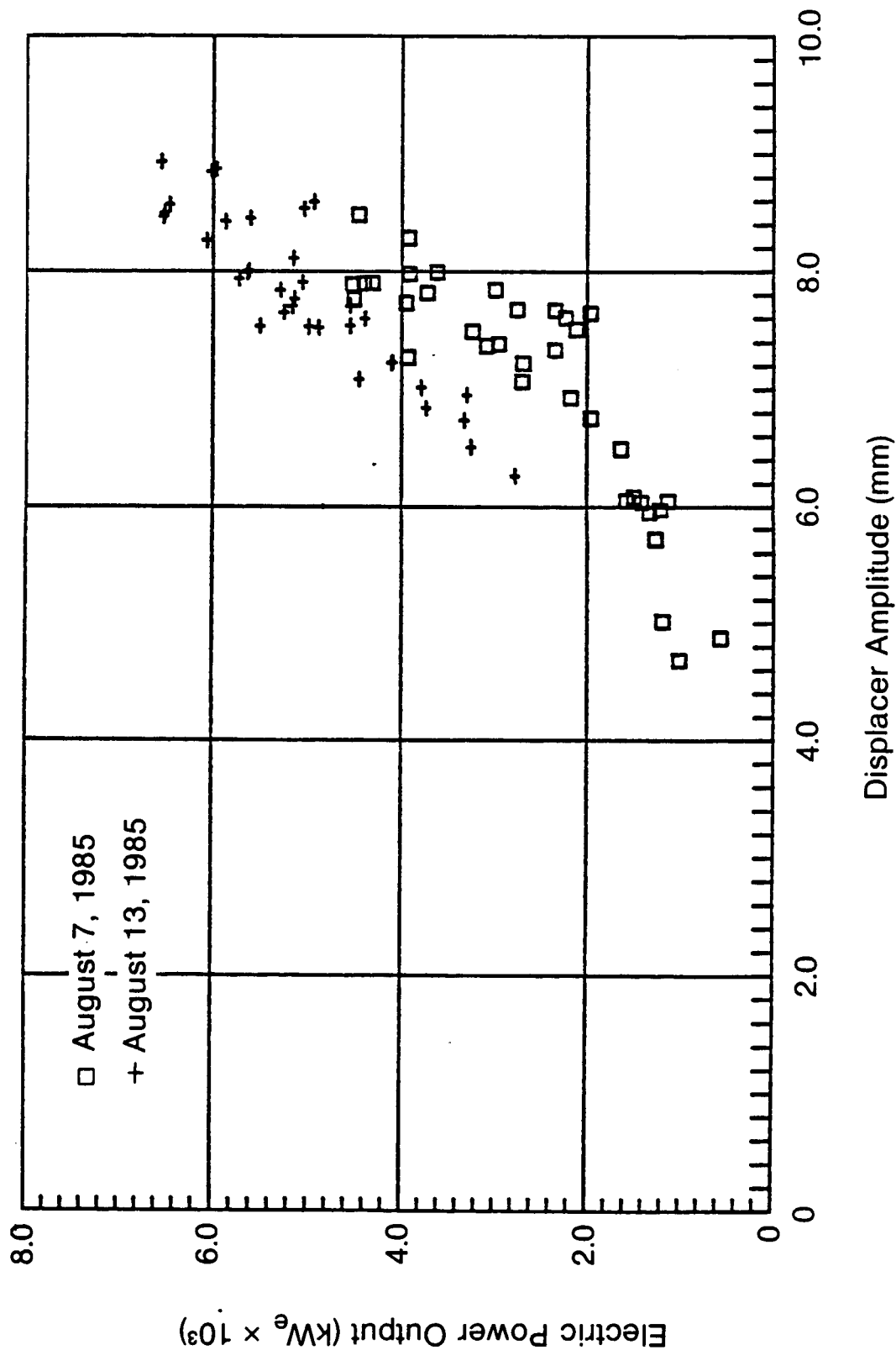
of 2.0, and full mechanical operation has been demonstrated. Efficiency at the low pressure point is ∼20% (electric power output/heat into the engine).

● <u>Weight (<8 kg/kW)</u> - The SPDE is a development engine and, as such, is not the final space configuration. However, with straight-forward material substitutions that would be made directly to the SPDE in a final space configuration, the adjusted weight is 7.2 kg/kW.

● <u>Dynamic Balance (<.003 Inches)</u> - To date, the engine has operated at full temperature ratio and full mechanical stroke. The piston and displacers of each engine half operate 180° out-of-phase and at similar strokes (within 10% on displacers and within 5% on pistons). Accelerometer readings taken during full stroke testing indicate a total .0004 inch peak-to-peak vibration level with less than .2g force.

1.6 Further Development Plans

The next phase of the development activity will be to increase pressure to the 150 Bar design conditions and develop the engine to its full operational potential.

1.7 Conclusions

The SPDE is a technology resource for the development of large FPSE power modules and FPSE technology. Testing of the SPDE will continue the steady development and will provide a test bed to evaluate new components/technologies for FPSE's. The SPDE needs to demonstrate the power and efficiency at full design conditions, but all other technical goals have been demonstrated (weight and dynamic balance). It is expected that the development work will require testing through 1986.

In conclusion, the SPDE, in 1985, has highlighted the potential of Stirling as a rapidly maturing technology for future space power conversion systems. Further technology development is required to realize its full potential.

2.0 INTRODUCTION

This report covers work performed under NASA-Lewis Research Center contract number NA3-23883 during the period February 1984 through September 1985. The objectives and approach were outlined in the proposal document "Space Power Demonstrator Engine - Design, Fabrication, and Test Program", MTI G4-746, January 19, 1984.

During 1983, the SP-100 Program Office was reviewing various technological approaches to meeting future requirements for electric power based on the use of a liquid metal cooled fast nuclear reactor. The electric power level needed was identified as about 100kW initially with growth needs to several hundred kilowatts. The means of launching would be the Space Shuttle. Weight and volume goals were established and theoretical and experimental studies were initiated to investigate the potential of various conversion technologies.

The Free-Piston Stirling Engine (FPSE) coupled to an electric generator was identified as a candidate energy conversion system. The primary advantages of an FPSE are:

1. The thermal efficiency attainable with a Stirling cycle heat engine is much higher than attainable with static devices (thermoelectric and thermionic) and higher than other closed heat engine cycles.

2. Non-contacting gas bearings on the moving pistons provide the potential for no wear and, consequently, high reliability and long life.

3. Engines with direct-coupled alternators can be hermetically sealed. This is essential to maintain gas pressure in the engine for the full seven year design life without the weight and complexity of a gas make-up and pressure control system.

A space power system utilizing four or five FPSE's in the 20 to 30kW range has the potential for meeting the 100kW power output goal, within the weight constraints, at lower reactor temperatures than required by some of the competing technolo-

gies. Multiple units permit redundancy so that single failures do not cripple the system.

Prior to initiation of the SPDE, the largest FPSE built by MTI was the 3kW Engineering Model (EM). Since it was developed for various land based applications, very little emphasis was placed on minimizing weight and extremely expensive materials were avoided. Additionally, no FPSE has been run for an extended period of time to demonstrate the lack of wear and consequent reliability.

The major changes made from existing technology to meet space engine requirements were:

1. Increase engine operating pressure from 60 Bar to 150 Bar.
2. Increase engine operating frequency from 60 Hz to 105 Hz.
3. Utilize beryllium in the displacer and power pistons to minimize moving mass and associated mechanical losses.
4. Utilize high strength magnets (samarium cobalt) and high quality laminations (HYPERCO 50) to minimize power losses in the linear alternator.
5. Utilize high strength materials in the pressure boundary to minimize weight.
6. Use a hot liquid to transfer heat into the engine.

The SPDE program was initiated to determine experimentally whether the power, specific weight, and efficiency levels required for a space power system could be obtained. A further requirement was that the vibration levels be exceedingly low to demonstrate that dynamic load transmission in a space application would not be a problem. A parallel effort was initiated to demonstrate life and reliability on an FPSE. This was designated the "Engineering Model Endurance Program". During the period August 10, 1984 to June 15, 1985, an EM engine logged over 5,000 hours with no failures or measurable degradation.

The technical objectives of the SPDE Program were to design, build, and test an engine to demonstrate:

- 25kW electrical power output;
- 25% conversion efficiency (power out/heat in);
- 8 kg/kW specific weight; and,

• dynamic balance (<.003" vibration amplitude).

The above to be at a temperature ratio TR = 2.0. The temperature ratio is defined as the average temperature of the outer surface of the heater channels divided by the average temperature of the outer surface of the cooler channels.

Additionally, the engine will utilize gas bearings pumped internally. Meeting this requirement will demonstrate that no auxiliary pump for the bearings would be required in a space application.

A space power reactor will utilize liquid metal (sodium, NaK, or lithium) as the heat transfer fluid. The operating temperature will be determined following detailed system studies and further development. It may also depend upon the particular conversion technology selected.

For the SPDE program, it was decided, based upon cost and schedule considerations, to delay demonstration of operation using a high temperature liquid metal heat source until the basic feasibility of meeting power and efficiency goals at lower heater temperatures was demonstrated. Since for a heat engine the power density and efficiency is determined primarily by the temperature ratio across the engine rather than temperature level, the operating temperatures were set by the availability of a reasonably economical way of providing the design temperature ratio of 2.0. An available water system on a skid was used to remove heat from the engine cooler in the range 300 to 350°K. A molten salt system was purchased to supply a nominal 100kW to the engine at the design temperature ratio of 2.0 and also permit testing above and below this ratio.

The design concept selected for converting the mechanical power delivered by the engine to the power piston into electric power is a direct-coupled linear alternator (LA). This concept has been used on previous MTI engines (EM and MERAD-COM). The plunger of a linear alternator, rigidly attached to the power piston, oscillates adjacent to an iron enclosed copper coil. Permanent magnets on the plunger create a magnetic field which couples with the coil to induce an electric power output.

The schedule for the SPDE program was very ambitious. The SP-100 Program Office was scheduled to make some basic decisions on which technologies to pursue by

July 1985; a bare 18 months was available from project inception to this decision date. The preliminary design was completed, reviewed, and approved in three months. The detailed design and hardware procurement were dovetailed to minimize the overall elapsed time.

The heat exchangers paced the schedule; they required many sequential operations. Each of four assemblies is composed of about 1600 tubes brazed into tube sheets. The potential for leakage due to imperfect joints was a concern. Braze samples were made and process options evaluated at two vendors prior to fabrication of the engine heaters and coolers. The drilling of 1600 holes in eight tube sheets and holding tolerance on diameter and position in a difficult material (Inconel 718) was a challenge for the vendor which was successfully met. The brazing of the 6400 tubes to tube sheet joints was accomplished with only a few joints having to be reworked by hand on two assemblies.

Final assembly, hydrotesting, and initial checkout tests at half pressure were accomplished in early June 1985; 16 months from the start of the program.

The details of the engine/alternator and facility design are presented in subsequent sections of the report.

The results of tests conducted between June and September 1985 are discussed in detail in Section 11.0.

3.0 ENGINE DESCRIPTION

3.1 Introduction

To meet the requirements outlined in Section 2.0, the engine concept selected is a two-cylinder linearly-opposed single-acting free-piston Stirling engine (FPSE) of the beta configuration. Power extraction is from direct-coupled linear alternators (LA) located inside the pressure vessels at the cold end of the engine. The engine is a "free oscillator" and there is no external excitation applied to the displacer or power piston.

The two-cylinder linearly-opposed arrangement was selected to meet the low vibration requirement without the weight penalty of an active vibration absorber. An FPSE/LA was selected as a concept which could be developed to meet the space requirements of long life, high reliability, and no maintenance. The incorporation of non-contacting hydrostatic gas bearings on the pistons results in an engine in which there is no wear to limit the potential life of the engine.

The direct-coupled linear alternators within the vessels permit an arrangement which can be hermetically sealed. The elimination of gas leakage from the engine will avoid the weight and complexity of a gas make-up system in a space application. Helium is the working fluid selected since it is easier to contain than hydrogen. Hydrogen would be preferred from engine efficiency considerations, but its permeation characteristics make it questionably practical for long life applications (i.e., seven years for SP-100 project).

The "free oscillator" concept was selected over a "thermal amplifier" for the following reasons:

1. There is no requirement for close control of the frequency of the AC output since it will be rectified to DC.

2. The overall weight is lower.

3. Reliability is improved by elimination of an exciter motor.

4. A motor would add weight to the displacer which requires an increase in displacer gas spring stiffness with a corresponding increase in gas spring hysteresis loss.

An isometric sketch of the engine with a cut-away of one-half is shown in Figure 3-1. A photograph of the engine located in the test cell is shown in Figure 3-2, and a labeled cross section of one engine half is shown in Figure 3-3. The two engine halves are welded together at their hot end to produce a linearly-opposed arrangement with the expansion space common to both engine halves. Each engine half comprises three major assemblies bolted together as shown in Figure 3-4. The assemblies are:

1. Displacer Drive Assembly
2. Heat Exchanger Assembly
3. Alternator Section Assembly

The displacer in the displacer drive assembly oscillates axially and shuttles the working gas back and forth through the heater, regenerator, and cooler, which are connected in series between the the hot expansion space and cold compression space. Heat is continuously added to the working gas as it traverses the heater, heat is absorbed from and rejected to the regenerator matrix during each half of the flow cycle, and heat is continually removed from the working gas as it traverses the cooler. Power is extracted from the engine in the alternator section assembly. The central power piston oscillates axially and extracts energy from the helium in the compression space. Magnets in the plunger assembly attached to the power piston induce a voltage in the coil of the alternator stator from which the power is extracted by connection to a suitable power conditioning system and electric load.

To meet the specific weight goals, the pressure of the working fluid is made as high as possible. A mean pressure of 150 Bar (2175 psi) was selected on the grounds that this is near the upper limit of experience with Stirling engines. It was also judged that 150 Bar was near the limit of practicality for future designs in which the heater would be at an elevated temperature. High pressure implies high stresses, which at high temperature require materials with adequate creep strength.

FIGURE 3-1

SPACE POWER DEMONSTRATOR ENGINE
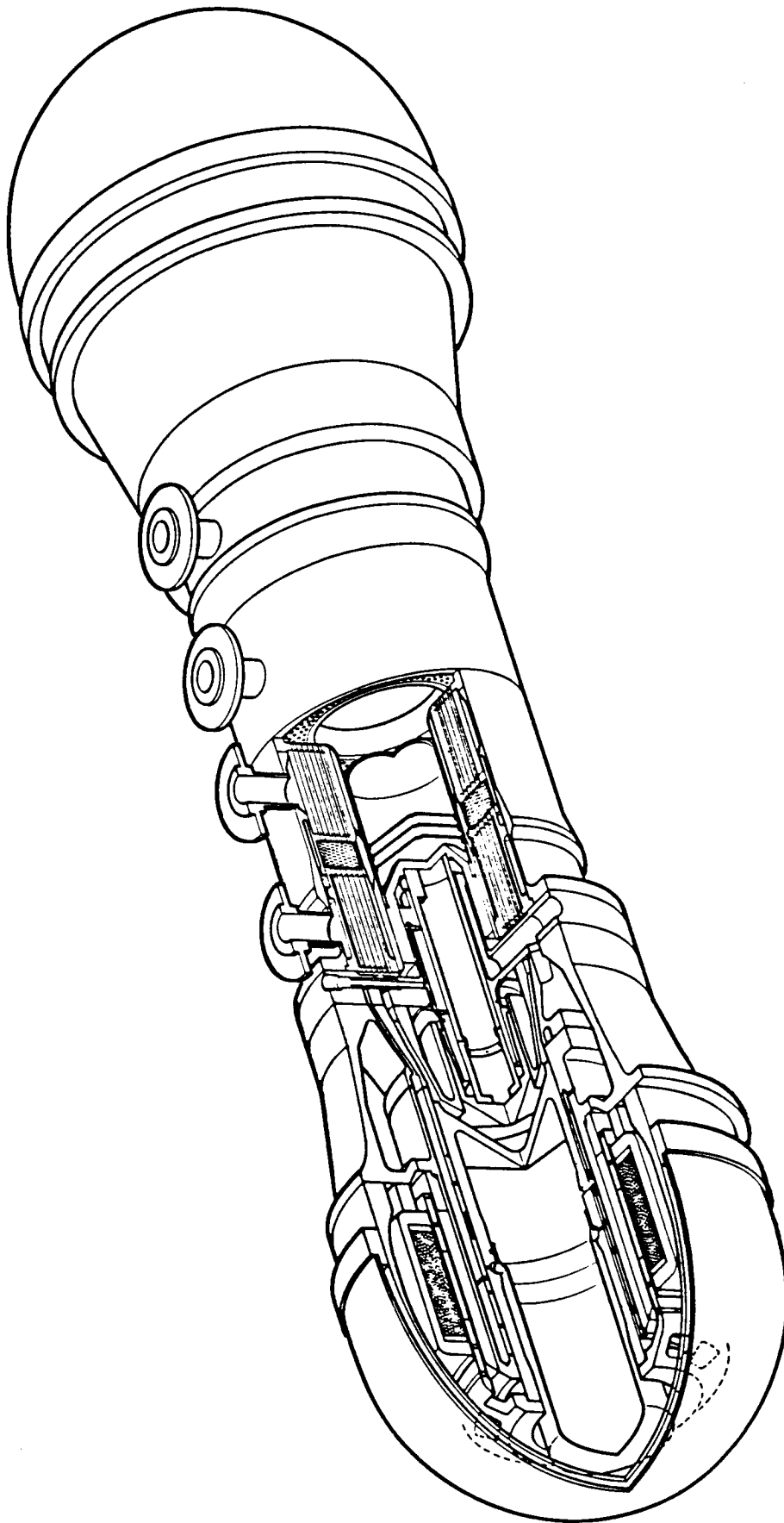
FIGURE 3-2
SPDE INSTALLED IN TEST CELL

CT85773A-14
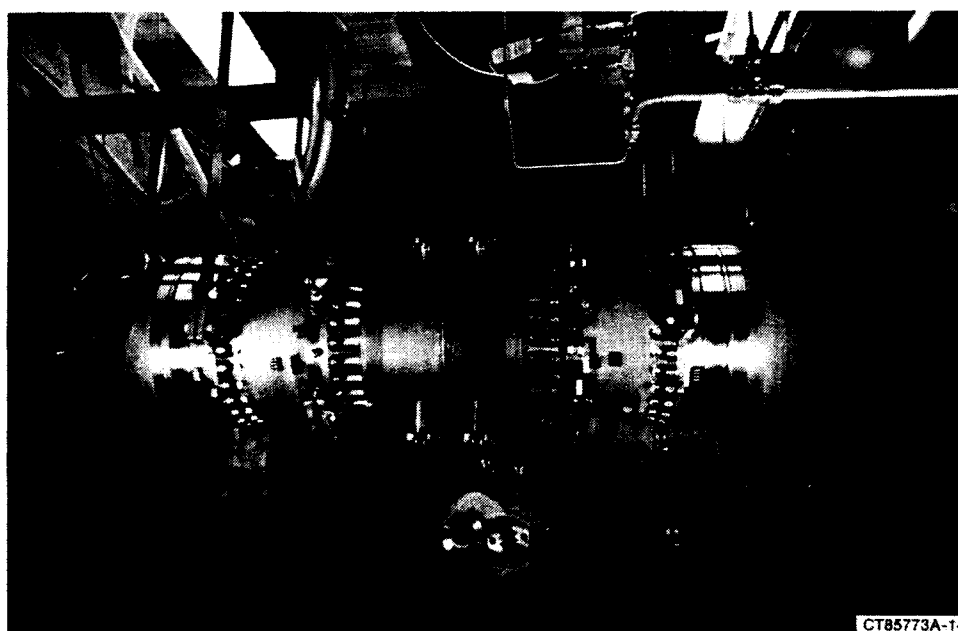
FIGURE 3-3

SPDE ENGINE CONFIGURATION
(½ of Power Module)
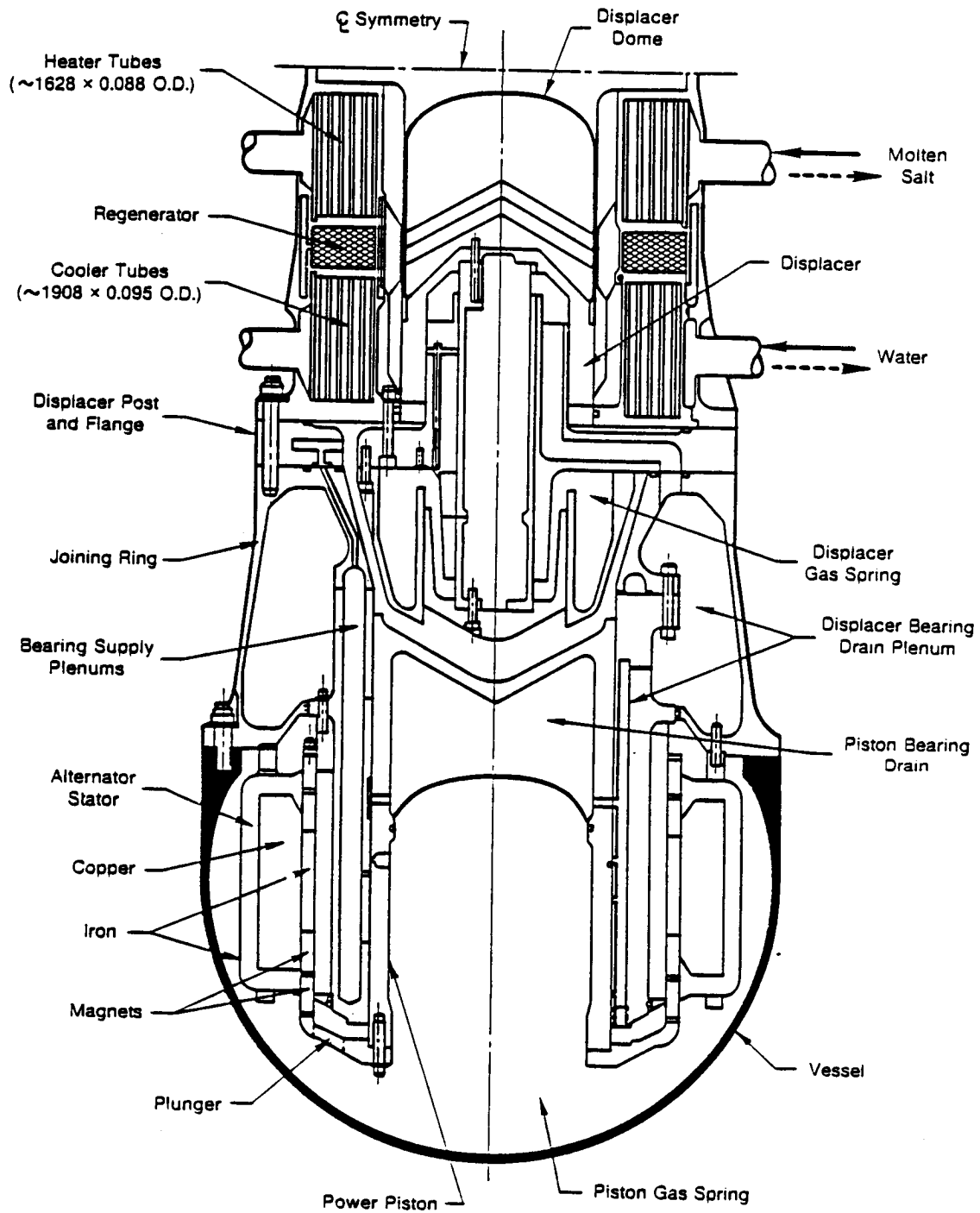
FIGURE 3-4

SPDE EXPLODED ARRANGEMENT

HEAT EXCHANGER ASSEMBLY

DISPLACER DRIVE ASSEMBLY

ALTERNATOR SECTION
ASSEMBLY
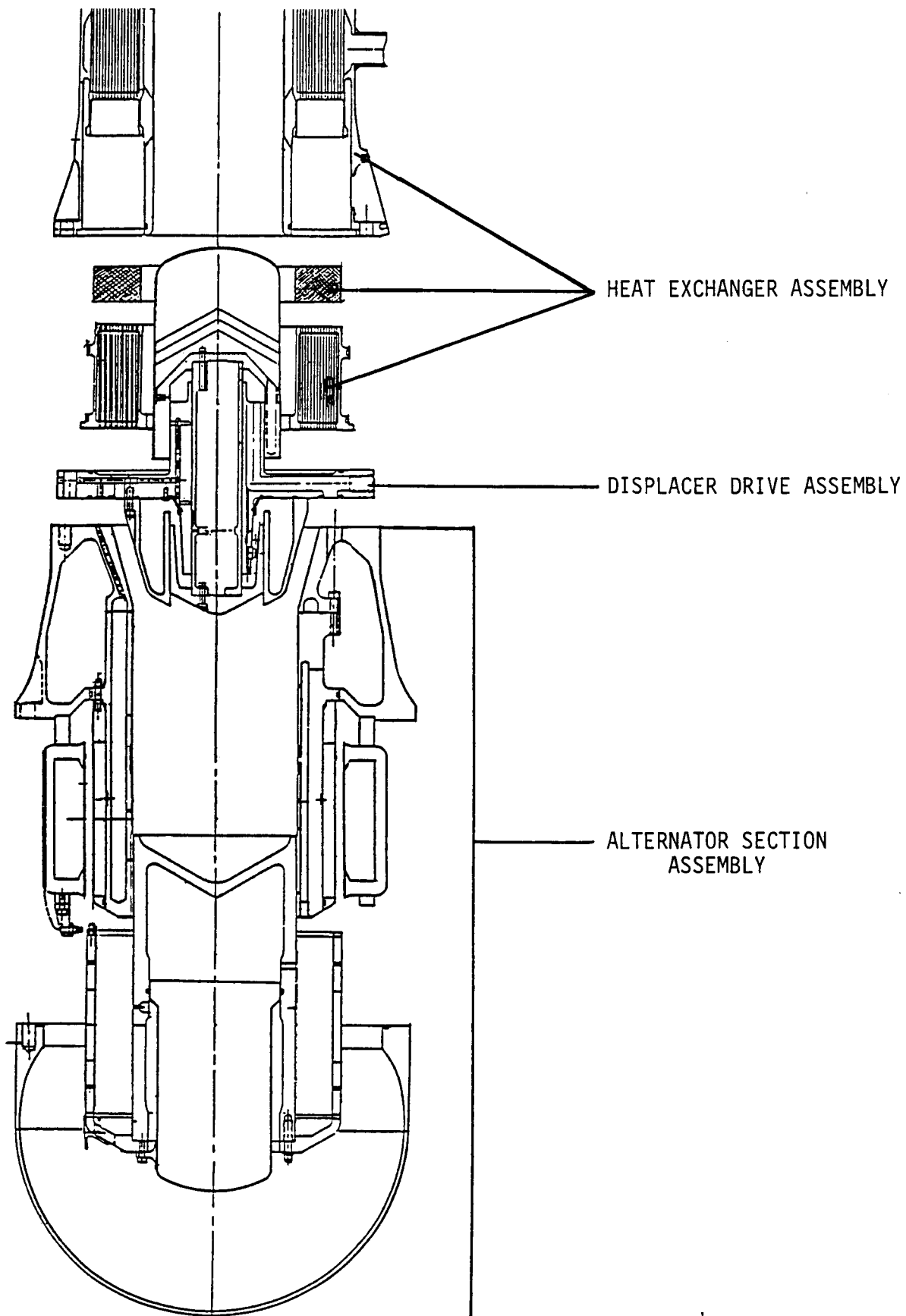
The engine operating frequency was set at 105 Hz. This was based on balancing the conflicting requirements for high thermodynamic power (high frequency), high thermodynamic efficiency (low frequency), and low alternator weight (high frequency).

A major difference between the SPDE and previous FPSE's is that to meet specific weight goals, the pressure and frequency are much higher. For example, MTI's EM engine operates at 60 Bar and 60 Hz. The SPDE also operates at a low temperature ratio (2.0 versus 3.3) which adds to the difficulty of meeting power density and efficiency goals.

Another significant deviation from previous engines is the use of beryllium. The following compares the properties of beryllium with aluminum and steel:

		BERYLLIUM	ALUMINUM	STEEL
Density	lb/in^3	.067	.10	.28
Elastic Modulus	psi/10^6	44	10	28
Elastic Modulus/Density		6.6	1	1

Beryllium was selected for the power piston and displacer because gas spring losses are a strong function of the required stiffness and the engine frequency. As the displacer or piston mass is decreased, the gas spring stiffness decreases for a selected operating frequency. Power losses due to hysteresis are proportional to the square of the gas spring stiffness; i.e., the square of the moving mass. By using beryllium with its low density, a direct mass reduction would be possible relative to aluminum or steel for the static internal parts of a flight engine.

The walls of the pistons must be very stable dimensionally to control the clearance on their bearing surfaces (0.0004 to 0.0006 inches is typical). The pistons are subject to alternating pressure loads on the walls which tends to deform them. The high modulus of elasticity of beryllium permits these to be thinner than would be possible with aluminum or steel with a further reduction of the moving mass.

3.2 Displacer Drive Assembly

Refer to Figures 3-3 and 3-4 for the components and arrangement of the displacer drive assembly.

The post and flange is the stationary backbone of the assembly. The gas spring cylinder is bolted to the post and flange to complete the stationary structure. The rod is located within the bore of the post and flange. The displacer comprising the support and the dome is bolted to one end of the rod and the gas spring piston to the other.

Hydrostatic gas bearings support the rod in the bore of the post and flange. They allow the moving assembly to travel back and forth axially without rubbing during normal operation.

The volume of the gas in the gas spring between the gas spring piston and cylinder can be adjusted by inserting stuffers. This is one of the adjustments available for tuning the dynamics of the engine. The inside of the rod and the inside of the displacer support are interconnected by passageways in the post and flange to the cavity in the joining ring. This results in a large volume with a very small pressure amplitude on it which is used as a drain for the displacer's hydrostatic bearings. It is referred to as the 'mean pressure volume'.

All sliding surfaces, with the exception of the bore of the post, are coated with chrome oxide. This has proved on other engines to have low galling tendencies during inadvertent rubs. The small size of the bore has precluded the use of chrome oxide in it. Polyond was used in this location. This is a teflon impregnated electroless nickel plating process. (This has not worked out as well in practice as was anticipated).

The stroke of the displacer relative to the stroke of the power piston is adjusted during operation by adjusting the 'displacer rod area' and also by introducing a parasitic damping power loss in the gas spring. The 'rod area' is the difference between the area exposed to the compression space pressure and that exposed to the expansion space pressure.

The compression space area is made up of two surfaces: the end of the skirt section of the displacer support, and the face of the gas spring piston. The expansion space area is the face of the dome. The rod area can be adjusted by using different size gas spring piston/gas spring cylinder pairs. Three sizes have been designed and built.

Further control of displacer stroke by parasitic damping is introduced by locating an adjustable valve in a line outside the engine. This line interconnects the displacer gas spring with the 'mean pressure volume'. When open, gas is pumped back and forth and dissipates energy due to losses at the valve. This valve can also be used to kill the engine by opening a large flow path between the gas spring and the mean pressure volume.

The assembly sequence for the displacer drive is:

1. Attach displacer support to rod;
2. Attach gas spring cylinder to post and flange;
3. Insert rod into the post;
4. Attach gas spring piston to the rod;
5. Supply air pressure to the bearings;
6. Check for freedom of axial movement; and,
7. Adjust gas spring piston cylinder if required.

The pilots for the gas spring cylinder have proven adequate for locating it without the need for fixtures such as is used on the EM.

Initially, it was intended to make the post and flange out of beryllium to meet the specific weight goal. Due to the high cost, it was decided to substitute a steel with a similar coefficient of expansion as beryllium (4130), recognizing that for a flight engine, the weight savings would justify the cost savings.

3.3 Heat Exchanger Assembly

The heat exchanger assembly comprises the heater assembly into which is inserted the regenerator and the cooler.

The heater, which is made of Inconel 718, contains 1632 tubes (.090" OD, .050" ID, 3.5" long) brazed at each end into holes in annular tube sheets, .25" thick. The tube sheets are electron beam welded into an inner cylinder and outer cylinder to form an annular cavity through which the tubes pass. The helium working gas is on the inside of the tubes and the molten salt heating fluid flows over the outside of the tubes. Diametrically opposed nozzles in the outer cylinder provide for inflow and outflow of the heating fluid. Perforated baffles in the inlet and exit plenums aid in distributing the flow into and out of the tube bundle. The outer cylinder extends to around the cooler and includes the connecting flange. The geometry is based on: 1) the desire to be able to replace regenerators; and 2) the need to control pressure and thermal stresses.

At the inception of the program, there was some uncertainty as to the eventual conditions under which the heater would be required to operate. Space applications being defined by the SP-100 Program called for using a liquid metal reactor heat source at temperature levels in the 1000-1300°K range. For the SPDE engine, no specific high temperature requirements were imposed, but it was considered appropriate to consider these future requirements to some extent. A decision was made to design the SPDE heater for a 1000-hour life at 900°K and be compatible with liquid sodium at these conditions. These requirements led to the selection of Inconel 718. It is a readily weldable alloy with reasonable creep strength at 900°K.

Brazing the tubes into the tube sheets required some development using samples to set the process conditions. A gold braze, recommended by NASA LeRc materials engineers was used to enhance joint ductility. A few leaks in two heaters had to be repaired by hand using silver solder. Mechanical drilling of the tube sheets proved to be tedious and time consuming. MTI worked with a local vendor to resolve problems with drill breakage and diametral tolerance control.

The regenerator is a simple stack of many stainless steel wire mesh screens stamped to the diametral dimensions of the regenerator section of the heater assembly. They are laid in by hand.

The cooler, of similar construction to the heater, contains 1584 tubes (.100" OD, .060" ID, 3.75" long). It is basically an annular box. Helium is on the inside of the tubes and cooling water is circulated circumferentially through the tube

bundle. The cooler is inserted into the heater assembly after the regenerator has been installed using O-rings as shown to seal the joints. For consistency, it is also made of Inconel 718.

3.4 Alternator Section Assembly

The components of the alternator section assembly are:

1. Joining Ring
2. Pressure Vessel
3. Power Piston Cylinder
4. Alternator Outer Stator
5. Alternator Inner Stator
6. Power Piston
7. Alternator Plunger
8. Cooling Jacket

The joining ring with the power piston cylinder bolted to it form the structural backbone of the assembly. The alternator outer stator is bolted to the joining ring and the inner stator is bolted to the power piston cylinder. The dimensions are such that an annular gap is created between the stators which is slightly wider (about .060 inches) than the plunger.

The power piston is located in the power piston cylinder with a small clearance (.0005 in radial) between them. The alternator plunger is bolted to the end of the power piston and is located in the gap between the stators. The pressure vessel, bolted to the joining ring, encloses the alternator cavity. A water jacket attached to the pressure vessel is used to remove heat generated within the alternator section assembly.

The joining ring and pressure vessel are made of PH13-8Mo. This is a tough, weldable stainless steel with the high strength characteristics required for lightweight pressure containing structures. The power piston cylinder is made of 4140 steel (in a space engine, this would be beryllium to meet weight goals). The power piston is beryllium, and the plunger is a composite structure. Eighteen titanum struts are welded to a titanium end plate. Samarium cobalt magnets and plastic spacers are keyed and epoxied to the struts. A carbon epoxy end ring is

used to hold the free end of the plunger. Carbon epoxy was selected for its high stiffness, which is desirable to minimize any tendency for the plunger to go out of round. The inner stator is a set of 18 blocks of Hyperco 50 laminations mounted in a plastic cage. The outer stator is formed by about 2,000 Hyperco 50 laminations in a shallow U-shape which enclose the copper stator coil. The alternator is described in more detail in Section 8.0.

The power piston is supported by hydrostatic gas bearings located on the inside diameter of the power piston cylinder. The gas cavity enclosed by the pressure vessel acts as a gas spring on the power piston. Its volume, along with the mass of the power piston assembly (i.e., power piston plus plunger) were adjusted in conjunction with estimated pressure amplitude in the compression space to produce the desired operating (resonant) frequency for the system.

The power piston gas spring is also used to supply the hydrostatic gas bearings. This is discussed further in Section 7.0. To summarize: when the piston is near the outermost position and the gas spring pressure is high, ports in the piston wall interconnect the gas spring to the bearing supply plenums located in the power piston cylinder wall.

Gas continuously flows through the bearing orifices to the drain grooves interconnected with the drain plenums in the cylinder wall. The volume of these drain plenums is augmented by interconnecting them with the volume enclosed in the interior of the power piston. The bearing flow is returned from the drain plenums to the gas spring by ports in the power piston wall which interconnect these volumes near mid-stroke of the piston motion.

4.0 THERMODYNAMICS AND DYNAMICS

4.1 Introduction

This section summarizes the thermodynamic and dynamic design analyses conducted on the SPDE power modules. The following system requirements have a direct impact on the thermodynamic and dynamic design of the machine:

- **Power Level** - 25kWe at alternator terminals dictates a mechanical power at the alternator plunger of 25.0kW/alternator efficiency (i.e., ∿27kW).

- **System Efficiency** - 25% at a temperature ratio of 2.0. The system efficiency is the product of thermodynamic, mechanical, and alternator efficiencies.

- **Specific Weight** - 8 kg/kW. The engine pressure, frequency, and stroke are the dominant parameters affecting the achievable specific weight.

- **Dynamic Balance** - casing motion amplitude less than .003 inches. Stable, balanced operation depends upon the method of interconnecting the two alternator circuits and the thermodynamic cycles.

In the following tables, the optimum values for engine parameters selected during the preliminary design are listed along with the final values of the 'as-built' engine.

As discussed above in Section 1.0, in order to minimize the weight and reduce the system complexity, it was decided to operate the system dynamically in a 'thermal oscillator' mode rather than in a 'thermal amplifier' mode. A description of these two dynamic modes of operation is given in Appendix 4-1.

4.2 Engine Thermodynamics

The objective of the thermodynamic analysis is to optimize the engine parameters (geometry, swept volumes) to maximize the system efficiency. The approach used to establish the thermodynamic design was:

- Select the working fluid and the average heater and cooler metal temperatures.

- Establish the 'fixed' engine parameters for performance optimization. Fixed parameters are the engine parameters which are not varied during the optimization runs.

- Optimize the heater, the cooler, the regenerator geometries, and the swept volumes at the design power output level.

- Evaluate the sensitivity of the major engine parameters on the system performance.

4.2.1 Working Fluid

The majority of modern high-performance Stirling engines utilize either hydrogen or helium as the engine working fluid. Because of potential metallurgical problems and the effect of hydrogen permeation on the space-application system, helium was selected as the working fluid for the demonstrator engine. By using hydrogen, a one point gain in thermodynamic efficiency was predicted.

4.2.2 Operating Temperatures

The requirement of the heat exchanger metal temperatures on the SPDE is that the ratio of the absolute average metal temperatures be 2.0. The absolute temperature levels of the heater and the cooler will depend on the type of external facility heat-transfer loops. The external hot-side, heat-transfer medium selected was molten salt solution. The details of the external heat-transfer loops are discussed in section 5.0. The average heater metal temperature was selected to be 630°K and, consequently, the cooler wall temperature was selected to be 315°K.

4.2.3 Engine Optimization

Performance analysis of the SPDE was carried out with the MTI thermodynamic/dynamic optimization code. For this analysis the average heater and cooler

surface temperatures, the operating frequency, the mean pressure and the piston stroke were all held fixed while the rest of the thermodynamic parameters (heater, regenerator, cooler geometries and the swept volumes) were optimized for the maximum system efficiency. A discussion of the design considerations associated with fixed parameters is presented below.

● Operating Frequency

In order to make a substantial reduction in the specific weight of the SPDE over past Stirling engines, the operating frequency, in the conceptual design phase, was increased from 60 Hz to 120 Hz.

● Mean Pressure

To improve the engine's capability to carry the higher inertia loads at 120 Hz operation, the engine mean pressure was raised to 150 Bar from the past maximum free-piston mean pressure of 60 Bar. Increase in mean pressure results in higher gas spring leakage and hysteresis losses. These losses were limited to acceptable levels by selecting beryllium for the engine reciprocating masses.

● Piston Stroke

The selection of piston stroke is a compromise between the conflicting engine and alternator requirements. For a fixed power level and weight, the efficiency of the linear alternator increases with increase in stroke (lower I^2R losses) while the efficiency of the free-piston Stirling engine decreases with increase in stroke (higher leakage losses). Based on past MTI experience, the piston stroke was fixed at 2.032 cm.

With the above parameters defined, the engine geometry was optimized with the following optimization parameters:

- Regenerator frontal area
- Regenerator matrix porosity
- Regenerator wire diameter
- Number of heater tubes
- Internal diameter of heater tubes

- Length of heater tubes
- Number of cooler tubes
- Internal diameter of cooler tubes
- Length of cooler tubes
- Cross-sectional area of the cold connecting ducts
- Relative phase angle between the displacer and the power piston

The optimization runs were made under the following constraints:

- A fixed pressure amplitude of 6.7 Bar in the piston gas spring. The pressure amplitude in the gas spring was set by the internal bearing feed requirement.

- Alternator efficiency was held fixed at 93%.

- The ratio between the effective displacer and piston areas was held fixed. This ratio was calculated from the concept layout for a geometrically balanced design.

- The reciprocating weight of the piston plunger was left floating. It was assumed that by using Beryllium as the piston material, the piston could be tuned to 120 Hz operating frequency with acceptable gas spring hysteresis and leakage losses.

- Due to the manufacturing and the assembly requirements, the maximum frontal area ratio between the heater and the regenerator, and between the cooler and the regenerator, was set at 0.2.

- The electrical power output at the alternator terminals was held constant at 12.5kW. The output power was held fixed during the optimization runs by varying the displacer stroke.

- The displacer was tuned to 120 Hz by varying the displacer gas spring volume.

• For each optimization run, the piston area was held fixed. In order to evaluate the influence of piston area on the system performance, optimization runs were made for different piston areas.

After completion of the above optimization runs and selection of the key design parameters, a dynamic analysis was performed to evaluate the sensitivity of the system performance to variations in the major dynamic parameters associated with the two sub-modules. The analysis indicated that at 120 Hz operation, the system was highly sensitive to variations in the displacer spring stiffness. The sensitivity to imbalances in the spring stiffness reduced with reduction in the operating frequency. In addition, the engine thermodynamic efficiency increased with the decrease in the operating frequency. However, for a given alternator size, decrease in the operating frequency results in a decrease in the alternator efficiency. From the overall system considerations, the operating frequency was reduced from 120 Hz to 105 Hz. The power module was re-optimized at 105 Hz frequency. The resulting engine geometry is shown in Table 4-1.

A final optimization run was made in which the mean pressure was also included as an optimization parameter. The mean pressure increased to 180 Bar with a corresponding thermodynamic efficiency gain of less than half a point. It was decided to retain the mean pressure at 150 Bar because of higher stress levels at 180 Bar.

4.2.4 Engine Performance

The predicted design point operating conditions are listed in Table 4-2. The power flow diagram of the engine generator set is shown in Figure 4-1. A description of various engine losses and sub-system efficiencies is given below.

● Thermodynamic Efficiency

The thermodynamic efficiency is defined as the total power generated by the engine pressure wave divided by the heat supplied by the engine heater. The total thermodynamic power is the sum of the displacer PV power, the power piston PV power, and the power required to overcome the compression and expansion space seal leakage losses.

TABLE 4-1

ENGINE GEOMETRY

	PRELIMINARY	FINAL
● DISPLACER		
Diameter	4.5 inch	4.5 inch
Effective Rod Area	0.18 sq. inch	.45/.30/?*
Maximum Amplitude	0.46 inch	0.46 inch
Mass	3.67 lbm	3.79 lbm
● PISTON		
Diameter	5.7 inch	5.7 inch
Maximum Amplitude	0.5 inch	0.5 inch
Mass	17.25 lbm	19.38 lbm**
● HEATER		
Number of Tubes	1628	1632
Tube ID	0.048 inch	0.050 inch
Tube Length (total)	2.85 inch	3.50 inch
● COOLER		
Number of Tubes	1905	1584
Tube ID	0.055 inch	0.060 inch
Tube Length	3.8 inch	3.8 inch
● REGENERATOR		
Frontal Area	33.93 sq. inch	37.15 sq. inch
Porosity	0.84	0.75
Length	0.97 inch	0.97 inch
Wire Diameter	0.001 inch	0.0016 inch

 * .45 used in initial tests

** 2.77 lbm added for tuning in initial tests

TABLE 4-1 Continued

	PRELIMINARY	FINAL
• TOTAL MEAN VOLUME	141.88 cu inch	122.5 cu inch
• VOLUME AMPLITUDE	10.234 cu inch	--
• VOLUME RATIO	13.863	11.970

	DEAD VOLUME (CUBIC INCH)		VOLUME RATIO	
	Prel.	Final	Prel.	Final
Expansion Space	26.00	20.14	2.54	1.97
Compression Space	7.67	11.97	0.75	1.17
Heater	8.38	11.33	0.82	1.11
Cooler	17.20	16.80	1.68	1.64
Regenerator	27.58	27.86	2.69	2.72
Cold Connecting Duct 1	5.37	6.10	0.52	5.96
Cold Connecting Duct 2	22.30	16.30	2.18	1.59
Appendix Gap	0.22	0.22	0.02	0.02
TOTAL	114.72	110.72		

TABLE 4-2

DESIGN POINT OPERATING PARAMETERS

- WORKING FLUID   Helium
- MEAN PRESSURE (BAR)   150
- FREQUENCY (HZ)   105
- AVERAGE HEATER METAL TEMPERATURE (°C)   358
- AVERAGE COOLER METAL TEMPERATURE (°C)   42
- DISPLACER AMPLITUDE (MM)   8.97
- PISTON AMPLITUDE (MM)   10.16
- DISPLACER/PISTON PHASE (°)   65

PRESSURE AMPLITUDES

Compression Space Pressure (Bar)   14.38
Expansion Space Pressure (Bar)   14.24
Load Side Displacer Gas Spring (Bar)   15.90
Heater Side Displacer Gas Spring (Bar)   1.57
Piston Gas Spring (Bar)   6.88

FIGURE 4-1

POWER FLOW DIAGRAM (Nominal Clearances)

$$n_{sys} = \frac{12.50}{49.49} = 0.25$$
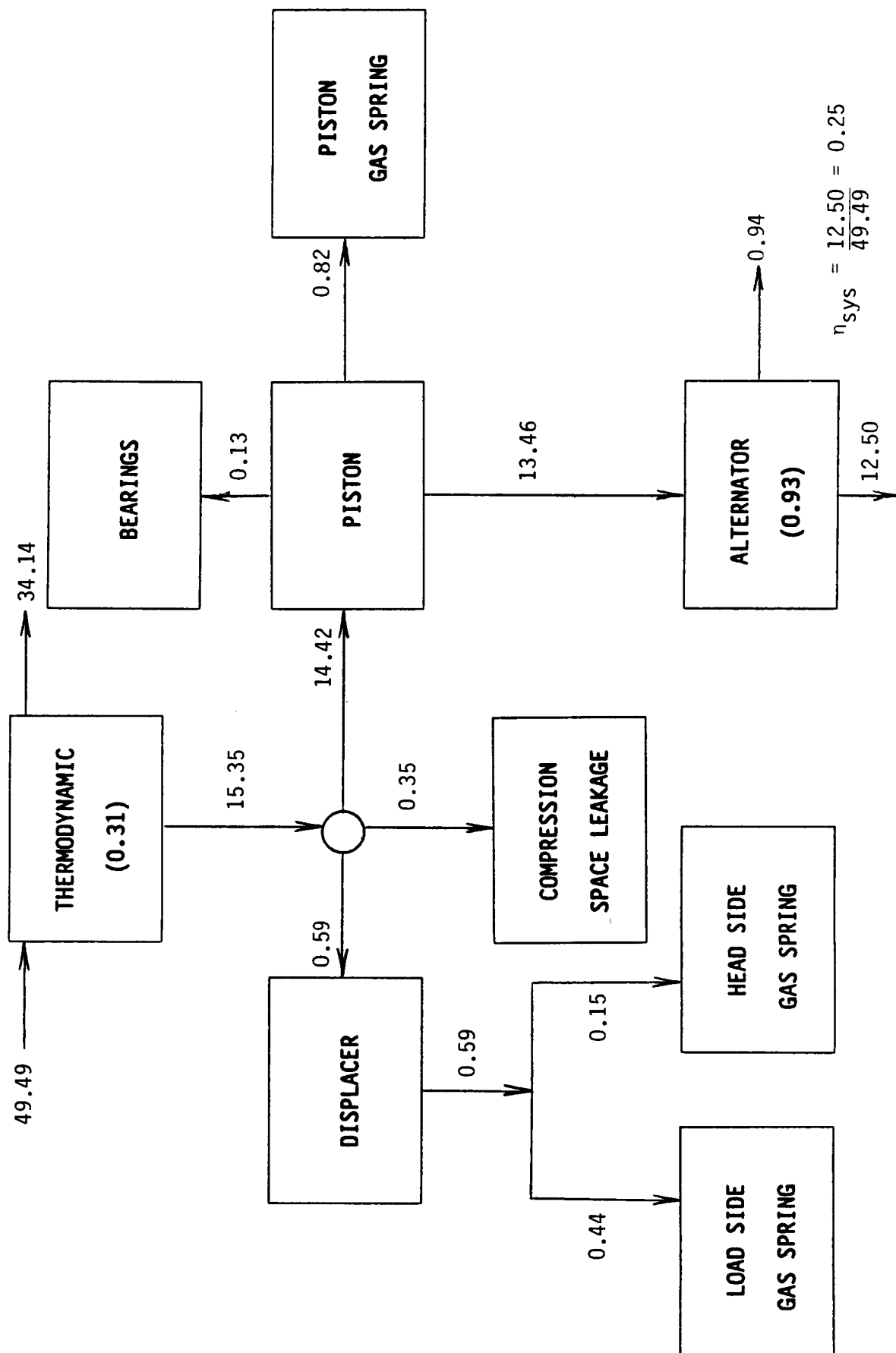
The thermodynamic losses are divided into three types. The first are those which impact the power (and thereby efficiency); the second are thermal losses which primarily impact the efficiency only; and the third are those which impact the working space temperatures and, therefore, influence the power and the efficiency of the engine.

Losses which impact power are the heat exchanger pumping, the thermal hysteresis, and the seal leakage. The seal leakage losses are not included in thermodynamic efficiency. These losses are considered to be engine mechanical losses so as to be consistent with the Kinematic engine configurations where the working spaces are sealed by piston rings.

The direct efficiency losses include conduction and radiation heat transfer from the hot end to the cold end, the reheat loss due to regenerator ineffectiveness, the appendix loss resulting from the gas shuttle between a moving displacer and a fixed cylinder and enthalpy transport in the displacer-cylinder gap, and the gas convection loss in the displacer and the regenerator stuffers.

Finite wall-to-gas heat transfer coefficient of the heater and the cooler results in a drop in heater gas temperature and an increase in the cooler gas temperatures with respect to the metal temperatures. This drop in effective gas temperature ratio across the engine reduces both the efficiency and the power generation capability of the engine.

The resulting thermodynamic efficiency is 0.31, which is 62% of the Carnot efficiency based on average heat exchanger metal temperatures.

● Mechanical Efficiency

All losses associated with the displacer and the power piston drives are logged as mechanical losses. The mechanical losses for the SPDE engine are:

- Compression space leakage
- Displacer and piston gas spring hysteresis and leakage
- Gas flow losses in the displacer and the piston volumes
- Porting losses associated with transferring the working fluid between various volumes for centering of the reciprocating components

• Bearing flow pumping power

The summary of mechanical losses is given in Table 4-3.

Mechanical efficiency is defined as the mechanical shaft power divided by the thermodynamic power. Mechanical shaft power is the net power supplied to the alternator plunger and is equal to the thermodynamic power minus the mechanical losses. The resulting mechanical efficiency is .876.

● Alternator Efficiency

The predicted alternator efficiency for the SPDE engine-generator is 0.93. The details of alternator loss mechanisms and loss numbers is given in Section 8.0.

● Overall Performance

A breakdown of the system efficiency and power is given in Table 4-4. The resulting overall system efficiency is 0.25. The system efficiency is defined as net electrical power available at the alternator terminals divided by the heat supplied by the heater.

4.2.5 Sensitivity Analysis

After the completion of the thermodynamic design, sensitivity of engine performance to critical engine parameters was evaluated. In the free piston engine configuration the two most critical parameters are the regenerator effectiveness and seal leakage losses.

The regenerator can be said to be the heart of the Stirling engine. It maintains the temperature gradient between the hot and the cold side of the engine and, therefore, provides the capability for the engine to generate power. The parameters that influence the screen regenerator performance are porosity, wire size, volume, frontal area, and the gas-to-matrix heat transfer coefficient. Out of all these parameters, the heat transfer coefficient value is most uncertain. Therefore, for a good design, system performance should have an acceptable sensitivity to reasonable variation in the heat transfer coefficient. Table 4-5 shows the sensitivity of thermodynamic and system efficiencies to changes in regenera-

TABLE 4-3

MECHANICAL LOSS SUMMARY

Thermodynamic Power = 15.35kW

Displacer Load Side Gas Spring = 0.45kW = 2.9%   (0.971)

Displacer Head Side Gas Spring = 0.15kW = 1.0%   (0.990)

Piston Gas Spring   = 0.82kW = 5.4%   (0.946)

Compression Space Leakage   = 0.35kW = 2.3%   (0.977)

Bearings   = 0.13kW = 0.8%   (0.992)

TOTAL   1.90kW

Mechanical Efficiency = (15.35-1.91)/15.35 = 0.876   (87.6%)

TABLE 4-4

OVERALL PERFORMANCE

- EFFICIENCY

Carnot Efficiency (Metal)	0.50
Thermodynamic Efficiency	0.31
Mechanical Efficiency	0.876
Alternator Efficiency	0.93
System Efficiency	0.253

- POWER (kW)

Thermodynamic Power	15.35
Piston PV Power	14.40
Alternator Plunger Power	13.44
Generated Power	12.50

TABLE 4-5

REGENERATOR EFFECTIVENESS

HEAT TRANSFER COEFFICIENT FACTOR	EFFECTIVENESS	REHEAT LOSS (kW)	THERMODYNAMIC EFFICIENCY	SYSTEM EFFICIENCY
1.0	0.984	3.83	0.310	0.253
0.5	0.968	7.70	0.286	0.232
2.0	0.992	1.92	0.324	0.264

CHANGE IN EFFECTIVENESS	CHANGE IN THERMODYNAMIC EFFICIENCY
-0.016	-0.024
0.008	0.014

tor heat transfer coefficient. This level of sensitivity is similar to the earlier kinematic and free-piston engine designs.

The sensitivity of mechanical and system efficiency to changes in various seal clearances is shown in Table 4-6. the system efficiency drops from 25.3% to 24.7% as the seal gaps are changed from the nominal clearances to the clearances obtained for the maximum tolerance band.

4.2.6 Power Margin

SPDE engine design was executed with 25% over-stroke capability in the displacer and piston strokes over the nominal strokes. Figure 4-2 shows a plot of power generated by the engine and engine efficiency at at various piston overstrokes.

4.3 Engine Dynamics

The SPDE power module consists of two identical 12.5kW sub-modules in an opposed in-line configuration. The following gives a brief description of the dynamic analysis performed on a single engine sub-module followed by the dynamic analysis of the overall power module system.

4.3.1 Single Engine Sub-Module Dynamics

The purpose of the dynamic analysis is to ensure that the engine reciprocating elements will oscillate with the frequency, amplitude and relative phase in a manner consistent with the assumptions made in the thermodynamic analysis. This is achieved by providing gas springs on the reciprocating elements so that the unbalanced forces due to working fluid and inertia are balanced by the gas spring stiffness forces.

The gas forces on the displacer are due to the heat exchanger pressure drop acting on the displacer hot side area, and the compression space pressure acting on the effective displacer rod area. Effective displacer rod area is the difference between the hot and the cold side areas of the displacer.

Analyses show that the displacer and the power piston of each engine sub-module will operate at the desired vibration mode under the steady-state operating

4-15

TABLE 4-6

SEAL SENSITIVITY - LOSS SUMMARY

	CLEARANCE	
	NC	UC
LOSSES		
● Load Side Gas Spring - Compressor	188W	307W
● Load Side Gas Spring - Mean	64W	116W
● Heater Side Gas Spring - Compressor	181W	290W
● Compressor - Mean	96W	166W
● Piston Gas Spring - Mean	27W	47W
EFFICIENCY		
● η Mech	0.875	0.854
● η Sys	0.253	0.247

NC - Nominal Seal and Bearing Clearances
UC - Seal and Bearing Clearances at the Upper Tolerance Limit

FIGURE 4-2

MECHANICAL POWER CAPABILITY AT OVERSTROKE OPERATION

$P_{TH} \propto X_p^{1.638}$

$P_{mech} \propto X_p^{1.62}$

* Efficiency – %

OVERSTROKE LIMIT = 25% x NOMINAL STROKE

Y-axis: POWER RATIO = $\dfrac{\text{OUTPUT POWER}}{\text{DESIGN POWER (NOMINAL)}}$

X-axis: STROKE RATIO (X_p/X_{pd})

Data points: 27.2*, 26.9*, 26.6*, 26.3*, 26.0*
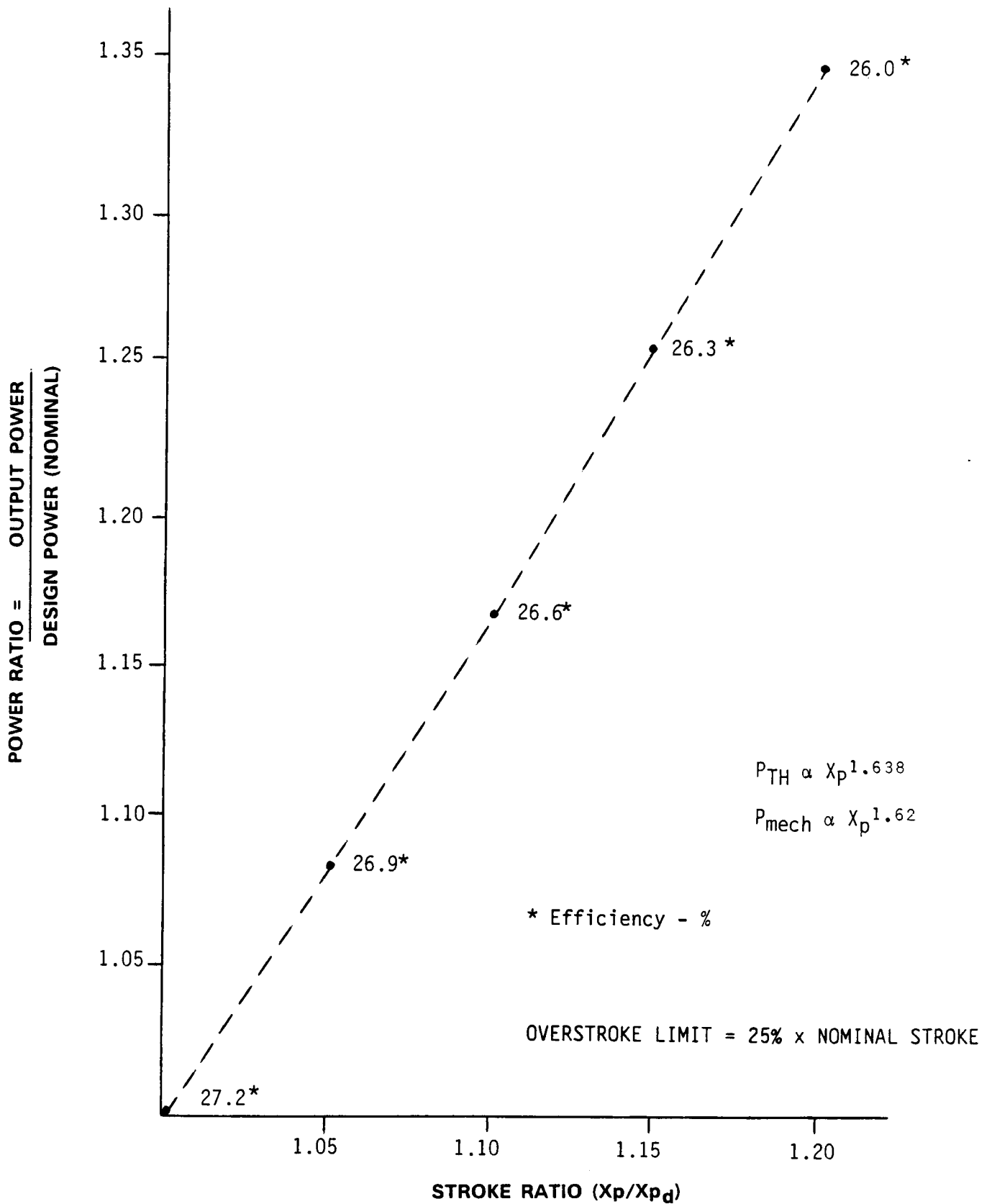
conditions. Whether the engine can reach the steady-state operating point depends upon the transient behavior of the power module and the load.

Figure 4-3 shows the dynamic model of the sub-module connected to the load by a rectifier-filter circuit.

For the demonstrator engine the load voltage is held constant by an active control means. This is achieved by dividing the load bank into ten individual resistors, out of which nine resistors are switched in or out discretely and the tenth is modulated proportionally by a fast response pulse width modulation scheme. In the dynamic model, the filter and the load at the rectifier output terminals can be simulated by a constant voltage source.

The transient analysis predicted that the system would be unstable with the design value of the alternator inductance. It should be noted that this analysis is conservative in that the engine parasitic damping was not included in the model.

Further analysis indicated that the system could be stabilized

- by reducing the alternator inductance to half of its designed value;
- by increasing the displacer mass by a factor of 2; or,
- by adding .15 ohms of series resistance in the AC side of the electrical circuit.

Since the alternator had already been designed before the stability analysis was performed, changing the alternator inductance was not a viable approach to stabilize the engine. Design studies indicate that the alternator inductance can be reduced. For space system applications, this will involve system weight tradeoffs.

Increasing the displacer mass increases the gas spring stiffness requirement resulting in higher gas spring losses and higher "Q" of the dynamic system.

Based on the above, it was decided, for laboratory testing, to stabilize the system by adding series resistance in the electrical circuit. Since the stabili-

FIGURE 4-3

SYSTEM ELECTROMECHANICAL SCHEMATIC
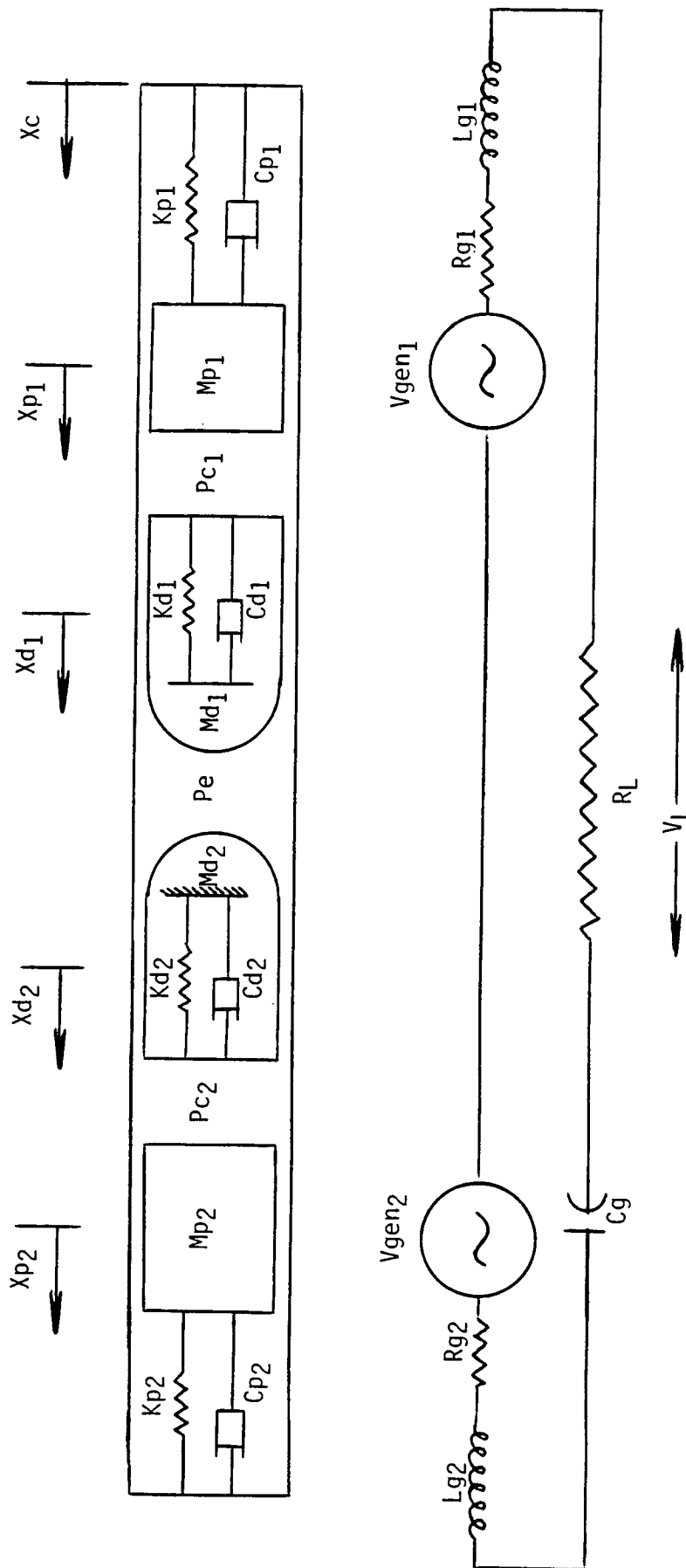
ty analysis was conservative, tests will be performed to evaluate the influence of the series resistance on the system stability.

4.3.2 Overall Power Module Dynamics

For the two engine sub-modules to operate at 180 degrees phase to each other (in order to have theoretically zero casing motion), a power flow path should exist between the two sub-modules that is stable in nature and provides minimum performance penalty. This power flow path can be provided

- electrically, by connecting the two alternators in series or parallel with each other;
- mechanically, by connecting the two thermodynamic cycles at the expansion space, or by connecting the two piston gas spring volumes; or
- both electrically and mechanically by the combinations of the above.

Parallel connection of the alternators can result in high circulation currents in the electrical circuits during transient operation. Series connection of the alternators without mechanical coupling of the modules results in a destabilizing power flow path.

The overall weight of the power module is lower if the two engines are connected at the expansion space compared to the two engines having a common piston gas spring.

Based on the above, the engines were connected mechanically by providing a common expansion space, and also electrically by connecting the two alternators in series with the load.

Figure 4-4 shows the transient response of the displacer and the piston motion. The dynamic model used for this analysis is shown in Figure 4-5.

4.3.3 System Vibration

Ideally, the SPDE power module will have no net casing motion because the two engine sub-modules are connected in opposed, in-line configuration. However, some net casing motion is expected because of unavoidable differences in the

FIGURE 4-4

TRANSIENT RESPONSE OF THE DISPLACER AND PISTON MOTION
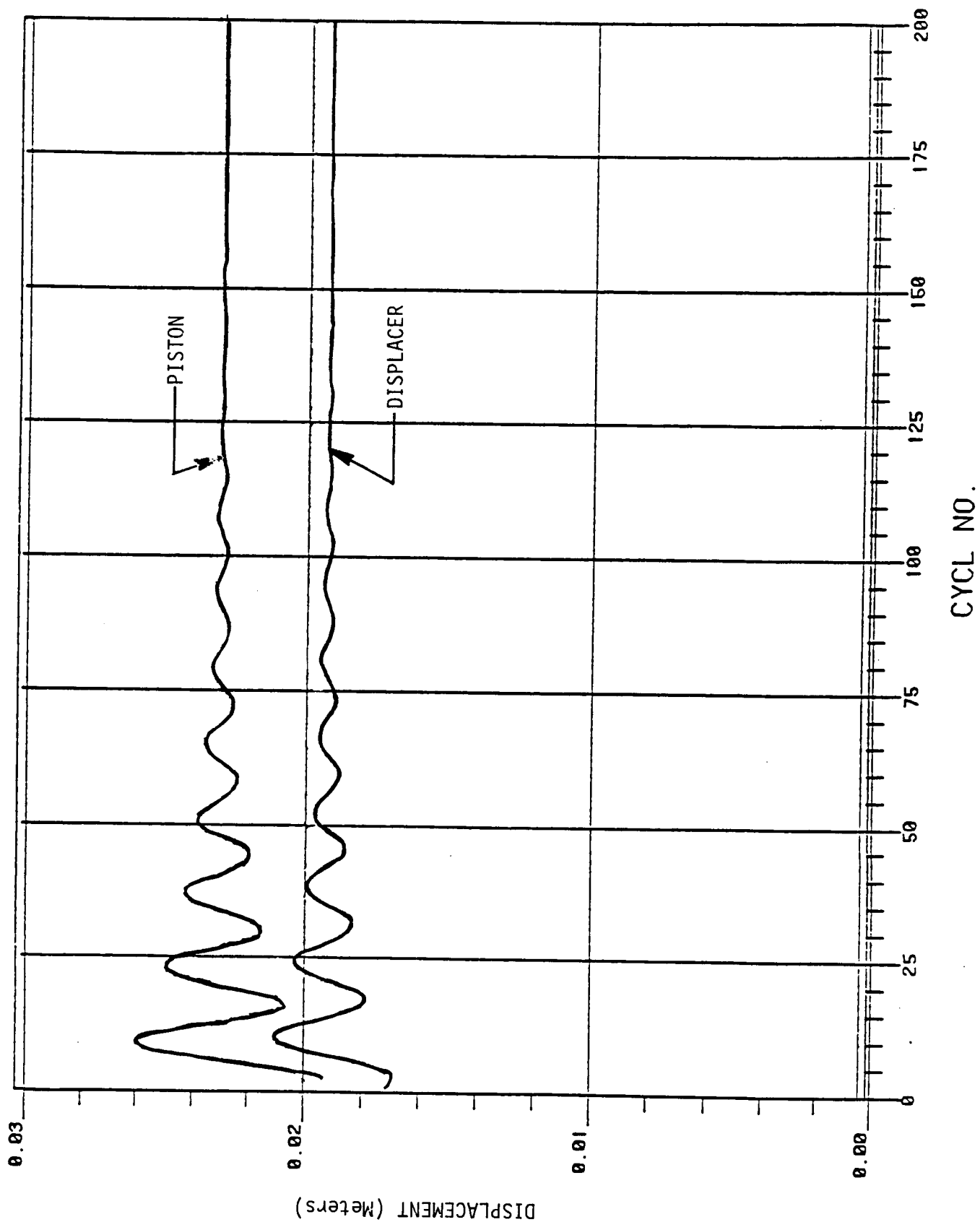
FIGURE 4-5

SPDE DYNAMIC MODEL
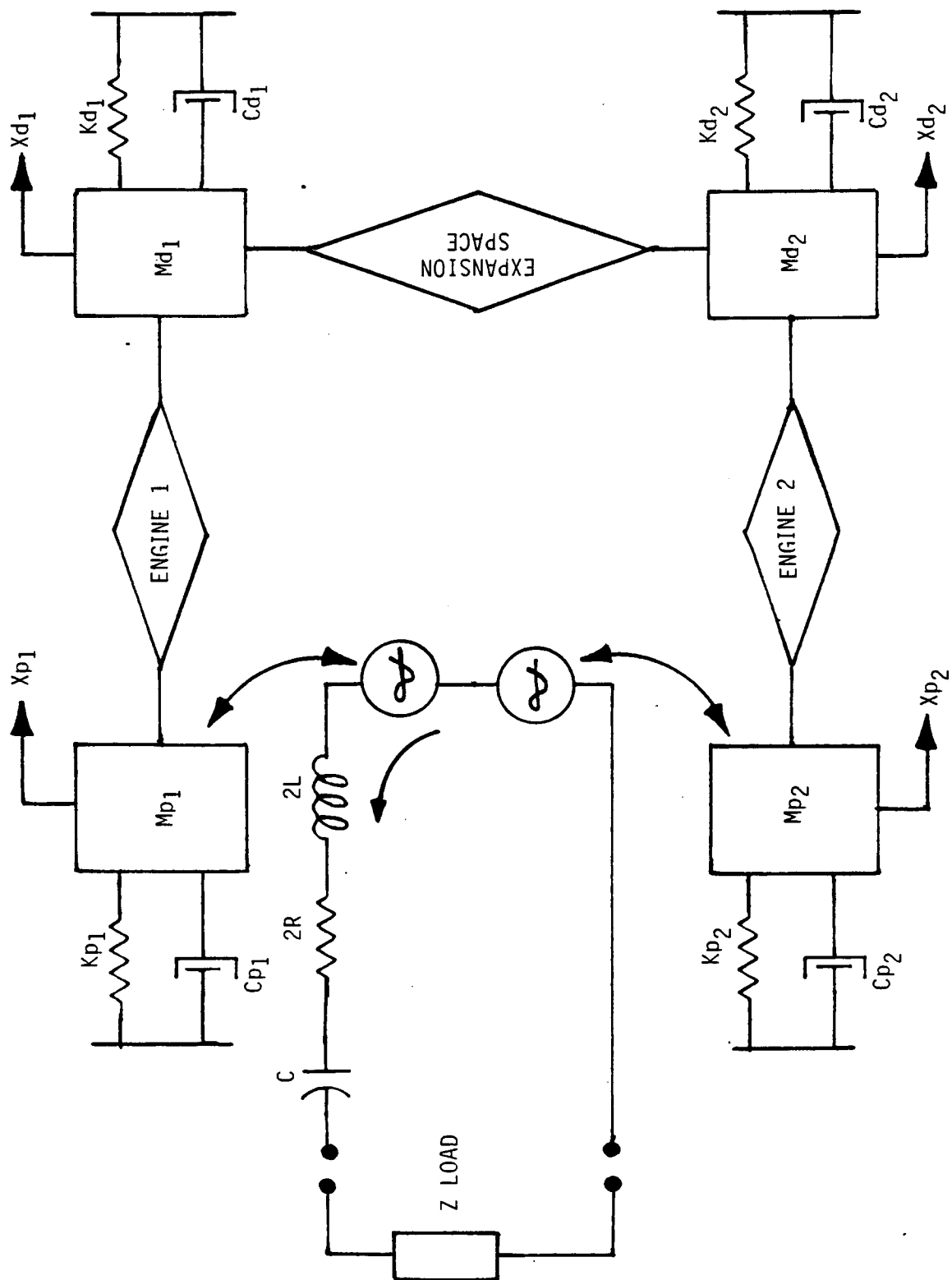
thermodynamic, mechanical, and electrical parameters associated with the individual sub-modules. Table 4-7 shows the sensitivity of power module performance to variations in the dynamic parameters associated with the two sub-modules. The analysis concluded that for reasonable imbalances imposed by the manufacturing tolerances, the impact on the available power is negligible, and the maximum casing vibration of .025mm is well under the allowable casing motion amplitude of .076mm.

CD, CP, KD and KP in the above table are the displacer damping, piston damping, displacer stiffness, and the piston stiffness coefficients. 1 and 2 refer to the two sub modules. R designates that the parameter has been normalized to the nominal design value.

XD and XP are the displacer and piston amplitudes respectively. PHID is the phase angle, in degrees, between the displacer and the power piston. FREQ is the operating frequency in hertz, and PWR is the power available at the rectifier input terminals.

XC is the casing motion amplitude in millimeters.

The damping coefficients, CD1, CP1, CD2, and CP2, were calculated from the manufacturing tolerance band. CD1 and CP1 are for seals with the minimum possible gap. CD2 and CP2 are for seals with the maximum possible gap.

The displacer and piston stiffnesses, KD1 KP1, KD2, and KP2, were calculated from the respective gas spring geometries and an assumed displacer and piston offset of 20% of the nominal design point amplitude. For KD1 and KP1, offsets were assumed to be out of the gas spring volumes, and for KD2 and KP2 offsets were assumed to be into the gas spring volumes.

TABLE 4-7

SENSITIVITY TO UNBALANCED DYNAMIC PARAMETERS

	CD1R 0.833	CD2R 1.516	CP1R 0.866	CP2R 1.180	KD1R 0.987	KD2R 1.103	KP1R 0.973	KP2R 1.029	Reference
XD1R	1.11		1.00		1.02		0.960		1.0
XP1R	1.01		1.00		1.01		0.984		1.0
XD2R	0.91		1.00		0.97		1.04		1.0
XP2R	0.99		1.00		0.99		1.02		1.0
PHID1	65.74		64.67		58.80		64.67		65.0
PHID2	64.27		65.21		71.25		65.11		65.0
FREQ	105.00		105.00		105.00		105.00		105.0
PWRR	1.01		1.00		0.985		1.00		1.0
XCR	0.285		0.0317		0.33		0.219		0.0

CD1R, CD2R, CP1R, etc. are normalized to nominal design damping and stiffness values

PHID is displacer phase angle relative to power piston (Xp)

PWRR is electrical power normalized to nominal design values

XCR is casing motion normalized to .003 inch amplitude

5.0 THERMAL ANALYSIS

The objectives of the thermal analysis performed to support the design of the SPDE engine and the associated facilities were:

1. Evaluate design variables (i.e., the fluid type, flow rate, heat exchanger geometry) for the external heating system, the engine heater, the engine cooler, and the external cooling system and recommend design parameters for these systems and assemblies such that the heat input, heat output, and temperature conditions (temperature ratio) can be attained, controlled, and measured within acceptable accuracy.

2. Select an acceptable method for controlling the temperatures in the alternator coil and alternator section assembly and predict key temperatures in the assembly.

3. Determine thermal losses associated with heat transfer from the hot side to the cold side of the displacer

The analyses are described below under the following headings:

- Heater-Shell Side Analysis
- Cooler-Shell Side Analysis
- Alternator Section Thermal Analysis
- Displacer Thermal Analysis

5.1 Heater-Shell Side Analysis

As described in Section 3.0, the heater design configuration is a large array of closely packed tubes located between tube sheets in an annular region around the displacer assembly. The number, length, and inside diameter of the tubes was selected based on thermodynamic analysis of the engine. The wall thickness was based on strength considerations.

The method selected to supply heat to the engine was to circulate a heated fluid circumferentially over the outer surfaces of the tubes in the heater. Following

a review of potential fluids for this use, the salt mixture called 'HITEC' was selected for the heating fluid. Table 5-1 lists the properties of HITEC. It can be used over the range 500°K to about 850°K. Design point testing on the SPDE (temperature ratio = 2.0) using water for the fluid in the cooler at 320 to 350°K requires that the heater operate in the 650 to 700°K range. HITEC meets this requirement and also provides flexibility to extend testing to higher temperatures if needed.

The objectives of the shell side thermal analysis were:

- Calculate tube surface temperatures as a function of
  - packing arrangement
  - flow rate
  - heat input

- Calculate pressure drop versus flow rate

- Select reference packing arrangement and flow rate (pump size)

Let: T_{fi} = Temperature of salt entering the heater

T_{fo} = Temperature of salt leaving the heater

G_f = Volumetric flow rate

ρ_f = Salt density

C_f = Salt specific heat

Q_{in} = Total heat into the engine heater

$$Q_{in} = \rho_f \, G_f \, C_f \, (T_{fi} - T_{fo})$$

$$T_{fa} = \text{Average fluid temperature} = T_{fi} - .5(T_{fi} - T_{fo})$$

During testing, the heat input (Q_{in}) to the engine and the average fluid temperature are determined from measurements of G_f, T_{fi}, and T_{fo} using known values of ρ_f and C_f. The following table show $T_{fi} - T_{fo}$ and T_{fa} versus G_f for Q_{in} = 50kW at T_{fi} = 650°K (710°F) which are nominal design operating conditions.

TABLE 5-1

HITEC PROPERTIES

TEMPERATURE °F	°K	VISCOSITY (μ) Cpoise	N-S/M²	DENSITY (ρ) gm/cc	kg/M³	THERMAL CONDUCTIVITY W/M°K	SPECIFIC HEAT(Cp) J/kg°K	ρ/μ
400	477	7.5	.0075	1.93	1930	.434	1563	2.57×10^5
500	533	4.4	.0044	1.89	1890	.426	1563	4.29×10^5
600	588	3.0	.0030	1.85	1850	.393	1563	6.17×10^5
700	644	2.2	.0022	1.81	1810	.362	1563	8.22×10^5

G_f	$T_{fi} - T_{fo}$	T_{fa}
(gpm)	(°K)	
10	28.0	650-14 = 636
15	21.0	650-10.5 = 649.5
20	14.0	650-7 = 643
25	11.2	650-5.6 = 644.4
30	9.3	650-4.7 = 645.3

The tube surface temperature equals the fluid temperature minus the film drop required to drive the heat into the tubes. Since there is no practical way to instrument the tubes to measure wall temperature, it is necessary to depend on calculations of film drop. To minimize errors associated with imperfections in analysis, it is desirable to make the calculated film drop as low as practical.

For uniform flow and heat transfer:

Let: h = Convective heat transfer coefficient

A = Surface area

Q = Heat input

Then: $\Delta T_{film} = Q/h\,A$

Reference "Heat Conduction", Ozisik, eq. 9.108b

For flow over an array of tubes of diameter D with lateral spacing S_T and longitudinal spacing S_L:

$$h = (K/D)(1.13C)\,R_e^n\,P_r^{.33}$$

K = Fluid thermal conductivity

R_e = Reynolds number = $V_{max}\,D\rho/\mu$

V_{max} = Maximum velocity in bundle between tubes

μ = Fluid viscosity

ρ = Fluid density

P_r = Prandtl number - $C_p\,\mu/K$

C_p = Specific heat

$$h = 1.13C\,K^{.67}\,\rho^n\,D^{n-1}\,C_p^{.33}\,\mu^{-(n-.33)}\,V_{max}^n$$

The constants C and n are functions of D, S_T, and S_L. V_{max} is a function of G, D, S_T, the number of transverse tube rows, and the uniformity of the flow G in the tube bank.

The packing arrangement was selected based upon a combination of fabrication considerations and heat transfer considerations. The holes in the end plates (and consequently the tubes) were arranged as uniformly spaced in concentric rows (i.e., the same number of tubes per row). The radius of each row of holes was selected so that the minimum dimension between the holes in adjacent radial rows was identical. The dimensions were selected so that the number of tubes desired for heat transfer on the gas side could be placed in the annular space adjacent to the regenerator. This arrangement is shown in Figure 5-1. It permits relatively simple indexing of the machine used to drill the holes while maintaining a pattern which has uniform flow resistance in the circumferential direction. This should help minimize non-uniformity of flow across the tube bank. Estimates of flow at the inner and outer edges were made and the effect on uniformity of flow was estimated to be small.

For the SPDE heater:

$$D = .09" \qquad S_T = .26" \qquad S_L = .16"$$

The constants C and n are functions of D, S_T, and S_L. From Table 9.3 of the reference, C = .469, μ = .569. Using these constraints and the material properties at $\sim$700°F and dimensions in SI units:

$$h = 12923 \, V_{max}^{.569} \text{ watts/m}^2 \text{ °K}$$

The surface area of the tubes is .893 in^2. The film drop is thus:

$$\Delta T_{film} = 4.3 \, (Q/50,000)/V_{max}^{.569}$$

Assuming uniform flow G in gpm:

$$V_{max} = .786 \, (G/25) \, m_s, \text{ and}$$
$$\Delta T_{film} = 5.0$$

FIGURE 5-1

HEATER TUBE LAYOUT

4.302 R
4.180 R
4.056 R
3.930 R
3.802 R
3.672 R
3.540 R
3.406 R
3.270 R
3.132 R
2.992 R
2.850 R

1.32°

.093 DIA THRU, 12 HOLE CIRCLES ON RADII SHOWN
.092 136 EQ SPACED HOLES PER CIRCLE AS SHOWN
1632 HOLES TOTAL

⊕ | .002 DIA
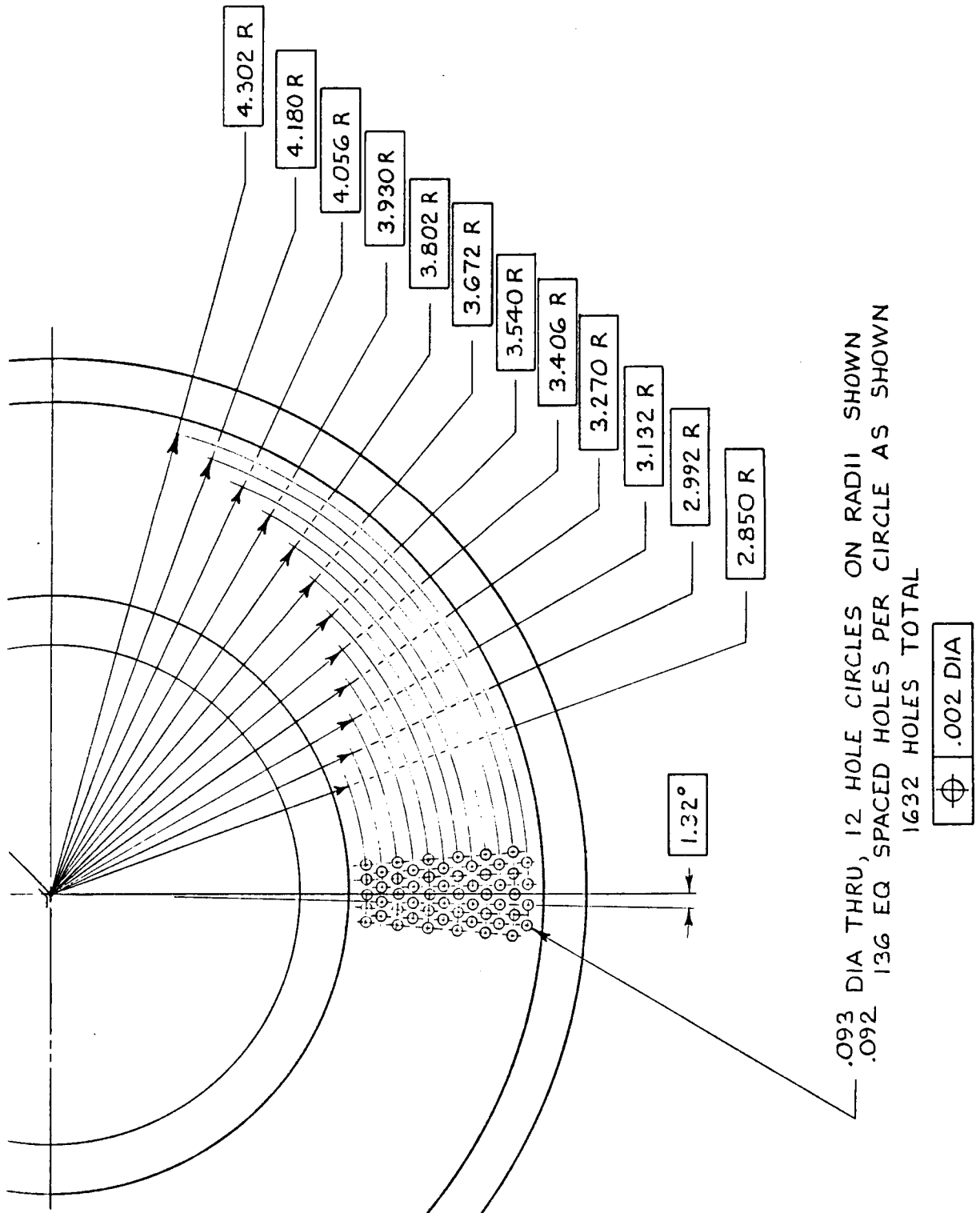
Since the film drop is only 5°K at nominal conditions, errors due non-uniformity of flow will be negligible.

5.2 Cooler-Shell Side Analysis

The configuration of the cooler is very similar to the heater. The coolant is a 50/50 mixture of water and ethyl glycol. Heat is rejected from the water by circulating it through an air-cooled radiator. The water temperature can be thermostatically controlled between 320°K and 350°K.

Following the same process as outlined above for the heater analysis, the temperature rise of the water between the inlet and the outlet as a function of flow rate in shown in the following table:

COOLER SHELL SIDE ANALYSIS

G_f (gpm)	$T_{fi}-T_{fo}$ (°K)
10	14.8
15	9.9
20	7.4
25	5.9
30	4.9

The above temperature difference is based upon a nominal heat rejection of 37.5kW per cooler.

The tubesheet hole layout selected for the same reasons as discussed above for the heater is shown in Figure 5-2.

The film drop between the tube walls and the water is calculated as for the heater for uniform flow to be:

$$\Delta T_{film} = 12.0 \ (25/G)^{.565} \ (Q/37,500)$$

FIGURE 5-2

COOLER TUBE LAYOUT

4.204 R
4.100 R
3.994 R
3.886 R
3.776 R
3.664 R
3.550 R
3.434 R
3.316 R
3.196 R
3.074 R
2.950 R

1.36°

.103 DIA THRU, 12 HOLE CIRCLES ON RADII SHOWN
.102 132 EQ SPACED HOLES PER CIRCLE AS SHOWN
1584 HOLES TOTAL

⊕ | .002 DIA
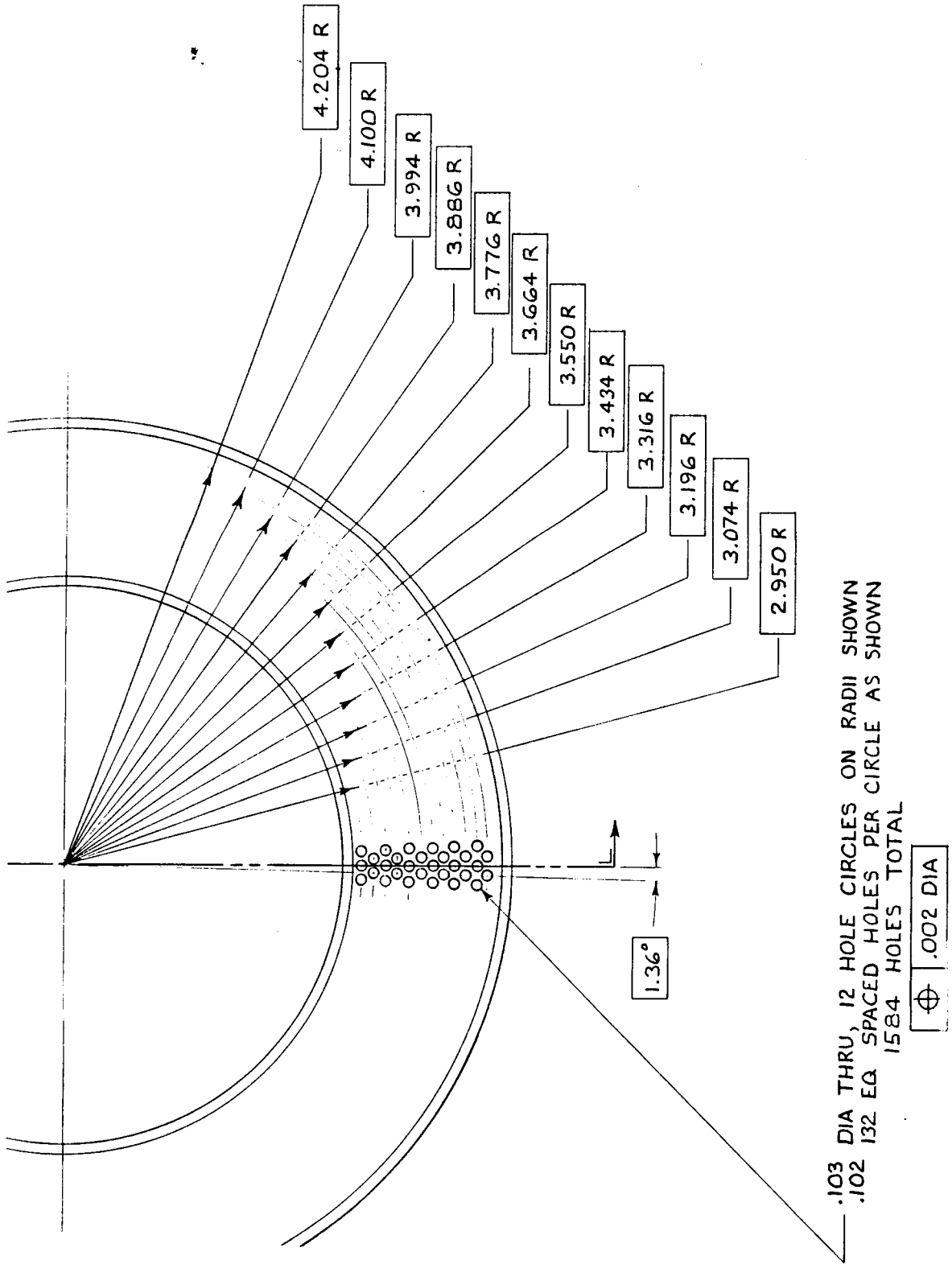
5.3 Alternator Thermal Analysis

Figure 5-3 shows the alternator section for one side of the engine.

The total heat generated at the design point (stroke=20mm, frequency=105 Hz) is
as follows:

ALTERNATOR		886W
Outer Stator Copper Loss	(500W)	
Outer Stator Iron Loss	(239W)	
Inner Stator Iron Loss	(147W)	
HYSTERESIS AT SURFACES		406W
GAS LOSSES		652W
Bearings	(200W)	
Ports	(200W)	
Leakage	(89W)	
Windage	(163W)	
TOTAL		1944W

Compared to the nominal 37.5kW rejected to the cooler, this is relatively small;
however, it must be dissipated without excessive temperatures.

The approach to removing the heat from the alternator section is to transfer it
to the pressure vessel by convection between the gas (helium) and the vessel wall
and remove it from the vessel by cooling on the outside of the vessel wall. In
SPDE, no attempt is made to simulate the cooling that might be applied in a space
application. Cooling in space, however, would probably be by active cooling of
the vessel or passive (direct radiation) cooling of the vessel.

Forced air cooling of the vessel outer surface was considered but rejected in
favor or water cooling. Water cooling was selected because:

FIGURE 5-3

ALTERNATOR TOROIDAL FLOW AND TEMPERATURES
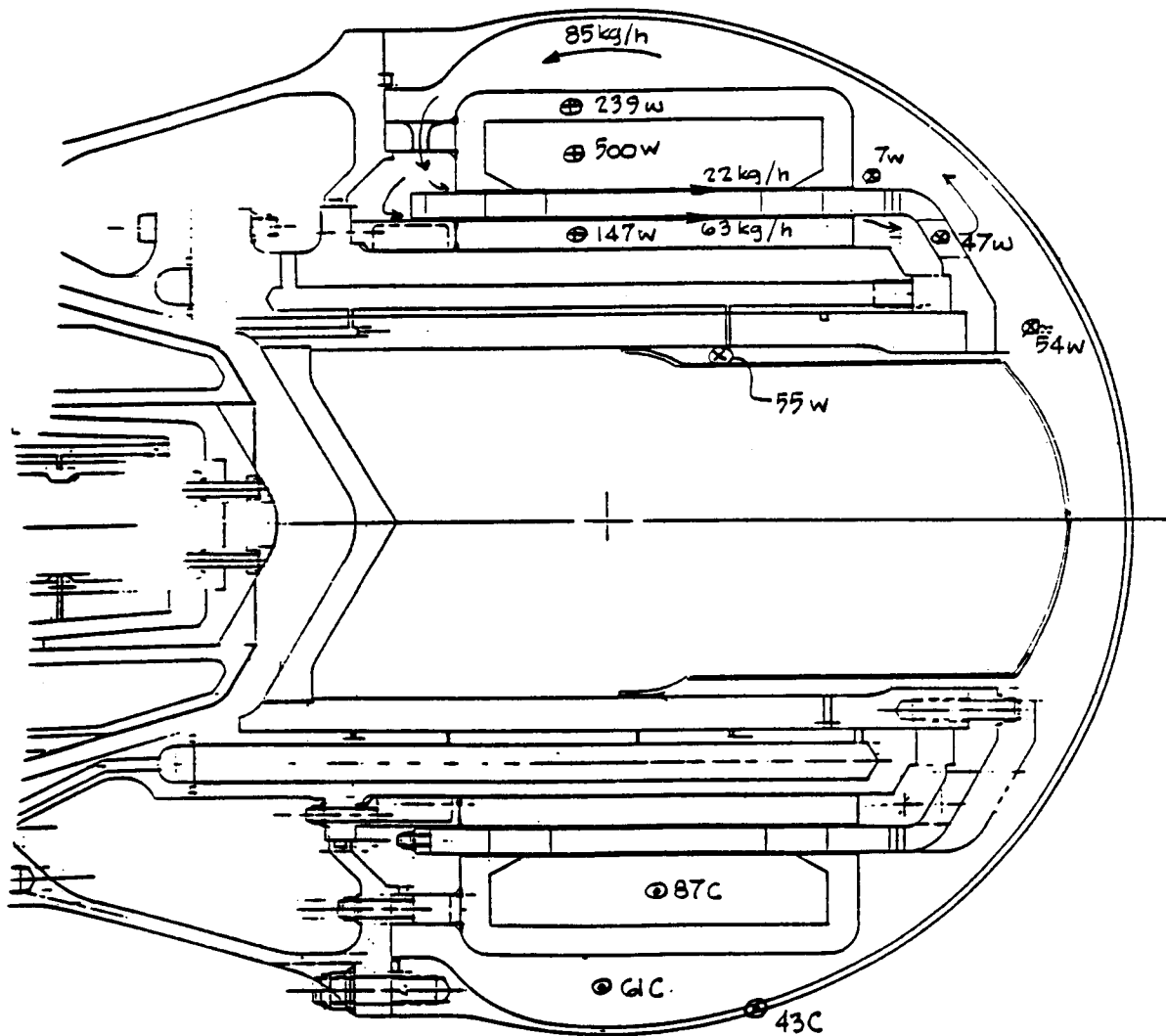
HEAT GENERATION	
Copper/Laminations	886 W
Hysteresis	406 W
Bearings and Ports	400 W
Pumping	163 W
Seals	89 W

⊗ Pumping

⊕ Copper/Laminations

⊙ Temperature

1. A water system was planned for the main engine heat rejection, so adding flow in a water jacket around the vessel was relatively simple and straightforward.

2. Measurements can be made on a water system to give a relatively accurate measure of the heat rejected from the alternator section. This is important for getting a heat balance on the engine and also for comparing actual heat loss to predictions.

3. Water cooling is very positive and results in a near isothermal vessel so non-axisymmetric gradients in the assembly and associated distortions are minimized.

Having selected water cooling for the vessel, it remained to design the alternator section assembly such that the heat was transferred to the vessel. The primary source of concentrated heat is in the alternator stators. The maximum temperature of the copper coil must be held below the breakdown level of the wire insulation.

As the power piston and plunger oscillate (±20mm at 105 Hz), the helium in the assembly is vigorously agitated which tends to enhance heat transfer between metal surfaces and the gas. To further augment heat transfer, a one-directional toroidal flow is induced around the alternator stator by incorporating passages through the alternator support ring, which have a high resistance to flow radially outward and a low resistance to flow radially inward. This is accomplished by providing a square edge entrance to the inside and a radiused entrance to the outside.

Table 5-2 shows the results of analyses conducted to determine the vessel, gas, and stator temperatures for:

*   No vessel cooling flow (radiation to ambient) and no toroidal flow;
*   Water cooling on the vessel and no toroidal flow; and,
*   Water cooling on the vessel and toroidal flow.

As can be seen, without vessel cooling, relatively high temperatures that could damage insulation are reached. With water cooling, temperatures are moderate.

5-11

TABLE 5-2

SPDE ALTERNATOR TEMPERATURES

105 Hz
0.4 inch Amplitude

	P.V. TEMPERATURE (°C)	AVERAGE HELIUM TEMPERATURE (°C)	MAXIMUM COIL TEMPERATURE (°C)	AVERAGE COIL TEMPERATURE (°C)
No Cooling Flow No Toroidal Circulation	339	357	454	∿400
Hemispheral Water Jacket No Toroidal Circulation	43	61	158	129
Hemispheral Water Jacket Toroidal Circulation	43	61	87	79

The toroidal circulation provides even more margin bringing the coil maximum temperature to below 100°C.

5.4 Displacer Thermal Analysis

Since the top of the displacer dome is exposed to the expansion space, it will operate at the expansion space gas temperature. The lower side of the displacer will run close to the cold side temperature. Heat transfer across the displacer will be a combination of radiation and convection. Baffles in the displacer dome break the dome region into cavities. One baffle results in two cavities, two baffles three cavities, etc.. Under steady state conditions from continuity considerations, the heat flow across each cavity must be the same.

If the effect of the oscillating motion of the displacer is neglected, the heat transfer from convection in a 1g environment can be computed from standard formula for natural convection.

Radiation can be estimated by approximating the dome cavity to rectangular boxes, hot on one side and cold on the opposite side.

The net heat flow for one baffle and two baffles is estimated at 193 watts and 120 watts respectively, which is relatively small compared to the nominal 50KW of heat input to each side of the engine.

An estimate was made of the effect of displacer vibration on convective heat transfer. This is a complex problem for which an exact solution is not available. A bounding calculation can be made by assuming the maximum acceleration of the displacer during each half cycle can be treated as a steady acceleration. From Figure 7.2 "Principles of Heat Transfer" by F. Kreith, the convective heat transfer is proportional to the Grashof number to the .32 power. For the mean displacer acceleration of 450g, the enhancement in convective heat transfer is estimated to be $(450 / \pi)^{.32} = 4.59$.

The bounding value for heat flow across the displacer due to radiation plus convection is calculated to be 650 watts for one baffle and 392 watts for two baffles. For the two baffle geometry selected, the net heat flow is between 120 watts and 392 watts, with 200 watts a reasonable estimate for design purposes.

6.0 STRUCTURAL ANALYSES

6.1 Introduction

This section summarizes the results of critical stress analyses performed on the SPDE described in Section 3.0.

The engine is designed to operate at a mean pressure up to 150 Bar (2175 psi) and a frequency of 105 Hz. For the current program, the molten salt enters the heater at approximately 650°K (710°F) and water/glycol enters the cooler at approximately 300°K (80°F) to provide an average heat exchanger metal surface temperature ratio of 2.0. There is an axial temperature gradient across the regenerator during initial tests of approximately 315°K (567°F). Since it may be desirable to test at higher heater temperatures in future follow-on testing using the SPDE hardware or new hardware of the same design, the design temperature level for the hot end of the machine was set at 900°K (1160°F), and a design life at this temperature was set at 1,000 hours. The corresponding design temperature gradient across the regenerator is 450°K (810°F).

The pistons oscillating at 105 Hz induce $.38 \times 10^6$ cycles/hour of alternating pressures in the engine and gas springs. Inertia loading of ∿700 g at overstroke conditions is also induced on the moving parts. The alternating pressure and inertia loads are relatively moderate; however, they are the source of high cycle fatigue loading which must be evaluated on the components involved.

Since the SPDE is primarily to demonstrate power level and efficiency at a prescribed temperature ratio, the weight limit for space application has been relaxed on this first engine. Extra margin has been built in by increasing pressure boundary wall thickness above the minimum required to meet the design criteria. The criteria, (Table 6-1), which is patterned on the approach used in the ASME Boiler and Pressure Vessel Code, was established for the SPDE analysis.

The primary structural concerns for the SPDE is the safe containment of the high pressure. The steep thermal gradient between the heater and cooler region also introduced stress conditions, which added to the pressure loads, required iteration between analysis and design to meet the structural criteria. The critical

TABLE 6-1

STRUCTURAL CRITERIA

1) Primary Membrane Stress - $\leq S_m$

   $S_m \leq 2/3 \ S_y$ S_y = Yield strength at optimum temperature

   and
   $S_m \leq 1/2 \ S_u$ S_u = Ultimate strength

   and
   $S_m \leq 2/3 \ S_r$ S_r = Stress to cause rupture in design life

   and
   $S_m \leq S_{c-1\%}$ $S_{c-1\%}$ = Stress to cause 1% creep in design life

2) Primary Surface Stress (Membrane & Bending)

   $S_s < 1.5 \ S_m$

3) Primary and Secondary Surface Stress

   $S^1_s < 3 \ S_m$

4) Cyclic stress shall not induce failure with a factor of safety of 1.5 when plotted on a Goodman diagram

5) Dynamic change in seal clearances < 1.0%

6) Bolt preloads 150% minimum required

7) Resonant frequencies > 3 x operating frequency

TABLE 6-1 cont'd

STRUCTURAL CRITERIA DEFINITIONS

PRIMARY STRESS   Stress which is not relieved by plastic deformation if the elastic limit (yield) is exceeded.

SECONDARY STRESS   Stress which is relieved by plastic deformation if the elastic limit (yield) is exceeded.

MEMBRANE STRESS   Average stress through the cross section of a structural element.

SURFACE STRESS   Stress at the material surface due to the combine effect of direct plus bending loads, but excluding stress concentration.

PEAK STRESS   Surface stress increased by the effect of local stress concentration.

MEAN STRESS   Average peak stress during cyclic loading.

ALTERNATING STRESS   Half the stress range (e.g., stress amplitude) during cyclic loading.

EFFECTIVE STRESS   Equivalent uniaxial stress determined from Von Mises formulation for treating biaxial and triaxial stress conditions.

elements analyzed and reported herein are the heat exchangers, studs, pressure vessel, and joining ring.

The following analyses were also conducted. However, because the criteria was easily met, for the sake of brevity they are not included in this report.

- Axial loading on heater and cooler tubes
- Local stresses in heater and cooler tube brazed joints
- Flow induced vibration of heater and cooler tubes
- Displacer assembly joints and dome stress analyses
- Power piston plunger stress
- Power piston resonant frequencies
- Dynamic reduction of all seal clearances

In addition to the stress analysis reported herein, an experimental study was made of the stud preload versus torque using two lubricants. Both torque wrench and ultrasonic techniques were evaluated by applying the torque to strain gaged studs. In addition to selecting the stud torques based on this procedure, the strain gaged studs were monitored during hydrostatic testing to confirm that the bolt stresses did not change significantly due to pressure loading.

6.2 Heat Exchanger Assembly

Figure 6-1 shows a typical cross-section through the heat exchanger assembly.

6.2.1 Loads and Temperatures

- Mean Pressure (Figure 6-2)
    - Nominal Operating   150 Bar   (2175 psi)
- Alternating Pressure (Figure 6-3)
    - Nominal Operating   15 Bar   (217 psi)
    - Design Operating   22.5 Bar   (326 psi)
- Maximum Pressure
    - Design Operating   172.5 Bar   (2500 psi)
    - Hydrotest   258.8 Bar   (3750 psi)
- Temperature
    - Initial Operation T_{hot} = 650°K T_{cold} = 315°K
    - Design T_{hot} = 900°K T_{cold} = 450°K

FIGURE 6-1

HEAT EXCHANGER FINAL DESIGN
(Removable Cooler)
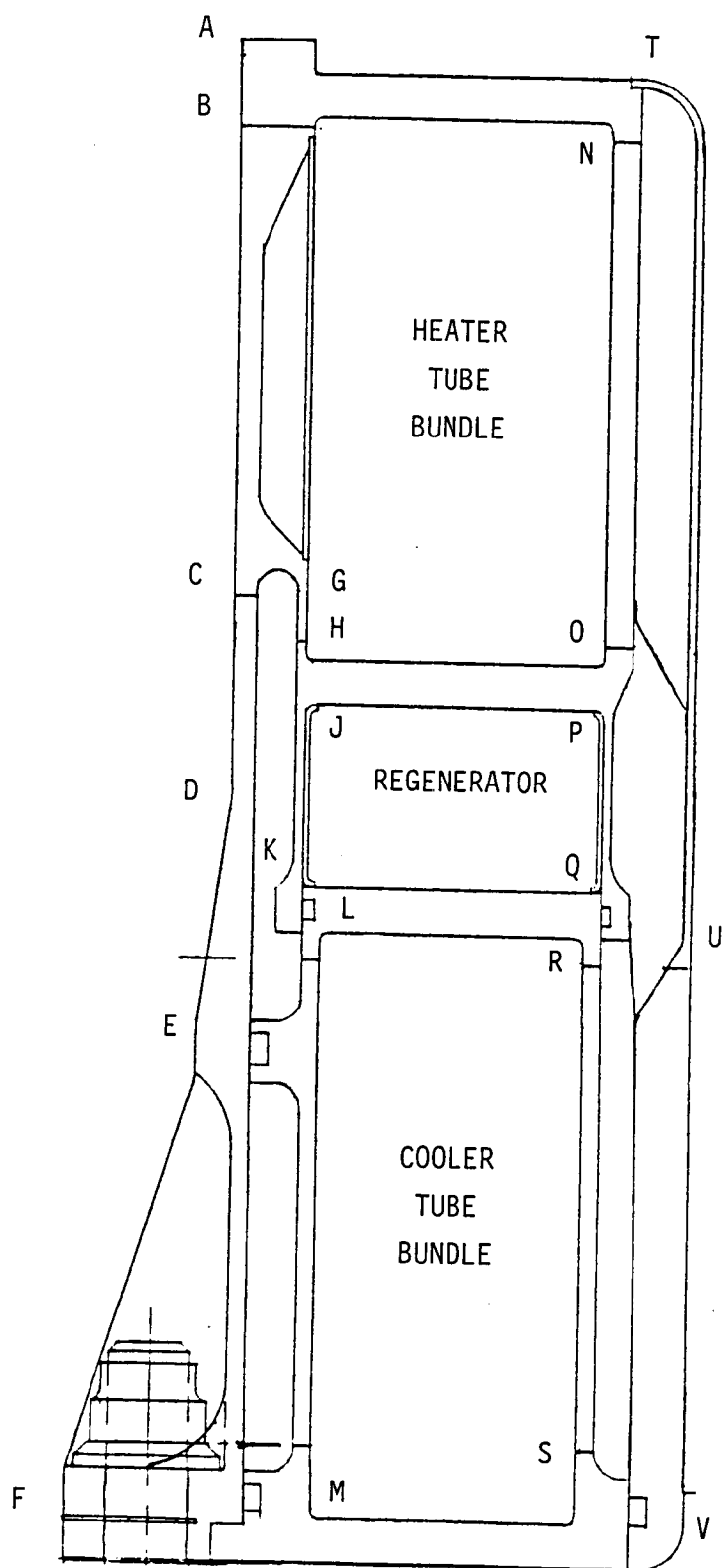
FIGURE 6-2

MEAN PRESSURE LOADING

F_{AX}

A

B

HEATER
TUBE
BUNDLE

(Pressure
inside tubes)

$Pm = 150$ Bar Operating
(2175 psi)

$= 258.8$ Bar Hydro
(3750 psi)

$F_{AX}=132.2$ Kips Operating
(4785 lbs/in)

$=228$ Kips Hydro
(8250 lbs/in)

N

C

G
H

O

REGENERATOR

J   P

D

K

L   R   U

E

COOLER
TUBE
BUNDLE

(Pressure
inside tubes)

F_{BOLT}
$= F_{AX}$

F

M   S

Q

T

V
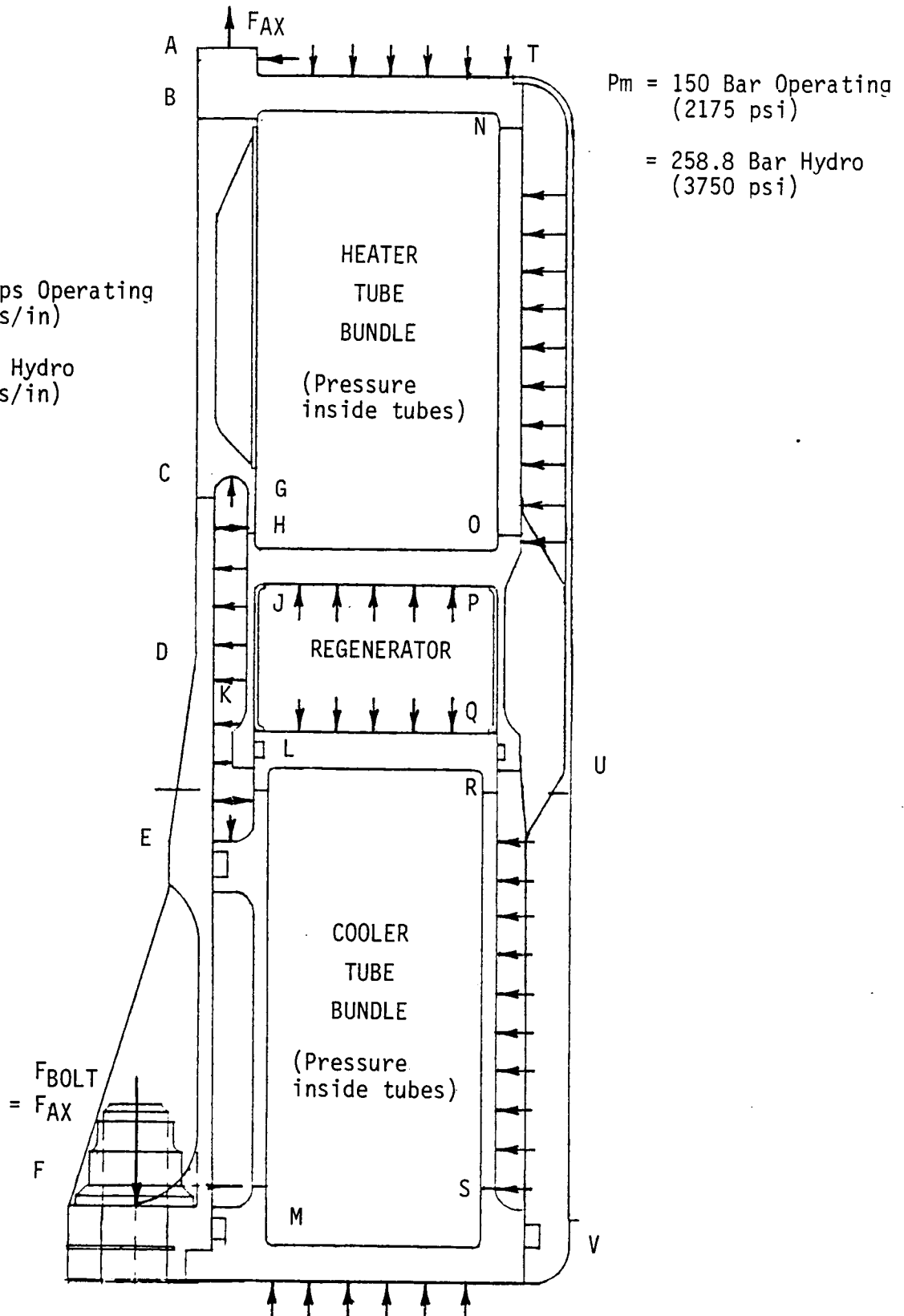
FIGURE 6-3

ALTERNATING PRESSURE LOADING

F_{AX} = ±13.2 Kips Nominal
(±19.8 Kips Design)

Palt = 15 Bar Nominal
(217 psi)

= 22.5 Bar Design
(326 psi)

HEATER
TUBE
BUNDLE

REGENERATOR

COOLER
TUBE
BUNDLE

F_{BOLT}
= F_{AX}
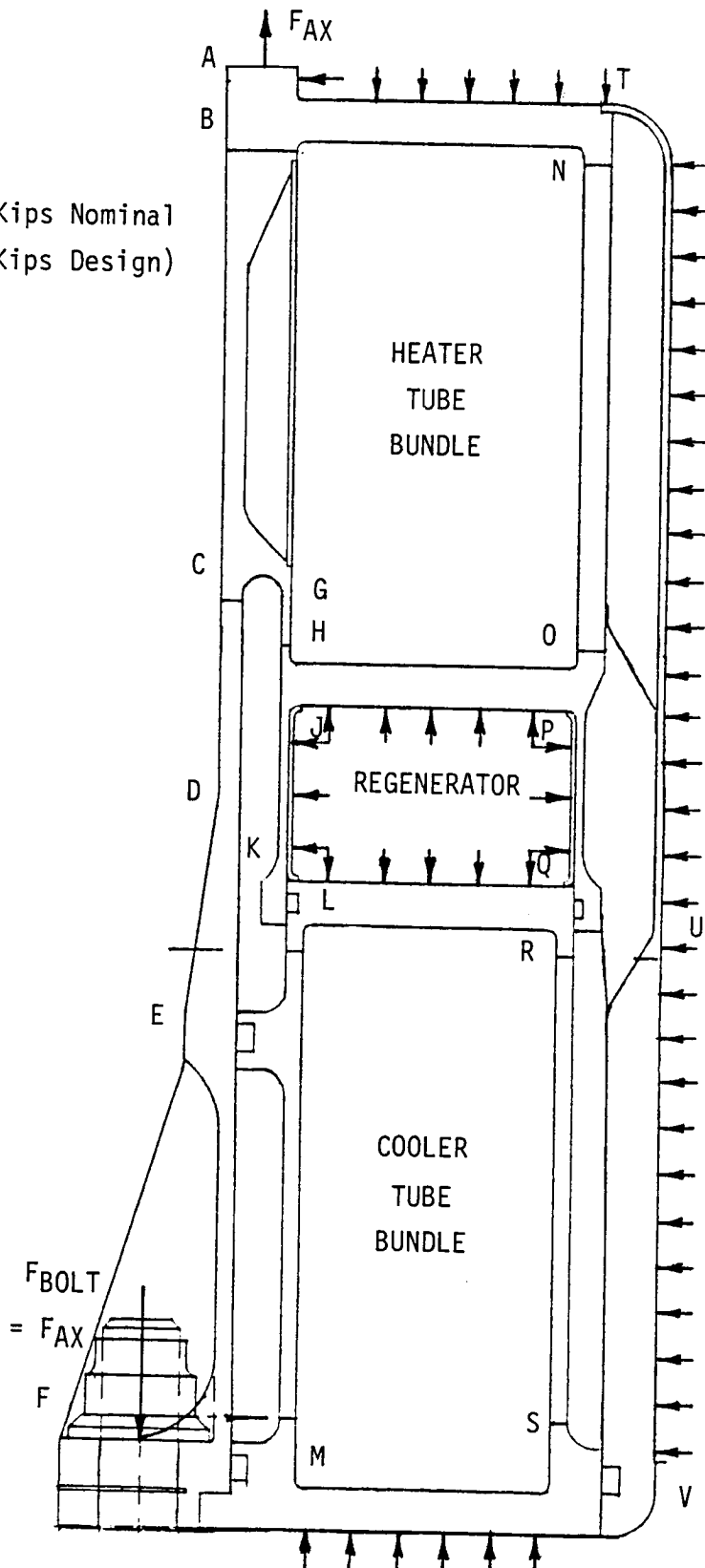
6.2.2 Materials

The structural material of the heater and cooler is Inconel 718 per AMS 5562. The heat treatment to be applied is 'Anneal 1700-1850°F, age 1325°F/8 hours, furnace cool to 1150°F, hold additional 10 hours, air cool'.

6.2.3 Stress Analysis

Stress analyses of the heat exchanger are a combination of conservative hand analyses and finite element analyses. The following hand analyses were performed:

- Membrane stresses due to mean and alternating pressures.
- Local stresses at shell to tube sheet intersections (weld locations).

The following analyses were performed using a linear elastic finite element structural code (ISOPDQ):

- Stress conditions at regenerator walls due to pressure and temperature gradient.
- Bolt loads at flanges
  - Integral cooler configuration
  - Removable cooler configuration

Membrane Stresses

Figure 6-4 lists the membrane stress and wall thicknesses in the heat exchanger at maximum design pressure conditions. As can be seen from the figure, wall thicknesses were not reduced to the absolute minimum possible. This was done to avoid pushing this first high pressure free-piston engine too hard from a structural point of view.

Local Weld Stresses (Hand Analysis)

The mean and alternating stresses at locations N, O, R, S, and M in Figures 6-2 and 6-3 were conservatively calculated by assuming the tube sheets are infinitely rigid.

FIGURE 6-4

MEMBRANE STRESSES
(Design Pressure)

p   = 2500
t   = .4
Sm = 62.0
σx = 13.8
FS = 4.5

p   = 325
t   = .05
Sm = 62.0
σθ = 15.0
FS = 4.1

p   = 2175
t   = .15
Sm = 62.0
σθ = 38.0
FS = 1.6

p   = 2175
t   = .125
Sm = 88.0
σθ =68.0*
FS = 1.3

p   = 325
t   = .05
Sm = 88.0
σθ = 17.9
FS = 4.9

p   = 325
t   = .05
Sm = 88.0
σθ = 28.6
FS = 3.1

p   = 2175
t   = .10
Sm = 90.0
σθ = 59.8
FS = 1.5

p   = psi
t   = inches
Sm,σ = ksi
FS   = Factor of
           Safety
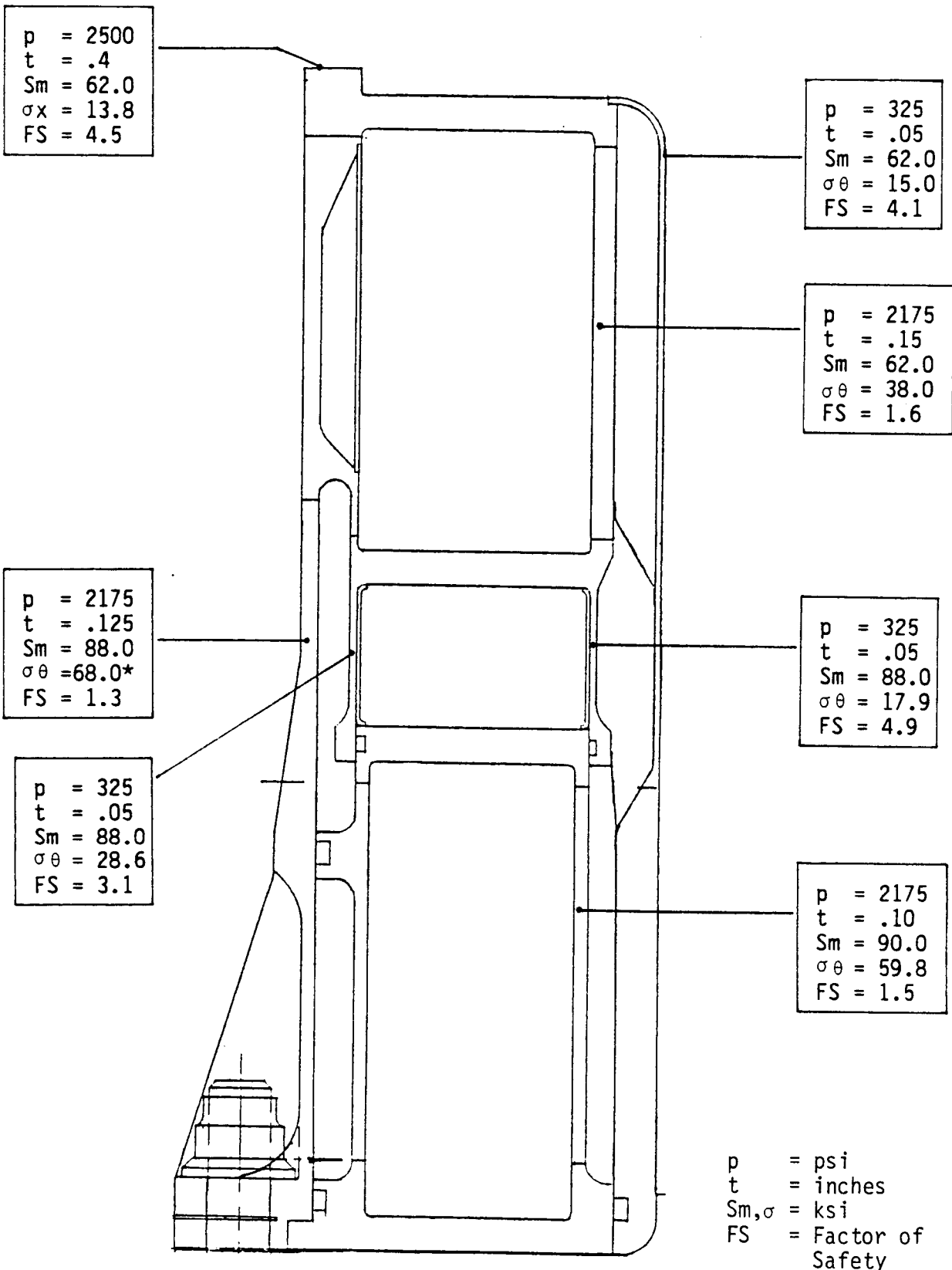
* From Finite Element Analysis

Finite Element Stress Analysis of Heat Exchanger Structure

Several design iterations were required to arrive at the final design. The results of the analysis conducted on the final design is summarized in this section. The region where stresses were most difficult to control is between the heater and cooler outboard of the regenerator. The large axial thermal gradient combined with the pressure load induces high stresses. In this region, it is also required to minimize the axial conduction between the heater and cooler, since this is a direct loss of thermal input energy. The cavity outboard of J-K and inboard of P-Q on Figure 6-1 runs at mean pressure. The outer wall (C-E) does not feel the cyclic radial pressure loading. It was decided for extra safety, however, to design it for cyclic loading also so that a structural failure of the outer wall would not occur in the event that a leak developed at the O-ring in location L.

The stress levels at locations 1 through 9 in Figure 6-5 are shown in Table 6-2 for:

- mean pressure = 2175 psi
- mean pressure + 800°F axial temperature gradient
- alternating pressure = 325 psi (locations 1 through 5)

As shown in the Table, positive factor of safety (FS) is calculated for all stress limits at all points.

Bolted Joint - Heat Exchanger to Post and Flange Joining Ring

The axial blow-off force which must be carried through this joint is the pressure on 9-inch diameter (i.e., area inside flange O-rings).

$$F \text{ net} = 63.6 \text{ p} = 138.4 \text{ kips at P mean}$$
$$20.7 \text{ kips at P alt}$$
$$159.1 \text{ kips at P max}$$
$$238.5 \text{ kips at P hydro}$$

The bolt circle contains 24 studs at 1.37-inch spacing. The net load per stud is 6,629 lbs. at P max and 9.938 lbs. at P hydro. The studs have a minimum stress

FIGURE 6-5

STRESS LOCATIONS FOR TABLE 6-2
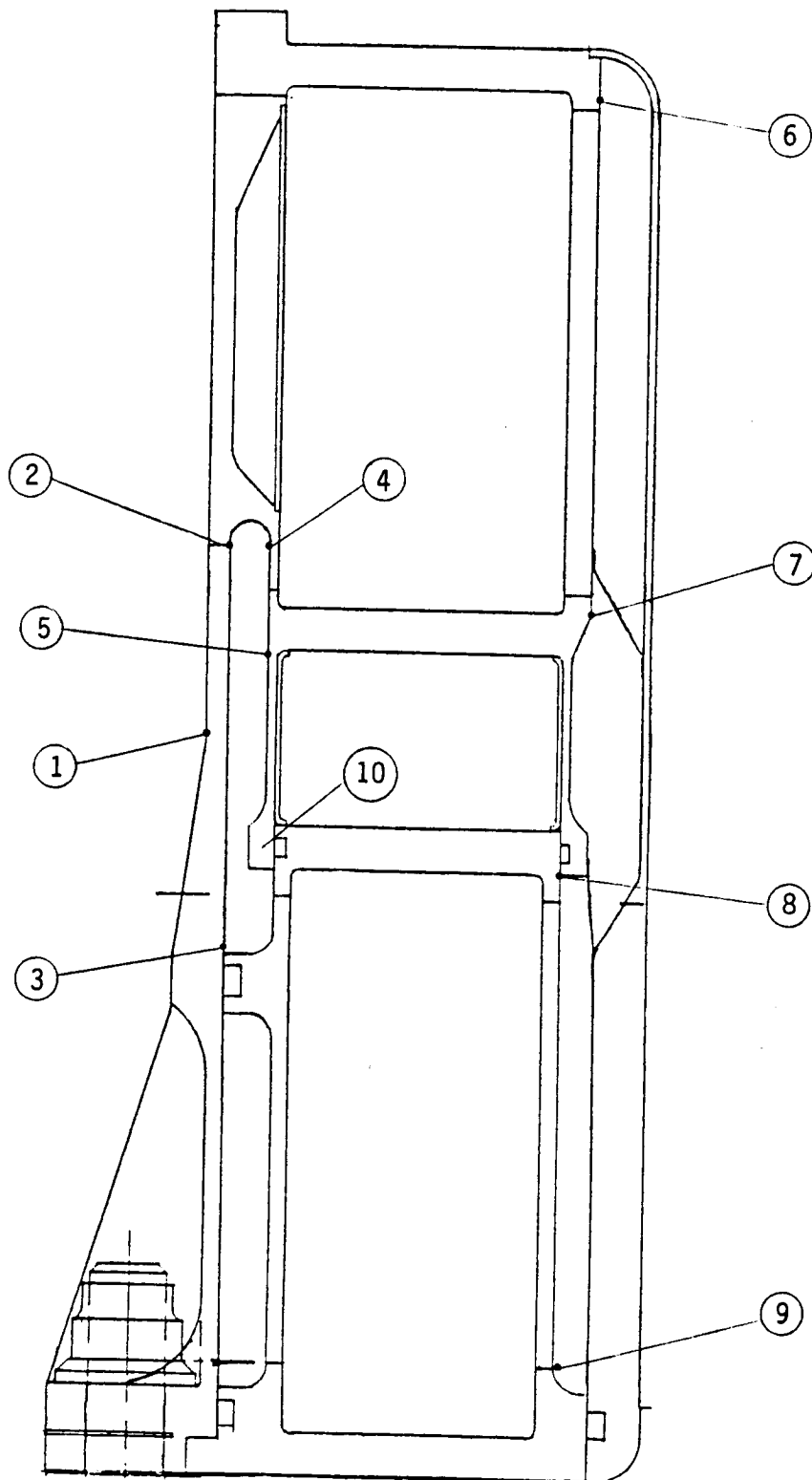
TABLE 6-2

HEAT EXCHANGER STRESSES (KSI)
(Refer to Figure 6-5 for Locations)

| | | | | LOCATION | | | |
Direction	1	2	3	4	5	6 & 7	8 & 9
	Axial	Effect	Axial	Effect	Axial	Axial	Axial
Mean Pressure Stress	90.1	76.2	39.1	82.3	-8.0	51.9	94.5
Mean Pressure and Thermal Stress	80.5	27.3	49.6	17.2	71.2	51.9	94.5
Alternating Stress	6.4	3.7	5.4	3.2	6.6	0	0
Sm	84.0	64.0	88.0	64.0	64.0	64.0	88.0
FS Primary Stress	1.4	1.3	3.4	1.2	High	1.8	1.4
FS Fatigue	1.2	1.2					
Method*	FE(45)	FE(64)	FE(28)	FE(97)	FE(105)	Hand	Hand

* FE = Finite Element
  (xx)= Node Number

diameter of .365-inch, which gives .105 square inches. The pre-stress required to balance the net load per stud is 63,100 psi at P max (94,700 psi at P hydro). The required preload must be increased above the net load to accommodate bending effects. To maximize design margin, the highest strength bolting available is used; i.e., maraging steel with a UTS of 260 ksi. By setting the preload at 200 ksi +/-10%, a minimum pre-stress of 180 ksi can be provided. To determine the amplification of the net load due to bending effects, a finite element analysis was conducted. A load equal to 450 kips (178.6 ksi/bolt) was simulated at the bolt circle along with the blow-off pressure loads. Based on the analysis, the joint is structurally adequate. To confirm this, strain gages will be applied to several (at least three) studs so that the stress condition in typical bolts can be monitored during preloading, hydrotesting, and engine operation.

6.3 Pressure Vessel and Joining Ring Stress

The joining ring and pressure vessel are fabricated from 13-8 Mo Stainless Steel. This has an ultimate strength of 205 ksi and a yield strength of 190 ksi, giving an Sm = 102.5 ksi. The thickness of these structures was arbitrarily increased on this first engine to give some extra margin against rupture failures. Table 6-3 summarizes the stress conditions in this structure excluding the bolt, which is discussed in the subsequent section.

<u>Bolted Joint - Pressure Vessel to Joining Ring</u>

This joint is shown in Figure 6-6. The axial blow-off force carried through this joint is the pressure on 12.2-inch diameter.

$$F\ net = 116.9\ p = 254.3\ kips\ at\ P\ mean$$
$$38.1\ kips\ at\ P\ alt$$
$$292.4\ kips\ at\ P\ max$$
$$438.4\ kips\ at\ P\ hydro$$

The bolt circle contains 30 .5-inch UNFJ studs with a stress area of .149-inch^2 (minor diameter). The net load per stud is 9,470 lbs. at P max and 14,600 lbs. at P hydro. The stud pre-stress required to balance the net loads is 65,500 psi at P max (98,000 psi at P hydro). Due to bending effects, the required pre-stress is much higher than that required to just balance the net load. The maximize design

TABLE 6-3

PRESSURE VESSEL AND JOINING RING STRESSES
(Refer to Figure 6-6 for Locations)

| | LOCATION | | | |
	1	2	3	4
Direction	Axial	Hoop	Effect	Effect
Pressure	2,275	2,200	2,175 +/-100	2,175 +/-30
Membrane Stress	69.2	54.0	---	---
Surface Stress	---	---	81.3 +/-3.7	83.9 +/-1.2
Sm	102.5	102.5	>102.5	>102.5
FS Membrane Stress	1.48	1.90	---	---
FS Primary Stress	---	---	1.81	1.80
FS Fatigue	---	---	>2.0	>2.0
Node	17-20	105-108	21	84

Bolted Joint

①   ③   ④   ②
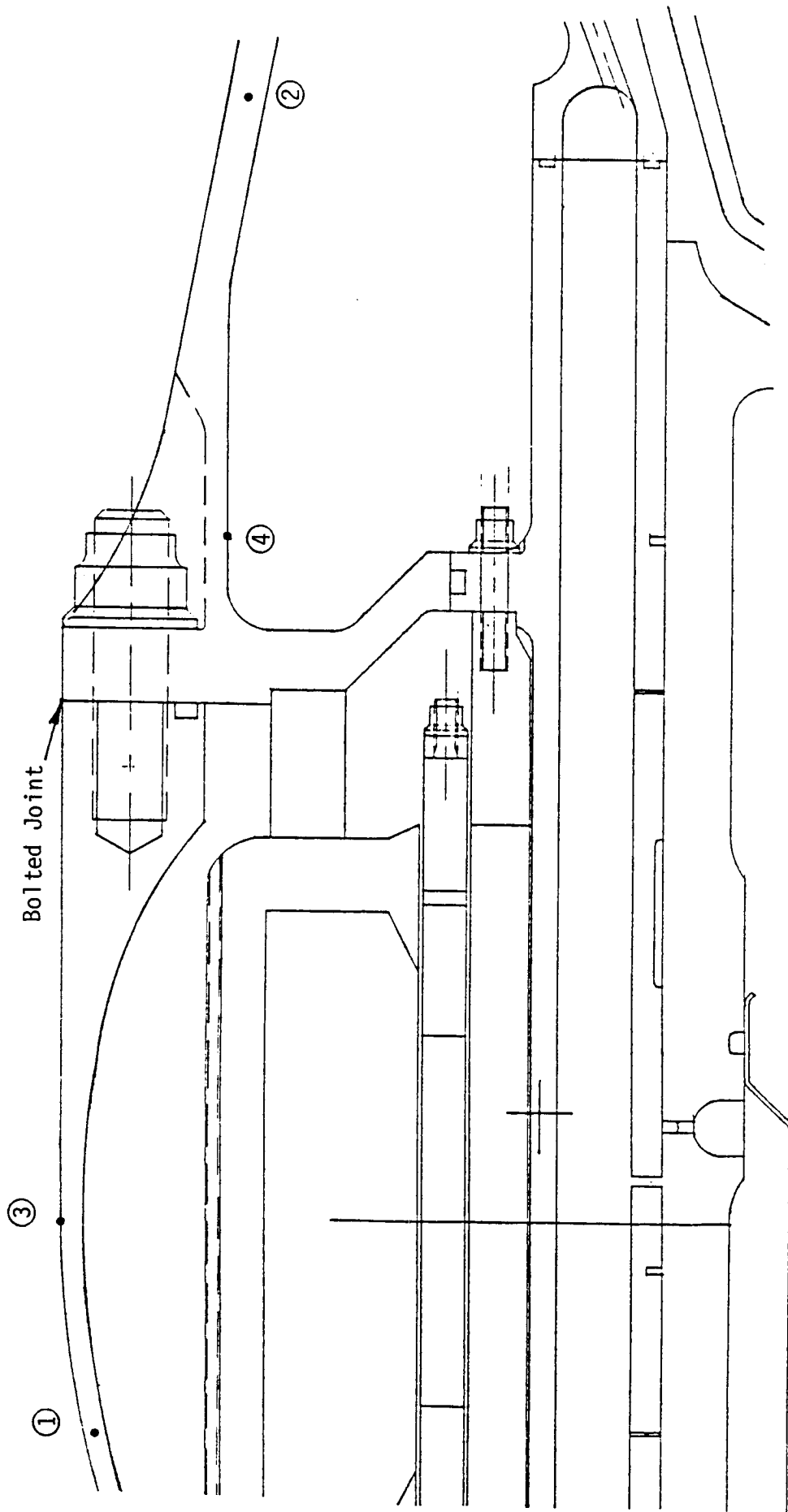
FIGURE 6-6

PRESSURE VESSEL AND JOINING RING

margin, high strength studs with UTS of 260 ksi have been selected. The preload is set at 220 ksi +/-10% or 200 ksi minimum. This produces a preload of 20,800 lbs. and pre-compression on the flange face of 24,500 psi. Based on finite element analysis, this results in a safe joint.

6.4 Material Properties

Figures 6-7 through 6-12 contain the material properties used in the analysis.

FIGURE 6-7

INCONEL 718 STRESS RUPTURE STRENGTHS

$S_m = 2/3 \times 84 = 56$ ksi
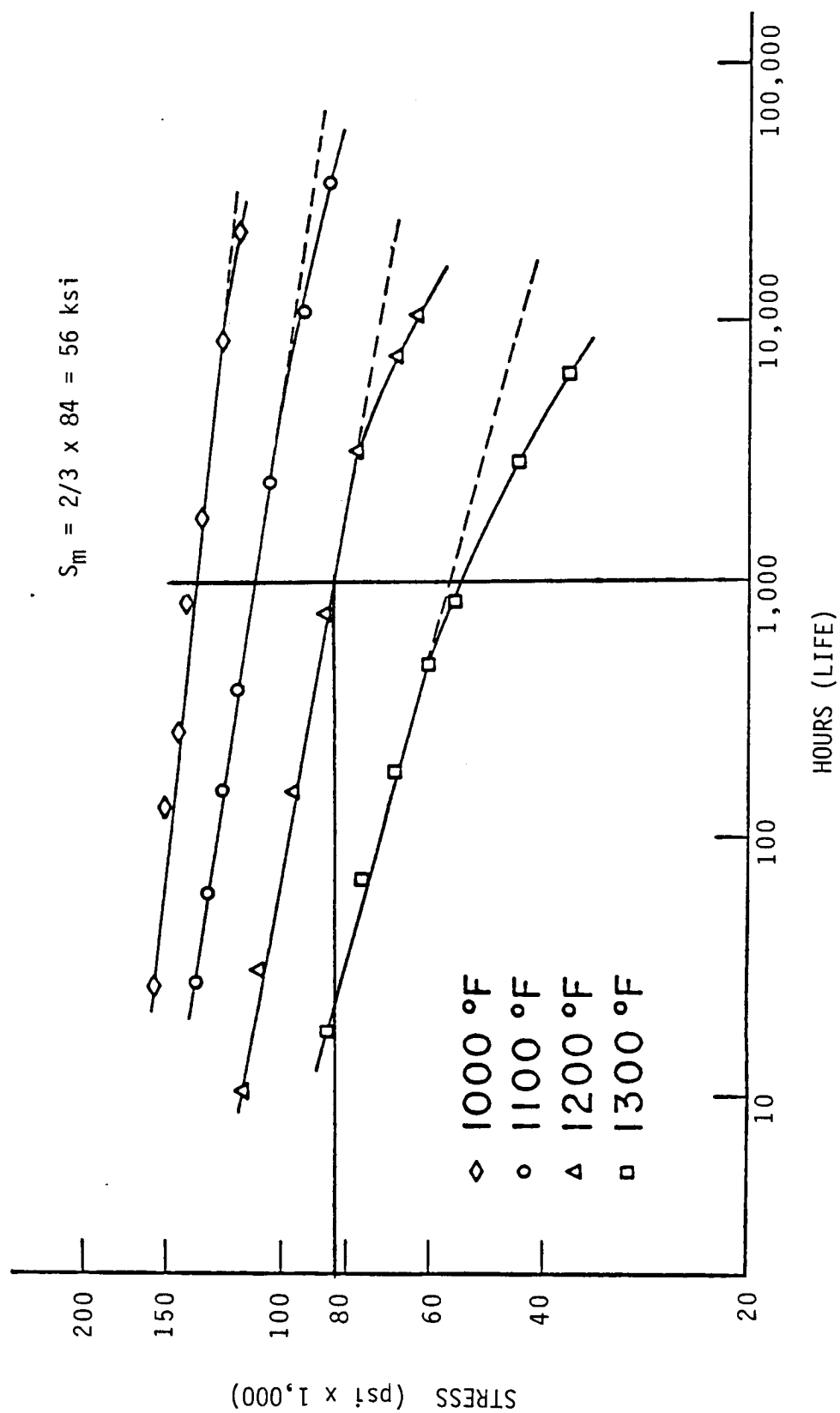
FIGURE 6-8

INCONEL 718 PROPERTIES

FIGURE 6-9

HIGH CYCLE FATIGUE – INCONEL 718 (10^9 Cycles)

Estimated from Huntingdon Alloy Handbook
Annealed 1 Hour/1750°F; Aged 1325°F/8 Hours + 1150°F/18 Hours Total

FIGURE 6-10

DESIGN MECHANICAL AND PHYSICAL PROPERTIES
OF PH13-8Mo STAINLESS STEEL (PRESSURE VESSEL)

TABLE 2.6.5.0(c). Design Mechanical and Physical Properties of PH13-8Mo Stainless Steel

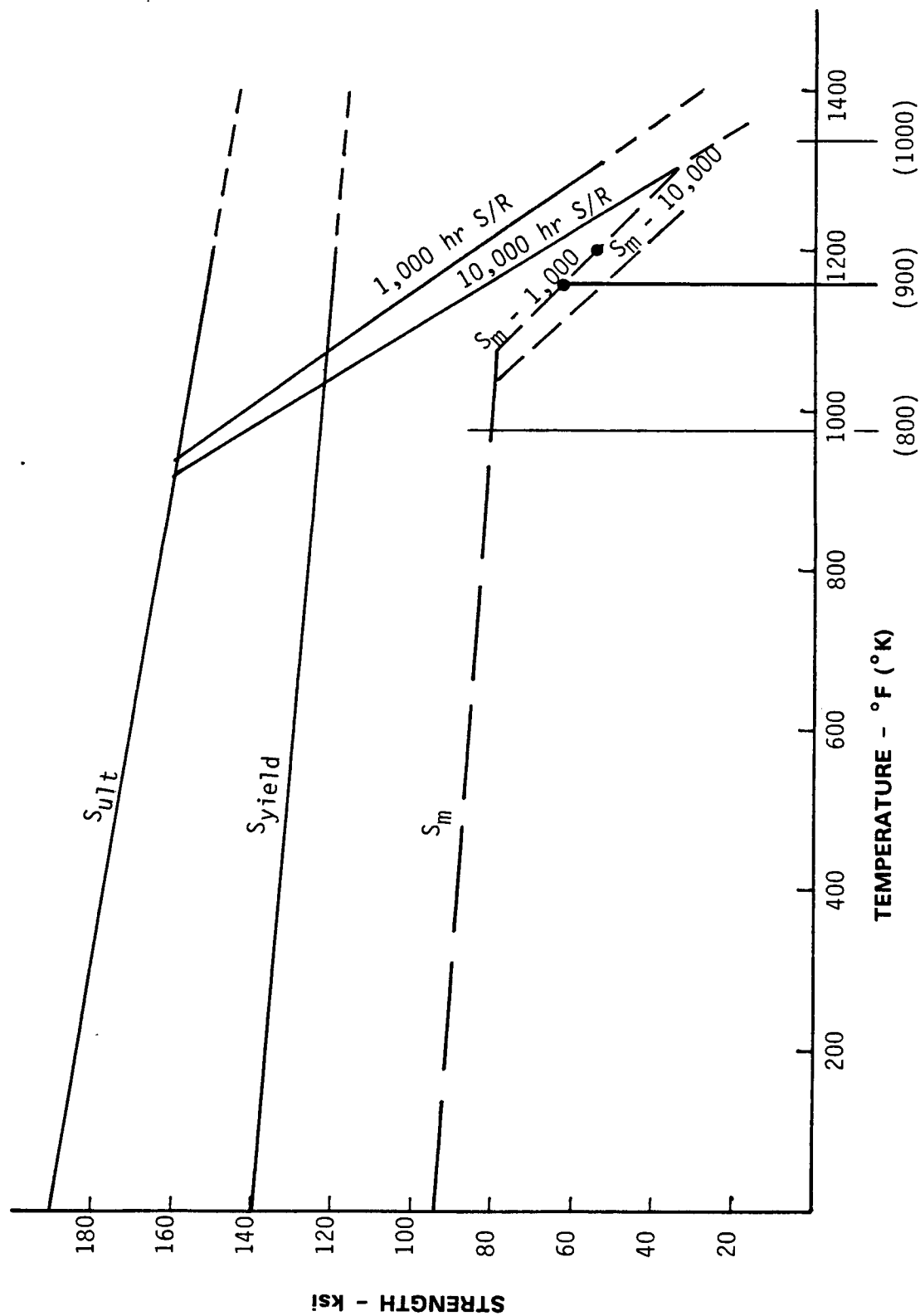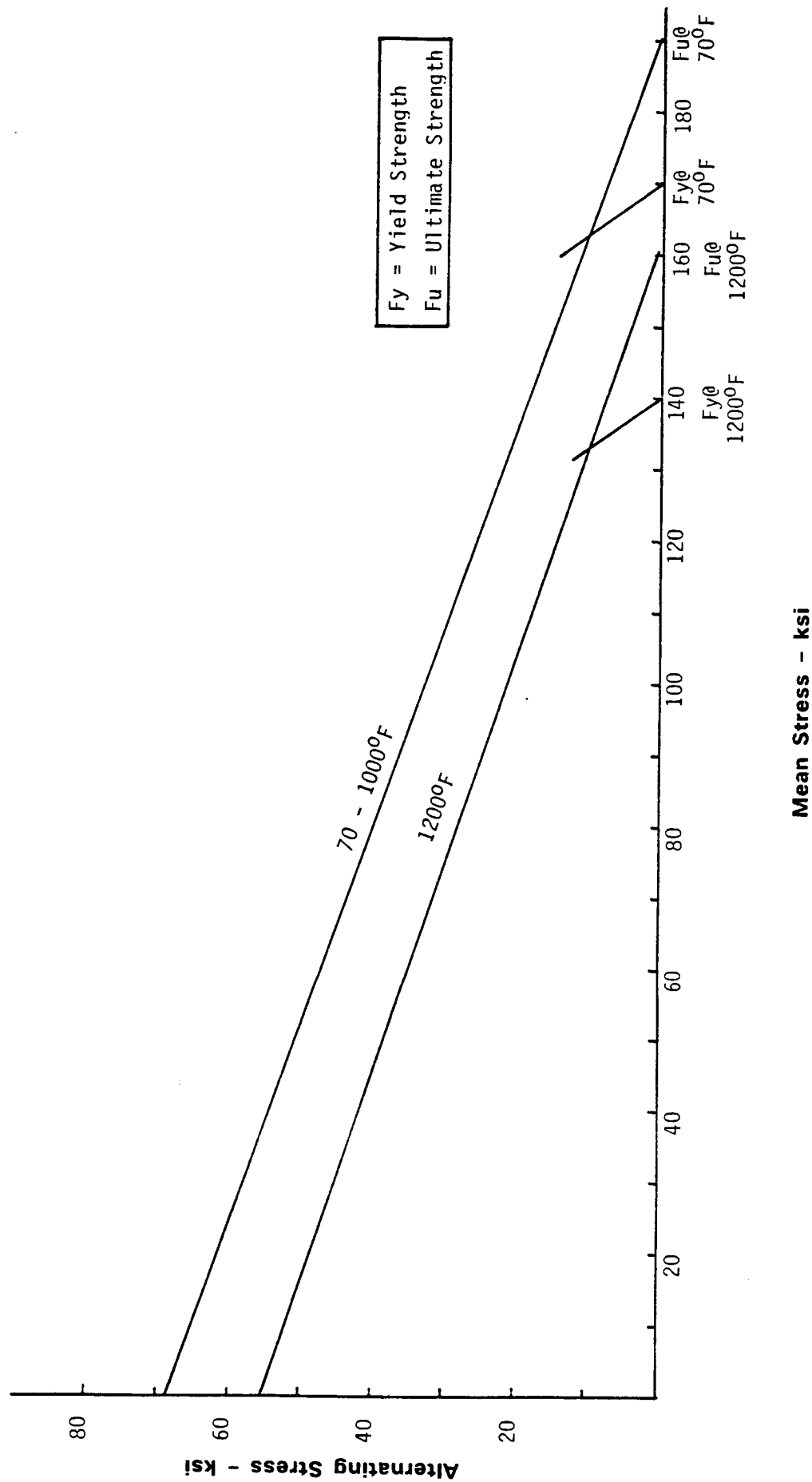| Specification	AMS 5629													
Form	Round, hex, square and flat bar								Forging, flash welded ring, and extrusion					
Condition	H950		H1000		H1025	H1050	H1100	H1150	H950	H1000	H1025	H1050	H1100	H1150
Thickness or diameter, in.	<90		<80				≤12.0					≤12.0		
Basis	A	B	A	B	S	S	S	S	S	S	S	S	S	S
Mechanical properties:														
Ftu, ksi: L	217	221	201*	208	185	175	150	135	220	205	185	175	150	135
T	217	221	201	208	185	175	130	135	220	205	185	175	150	135
Fty, ksi: L	198	205	190*	200	175	165	135	90	205	190	175	165	135	90
T	198	205	190*	200	175	165	105	90	205	190	175	165	135	90
Fcy, ksi: L	...	...	200[b]	211[b]	211[b]	...	...	...	...	...	...	...	...	...
T	...	...	200[b]	211[b]	...	...	...	...	...	...	...	...	...	...
Fsu, ksi	...	...	117	122	...	...	...	...	...	...	...	...	...	...
Fbru, ksi: (e/D = 1.5)	...	...	302[b]	313[b]	...	...	...	...	...	...	...	...	...	...
(e/D = 2.0)	...	...	402[b]	416[b]	...	...	...	...	...	...	...	...	...	...
Fbry, ksi: (e/D = 1.5)	...	...	263[b]	277[b]	...	...	...	...	...	...	...	...	...	...
(e/D = 2.0)	...	...	338[b]	356[b]	...	...	...	...	...	...	...	...	...	...
e, percent (S basis): L	10	...	10	...	11	12	14	14	10	10	11	12	14	14
T	10	...	10	...	11	12	14	14	10	10	11	12	14	14
RA, percent (S basis): L	45	...	50	...	50	50	50	50	45	50	50	50	50	50
T	35	...	40	...	45	45	50	50	35	40	45	45	50	50

Physical properties:	
E, 10³ ksi	28.3
Ec, 10³ ksi	29.4
G, 10³ ksi	11.0
μ	0.28
ω, lb/in.³	0.279
C, Btu/(lb)(F)	0.11 (32–212 F) (Est.)
K and α	See Figure 2.6.5.0

*The A value of 193 ksi is higher than S value. $* S_m = .5\ F_{tu} = 100\ ksi$
[b]Tentative values based upon limited data.

FIGURE 6-11

FATIGUE DIAGRAM FOR PH13-8Mo STAINLESS STEEL
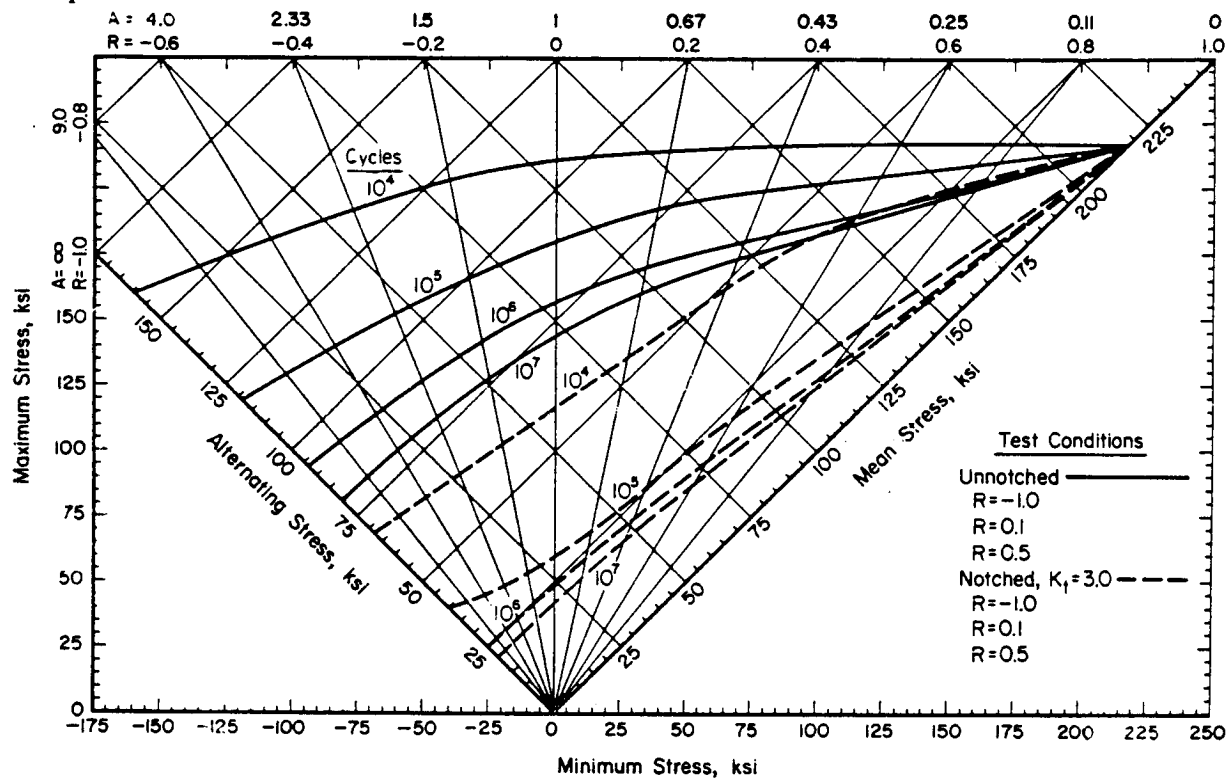
FIGURE 2.6.5.1.8. *Typical constant life fatigue diagram for PH13-8Mo (H1000) stainless steel (bar) at room temperature (longitudinal and long transverse).*

Correlative Information for Figure 2.6.5.1.8

Product Form: Bar, 2x6 inches

Test Parameters:
Loading - Axial
Frequency - 1800 cpm
Temperature - RT
Atmosphere - Air

Properties:

TUS, ksi	TYS, ksi	Temp, F
217.0	207.0	RT (Unnotched)

Specimen Details: Unnotched
0.250-inch diameter

Notched, V-Groove, $K_t = 3.0$
0.375-inch gross diameter
0.250-inch net diameter
0.013-inch root radius, r
60°° flank angle, ω

$$K_N = 2.75; \ \rho = 0.00012 \text{ inch, where } K_N = 1 + \frac{K_t - 1}{1 + \frac{\pi}{\pi - \omega}\sqrt{\frac{\rho}{r}}}$$

Surface Condition: Unnotched: Mechanically polished in longitudinal direction.
Notched: Polished mechanically with abrasively charged wire.

FIGURE 6-12

**DESIGN MECHANICAL AND PHYSICAL PROPERTIES
OF 250 MARAGING STEEL (BOLTS)**

SPECIFICATION	AMS 6520			AMS 6512	
FORM	Sheet	Plate		BAR	
CONDITION	Maraged at 900 F			Maraged at 900 F	
THICKNESS OR DIAMETER, IN	< 0.187	.188-.250	> 0.250	< 4.000	4.000-10.000
BASIS	S	S	S	S	S
MECHANICAL PROPERTIES:					
F_{tu} ksi:					
L	247	252	...	255	245
T	255	255	255	255	245
F_{ty} ksi:					
L	238	242	...	250	240
T	245	245	245	250	240
F_{cy} ksi:					
L	221	...	...	260	...
T	225	255	...	...	...
F_{su} ksi	148	155	...	148	...
F_{bru} ksi:					
(e/D=1.5).............	327	352	...	...	...
(e/D=2.0).............	444	448	...	...	...
F_{bry} ksi:					
(e/D=1.5).............	278	324	...	...	...
(e/D=2.0).............	353	354	...	...	...
e, percent					
L	...	...	...	6	5
T	a	a	a	4	3
RA, percent					
L	...	...	...	45	30
T	...	...	...	35	20
E, 10^3 ksi	26.5				
E_c, 10^3 ksi:					
L	28.2				
T	29.4				
G, 10 ksi	....				
μ	0.31				
PHYSICAL PROPERTIES:					
lb/in	0.286				

a <0.091   2.5%
  0.091-0.125 3.0%
  0.126-0.250 4.0%
  0.251-0.375 5.0%
  >0.375   6.0%

MIL-HDBK-5C
12-1-79

7.0 BEARINGS AND PORTS ANALYSIS

7.1 Introduction

The SPDE FPSE-linear alternator system is designed to operate stably at the steady-state design point conditions with no mechanical rubbing contact. The displacer and power piston are floated on hydrostatic gas bearings which are supplied from the piston gas spring through an internal porting arrangement. The porting system also provides a return flow of the bearing gas to the gas spring, and is designed to maintain centered operation of both the displacer and power piston.

MTI computer codes were utilized to analyze both the hydrostatic gas bearing and the port characteristics. The effects of high operating frequency, non-steady pressures in the bearing plenums, and time-varying magnetic moments acting on the power piston were included in the analysis. All assumptions were made conservatively, thereby providing a design margin in the predicted performance.

As a result of this work, one double-plane hydrostatic gas bearing was selected for the displacer, and two single-plane bearings were selected for the power piston. Design point bearing losses were calculated to be 105 watts (210 watts for entire module). The bearings are internally pumped off the power piston gas spring through a set of end-of-stroke ports, and drain back to the gas spring via mid-stroke ports. The displacer is also equipped with mid-stroke ports for centering. The ports were designed to perform the above functions and maintain axial centering of the displacer and piston with a power loss of 350 watts (700 watts/module).

This report summarizes all considerations taken in designing the gas bearing and gas porting systems, leading to the final design recommendations.

7.2 Engine Description and Operating Conditions

The SPDE is comprised of two identical beta-type displacer engines, joined in opposition along a common piston axis to balance inertia forces, with a shared expansion space. The engine design features two gas springs acting on the

$\subset -2$

$\mathcal{C}-2$

displacer: a stiff load-side gas spring (6.2 % volume amplitude) in phase with displacer motion, and a soft heater-side gas spring (0.6 % volume amplitude) in anti-phase with displacer motion. The power piston, whose motion lags the displacer by 65°, has a moderate gas spring (2.7 % volume amplitude) essentially 180° out of phase with the piston motion. All engine spaces (working spaces and gas springs) are designed for a mean pressure of 150 bar. Design point operating frequency is 105 Hz. It is assumed that the engines behave similarly, thus only a single engine is considered for analysis.

Terrestrial testing of the SPDE power module is in a horizontal attitude with the displacer inertia and the power-piston/alternator-plunger inertia balanced by the pressure forces of the engine working spaces and gas springs. The in-line opposed engine design eliminates transverse vibration loads, and the gas bearings must support only the reciprocating masses and any magnetic side loads (which act on power piston only).

7.3 Bearing Design Analysis

7.3.1 Bearing Design Goals

The design goals for the hydrostatic gas bearings were as follows:

1. Sufficient capacity to carry all expected loads at maximum eccentricities of less than 0.25 (eccentricity is defined as the ratio of radial deflection to radial gap).

2. Sufficient radial and torsional stiffness to provide stable support at undamped natural frequencies (transverse and angular) greater than three times the operating frequency.

3. Achieve goals (1) and (2) while minimizing bearing flow, thereby reducing the bearing supply and return porting requirements.

7.3.2 Bearing Design Considerations

Magnetic Side Load

The SPDE alternator has four rings of permanent magnets, two at each end of the plunger. The plunger moves between an inner stator of constant cross section and an outer stator with poles adjacent to the magnet rings as shown in Figure 7-1. Three regions are denoted in the figure: region I outside of the stator poles, region II adjacent to the poles, and region III between the poles. As the piston oscillates, the magnets move relative to the stator, but the total amount of magnet in each of the regions I, II, and III remains constant. The total amount of magnet in region III remains fixed since as a ring at one end enters, the interior ring at the opposite end departs.

The magnetic side pull results from an imbalance between the attraction of the magnets to the inner and outer stators. When a magnet is in region I, there is no iron in close proximity, and both the inner and outer forces are nearly zero (a balanced condition). In region II, the inner and outer magnetic attraction forces are nearly equal, resulting in little net side load. However, in the central region (III), the inner iron still provides the same attractive force, but the force from the outer iron drops to nearly zero, and the maximum side pull can result. If the magnetic center and the geometric center of the plunger coincide, the side pull force in region III is zero for zero radial displacement of the plunger. The side pull varies with the radial displacement of the magnetic center as shown in Figure 7-2, taken from test measurements. To be conservative, an offset of the magnetic center of 0.016 in. was assumed for bearing design, giving a 30 lb_f side pull in region III.

The change in the position of the magnets in the central region (III) as the piston oscillates causes a movement of the side force line of action. Figure 7-3 shows a schematic of the piston loads and deflection at the ends of its stroke. When the piston moves to TDC (top dead center) (toward compression space), the magnetic side pull is concentrated at the gas spring end of the power piston. At BDC (bottom dead center), the side pull resultant falls inside the compression space stator pole, close to the piston center of mass. At piston mid-stroke, equal amounts of the upper ring and lower ring are in the central region, and the net magnetic side pull acts through the center of the alternator.

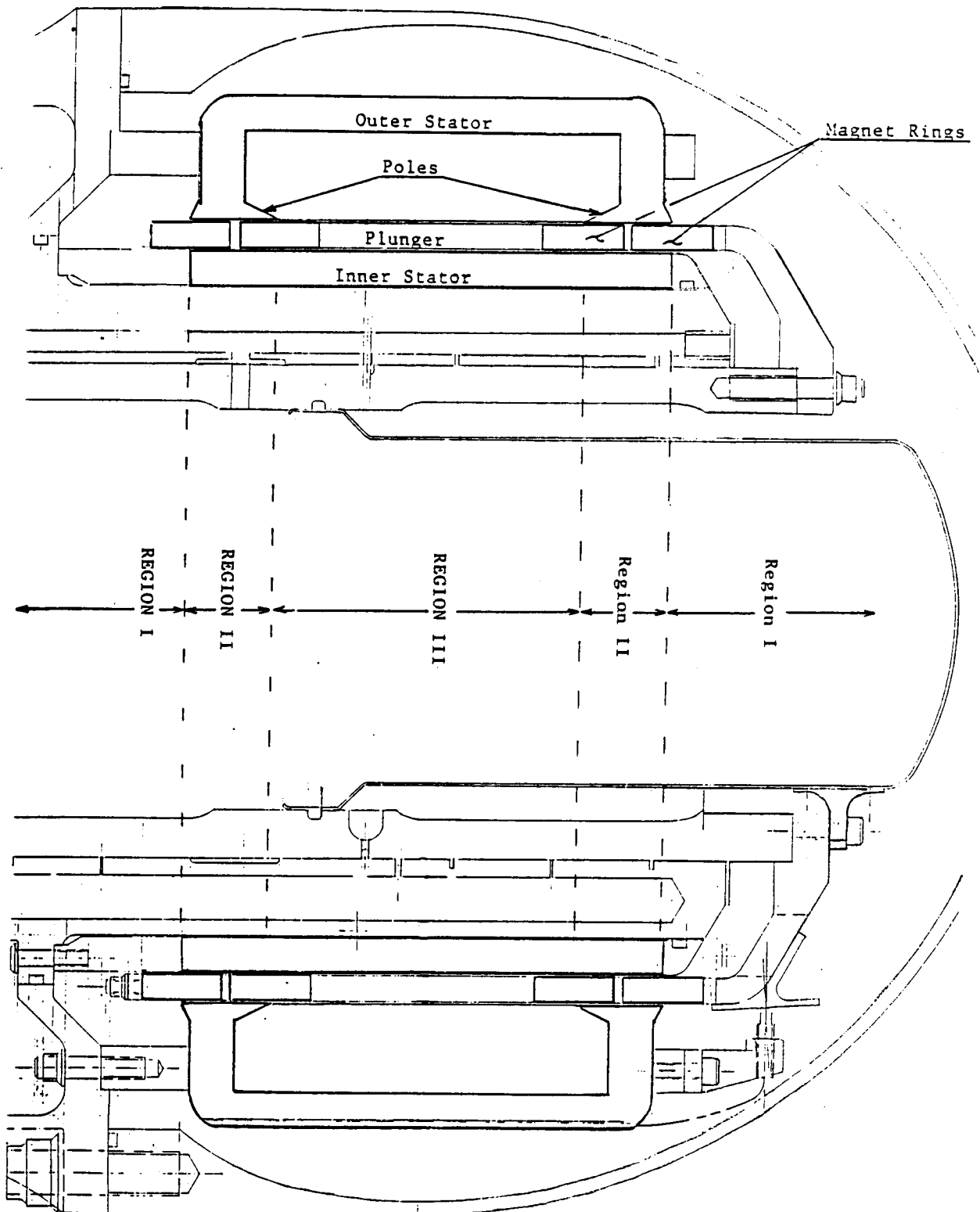# FIGURE 7-1

ALTERNATOR SECTION LAYOUT

Outer Stator

Poles

Magnet Rings

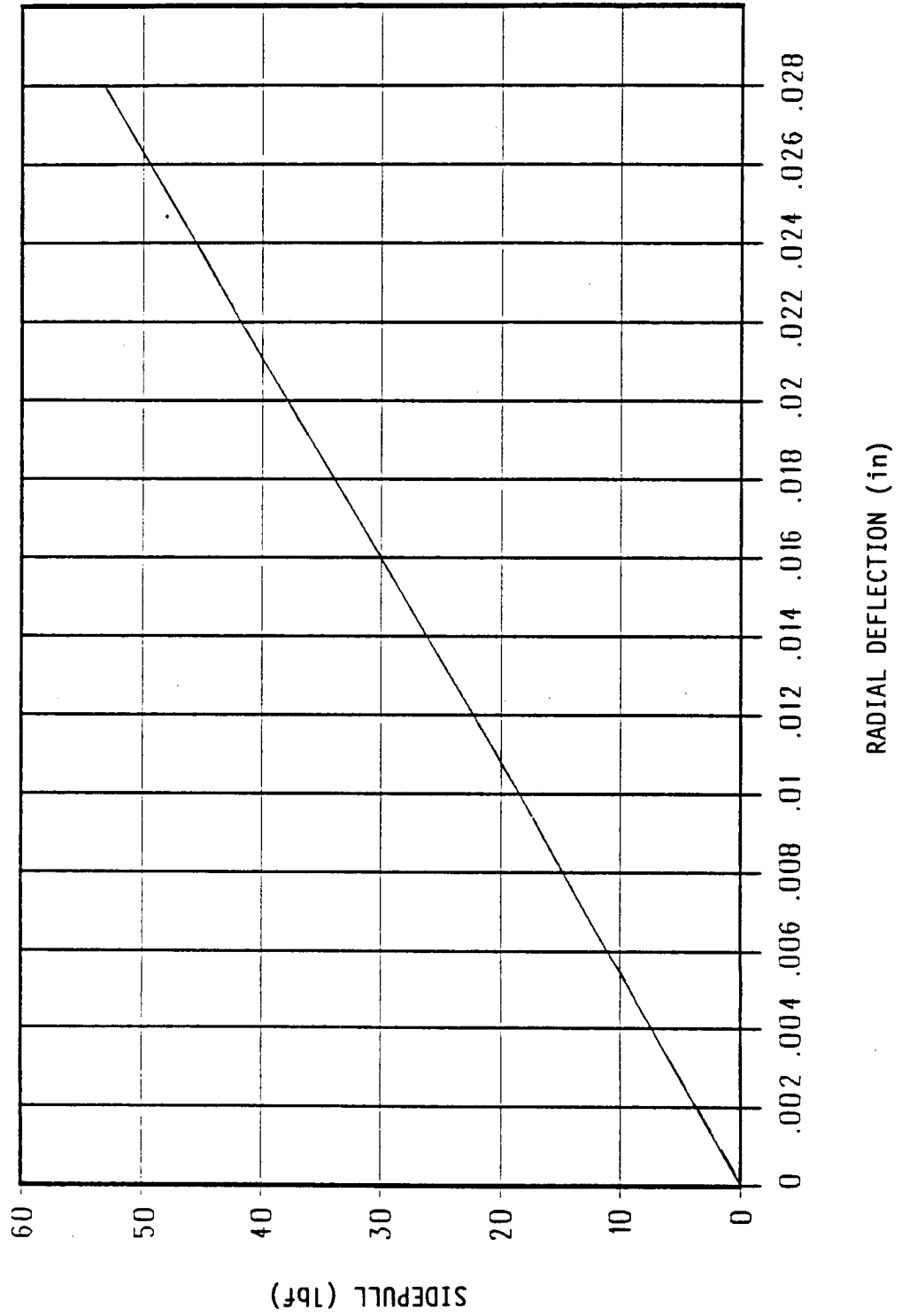Plunger

Inner Stator

REGION I   REGION II   REGION III   Region II   Region I

FIGURE 7-2

SPDE ALTERNATOR MAGNETIC SIDEPULL

FIGURE 7-3

PISTON LOAD AND DISPLACEMENT SCHEMATIC

30 lb
(Mag)

17 lb (Grav)

Gas
Spring

26.3 lb

Compression
Space

20.7 lb

① ②

Bearing
Reactions

Piston at BDC

· 30 lb (Mag)

17 lb
(Grav)

31.7 lb

15.3 lb

① ②
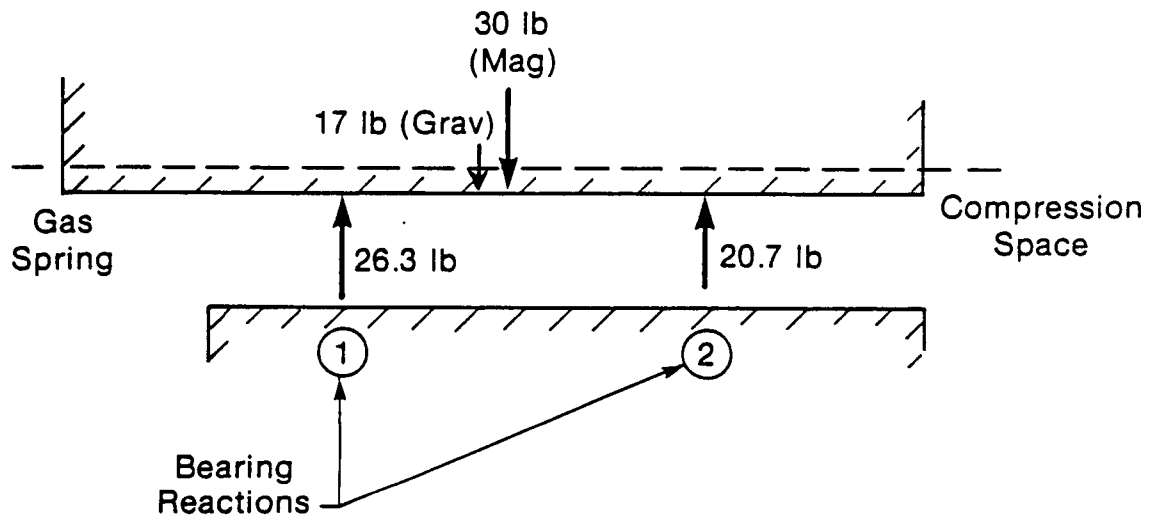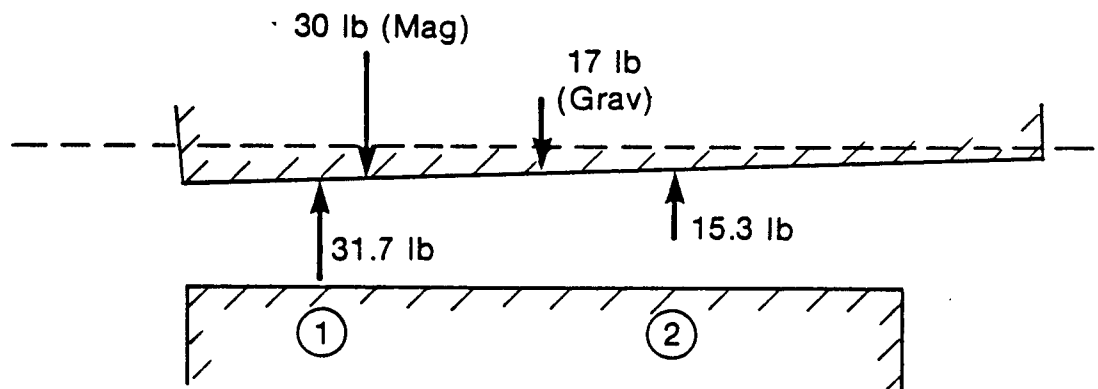
Piston at TDC

86185

Bearing Pressure Variation

In previous MTI Stirling engine applications, hydrostatic gas bearings have been designed with a constant supply pressure draining to a reservoir of nearly constant pressure. Thus the bearing ΔP (supply pressure minus drain pressure) has been constant. For SPDE, volume constraints limited the available drain reservoir, resulting in a fluctuating drain pressure. During the conceptual design phase of the engine, the upper displacer gas spring, which also served as the drain reservoir for both the displacer and power piston bearings, was limited to a minimum pressure amplitude of 2.0 bar due to the volume constraints.

7.3.3 Gas Bearing System Analysis & Design

The bearing characteristics were generated using MTI's Gas Bearing code (PAM 080), which gives the bearing stiffness (radial and angular) and gas flow rate for specified bearing geometry and operating pressure. Predicted bearing flow was increased by a factor of 2.0 for loss calculations and porting requirements, based on previous code correlations with test measurements.

To analyze the bearing characteristics with a moving magnetic side load and a time dependent bearing pressure ratio, a computer code was developed to calculate the instantaneous and time-averaged bearing stiffness and flowrate, piston radial deflection, and natural frequencies (transverse and angular) of both displacer and power piston.

Table 7-1 shows the bearing stiffness requirements to satisfy design goal (2).

Power Piston Bearings

The moving magnetic side load on the power piston necessitated a wide bearing "wheel-base" to stabilize the piston. The long length of the piston made the bearing requirements difficult to achieve, since a maximum eccentricity of 0.25 at the piston end limits the allowable deflection at the bearing to a smaller value due to the distance between the bearing support and the piston end. The allowable bearing length and the axial location of the bearing(s) were determined by clearance seal requirements at the two ends of the piston, and porting space

TABLE 7-1

BEARING STIFFNESS REQUIREMENT

POWER PISTON

- Radial   173,000 lb/in
- Torsional   27,000 in-lb/rad

DISPLACER

- Radial   34,000 lb/in
- Torsional   720,000 in-lb/rad

requirements. Within these constraints, three configurations were considered for evaluation:

Power Piston Bearing Design Options

1. One long double-plane* bearing. Porting system at gas-spring end of piston.

2. One single-plane and one double-plane bearing, sharing a common central drain groove. Porting system at gas-spring end of piston.

3. Two single-plane bearings with the porting system occupying the central region separating the bearings.

Option (1) did not meet the piston eccentricity goal due to insufficient angular stiffness. Option (2) had much higher angular stiffness than option (1) due to the addition of the single-plane stabilizer bearing, and met the load requirements. Option (3), with a large wheel base (bearing separation), also met all design goals but with less bearing flow (i.e., power loss) than option (2) due to the reduction in admission planes. The porting arrangement used with option (3) is also the "cleanest", with the supply and return ports sharing a common moving groove in the piston (for details see Section 7.4).

Displacer Bearing

The SPDE displacer has no magnetic side loading, therefore its bearing(s) must only support its mass at sufficiently high natural frequencies to avoid resonance problems. Previous MTI free-piston engines (thermal amplifiers - motored displacer) have used a double-plane and single-plane bearing combination to support the motor loads. For this design one double-plane bearing provides ample radial stiffness, and nearly enough angular stiffness to meet the natural frequency goal. It was felt that the addition of a stabilizer bearing

---

*Note: Double-plane bearings have two planes of gas admission; single-plane bearings have only one.

(single-plane) to increase the angular stiffness, at the expense of increasing the flow burden on the porting system, was not justified.

7.3.4 Bearing Design Details and Performance

Table 7-2 summarizes the power piston and displacer bearing loads. The number and size of bearing orifice jets were selected to achieve the desired bearing characteristics (load capacity, gas flow) and provide a sufficient number of supply plenum drillings to maintain nearly steady supply pressure. All design goals were met or exceeded, with the exception of the torsional natural frequency of the displacer as previously discussed.

7.4 Porting Design Analysis

7.4.1 Porting Fundamentals

In a free-piston machine, some means of piston centering, either active or passive, is required to minimize axial piston drift. Off-center operation reduces the attainable stroke and capacity of the machine, and often results in impact with mechanical stops. In the SPDE, the gas springs and working spaces are interconnected through clearance seals. For a constant geometry clearance seal operating between two gas volumes at the same mean pressure, a net gas flow will occur from the volume with the greater pressure amplitude to the volume with the lesser pressure amplitude. This is due to the difference in average gas density for the two leakage flow directions. If not countered by some means of inventory management, the mean pressures in the volumes would change and the resulting net force on the piston would cause it to drift until the average pressures were again balanced. In the absence of any other forces on the piston, drifting would continue towards the higher pressure amplitude space until mechanical stops were reached. Gas porting between the volumes acting on the piston is an effective form of passive centering. By judicious selection of the port(s) size and location, a stabilizing force can be generated which increases with increased offset. Thus with knowledge of the gas leakages to and from all active gas volumes, a porting system can be sized to provide sufficient stabilizing stiffness to maintain the desired degree of centering. However, the penalty for increased port strength is a larger port flow loss.

TABLE 7-2

BEARING LOADS

<u>POWER PISTON</u>

- Weight   17 lbf
- Alternator Side Load   30 lbs (.016" offset)
- Alternator Stiffness   1800 lbf/in

<u>DISPLACER</u>

- Weight   3.3 lbf
- Side Load   0

The need for internally pumped bearings complicated the SPDE porting design. By utilizing peak pressures in the working spaces or gas springs, pressurization of the supply plenum, from which the gas bearings are fed, can be achieved by using check valves or position dependent ports. For long life operation, gas ports were selected as the primary bearing supply approach. Thus, the porting system must maintain both piston centering and bearing supply flow.

7.4.2 Porting Design Goals

The design goals for the SPDE gas porting system were as follows:

1. Provide required bearing flow to the supply plenum at a minimum pressure of 5 bar over mean engine pressure.

2. Provide sufficient axial stiffness to the power piston and displacer to maintain centering at design point operation.

3. Operate stably in the region of the design point operating conditions.

4. Achieve goals (1), (2), and (3) while minimizing port and seal flow losses.

The first porting design goal above was set by the bearing requirements. The porting losses are lower when clipping a gas spring pressure wave as compared to the compression space pressure wave due to the much smaller pressure wave phase angle for a gas spring. A greater phase angle results in a significant difference in port ΔP (driving pressure head) during the two porting intervals over a cycle. To avoid flow reversal (change in sign of port ΔP), a larger port offset is then required, with a correspondingly higher effective ΔP and higher losses. With flow reversal, the desired flow is partially negated by the reverse flow, thereby increasing the pumping power per unit gas transfer.

The approach taken was to use the power piston gas spring for bearing supply. To maintain piston equilibrium, the bearing gas must then be returned to the gas spring at the same rate it is taken.

7.4.3 Porting Design Considerations

The following effects on porting system performance were considered:

- Clearance seal leakages.
- Interactions between port and seal flows.
- Port geometry.
- Gas inertial pressure drop.
- Plenum pressure variation.

At steady-state operation, for each volume the cycle averaged mass flows (leakage flows and port flows) must sum to zero. For clearance seals of constant length the net leakage flow is from the higher to lower pressure amplitude spaces as explained above. For some seal configurations, the seal length varies with the piston (or displacer) stroke and the net leakage can differ in both magnitude and direction from a constant length seal. If the seal length varies in phase with the piston stroke, its length would be shortest when the piston is at BDC and the cylinder pressure is near its minimum, and longest at TDC when pressure is near maximum. This results in a net leakage into the space. A variable length seal can be made constant length, or constant length over part of the cycle and varying length over the rest, by designing reliefs into the cylinder.

When the ports are directly communicating with the opposing groove, the calculated flow is purely port flow. When the port and groove are partially engaged or not directly communicating at all, a leakage occurs in the annular "curtain", which in some cases is also the seal flow path. The interaction between port flow and curtain flow was neglected, but the interaction between curtain and seal flows was accounted for as follows: When the curtain flow and seal flow share the same path, the slit flow capacity of the seal determines the total flow through the annular gap. The curtain flow contribution then reduces the seal flow portion.

Preliminary analysis showed square ports pass a given flow with minimum loss compared to oblong rectangular ports. Due to ease of manufacturing, round ports of the same area were selected for the final design.

The high (105 Hz.) SPDE operating frequency increases the gas inertia effects in oscillating or pulsatile flow areas such as ports. The amount of driving pressure lost in overcoming gas inertia was reduced to less than 20% for this design by minimizing the length to area ratios for all port flow passages.

The alternator magnets provide a stabilizing stiffness of 760 lb$_f$/in on the power piston. For porting design conservativeness, this force was neglected.

7.4.4 Porting System Analysis and Design

A port and seal flow analysis code was developed for the purpose of modeling the power piston and displacer port systems. Using input geometry and prescribed gas pressure waves the code time steps through the cycle, calculating the net mass transfer associated with each volume and the time averaged power loss in the seals and ports. Direct port flow is calculated by the classical orifice flow relationship; port curtain flow and seal flow are treated as either slit flow or orifice flow, depending on which provides the dominant resistance. Port curtain flow assumes half of the total port perimeter participates in the flow, thus accounting for spreading of the flow in the annulus. Seal clearances were set by the minimum practical values. Seal eccentricity ratios were set at 0.25 based on the expected bearing performance.

The developed code was checked against the MTI code CYLINDER, which has shown good correlation with actual test performance of free-pistons machines. The two codes agree very closely on both port and seal flow characteristics.

Power Piston Ports

Figure 7-4 is a cross-section of the power piston and cylinder with the bearing, seal, and port flow paths shown. Gas enters the supply plenum from the gas spring through the supply ports. The plenum feeds the bearings, which drain to the four grooves in the cylinder wall. All the grooves are connected to the drain plenum, which includes the piston interior due to the constant connection through the wide groove. The return port then pumps the gas back to the gas spring.

ORIGINAL PAGE IS
OF POOR QUALITY

FIGURE 7-4

PISTON PORT AND BEARING FLOWS
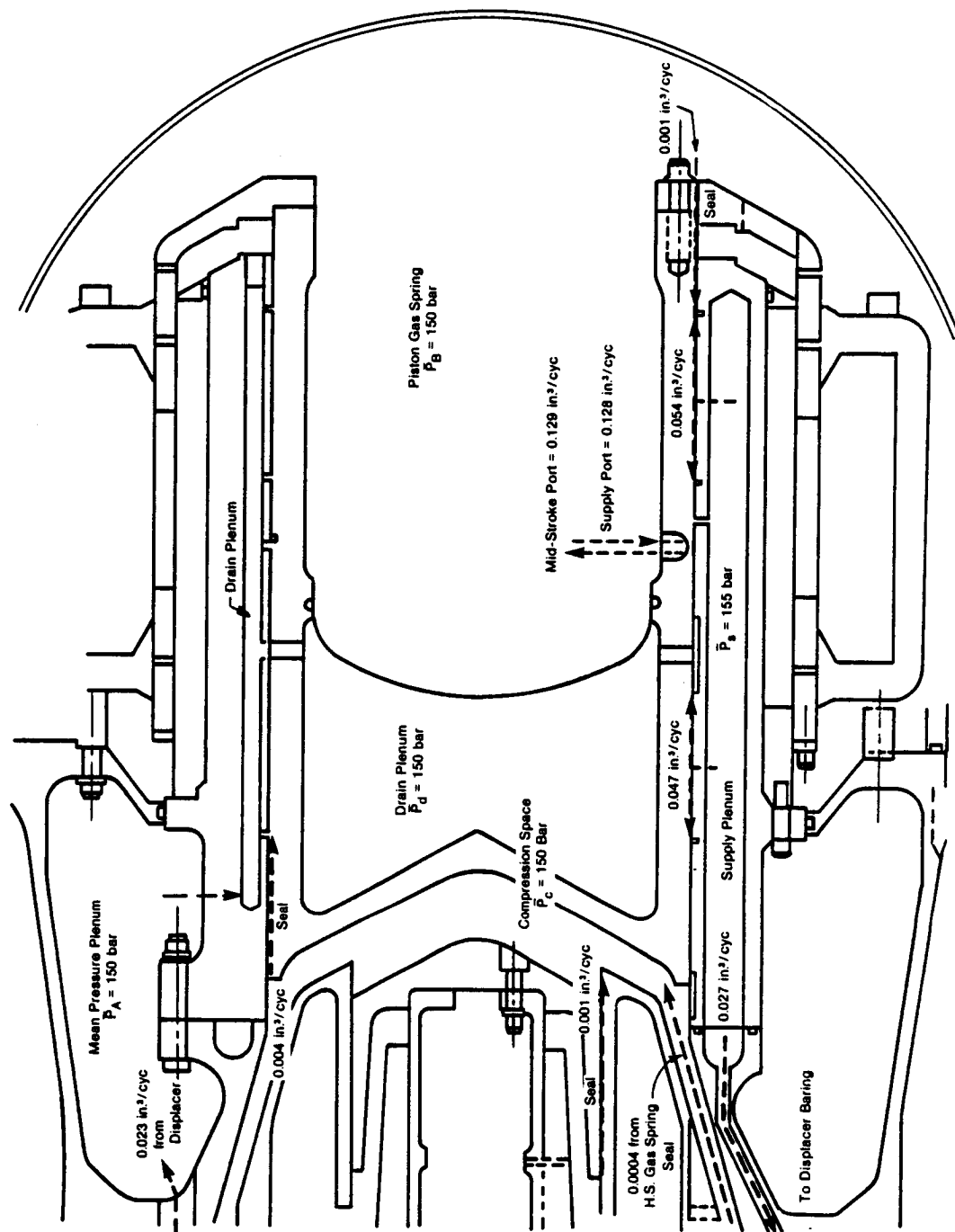
The power piston porting system was separated into two sub-systems: the bearing supply port, and the centering and bearing return port. Each sub-system was analyzed independently with the piston gas spring as the common boundary condition, to which flows must balance.

In the preliminary design phase, supply port options included the following:

1. End-of-stroke ports located at the gas spring end of the piston, beyond the aft bearing drain groove.

2. End-of-stroke ports located between the two bearings.

The seal on the gas spring end of the power piston separates the gas spring from the bearing drain groove on the cylinder wall, thus its length is independent of stroke. The seal length was set at 0.8 in. as a compromise between higher leakage loss and increased bearing angular stiffness. The placement of the supply ports in accordance with option (1) produced a shorter bearing wheelbase (lower angular stiffness) and the space limitations led to high port leakage losses. By moving the ports between the bearings, the bearing stability increased and port leakages decreased. Therefore option (2) became the primary design approach.

With the selection of the location of the bearing supply ports, the return ports fit cleanly into the arrangement by using the same groove in the piston which feeds the supply ports at BDC to pick up the return ports near mid-stroke. The design problem was to determine the port sizes and offsets to achieve the design goals.

With the large 2 bar drain plenum pressure amplitude in the preliminary design, a large return port offset was required to return all bearing flow to the gas spring without incurring excessive flow losses due to port flow reversals. However, the large return port offset would cause the piston to center on the port at low strokes (during startup) when the supply port is not yet engaged, resulting in a large piston offset (see Figure 7-5a). The mechanical stops would then limit the piston stroke, preventing the engagement of the supply ports. This problem was resolved by isolating the drain plenum from the displacer upper gas spring through a set of orifices, and adding the piston interior volume to the drain plenum, thereby reducing the drain plenum pressure amplitude to approx-
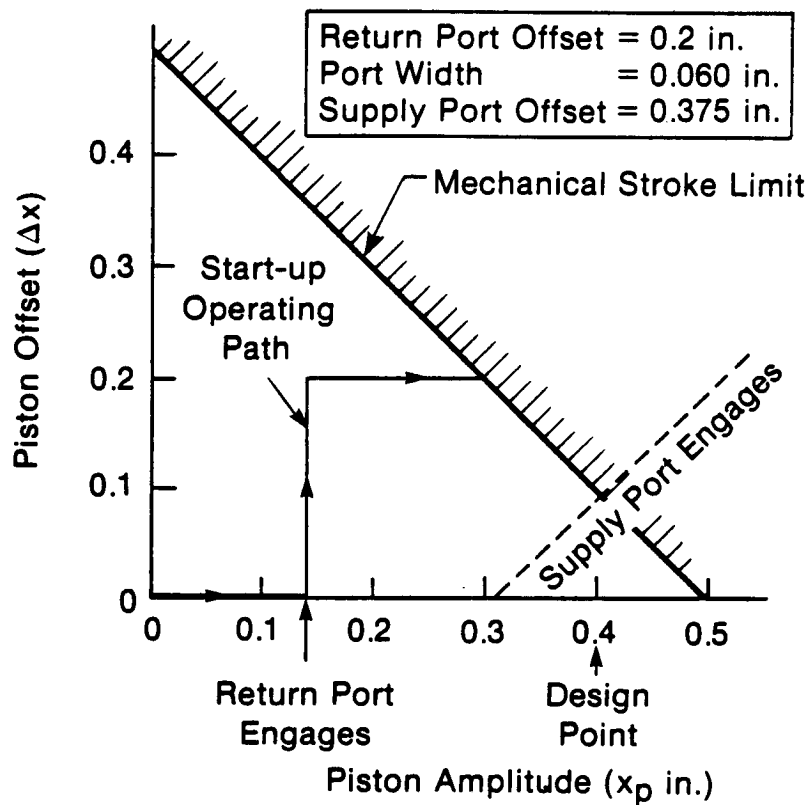
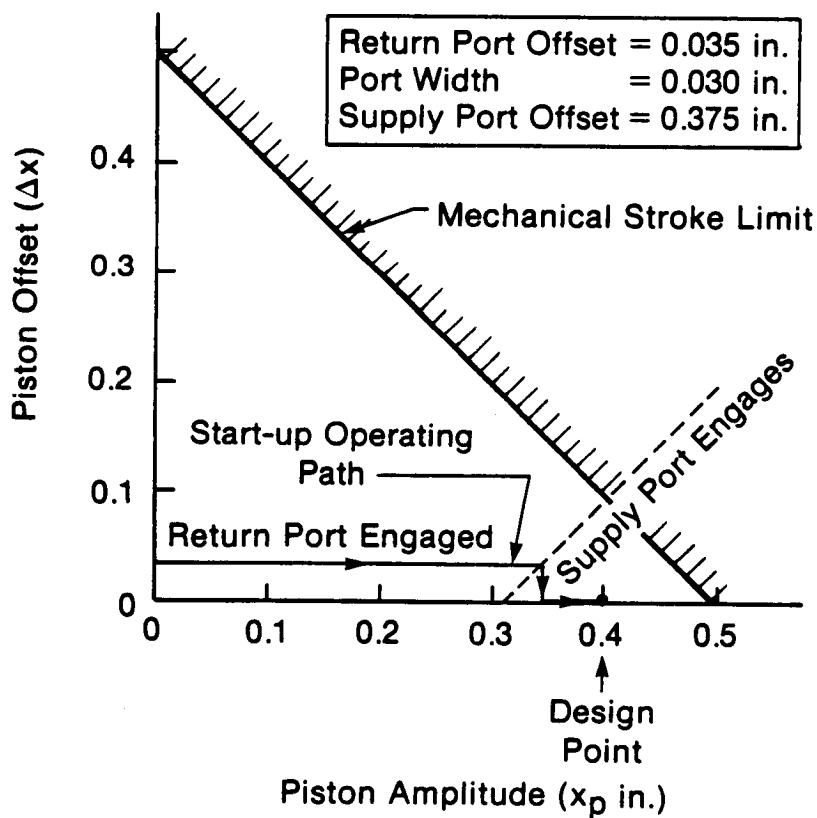FIGURE 7-5

PISTON OFFSET VS. PORT LOCATION

Return Port Offset = 0.2 in.
Port Width = 0.060 in.
Supply Port Offset = 0.375 in.

FIGURE 7-5a

Piston Offset (Δx)

Mechanical Stroke Limit

Start-up Operating Path

Supply Port Engages

Return Port Engages

Design Point

Piston Amplitude (x_p in.)

Return Port Offset = 0.035 in.
Port Width = 0.030 in.
Supply Port Offset = 0.375 in.

FIGURE 7-5b

Piston Offset (Δx)

Mechanical Stroke Limit

Start-up Operating Path

Return Port Engaged

Supply Port Engages

Design Point

Piston Amplitude (x_p in.)

86186

imately 0.6 Bar. The return port was then placed as close to geometric center as possible, without paying a large loss penalty, to provide increased centering stiffness (see Figure 7-6) and a stable startup operating path (Figure 7-5b). The flow loss increases below a certain port offset because the port area must increase to enable return of the bearing flow (see Figure 7-7), and the longer porting interval results in a larger variation in port ΔP and possible flow reversal.

The placement of the supply ports in the piston cylinder wall was made to minimize the port curtain leakage losses from both the supply ports (155 bar) and the moving piston port groove (P_{pgs}) to the adjacent bearing drain grooves (P_m). Figure 7-8 shows the net leakage loss from the above sources to the gas spring side and compression space side bearing drains as a function of the supply port placement. Minimum total port leakage was obtained with the supply ports located 0.6 inch from the gas spring drain groove.

The port groove, located in the piston, was sized to handle the supply and return flows with minimum pressure loss due to gas inertia. To achieve this the groove depth was increased to the maximum allowed by the piston thickness and the number of ports was increased to shorten the flow path length. The supply flow enters the groove radially at each of the 24 entrance holes and splits into circumferential flow until the holes in the cylinder wall are reached. In the worst case alignment between piston holes and cylinder holes the circumferential path length is 0.37 inches (piston circumference/48). The return flow follows the same path, but from the return ports, and in the reverse direction.

In the preliminary design a port on the compression space end of the power piston was also planned to maintain pressure balancing of the compression space and provide additional power piston centering stiffness. The compression space seal on the piston varied in length with the piston stroke and the sum of all compression space leakage flows required a small port offset toward BDC in order to remove the leakage. However, due to the compression space pressure phase angle, the porting losses were large, thereby penalizing the mechanical efficiency of the engine. By designing the compression space seal with a constant length (L_s=1.6 in.), its net leakage per cycle was out of the compression space and balanced the sum of the other compression space leakages, therefore the port was not needed to balance leakage flows. The gas spring mid-stroke port was consid-
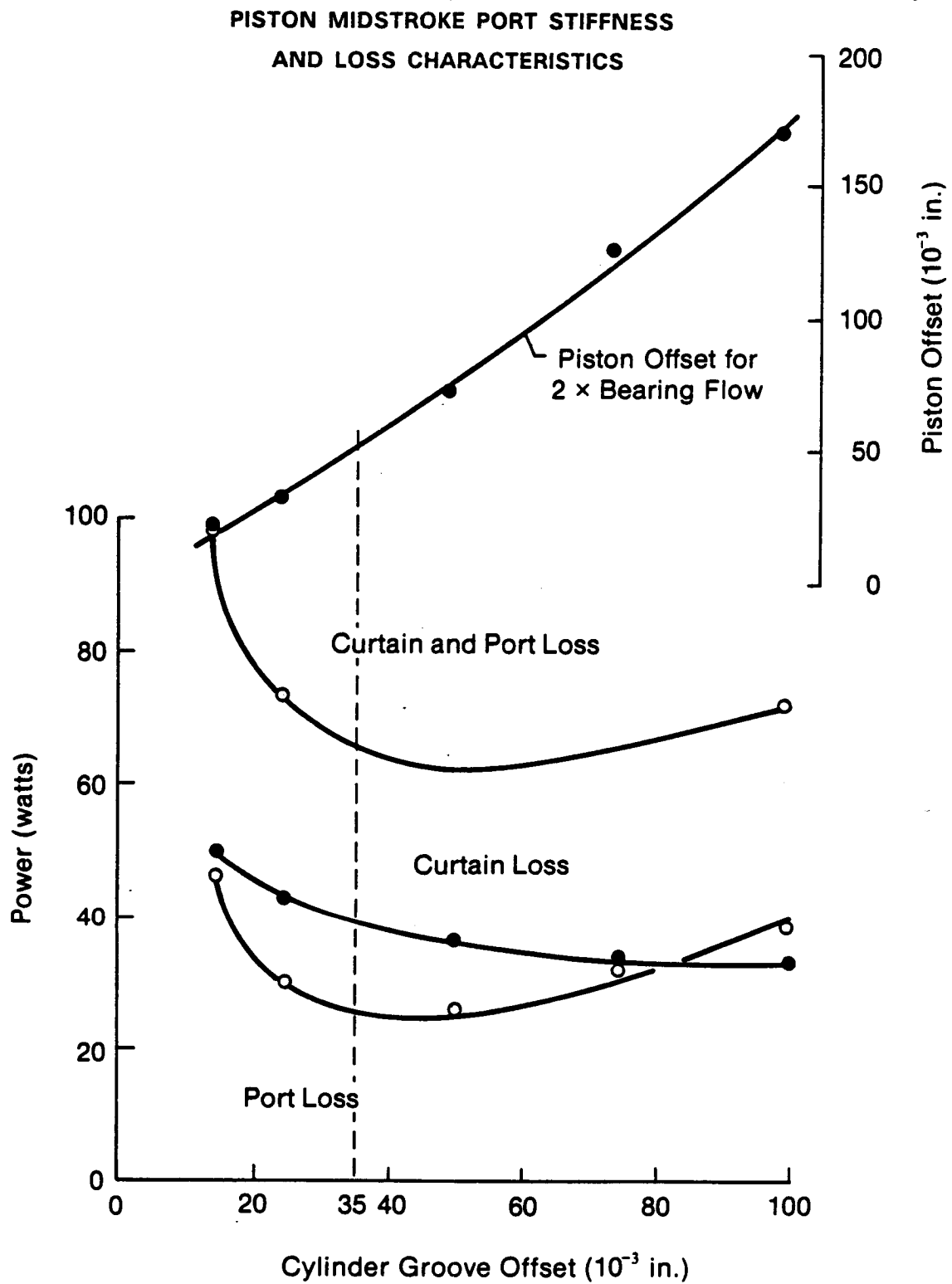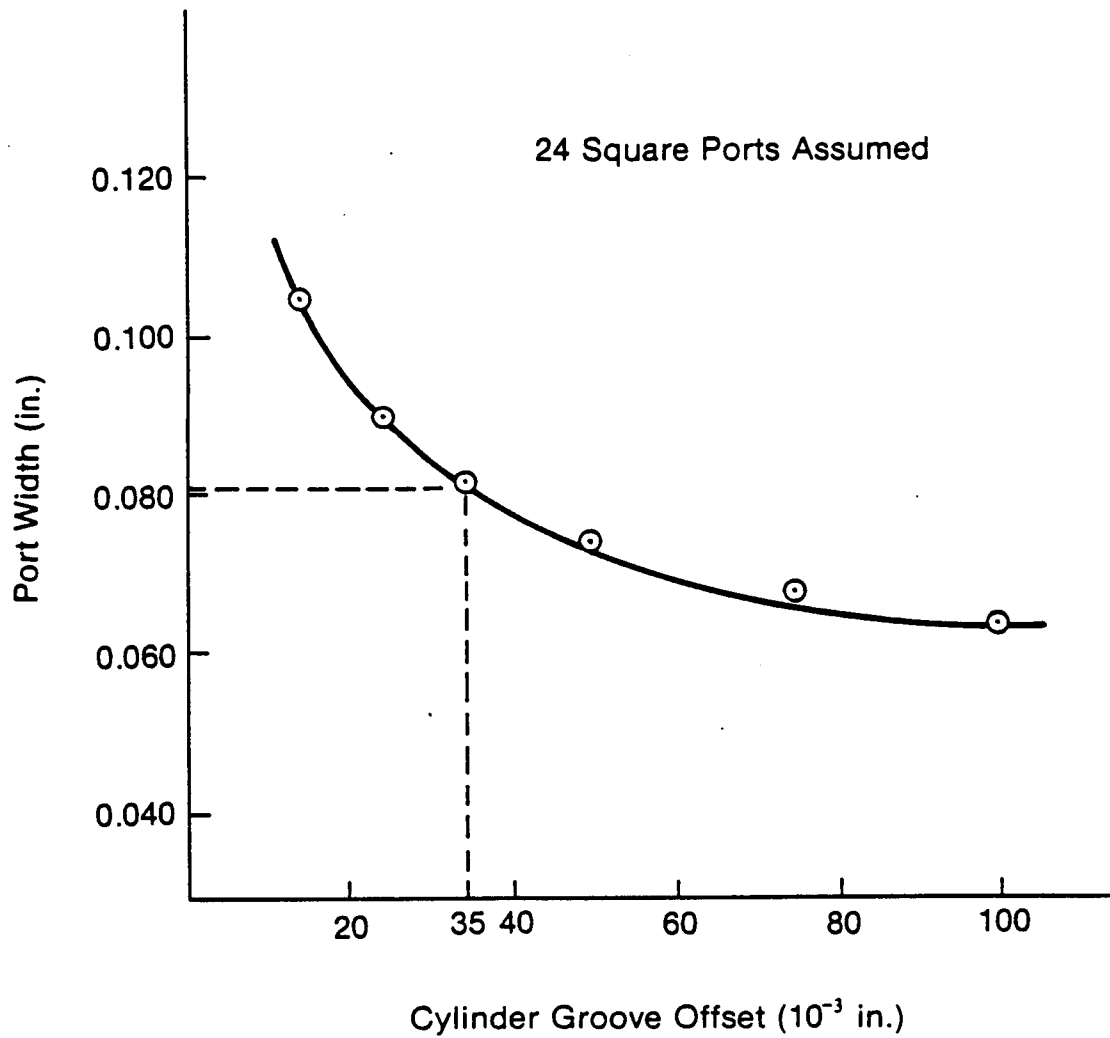
FIGURE 7-6

PISTON MIDSTROKE PORT STIFFNESS
AND LOSS CHARACTERISTICS
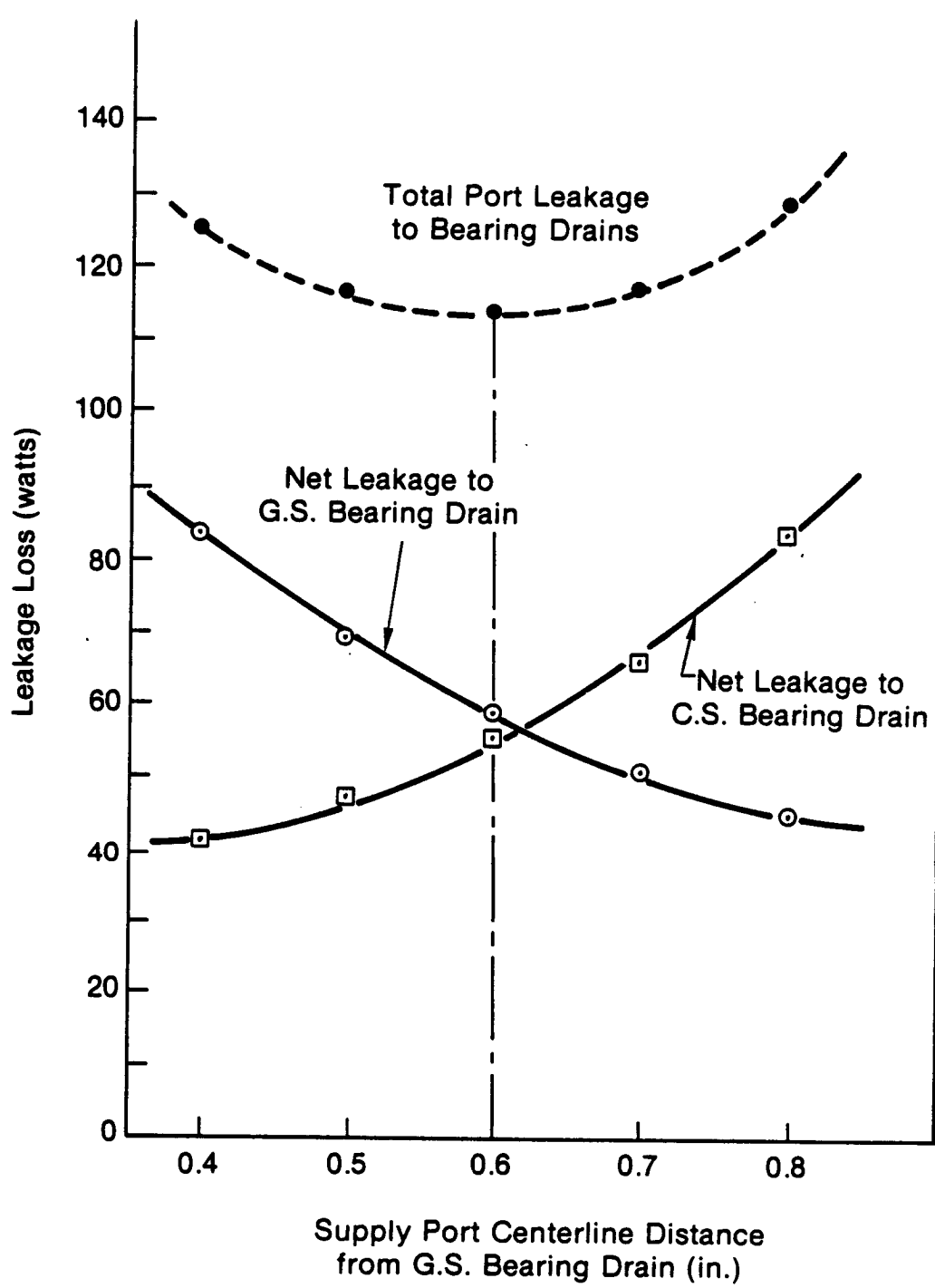
7-19

FIGURE 7-7

REQUIRED PORT SIZE TO BALANCE

DESIGN POINT BEARING FLOW VS. CYLINDER GROOVE OFFSET

FIGURE 7-8

POWER PISTON PORT LEAKAGE VS. PORT LOCATION

86182

ered sufficiently stiff to maintain piston centering without the extra port, and the additional port losses were avoided.

Displacer Ports

A diagram of the displacer bearing, seal, and port flows is shown in Figure 7-9. The displacer bearing flow leaves the bearing supply plenum in the power piston cylinder and feeds the double admission plane bearing jets at the displacer. The upper side of the displacer bearing drains directly to the heater side gas spring, while the lower side drains to a moving port groove on the displacer rod. The groove connects to the heater side gas spring through holes in the rod at the base of the groove.

The load side gas spring has two clearance seal leakage paths: one to the upper gas spring, and one to the compression space. The compression space seal is of constant length and the net leakage is out of the gas spring (but small) since the seal aspect ratio (D/L) is relatively small and the clearance (0.0006 in. radial) is tight. To minimize the displacer porting flow requirements, the rod seal (to upper gas spring) was designed with a constant length to reduce the leakage into the load-side gas spring, enabling the compression seal leakage to be nearly balanced.

The displacer mid-stroke port connects the load-side gas spring with the groove. The displacer ports were designed for high stiffness and low net flow, thus the port offset from mid-stroke is small (0.015 inch), towards the compression space.

7.4.5 Porting Design Details and Performance

Table 7-3 gives the final port geometries and predicted losses.

The centering of the power piston and displacer are only weakly coupled. The stiffness of the displacer and piston ports are sufficient to maintain centering for variances in leakage and bearing flows, and because of the small leakages between spaces an operating offset of one member does not strongly perturb the other.
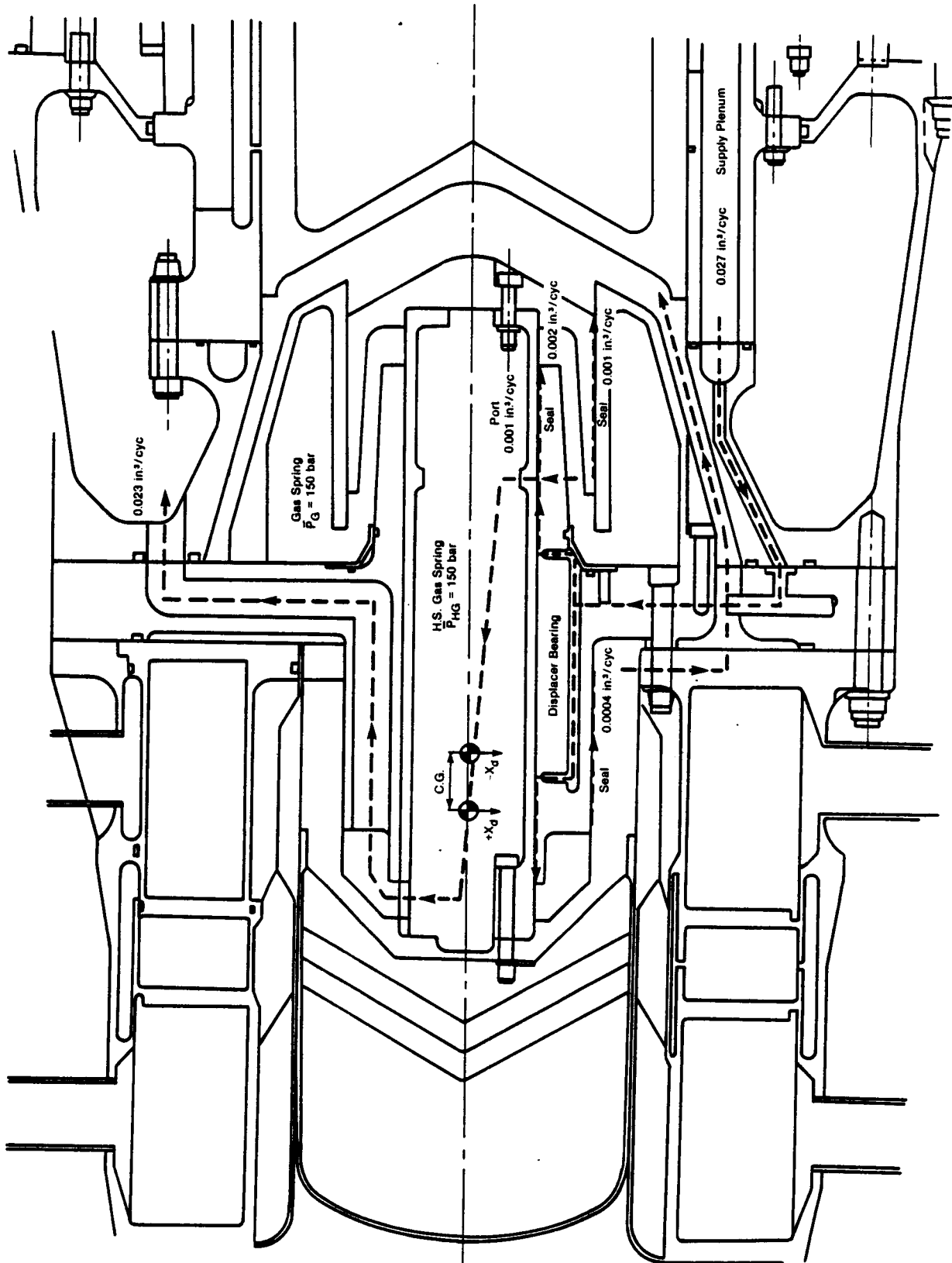
DISPLACER BEARING AND PORTING FLOWS

FIGURE 7-9

Labels within figure:

Supply Plenum

0.027 in.³/cyc

0.002 in.³/cyc

Seal 0.001 in.³/cyc

Port 0.001 in.³/cyc

Seal

Displacer Bearing

Gas Spring $\bar{P}_G = 150$ bar

H.S. Gas Spring $\bar{P}_{HG} = 150$ bar

C.G.

$-x_d$

$+x_d$

Seal 0.0004 in.³/cyc

0.023 in.³/cyc

86199

TABLE 7-3

PORT PARAMETERS

		DISPLACER MID-STROKE	PISTON MID-STROKE (BEARING DRAIN)	BEARING FEED
# Ports		4	24	24
Port Size	(In)	0.060	0.080	0.055
Xp Start*	(In)	+0.075	+0.115	-0.308
Xp End*	(In)	-0.045	-0.045	--
Net Port Flow (In³/Cycle) (Direction Indicated in Respective Port Flow Diagrams)		0.001	0.129	0.128
Loss (Watts)				
- Port		3.6	26.0	43.0
- Curtain		37.0	114.0	97.0

* Piston position (relative to mid-stroke) at
   initiation or completion of port engagement

The offset of the bearing supply port was reduced from a true end-of-stroke condition to allow for full bearing supply capability with reasonably small piston offset and variations in piston stroke.

The groove on the displacer rod, which handles both bearing and port flows, is connected to the heater side gas spring by eight holes of 0.060 inch diameter. For the ports in the cylinder wall, although six holes were specified for the engine hardware, only four ports were necessary to achieve balanced leakage flows with high centering stiffness. The extra holes were added to accommodate larger leakages and can be filled if the ports are too strong (show high losses) in tests.

The displacer bearing flow drains back to the piston gas spring through six orifices (0.020 inch dia.) between the upper displacer gas spring and the drain plenum drillings (see Figure 7-4). The 1.5 bar pressure amplitude in the mean pressure plenum (also the upper displacer gas spring) causes reversing flow through the orifices, but the total orifice flow loss is small (< 20 watts).

The drain plenum is directly connected to the piston interior via a 1 inch wide drain groove in the cylinder wall and six holes of 0.201 inch diameter. Thus the drain plenum volume is comprised of 24 drillings in the cylinder (11 in^3) and the piston interior (150 in^3).

Figure 7-6 shows the stiffness and loss characteristics for the piston mid-stroke (bearing return) ports. For a particular design offset of the port groove, the diagram shows the piston offset which would result if the bearing flow doubled. The ports are sized for the same design bearing flow at each point (see Figure 7-7 for port dimensions). With the design groove offset of 0.035 in., a doubling of bearing flow would result in a .050 in. piston operating offset from center. If a stiffer port were desired, a smaller groove offset would be selected (with a correspondingly larger port area) and the piston offset would decrease, but at the expense of increased losses.

Figure 7-10 shows a similar diagram for the displacer port characteristics.

FIGURE 7-10

DISPLACER GAS SPRING PORT STIFFNESS
AND LOSS CHARACTERISTICS

86181
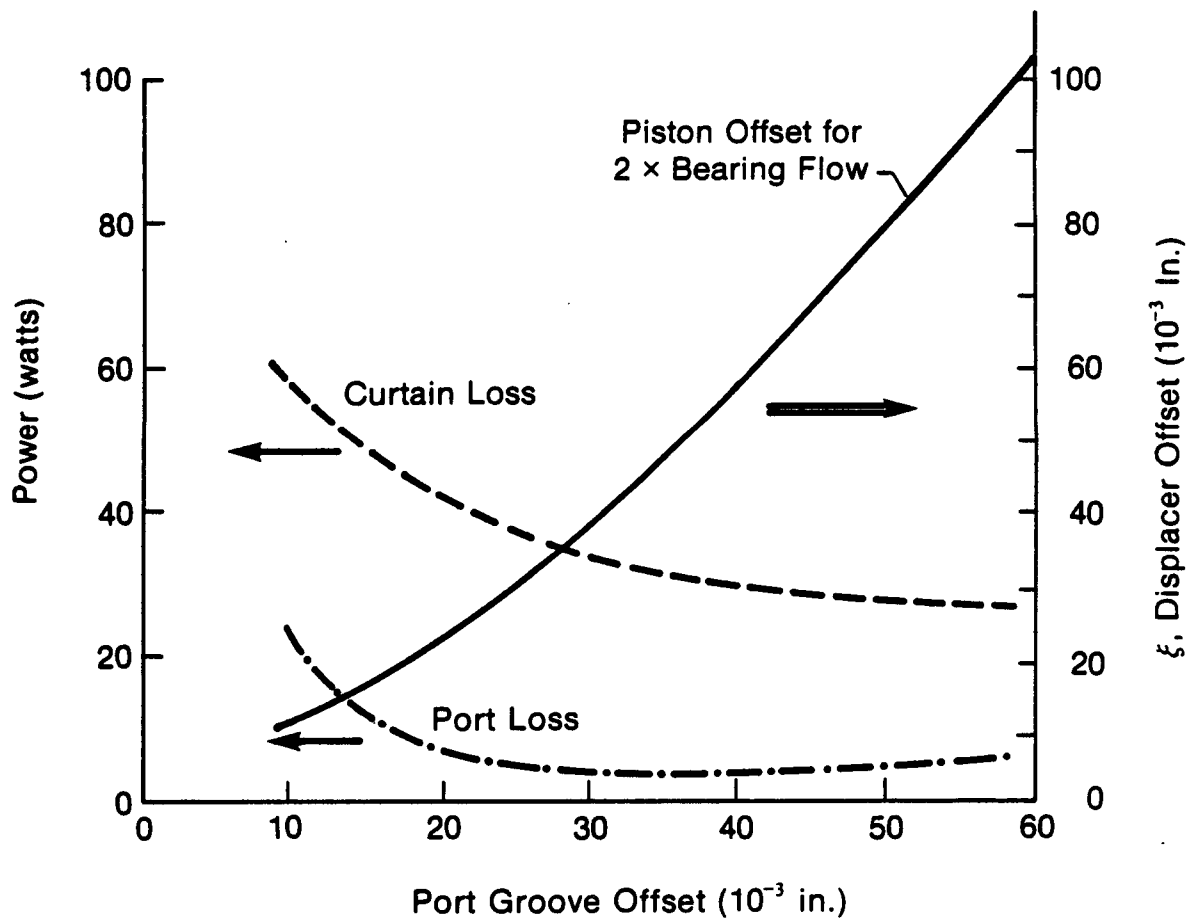
8.0 ALTERNATOR DESIGN AND ANALYSIS

8.1 Alternator Description

Figure 8-1 presents the basic features of the SPDE alternator. It has three separate parts:

- the inner stator;
- the moveable plunger carrying radially magnetized magnets; and,
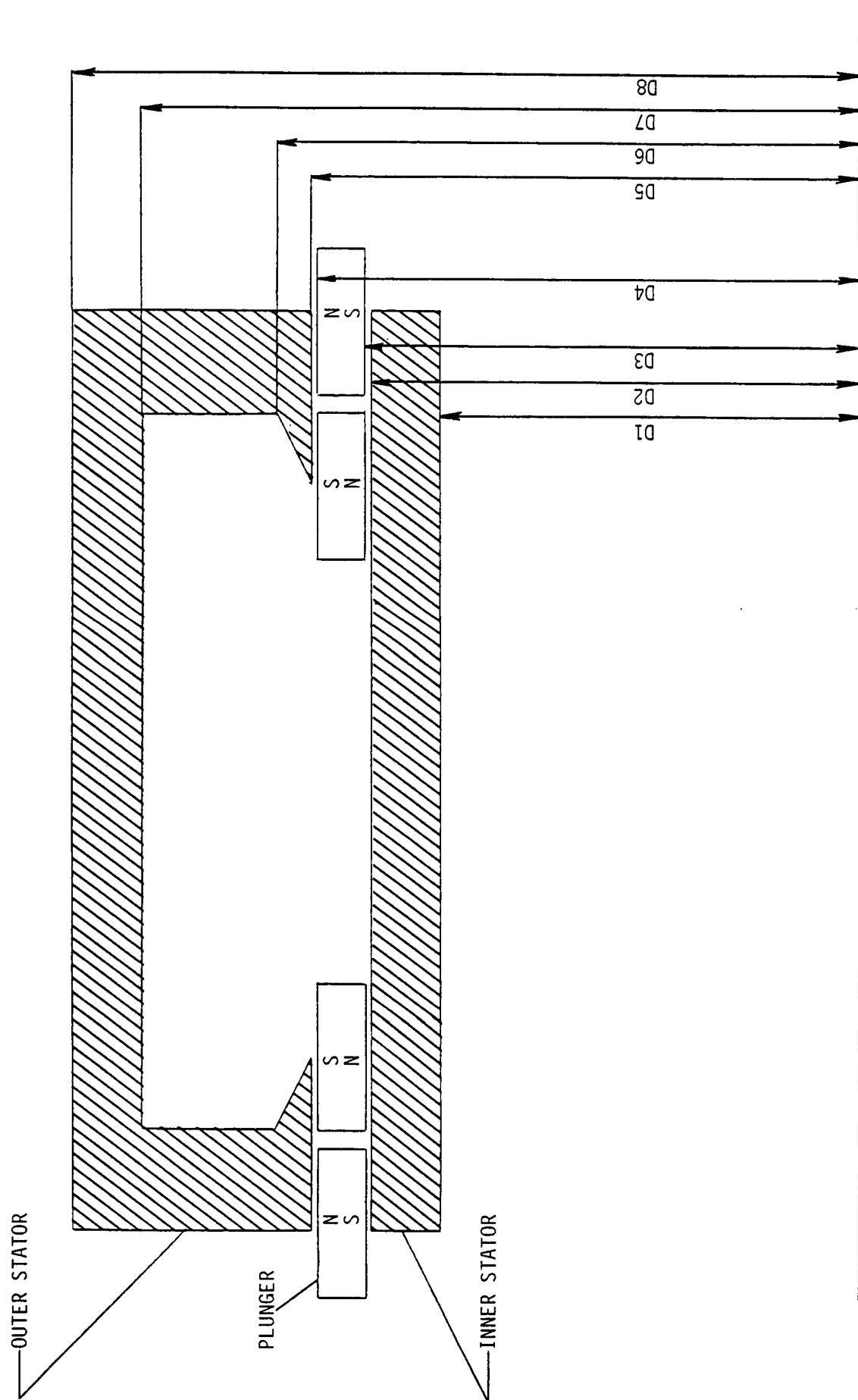- the outer stator.

The inner stator is in the shape of a cylindrical sleeve. It is radially laminated to prevent currents induced in the circumferential direction. It is made of high permeability, high resistivity material such as electrical steel. The inner stator is necessary to complete the magnetic path of the system. The linear alternator is a cylinder consisting of axially oriented stacks of steel laminations supported in a phenolic cage.

The outside stator is also radially laminated and made of electrical steel. The outer stator is cylindrical-shaped and consists of a large, wound copper wire coil encased in steel laminations. These laminations are shaped to surround a doughnut-shaped coil.

The moving plunger consists of four cylindrical rings of radially magnetized permanent magnets of high magnetic strength magnet material (samarium cobalt). This material is structurally very weak and, hence, the moving plunger is made from a lightweight, structurally strong non-magnetic material (titanium) in which the permanent magnet pieces are held to form the desired permanent magnet rings. The relative location and polarities of the magnet rings is shown in Figure 8-1. All three parts are concentric to each other and, thus, the moving plunger reciprocates in the annular space formed between the inside and outside stators, and the interaction between magnetic flux and the outer stator coil generates electrical energy.

FIGURE 8-1

SPDE ALTERNATOR CONFIGURATION

8.2 Alternator Mechanical Design

Major design and fabrication challenges were addressed for each of the three alternator parts, which were:

- Assembling the large, heavy wire outer stator coil in the restricted steel lamination slot.

- Formation of a structurally sound plunger cylinder without the use of an inner and outer support sleeve. This was required because of the small radial gap between the plunger and outer and inner stators.

- Assembly of the inner stator laminations in a cylindrical configuration that was structurally rigid using cage material that was non-magnetic and non-conducting.

8.2.1 The Outer Stator Details

The outer stator assembly consists of four main parts:

- The coil;
- Laminations;
- Terminals; and,
- End Rings.

Coil – The coil, which is pre-wound on a bobbin, actually consists of four concentrically wound coils which are connected together in parallel. Each of the four coils has 67 turns and is wound from #9-1/2 AWG heavy film coated magnet wire.

During the coil winding, strips of insulation were placed between each layer of wire. Epoxy was coated liberally throughout the coil during winding. The coil winding bobbins were lined with vomex insulation paper before the winding was started. This adhered to the coil when the epoxy cured and insulated the coil from the laminations.

Laminations - The laminations were punched from .014 inch thick Hyperco-50 electrical steel. After punching, the laminations were heat treated to reduce stresses and then coated with a layer of insulating resin.

The laminations are rectangular with a wide coil slot which is restricted at the bore edge. The laminations were assembled on the coil by flexing the legs and working them over the coil. This was easily done because the laminations were thin.

The laminations are spaced equally at the outer diameter of the stator while they touch at the inner bore. The laminations are dimpled near the outer edge to maintain an even spacing.

Terminals - The four concentric coils described earlier had to be connected in parallel. Since each of the four branches conducts less current, the I^2R loss is minimized. The terminals consist of copper blocks with holes to accommodate the coil ends. A large projecting terminal post is provided for output connections. The coils were soldered to the terminals which are located 180° apart on one end of the stator.

End Rings - Two non-magnetic stainless steel end rings are required to complete the stator. An end ring is positioned at each end of the stator coil/lamination combination. A fixture was used to position the end rings accurately. The end rings were welded to the laminations. The stator was potted after welding and then final machined.

8.2.2 The Plunger Details

The plunger consists of four major elements which are:

- Titanium cage;
- Magnets;
- Spacers; and,
- End Ring.

Titanium Cage - The titanium cage consists of a plunger carrier and I-beams. Eighteen I-beams are evenly spaced and welded to the carrier to form an

open-ended cage. Titanium was chosen because it is non-magnetic and results in very low electrical losses. Since the plunger reciprocates axially at high frequency, the assembly requires tensile strength. This is provided by the titanium beams. The I-beam cross-section, in combination with projections on the ends of the magnets, form an assembly method. The outboard ends of the I-beams are threaded to accommodate an end ring at final assembly.

Magnets - The magnets are a rare earth composition which are compounded to give the required design characteristics. The magnets underwent a series of steps leading to the final assembly. These steps were:

1. Compounding the magnet powder ingredients;
2. Pressing the powder into a trapezoidal shape of the required thickness;
3. Form-grinding the end projections onto the magnets which interlock with the titanium beams; and,
4. Magnetizing the keystone shaped magnets so that adjacent plunger magnet rings have opposing polarity.

The magnetized partially-shaped segments were ready for the plunger assembly.

Spacers - The spacers provide the correct spacing for the magnet rings. They are made of G-10 glass epoxy sheet material. This material is non-magnetic and non-conducting. The spacers were fabricated to the same outline as the magnets. They sandwiched the magnets at assembly.

End Ring - The end ring is a wound filament composite material selected for high strength and rigidity. It is positioned on the threaded outboard of the titanium I-beams at the final assembly of the plunger and bolted in place.

The cage, magnets, spacers, and end rings were bonded together with epoxy. The final step was the grinding of the plunger outer diameter and bore.

8.2.3 The Inner Stator Details

The inner stator consists of a G-10 phenolic cylindrical lamination cage which positions and supports 18 lamination sub-assemblies.

Phenolic Lamination Cage - The lamination cage was machined from a single cylindrical tube of G-10 glass phenolic. The tube was manufactured by wrapping fiber glass cloth on a mandrel and loading the structure with epoxy. The material was chosen for its non-magnetic and non-conducting electrical properties. Although the inner stator is supported at one end, structural strength and rigidity were selection criteria for the material.

Lamination Sub-Assembly - The purpose of the inner stator is to complete the plunger flux path. This is done by providing stacks of axial laminations in the inner stator. Eighteen stacks of Hyperco-50 steel laminations were pre-assembled and positioned in the phenolic cage. Each sub-assembly consists of a stack of .014 inch thick Hyperco-50 strips which were bonded together in a fixture and oven cured. A thin steel tab was inserted in the slotted ends of each lamination stack. At assembly, the stack was positioned in the phenolic cage. The tab on one end of the stack was fitted into a mating slot in the phenolic cage. The tab on the other end was clamped in a recess in the cage. The assembly was bonded with epoxy followed by machining of the final bore and outer diameter.

8.3 Alternator Operation

Figure 8-2a shows the plunger in the extreme left position with associated flux paths. When the plunger is moved to the extreme right, the flux paths are as shown in Figure 8-2c. The flux linking the coil has opposite directions between these two extreme positions. Figure 8-2b shows the flux paths when the plunger is in the central position. From these flux paths, it is seen that no flux links the coil when the plunger is in the central position. Thus, the plot of flux linking the coil versus plunger displacement is shown in Figure 8-3.
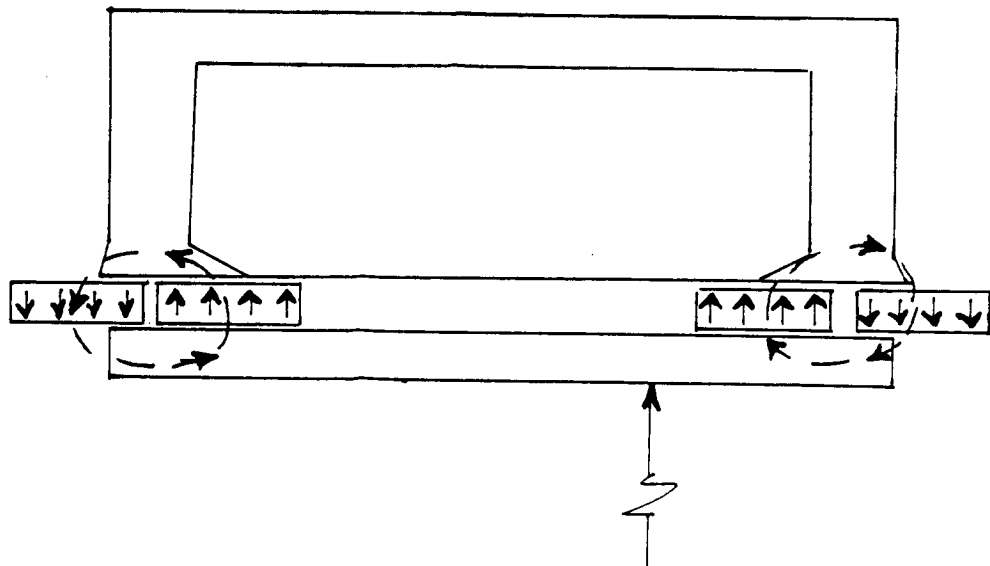
When the plunger is reciprocated by the engine sinusoidally, the flux linking the coil will likewise vary sinusoidally and a voltage V_{gen} will be induced in the coil.

FIGURE 8-2
SPDE ALTERNATOR OPERATION

PLUGER AT
EXTREME RIGHT
Figure 8-2c
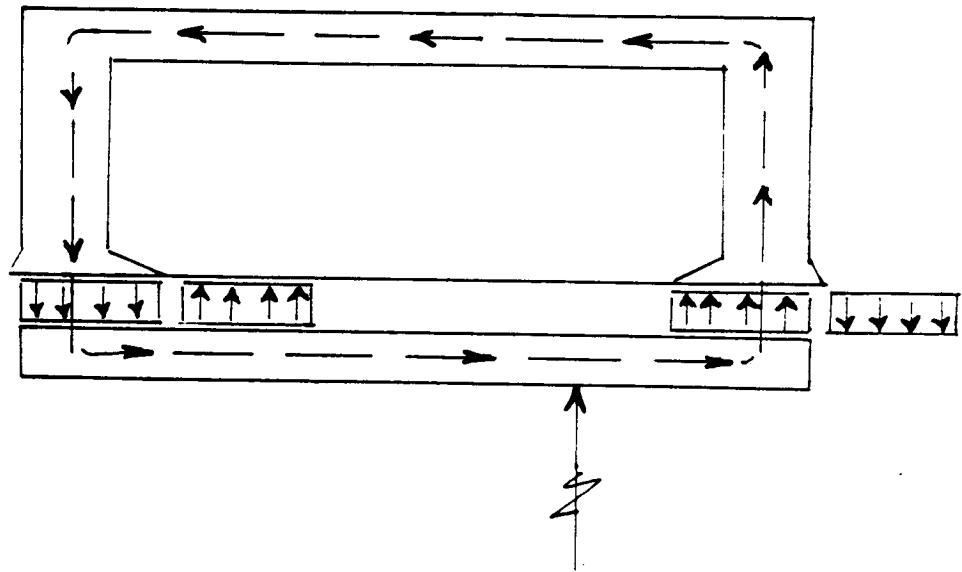
PLUNGER AT
CENTER
Figure 8-2b
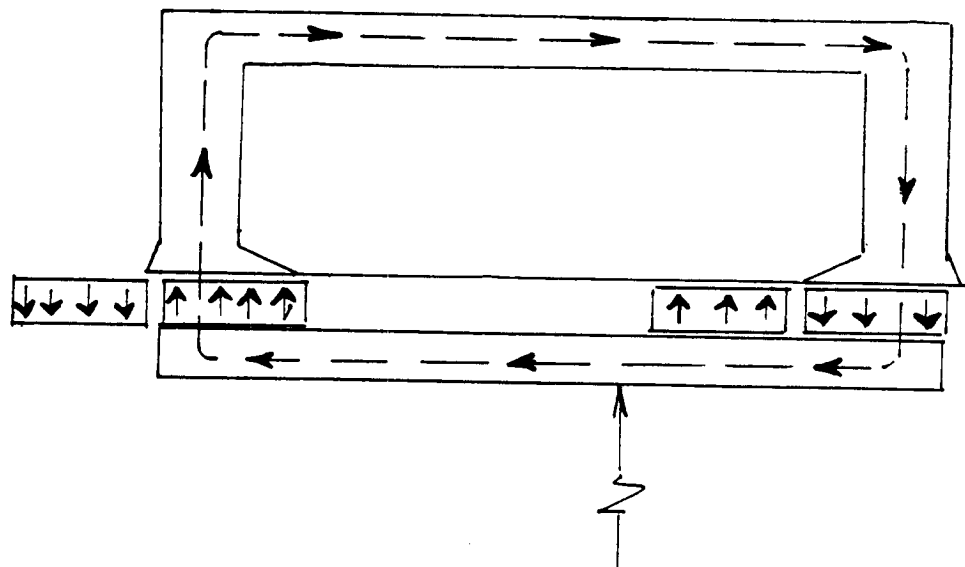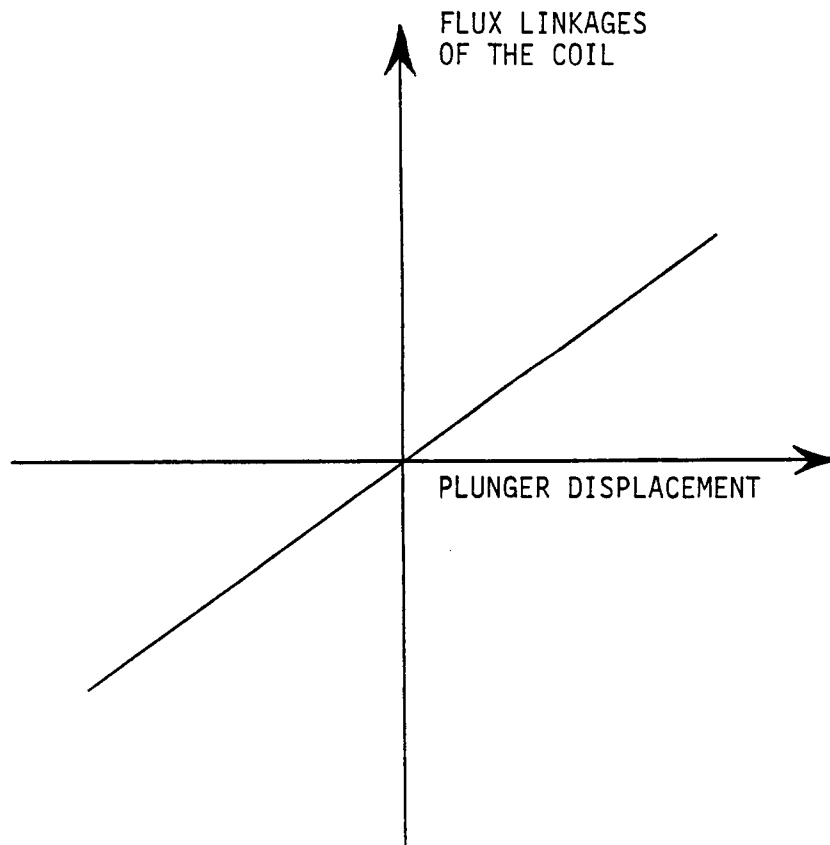
PLUNGER AT
EXTREME LEFT
Figure 8-2a

FIGURE 8-3

**VARIATION OF THE LINKAGES OF THE COIL
VERSUS PLUNGER DISPLACEMENT**

The lumped parameter equivalent circuit of this alternator is shown in Figure 8-4. The reactance and the resistance shown in this Figure are the reactance due to self inductance of the coil and winding resistance respectively.

A flat model was constructed to simulate an arc of 60 degrees of the alternator designed for space power. The purpose of this model was to determine flux linkage versus displacement curve. In the model, the permanent magnets were simulated by air core coils conforming to the periphery of the magnets. The flux linkage versus displacement curve measured on this model is shown in Figure 8-5 which is remarkably linear over the stroke range desired.

8.4 V_{gen} Calculation

The open circuit voltage V_{gen} is computed by using Faraday's law of induction stated as:

$$e = \frac{d\psi_{eff}}{dt} \qquad (8.1)$$

Where: e = instantaneous induced voltage in the coil of the alternator

ψ_{eff} = instantaneous value of the flux linkages of the coil of the alternator

The rms value of open circuit voltage is then derived as:

$$V_{gen} = \frac{(2\pi f)\psi_{effmax}}{\sqrt{2}} \qquad (8.2)$$

Where: π = 3.1416

f = frequency of oscillator (assumed sinusoidal)

ψ_{effmax} = maximum value of the effective flux linkages of the coil

The value of ψ_{effmax} has to be obtained by integrating the flux linkages over the whole coil cross section when the plunger is in the extreme right position

In magnetic circuits where most of the flux path is confined to iron parts such as in the case of a transformer, integration of flux linkages over the whole coil

FIGURE 8-4

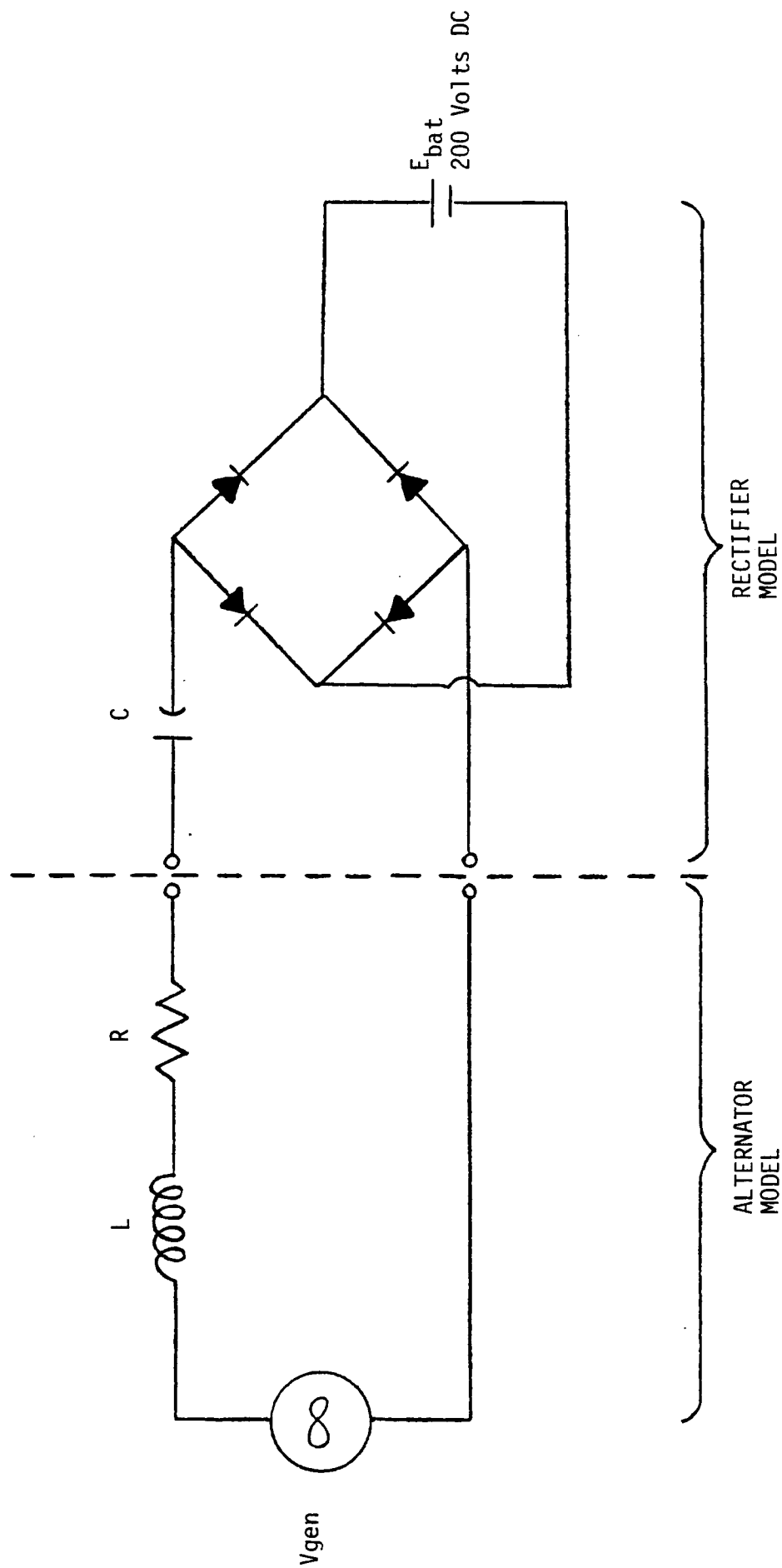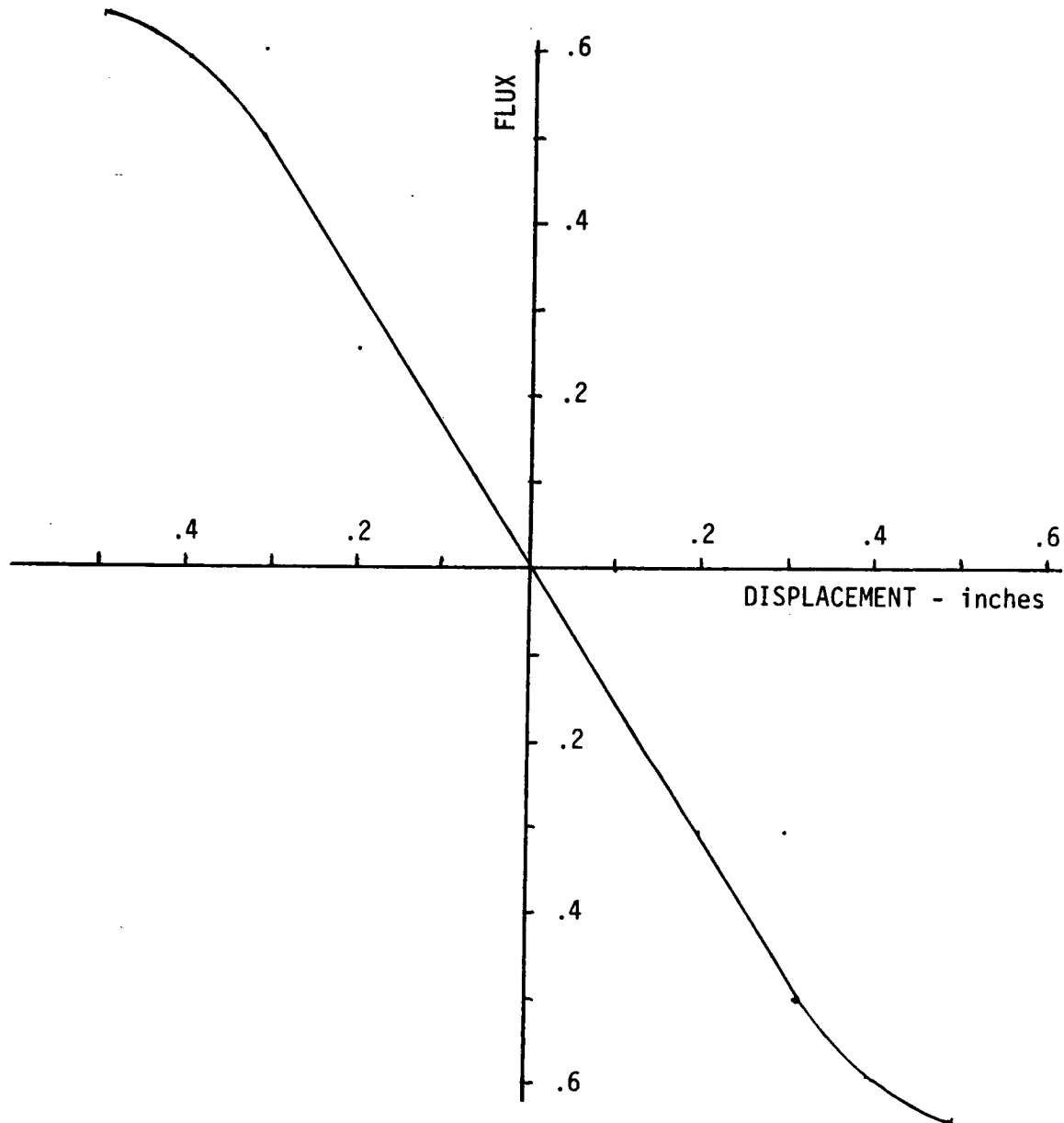**LUMPED PARAMETER ALTERNATOR – RECTIFIER CIRCUIT**

FIGURE 8-5
FLUX VS. DISPLACEMENT MEASURED ON THE MODEL

cross section reduces to simple calculation of flux in the iron paths. However, in the magnetic configuration of the SPDE alternator, a significant quantity of flux exists in the coil space due to large effective air gaps in the magnetic circuit. (Note that the relative permeability of the permanent magnet material is close to unity and, hence, the space occupied by the magnets acts similarly to an air space occupying the same volume). Hence, the computation of the effective flux linkages of the coil requires a knowledge of the flux distribution in the coil space. This was determined by the use of a finite element technique and verified by the use of an experimental model simulating a small circumferential section of the alternator. The details of the finite element study is given in Appendix 8.1 and the details of the experiment are given in Appendix 8.2.

The results of the finite element analysis and the experimental model can be closely simulated by the following analytical procedure:

1. Figure 8-6a shows the cross-section of the SPDE alternator for the condition when the plunger is moved to the extreme right position. An approximate magnetic equivalent circuit corresponding to this situation is shown in Figure 8-6b with only one magnet excitation to be active. Principle of superposition is to be employed to obtain the affect of all magnet excitation present simultaneously as in the actual case. In this magnetic equivalent circuit, the magnet is represented by a source of mmf (battery) in series with a reluctance. The derivations for the expressions for the various reluctances in this equivalent circuit are given in Section 8.5. This magnetic circuit is solved using the magnitude of this mmf excitation to be unity.

2. The flux $\phi_{3,1}$ links the whole coil. The flux $\phi_{2,1}$ (which is the flux through the reluctance R_2) is distributed over the entire section of the coil. In the derivation of the magnetic equivalent circuit of Figure 8-6b, it is implicitly assumed that the flux $\phi_{2,1}$ is uniformly distributed over the entire axial length of the coil. The flux linkages of the alternator coil due to the flux $\phi_{2,1}$ can be shown (by integrating over the entire cross section of the coil) to be:

$$\phi_{2,1} / 2 \ N_{turns}$$

FIGURE 8-6a

**ALTERNATOR CROSS SECTION WITH
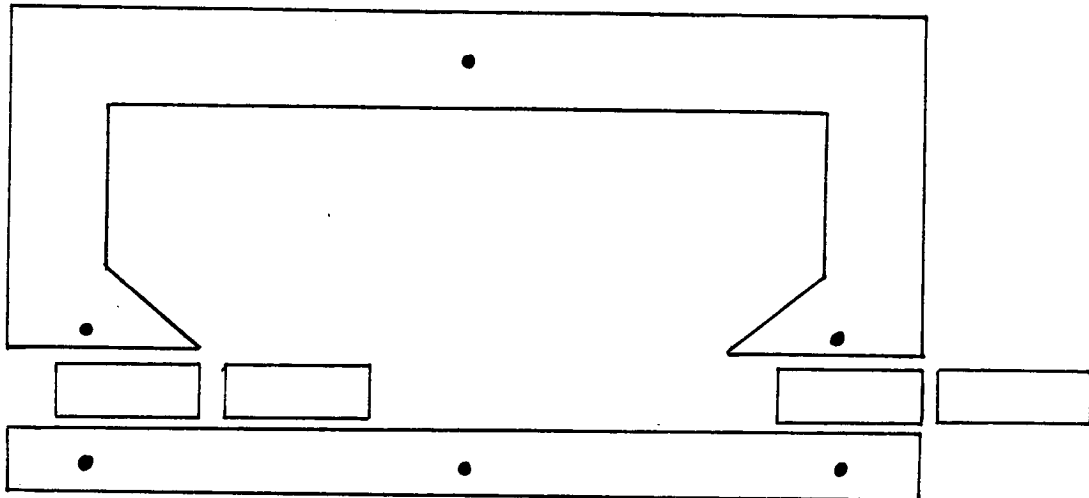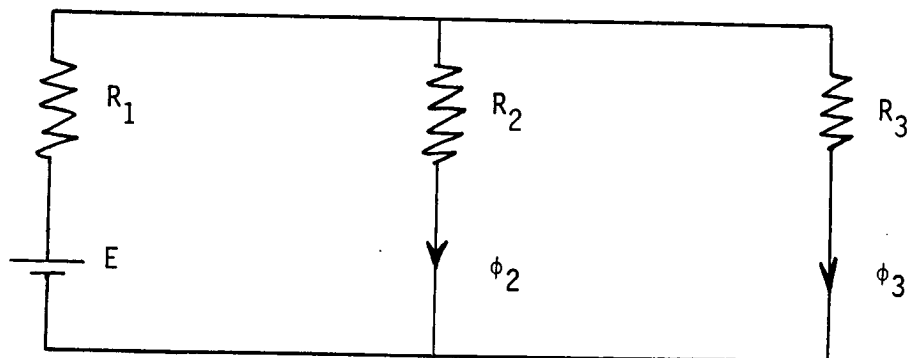PLUNGER IN FAR RIGHT POSITION**

FIGURE 8-6b

EQUIVALENT MAGNETIC CIRCUIT OF FIGURE 8-6a

Thus, the flux linkages of the coil due to the flux pattern set-up by the excitation of one magnet (with magnitude of mmf equal to unity) are given by:

$$\psi_1 = \left(\phi_{3,1} + \frac{\phi_{2,1}}{2} \right) N_{turns} \qquad (8.3)$$

3. The effect of excitation of all magnets acting simultaneously has been determined experimentally as:

$$\psi_{resultant} = 1.17 \, \psi_1 \qquad (8.4)$$

4. The actual value of the mmf of the magnet is then used to obtain ψ_{effmax} as:

$$\psi_{effmax} = \psi_{resultant} \, E \qquad (8.5)$$

Where E is the magnitude of the mmf of each magnet and is given by:

$$E = Br \left[\left(\frac{D4 - D3}{2} \right) \frac{1}{\mu_0 \mu_r} \right] \qquad (8.6)$$

Where: B_r = Residual induction of the magnet (a magnet property)
          μ_r = Relative permeability of magnet material
              = Permeability of free space

       D_4 and D_3 are defined in Figure 8-1.

Hence, substituting for $X_{resultant}$ and E from (8.4) and (8.6) respectively in the above expression (8.5) for ψ_{effmax}, we get:

$$\psi_{effmax} = \left(\phi_{3,1} + \frac{\phi_{2,1}}{2} \right) \times 1.17 \times \frac{Br}{\mu r} \left(\frac{D4 - D3}{2\mu_0} \right) \times N_{turns} \qquad (8.7)$$

Hence, substituting in (8.2), we get:

$$V_{gen} = \left(\frac{2\pi f}{\sqrt{2}} \right) \left(\frac{1.17}{\mu_0} \right) \left(\frac{D4 - D3}{2} \right) \left(\phi_{3,1} + \frac{\phi_{2,1}}{2} \right) \frac{Br}{\mu r} N_{turns} \qquad (8.8)$$

In design calculations presented earlier, the V_{gen} calculations were based on the dimensions shown in Table 8-1 and the following data:

B_r = 0.8 Tesla (assumed low value to have a conservative design)
μ_r = 1.0
N_{turns} = 69

This resulted in a V_{gen} value of 148 volts RMS.

As the SPDE was built, these numbers were modified to the following:

B_r = 1.085 Tesla (measured value reported by the magnet manufacturer)
μ_r = 1.075
N_{turns} = 67

The revised value of calculated V_{gen} would therefore be:

$$V_{gen} = 148 \times \frac{1.085}{0.8} \times \frac{67}{69} \times \frac{1}{1.07} = 181.3 \text{ volts}$$

The value of V_{gen} to be expected from the measured value of flux linkages on the SPDE = 208.4 volts.

Hence:

$$\frac{V_{gen} \text{ derived from static measurements}}{V_{gen} \text{ calculated}} = 208.4/181.3 = 1.15$$

Thus, the measured value based on static test results is about 15% more than the model predicts.

8.5 Calculation of Reactance X

Reactance X is obtained as:

$$X = (2\pi f)L \tag{8.9}$$

Where: L = the self-inductance of the alternator coil
f = the frequency

The self-inductance of the coil is obtained as follows:

1. Assume magnets provide no excitation to set up any flux in the magnetic circuit.

2. Determine the flux linkages 'X_{self}' of the coil when the coil carries DC current 'I_{DC}'.

3. The self-inductance L is given by:

$$L = \frac{d\psi}{di} = \frac{\psi_{self}}{I_{dc}} \qquad (8.10)$$

The determination of ψ_{self} follows steps similar to those used for computing ψ_{effmax} in the computation of V_{gen}. The magnetic equivalent circuit employed is shown in Figure 8-7. In this circuit, the coil is assumed to be concentrated in a very narrow band in the center of the slot as shown in Figure 8-8.

This assumption will result in a higher self-inductance than actual. However, this is balanced by the fact that the flux in the fringing paths are ignored in this calculation due to the difficulty of representing them by simple network for use in optimization studies.

In the computation of L, first fluxes $\phi_{L1,2}$ and $\phi_{L3,1}$ through the reluctance R2 and R3 of Figure 8-7 are computed for the magnitude of source mmf equal to unity. Thus, when a current I_{DC} flows through the coil having N_{turns} turns, the magnitude of mmf is $N_{turns} I_{DC}$, and the fluxes ϕ_{L2} and ϕ_{L3} through the reluctances R2 and R3 of Figure 8-7 are given by:

$$\begin{aligned} \phi_{L2} &= \phi_{L2,1} \, N_{turns} \, I_{DC} \\ \phi_{L3} &= \phi_{L3,1} \, N_{turns} \, I_{DC} \end{aligned} \qquad (8.11)$$

The flux linkages of the alternator coil (assumed concentrated in a very narrow slot in the center) are given by:

$$\begin{aligned} \psi_{self} &= (\phi_{L2} + \phi_{L3}) \, N_{turns} \\ \psi_{self} &= (\phi_{L2,1} + \phi_{L3,1}) \, N^2_{turns} \, I_{DC} \end{aligned} \qquad (8.12)$$

FIGURE 8-7

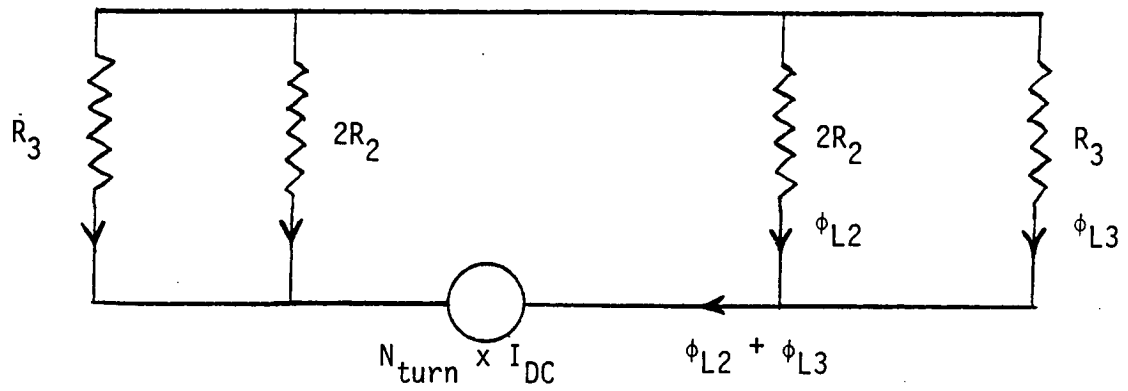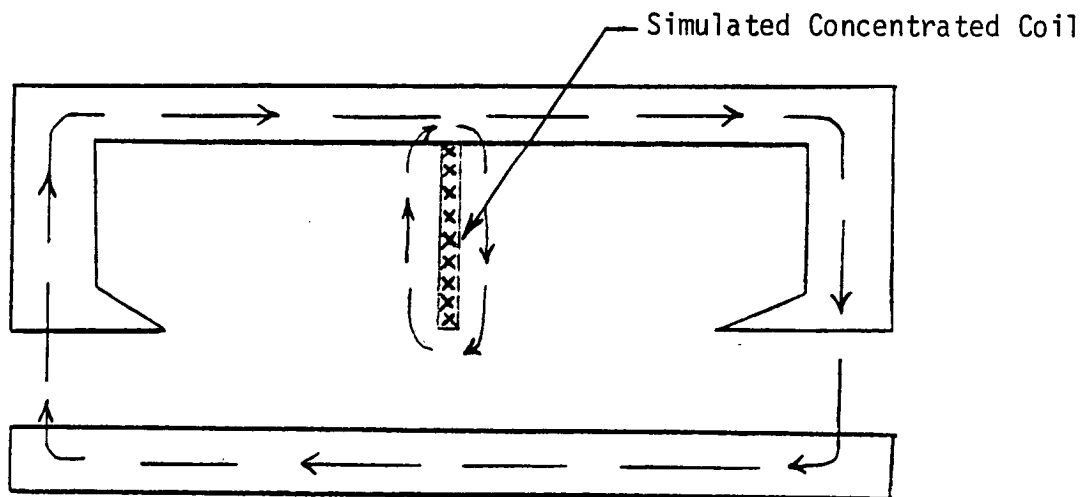**MAGNETIC EQUIVALENT CIRCUIT FOR DETERMINING**
SELF INDUCTANCE (L)

FIGURE 8-8

MAGNETIC CONFIGURATION FOR DETERMINING
SELF INDUCTANCE (L)

Simulated Concentrated Coil

Hence, expression (8.10) for L and substituting for ψ_{self} from (8.12) we get:

$$L = (\phi_{L2,1} + \phi_{L3,1}) N^2 turns \qquad (8.13)$$

In the above expression, the $(\phi_{L2,1} + \phi_{L3,1})$ is dependent only on the geometry of the alternator. The quantity ϕ_{L3} is dependent on the stroke (pole width), and D5 on the diameter of the air gap and the radial air gap between the inner and outer stator (D5-D4/2) (refer to Figure 8-1).

The quantity $\phi_{L2,1}$ is dependent on the axial length of the coil and the radial height of the coil plus the radial air gap between the inner and outer stator. Thus, by increasing the radial height of the coil and reducing its axial length, one could minimize the quantity $\phi_{L2,1}$ and still maintain constant cross-sectional area on the resistance of the coil.

The data presented at the SPDE Preliminary Design Review was based on dimensions of Table 8-1 and $N_{turns} = 69$. For the final as-built alternators, $N_{turns} = 67$. The reactance at 105 Hz to be expected is given by:

$$X_{calc} = X_{design\ review} \times (67/69)^2$$
$$= 5.8 \times (67/69)^2$$
$$= 5.47\ ohms$$

The reactance measured on the SPDE during static tests was 6.495 ohms. Hence:

$$X_{measured}/X_{calc} = 1.188\ ohms$$

Thus, the measured reactance is 19% higher than predicted by the model.

8.6 Performance of the Alternator Under Steady-State

When the alternator is working under steady-state, it can be represented by the electrical equivalent circuit of Figure 8-9. The capacitor shown in this figure is a component external to the alternator connected in series with the alternator to cancel the self reactance of the alternator. In the absence of this series capacitor, the output of the alternator will be severely limited due to the voltage drop in the self reactance of the alternator. The expressions for the magni-

FIGURE 8-9
EQUIVALENT ELECTRICAL CIRCUIT OF THE ALTERNATOR
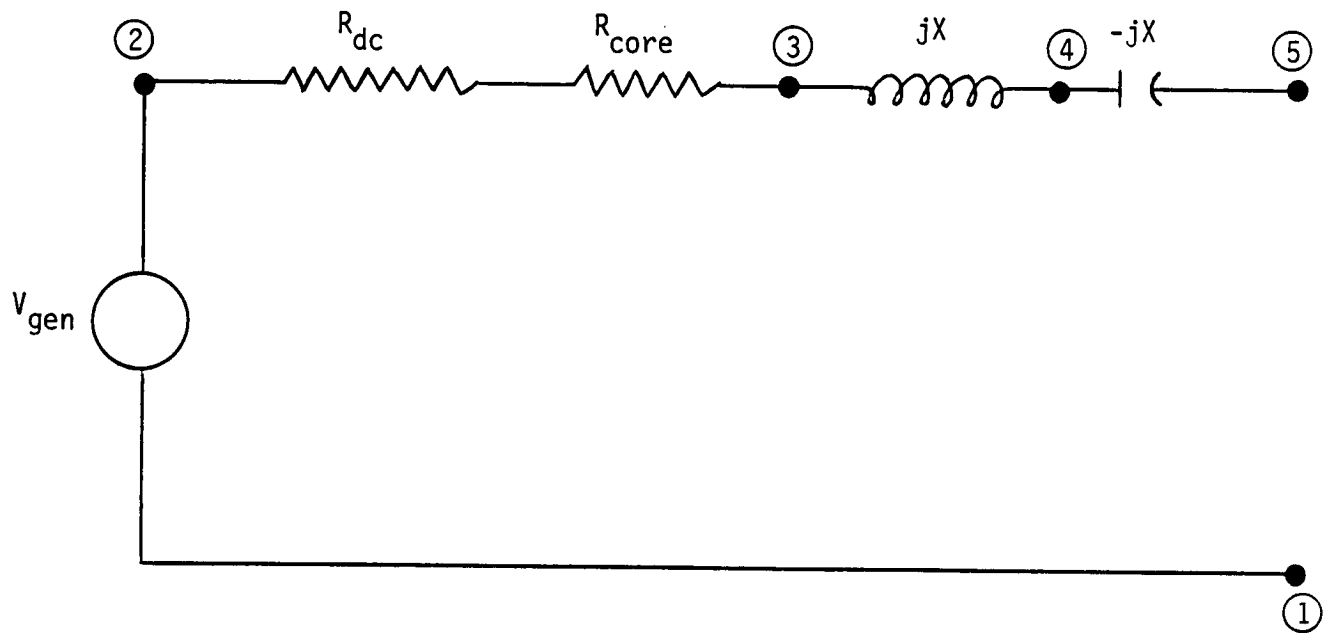
tudes of V_{gen} and the self reactance X of the alternator are given by equations (8.8) and (8.13) respectively.

The effective resistance R consists of two components; R_{DC}, the DC resistance of the coil, and R_{core}, the fictitious resistance added in series to account for the core loss in the magnetic circuit. Thus, $R = R_{DC} + R_{core}$.

The value of R_{core} is determined by estimating the core loss based on the weight of the steel in the stators of the alternator, the loss per unit weight in the steel used in the construction of the alternator at the operating frequency, the flux density, and the lamination thickness used. This value of loss per unit weight is significantly dependent on the heat treatment given to the laminations. In the estimate of core losses, it is assumed that the heat treatment would result in the core losses reduced to their minimum value - specified in the material property sheets.

In Figure 8-9, terminals 1 and 4 are the physical terminals of the alternator, while terminals 1 and 5 are the terminals to which the load is connected. The load expected in service will consist of a full bridge rectifier followed by a DC load. The operation of such a load will cause non-sinusoidal currents in the alternator and, hence, the parameters of the equivalent circuit of Figure 8-9 will have to be expressed in terms of inductance and capacitance instead of their reactive values. The core loss resistance, R_{core}, will have to be modified for such operation. However, adequate experimental and/or analytical data is not available to give an expression for this modification.

Figure 8-10 shows a phasor diagram of the alternator when loaded with a resistance load.

Table 8-1 shows various parameters associated with the design and performance under resistive load conditions.

Various dimensions are shown in Figure 8-11a and 8-11b.

FIGURE 8-10

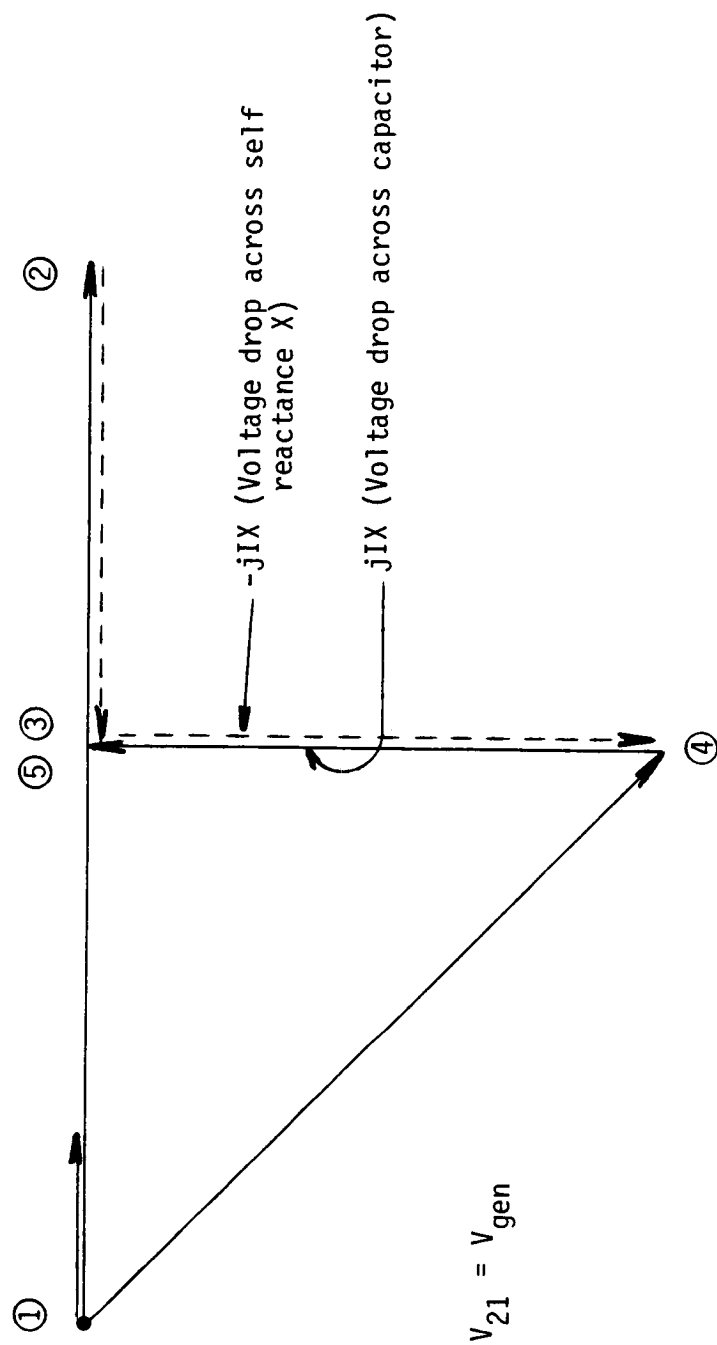PHASOR DIAGRAM FOR ALTERNATOR FEEDING A RESISTIVE LOAD

-jIX (Voltage drop across self reactance X)

jIX (Voltage drop across capacitor)

$V_{21} = V_{gen}$

TABLE 8-1
COMPUTED PERFORMANCE OF THE ALTERNATOR

Frequency - 105 Hz   Stroke   - 0.8 in (p-p)
Power   - 12.5kW   Alpha Angle - 0

	A	B	C
• Terminal Voltage (with Tuning C)	143 Volts (RMS)	176.7 Volts (RMS)	
• Open Circuit Voltage	148 Volts (RMS)	181.3 Volts (RMS)	208.4 Volts (RMS)
• Rated Current	87.4 Amps	73.61 Amps	
• Resistance	.057 Ohms	.06255 Ohms	.082 Ohms*
• Reactance	5.8 Ohms	5.47 Ohms	6.5 Ohms
• I R Loss	435 Watts	338.9 Watts	
• Core Loss	320 Watts	} 506 Watts	
• Stray Loss	186 Watts	}	
• Total Loss	941 Watts	845 Watts	
• Power Input	13,441 Watts	13,345 Watts	
• Efficiency	93%	94%	

A = Preliminary Design Calculations
    Nturn = 69   Br = .8 Tesla
    3 coils-9 AWG 1 coil-10 AWG

B = As-Built Design Calculations
    Nturn = 67   Br = 1.085 Tesla
    4 coils-9-1/2 AWG

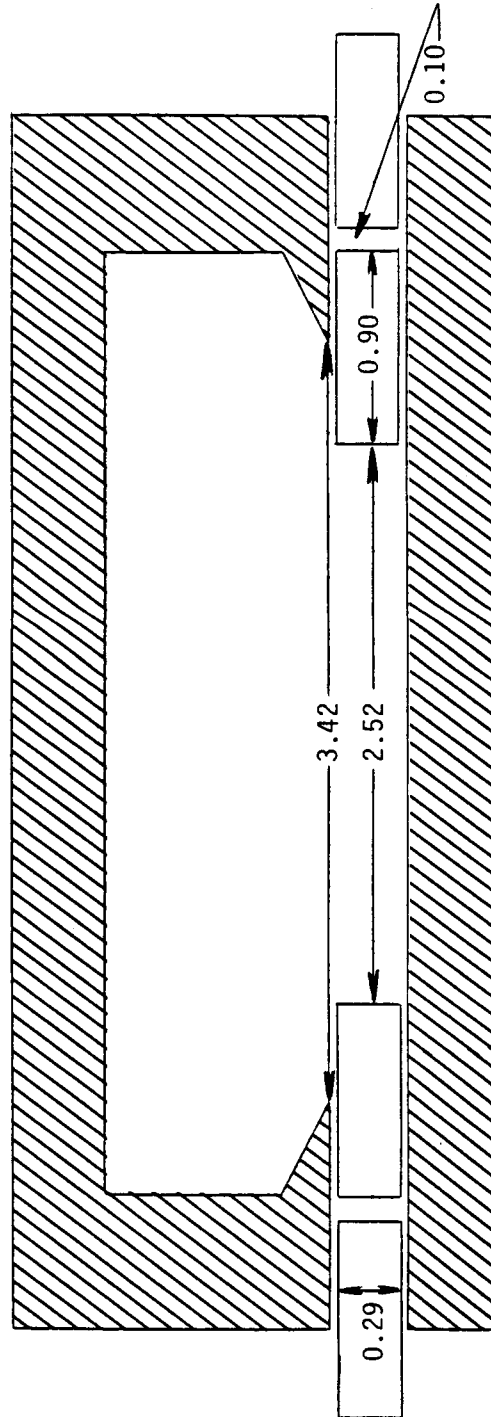C = Based on Static Test of As-Built Alternator

* Includes Lead Resistance

FIGURE 8-11a
DIMENSIONS OF STATORS

(All Dimensions in Inches)

FIGURE 8-11b
DIMENSIONS OF PLUNGER

(Plunger is in Central Position – All Dimensions in Inches)

8.7 Sidepull

The plunger of the space power alternator is made of four rings of permanent magnet material. Each ring is .9 inches long axially, .290 inches radial thickness, and 8.65 inches mean diameter. A pair of these rings reciprocate in the annular gap between the inner stator and the left pole of the outer stator. The second pair is located on the plunger such that it reciprocates in the annular space between the inner stator and the right pole of the outer stator.

The axial length of each pole is 1-inch. Thus, only a part of the magnet will be in the annular spaces mentioned above. Any segment of the magnet which is in these annular spaces is attracted radially outward by the poles of the outer stator and radially inward by the inner stator surface. The net radial force on the segment is more or less zero. Hence, the part of the magnet ring within the annular space has very little sidepull.

A part of the magnet ring is overhanging beyond the outside of the poles of the outer stator. In this case, there is no iron on either side of any circumferential segment of the magnet and, hence, little net radial force will be experienced by any such circumferential segment. Thus, the part of the magnet ring which overhangs beyond the outer extremities of the stator will produce little sidepull.

The remaining length of the magnet will be in the annular space between the coil and the inner stator. Any circumferential segment in this part will have a large inward radial force due to the attraction toward the inner stator. The outward radial force will be significantly smaller as the iron surface behind the coil is much farther away. Thus, there will be a large net inward radial force on the segment. This force will depend on the gap between the inner stator and the magnet segment.

When the plunger is located concentric to the inner stator, this radial gap between the inner stator and the magnet ring is of constant magnitude all around the periphery, and the radial inward force density is constant all around the periphery. Hence, the radial force on any segment is cancelled by another segment located diametrically opposite and of equal angular span. No net radial force is experienced by the plunger as a whole.

However, when the plunger is moved eccentric, the magnitudes of the forces on the diametrically opposite segments are different and a net radial force appears on the plunger in the direction along the line joining the centers of the plunger and inner stator.

The magnitude of this sidepull was estimated by the following procedure:

1. The force density versus gap characteristics was obtained experimentally by measuring the force on a small piece of the magnet with thickness in the direction of magnetization equal to that of the radial thickness of the magnets used in the construction of the alternator.

2. For any given eccentricity, the variation of the radial gap (between the magnets and the inner stator) around the periphery is computed.

3. Using the experimental data and the gap variation calculations, the variation of the force density around the periphery is computed.

4. The force density is integrated (vectorially) around the periphery of the plunger.

Table 8-2 shows the results based on a computer program written to perform the numerical calculations of the above procedure.

TABLE 8-2

SIDEPULL VERSUS ECCENTRICITY

ECCENTRICITY (Inches)	SIDEPULL (Lbf)
0.000	0.00
0.002	3.69
0.004	7.38
0.006	11.08
0.008	14.77
0.010	18.46
0.012	22.27
0.014	26.16
0.016	30.07
0.018	34.00
0.020	37.93

9.0 FACILITIES

The SPDE was installed and tested in Test Cell #5 of the free-piston laboratory at MTI's New Karner Road facility. This section describes the general layout of the test cell; the heating, cooling, and helium charging systems, and the load control system required for operating the SPDE engine. The engine installed in the test cell is shown in Figure 3-2.

The general arrangement of cell #5 is shown in Figure 9-1. The engine is supported from the ceiling by flexible straps in the center of the cell. The services connected to the engine come from the ceiling of the cell, with the exception of the hot salt piping which comes into the side of the engine from the back of the test cell. The engine is mounted horizontally across the cell and its centerline elevation of 6' 2" above floor level was dictated by the requirement that the salt piping must drain by gravity to the salt reservoir in the event of a pump failure.

The hot salt system is a skid mounted package purchased from American Hydrotherm Corporation. This system is located in the alley between the free-piston and ASE laboratory buildings. The salt supply and return are piped into the back of the test cell and sloped toward the salt reservoir tank. The system is described in detail in Section 9.1.

The engine cooling system is also located outside of the building and is piped into the test cell. The cooler is a skid mounted, air-cooled radiator, pump and coolant storage tank originally assembled for the ASE P-40 work-around tests.

The engine load, load controls, and starter are located on the south wall of the test cell. All power components and wiring are contained in cabinets and conduits for safety and EMI isolation.

The engine instrumentation is routed to the north wall to provide maximum physical separation from the high power wiring. The signal conditioning for the position and pressure transducers is located in an overhead cabinet on the front (west) wall of the test cell. The general instrumentation, DAS, and engine controls are located in the control cabinets outside the test cell adjacent to the front (west) wall.

FIGURE 9-1

CELL #5 GENERAL ARRANGEMENT
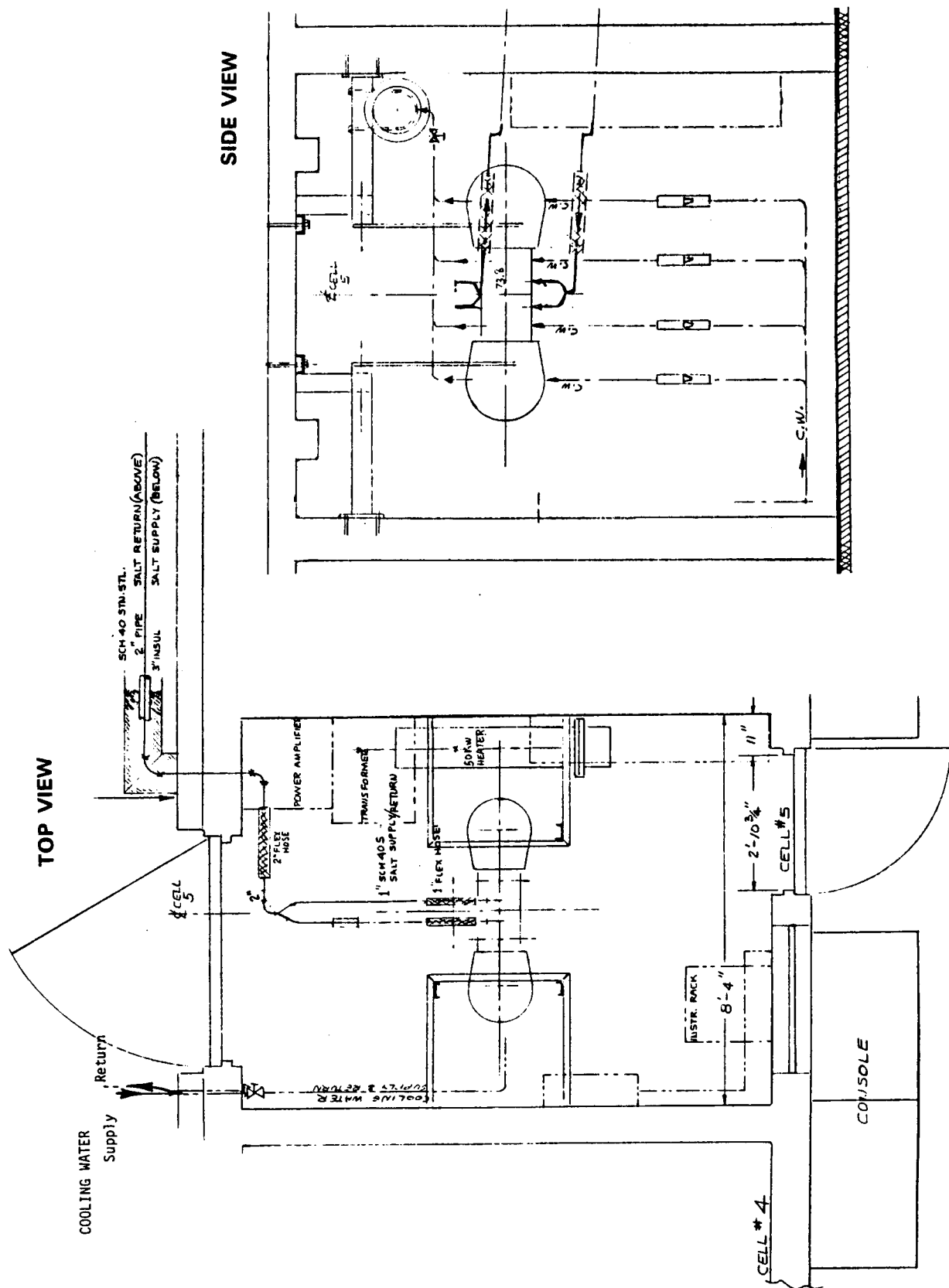
The helium charging system is supplied from 2500 psi bottles located adjacent to cell #6. The helium is piped overhead to the cell. The flow to the engine is controlled by solenoid valves above the engine in the test cell. No high pressure piping is located in or around the control cabinets. The auxiliary air-driven gas booster supplying the engine bearings is located above the test cell.

The following sections describe each of the major facility systems required to operate the SPDE engine:

- Heating System
- Cooling System
- Helium Charging System
- Electrical Load System

9.1 Heating System

The SPDE engine has a tube and shell heater designed to be adaptable to a liquid metal pumped transfer loop. After review of several alternative liquid heat transfer materials, a molten salt was selected to simulate the liquid metal loop for the engine. The molten salt selected is a eutectic mixture of:

- 53% Sodium Nitrate ($NaNO_3$)
- 7% Sodium Nitrite ($NaNO_2$)
- 40% Potassium Nitrate ($K NO_3$)

This is known in the chemical industry by its trade name of 'HITEC'. This material was selected based on the following:

1. high temperature stability (>1000F);
2. low vapor pressure at ambient pressure;
3. low personnel and environmental hazard;
4. 30 years of operation in the chemical process and material heat treating industry; and,
5. good thermal transport properties.

American Hydrotherm Corporation (AHC) was the vendor identified as having experience with building systems for applications similar to ours. The AHC system has the additional advantage of a water dilution process which lowers the melting point of the salt to normal ambient temperature levels of 100-160°F. This has two advantages: first, the engine may be started with minimal thermal shock to the heater; and, second, the engine can be operated at temperatures below the normal melting point of 142°C (288°F).

The heating system installed at MTI is shown in Figure 9-2. The basic salt flow loop in this system is very simple in that the salt is pumped out of the reservoir with a vertical cantilever pump to the engine heat exchanger. It then flows back to the salt reservoir through a flow control orifice. The flow is split before entering each engine, and the entering temperature is measured with both an RTD and a T/C. The outlet temperature is measured, again with both an RTD and T/C, and the flow through each heater is measured with high temperature turbine flow meters. The salt temperature in and out of the salt tank is also measured with RTD's.

The engine heat exchanger and the salt piping is arranged such that when the pump is stopped, the system will drain by gravity to insure that pure salt will not accumulate and possibly freeze in the heater and/or piping in the event of a power failure. There are no flow control valves in the salt lines as molten salt has a very strong tendency to wick past valve packing resulting in leaks. The salt flow has been reduced to about 50% of design to increase the temperature drop across the heater by installing an orifice at the return flange of the salt tank. The possibility of installing orifices to balance the flow through each engine half was also provided for, though it has not proved to be necessary.

The salt tank is heated by two banks of electric heaters with a total capacity of 150kW. The power input to the salt tank is measured and displayed at the operator's station. The power is controlled manually (during start up while steaming off) or automatically by a proportional/integral (PI) controller which maintains a set tank temperature.

During start up, water in the salt is boiled off by the electric heaters and vents out of the tank via a spray condenser. The spray condenser is used to condense

FIGURE 9-2

SPDE HEATING SYSTEM SCHEMATIC
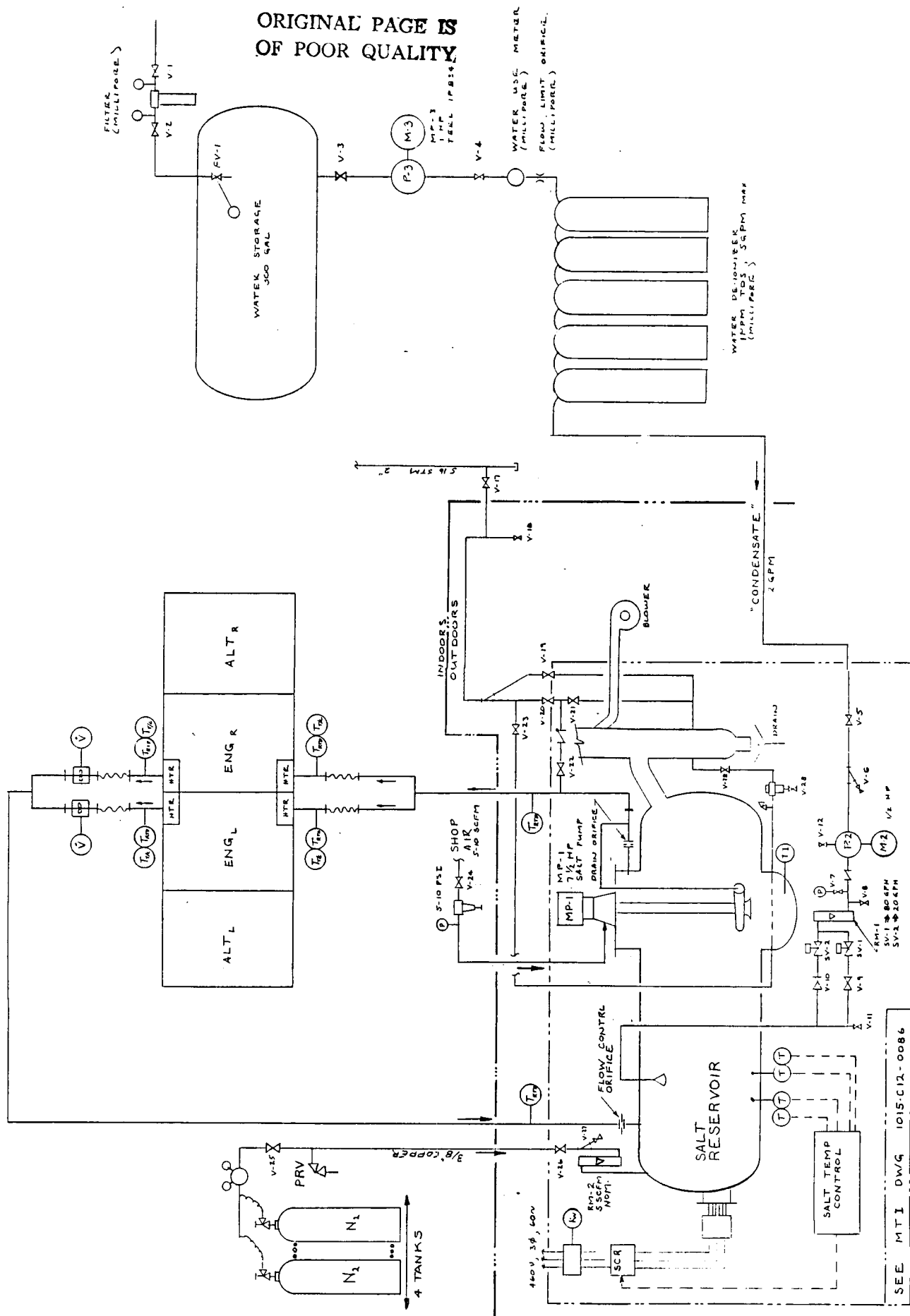
the steam coming off the tank, thus eliminating the steam plume which would tend to condense and freeze on surfaces around the salt package during colder months.

When the salt is cooled down, the salt must be diluted to lower the melting point. A supply of 'condensate', which in this case is de-ionized water, is used for this purpose. The salt system automatically controls the rate and amount of dilution water added to the salt. The dilution process accelerates the rate at which the engine cools.

The salt package is also supplied with 5-10 scfm of compressed air for cooling the main pump bearings at high system temperatures. Also, bottled nitrogen is piped to the package to reduce salt degradation when its temperature is above 400°C.

The salt system is instrumented to allow measurement of the engine heat input by two methods. The prime method uses the product of flow rate, temperature drop, and the specific heat of the salt. The flow to each engine is measured by high temperature turbine flow meters. The temperature into and out of each engine is measured with platinum RTD's which were selected for their high accuracy and excellent repeatability. The RTD's measure the absolute temperatures from which the difference is obtained. A back-up measurement using type-K T/C's in a delta configuration was originally planned and has been recently installed. The above measurements are made at the engine heater, thus minimizing heat losses in the piping. The salt package is also instrumented to measure the total power into the salt tank using an electric power meter and out of the salt tank using differential RTD's. In this case, a separate flow measurement is not made; rather, the flows measured at the engine are added to obtain total flow.

The general specifications of the salt system are shown in Table 9-1.

9.2 Cooling System

The SPDE engine has a tube and shell cooler to remove heat from the thermodynamic cycle and an additional water jacket around the pressure vessel to cool the alternator.

TABLE 9-1

MOLTEN SALT TRANSFER LOOP

- Nominal Heat Input (to Engine)   100 kW

- Nominal Losses to Ambient   4 kW

- Nominal Heater and Fluid Temperatures
  - heater wall (tubes)   373°C
  - average fluid   378°C
  - inlet fluid   384°C
  - outlet fluid   372°C

- Transfer Fluid   Hitec

- Useable Temperature Range Without   142°C - 540°C
  Water Dilution

- Total Flow Rate   3 L/S (48 GPM)

- System Pressure   ATM

The engine is cooled using a pumped glycol solution (50% water, 50% ethylene glycol) and an air-cooled radiator. The radiator, fan, water pump, etc. are contained on a packaged skid originally used for early ASE P-40 testing. This system has over 150kW of cooling capacity vs. a nominal required capacity of 100kW. Detail specifications are given in Table 9-2. The cooling system can be operated in either a manual or automatic mode. Presently, when data is obtained, the manual mode is used as the coolant temperature is more stable than with the automatic mode, which is a simple on-off fan controller. This results in daily and seasonal changes in the coolant temperature; however, since the engine temperature ratio is controlled by the operator, this should have a second order effect on engine performance.

The cooling water supply splits into four parallel paths feeding each of the two engine coolers and two alternator coolers. The total flow leaving the engine is used to cool the alternator load resistances. The total flow to each engine/alternator is measured by turbine flow meters, and the flow to each alternator is measured by rotometers.

The temperatures in and out of the coolers are also made with absolute reading platinum RTD's, again selected for their accuracy and repeatability. Since the inlet to the four coolers are from a common source, only two inlet measurements are made with RTD's, while all four outlet temperatures are made by RTD's. The inlet measurements are currently backed-up by using type-K thermocouples in the inlets to the alternator coolers. In the future, the temperature rise across each cooler will be backed-up by matched T/C's. The temperature rise across the load coolers is also measured with RTD's. This measurement, in combination with the electric power delivered to the load coolers, is used to verify the heat capacity of the glycol solution.

The overall cooling system schematic is presented in Figure 9-3.

9.3 Helium Charging System

The helium charging system is designed to control the engine pressure, provide for pneumatic centering of the displacers, and provide an auxiliary supply for operation of the hydrostatic gas bearing in the engine.

TABLE 9-2

COOLING SYSTEM REQUIREMENTS

- Total Heat Rejected
  - engine cooler   71 kW
  - alternator   4 kW
  - load cooler   25 kW

             ───────

             100 kW

             (125 kW max)

- Coolant   Water/Glycol (50%/50%)

- Nominal Cooler Temperature   50°C

- Average Coolant Temperature   55°C
  - coolant inlet temperature   50.2°C
  - coolant outlet temperature   59.8°C
  - ambient temperature (max)   36°C

- Radiator System
  - ASE workaround skid #1
  - Young 66D5 radiator package
  - 3 HP coolant pump
  - reservoirs and controls
  - system cooling capacity   152 kW (min)

- Flow Rate   3 L/S (48 GPM)

FIGURE 9-3

SPDE COOLING SYSTEM SCHEMATIC
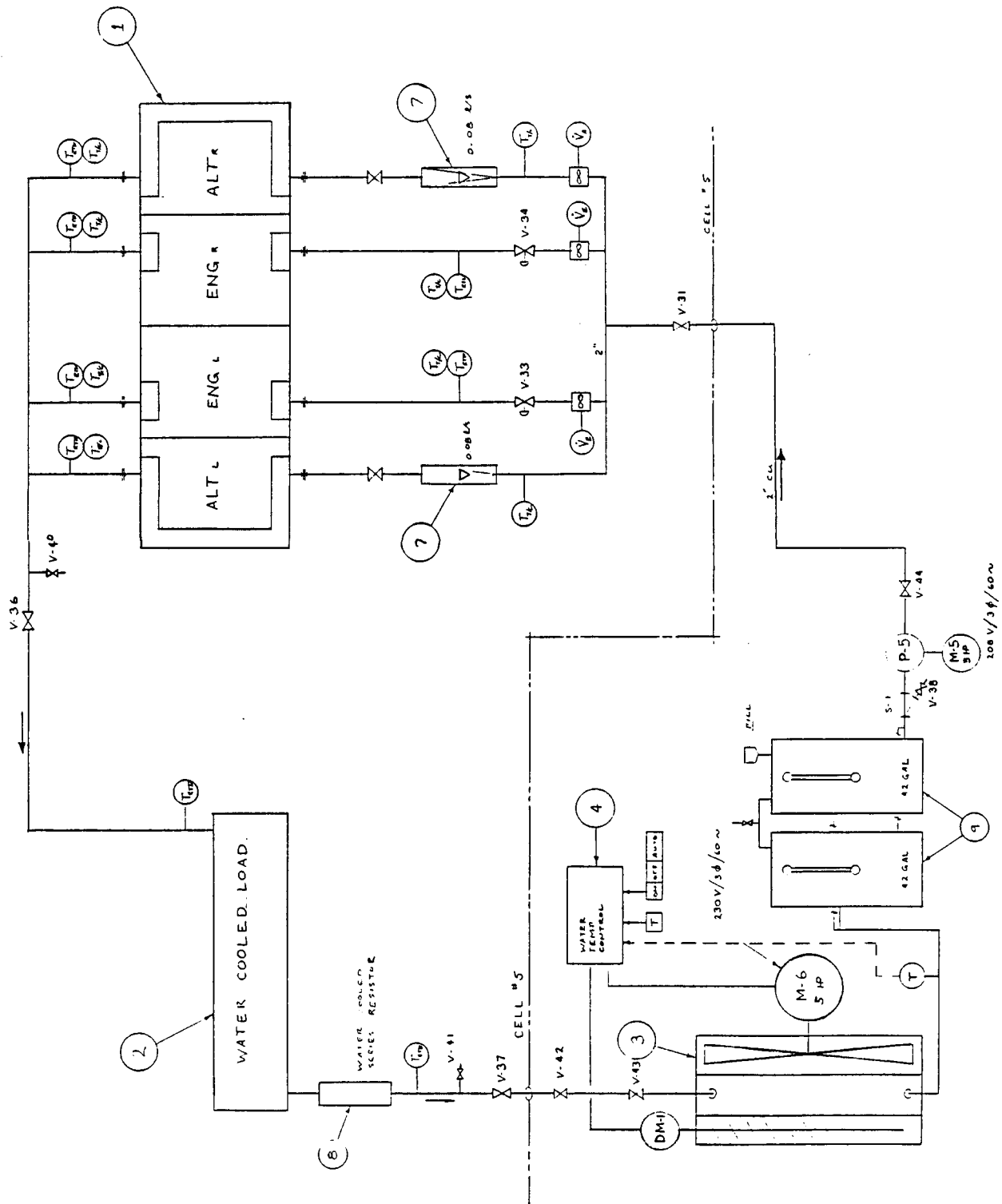
The helium for engine charging is supplied from gas bottles and is pumped to the engine with a gas booster pump. All helium drains are vented to the atmosphere via a filter which was installed to trap beryllium dust in the event of an engine failure that would cause significant damage to the beryllium components. All high pressure piping is located in the test cell; this required the use of remotely operated valves to control the system as opposed to manual valves as had been done in the past.

The pressure in the engine is controlled by an electronic control which senses the engine pressure and either supplies or vents the engine. The mean pressure (Pmean), measured by a piezoresistive transducer, is used for both the mean pressure control and the Data Acquisition System (DAS), and is backed-up by a conventional gage. A similar transducer is used to monitor the bearing supply pressure (Pbrng). The difference between this pressure and Pmean is displayed for the operator as the bearing supply pressure. This difference is also measured directly by a conventional pressure gage.

The auxiliary bearing supply uses a double-acting air-driven gas booster pump to maintain 5-10 Bar differential pressure across the engine bearings. Pulsations generated by the gas booster are isolated by accumulators in the supply and return lines. Finally, the booster system can be completely isolated from the engine by valves in the supply and return lines during start up and for internally supplied bearing operation.

The helium system also provides for pneumatic centering of the displacers. This is also done via electrically operated solenoid valves which connect the aft displacer gas spring to either the charging supply (negative displacer motion) or atmosphere via the vent filter (positive displacer motion).
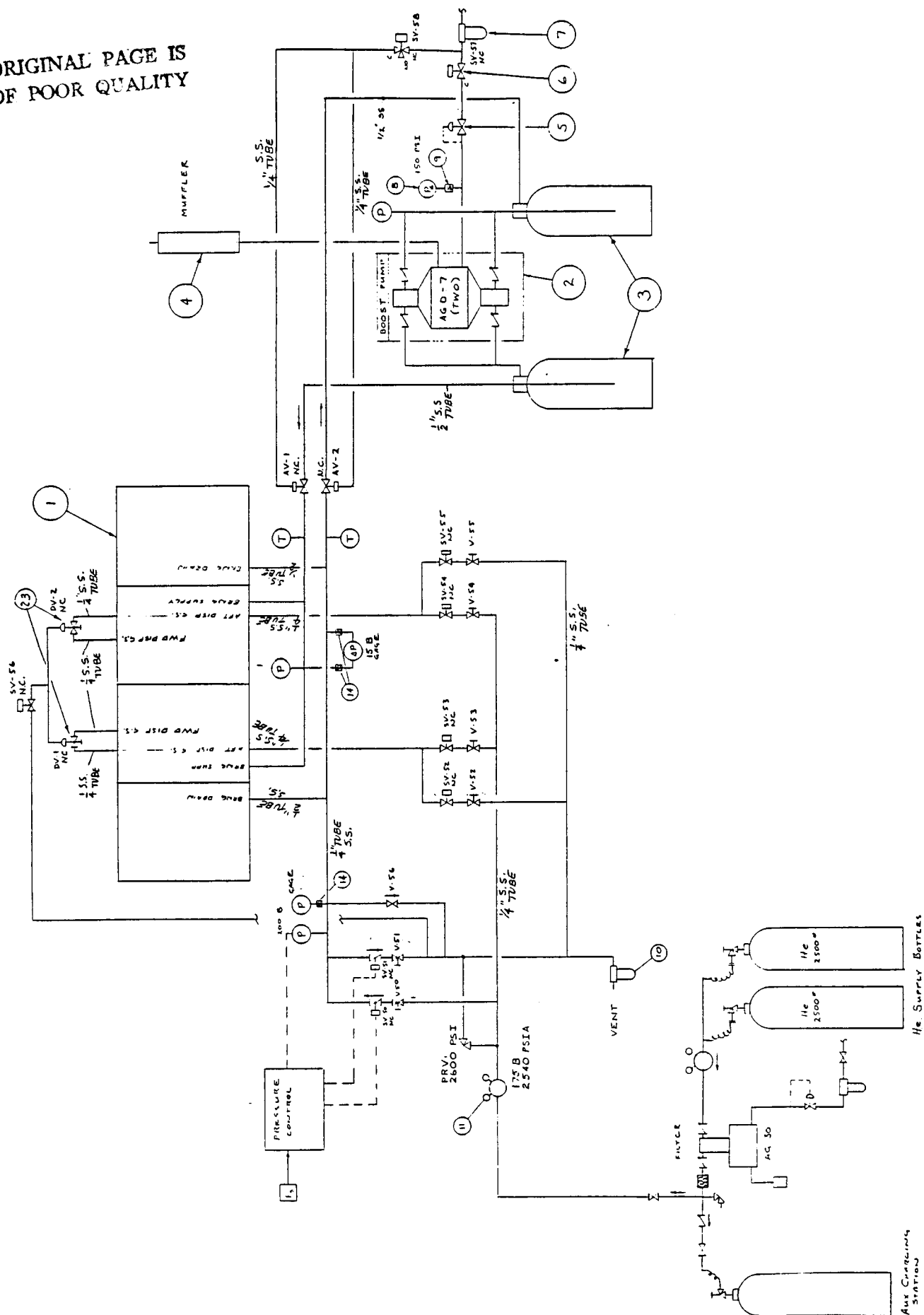
The helium system schematic is shown in Figure 9-4.

9.4 Electrical Load System

The electrical load and starter system is described below. The load system is designed to simulate the electrical load characteristics of a hypothetical satel-

FIGURE 9-4

SPDE HELIUM SYSTEM SCHEMATIC

lite system in which the engine/alternator is feeding a constant voltage load. The load system, Figure 9-5, consists of the following major components:

- AC tuning capacitors;
- water cooled AC resistors;
- impedance matching transformer;
- starter control and power supply;
- full wave rectifier;
- DC filter capacitors;
- water cooled DC resistors;
- load controller; and,
- instrumentation.

The functions of the starter and load systems are to:

1. provide for controlled engine/alternator start up;
2. provide the electrical load required to dissipate the power generated by the engine/alternator; and,
3. control and stabilize the output voltage.

The AC tuning capacitors are designed to cancel the inductive reactance of the alternator coils. These capacitors are set up to tune the SPDE alternator at pressures of 75, 100, 125, and 150 Bar. The capacitor voltage can exceed the rating of a single capacitor at operating frequencies above 90 Hz. Therefore, the capacitors are connected in series pairs to reduce the voltage across each capacitor to below their rated voltage. These are then connected in four parallel banks, where three banks are manually switchable, to provide the required net capacitive reactance.

A small (0.3 ohm) water cooled AC resistance is included in the AC circuit to eliminate a potential system instability due to the very high slope of the load power versus voltage characteristic of the voltage controlled rectifier load.

The impedance matching transformer is provided to match the alternator voltage output to the voltage capability of the rectifier and DC load. This was motivated by some uncertainty in the alternator magnet properties obtainable and, therefore, the alternator output voltage and the conflicting requirement of

FIGURE 9-5

SPDE ELECTRICAL LOAD SCHEMATIC

completing the DC load design. Further, the final AC output would have required DC filter capacitors with higher voltage ratings than were commercially available or a series/parallel arrangement, both of which are avoided by using a matching transformer.

The starter control and power supply consists of a manually operated function generator and a 3.8kWe industrial amplifier. The operator sets the voltage and frequency output of the function generator. This signal is amplified to the voltage required to drive the alternator, thus motoring the power pistons of the engine. The engine is motored in this fashion while the engine is heated until the current through the alternators drops to zero, at which time the power supply is disconnected from the AC circuit by a manually operated relay.

The full wave rectifier converts the AC alternator output to DC. The diodes specified for the rectifier have the following specifications:

Forward Current	250 Arms
Ifsm	3000 A
Vrms	600 V
Reverse Recovery Time	<1.0 micro second

The above specifications are conservatively above the design current of 94 Arms and voltage of 266 Vrms at the rectifier.

The DC filter capacitors remove AC voltages on the DC side of the rectifier. Electrolytic capacitors are used for this application. The filter is sized to result in an approximate 0.5 second time constant for the load system at the design load. Thus, the filter controls the short term stability of the engine/alternator load system fixing the load voltage. The filter specifications are:

Capacitance	2.174 farads
Max Capacitor Voltage	600 VDC

The filter capacitor is provided with a parallel shunt resistor to assure safe discharge of the capacitor at shutdown. The instrumentation is arranged to include the losses inherent to electrolytic capacitors and the shunt resistor as

part of the DC load. Further, the capacitor can be disconnected from the DC load in the event of an emergency shutdown.

The primary system load is a bank of water cooled DC resistance elements. For this application, a commercially available electric process heater was purchased and modified. The 18 elements in the heater are individually controlled by the load controller. The load capacity at the design voltage of 240 VDC is 2.8kW for each element for a total capacity of 50kW. The capacity at lower operating voltages is plotted in Figure 9-6. The 18 load elements are divided into 16 individual elements that can be manually switched for coarse control and two elements which are switched by a pulse width modulated (PWM) transistor for fine voltage control. In the event of an emergency shutdown, the entire load is switched on.

The load controller consists of an operator control panel, the logic required to operate the manual portion of the load, the emergency shutdown logic, and the PWM regulator electronics. The PWM regulator senses the DC bus voltage and compares it to the set point voltage which is set by the operator. The resulting error signal automatically adjusts the duty cycle (percent of on time) of the transistor switch to maintain constant DC voltage. As the error increases, the duty cycle increases proportionally increasing the time the two fine resistors are on, thereby increasing the average power draw. As the error decreases, the power draw is reduced. The PWM duty cycle is displayed for the operator. Manual switching of one coarse load element is automatically compensated by the fine control, provided the final duty cycle remains in the effective range of the fine control. This is the case, since each manual load is the equivalent of 50% of the total fine control load.

The load system is instrumented on both the AC and DC side of the rectifier to permit operator monitoring and allow evaluation of the electrical performance. The AC voltages and current are measured after the tuning capacitors and before any load resistance. These signals are conditioned by an AC power meter and provide an output proportional to the total electric power. The instrumentation is discussed further in Section 10.0.

FIGURE 9-6

SPDE LOAD CAPACITY
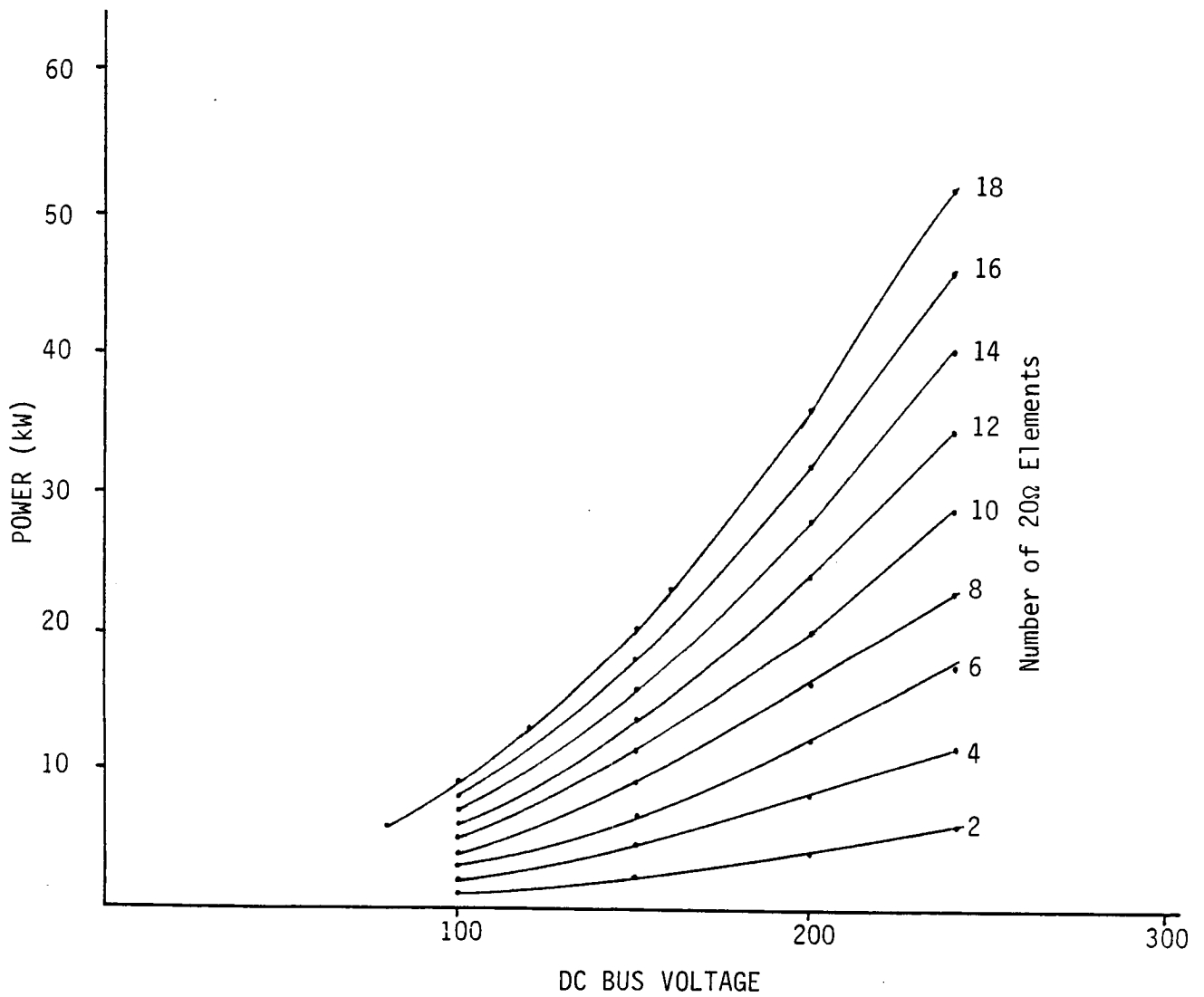
10.0 PERFORMANCE MEASUREMENTS

10.1 Instrumentation

The instrumentation package assembled for the SPDE is essentially modeled after systems previously assembled and tested on such program designs as the Engineering Model and the Heat-Activated Heat Pump engines. Special consideration was given to differences in the operational environment, such as higher internal pressures and temperatures; to higher operating voltages, currents and frequency; and to nonstandard fabrication materials and methods of heat transfer. These concerns did not present significant problems in instrumentation selection or procurement.

The instrumentation utilized on the SPDE provides the quantities necessary to satisfy four basic equations pertaining to the thermodynamic heat balance analysis; and hence, system efficiency, for the SPDE. These are:

1) Q in (to Heaters) $= m_H \, \Delta T_H \, C_{pH}$
2) Q rej (by Coolers) $= m_C \, \Delta T_C \, C_{pC}$
3) Power Developed $= P_A \, X \, \pi f \, A \sin \phi$
4) Electrical Power Output $= VI \cos \Theta$

The "m" measurements are obtained from Hoffer turbine-type flowmeters selected for the particular media, environment, and flow rate conditions found in the high temperature salt and cooling water heat exchanger loops. The differential temperature "ΔT" information is derived from special resistance temperature detectors (RTD's) placed in the main inlet and outlet legs of each flow loop. The specific heat capacities of the fluids, "Cp", are determined from available thermodynamic properties tables.

Electrical energy supplied to the AHC salt reservoir to establish and maintain the operating temperature is carefully regulated and controlled by a programmable temperature controller. The kilowatt input is measured by an AC Watt transducer using the three-phase watt meter.

The power developed within the various engine volumes is determined from equation (3). Pressures within four specific volumes in the engine containment vessel are measured by Kistler 601B2 piezoelectric pressure transducers, as only the amplitudes of the dynamic pressure waves are required. The locations of these pressures are:

- Forward displacer gas spring (P_{FDGS})
- Aft displacer gas spring (P_{ADGS})
- Compression space (P_{CS})
- Alternator gas spring (P_{AGS})

In addition, two Kistler 4045A 200 Bar piezoresistive pressure transducers are installed external to the pressure vessel to measure mean and bearing plenum pressures.

The alternator and displacer piston displacement signals, "X", found in equation (3), are generated by individual eddy current displacement measuring systems, each contained in a Kaman Instruments KD-4300 mainframe. Each of eight transducers is driven by its own oscillator/demodulator unit. Each piston stroke is continuously monitored by measuring the gap between a target surface and the appropriate probe sensor. To reduce inaccuracies due to irregularities in the target surfaces and eccentric piston motions, two probes positioned 180° apart are used for each of the four measurements; summation and scaling effectively cancel these sources of error. One of the displacement signals is also used to generate a value for the engine operating frequency, "f". Through a Fast Fourier Analysis technique in the Data Acquisition System (DAS) software routines, the phase angle, "ϕ", between the displacement and applicable pressure, can be determined and the PV losses in each engine volume calculated.

The electrical power actually supplied by the engine is calculated in the following manner. The AC voltage is measured by stepping down the voltage with a potential transformer and measuring the resultant in the DAS. The current is sensed by a 20:1 current transformer having a precision 0.2 ohm burden resistor, such that the measured RMS voltage represents 1/100 of the actual current; the voltage drop across this resistor is monitored by the DAS. Utilizing software routines, a measurement is then made of the phase angle between the voltage and current, and the electrical power is calculated using equation (4). A secondary power

TABLE 10-1

ANTICIPATED ACCURACY OF THE SPDE INSTRUMENTATION

INSTRUMENTATION	ANTICIPATED SYSTEM ACCURACY
PRESSURE	
• Piezoelectric	+/- 1.5%
• Piezoresistive	+/- 1.0%
DISPLACEMENT	
• Displacer	+/- 2% over 0.8" stroke
	+/- 4% over 0.9" stroke
• Alternator	+/- 2% over 0.8" stroke
TEMPERATURE	
• RTD's (500 Platinum)	Matched system for correct ΔT; +/- 0.5%
• Thermocouples	2.2°C or +/- 7.5%, whichever is greater
FLOW	
• Turbine Flowmeter, mc	+/- 1%
• Turbine Flowmeter, MH	+/- 1%
VOLTAGES	
• Alternator (left)	+/- 1%
• Alternator (right)	+/- 1%
• Alternator (total)	+/- 1%
CURRENT	
• Alternator	+/- 1%
POWER SUPPLIED TO SALT LOOP HEATERS	+/- 1%

measurement is taken using a Hall-Effect watt transducer, a 4:1 step down potential transformer, and a 20:1 current transformer.

A number of thermocouples have been installed in the engine hardware and external flow loops to monitor operating temperatures. These are sheathed type-K (Chromel-Alumel) grounded junction thermocouples. The thermoelectric voltage-to-temperature conversion is performed by a reference junction and a software routine in the DAS.

Table 10-1 summarizes the anticipated accuracies of various instrumentation used on the SPDE. A schematic of all the instrumentation within the engine, shown in their appropriate locations, is presented in Figure 10-1.

10.2 Data Acquisition System (DAS)

10.2.1 Hardware

The computer system (Figure 10-2) centers around an HP1000 XL computer with 512K bytes of memory. Peripherals include a 27M byte hard disk with a cartridge tape unit for streaming tapes, two floppy disk drives, an HP2631G graphics printer, an HP Thinkjet printer, five terminals and six ASIC (Asynchronous Serial Interface Cards), five HPIB controllers (two with bus extenders), and the following instruments:

- (2) HP3456A digital voltmeters
- (1) HP5316A frequency counter
- (1) HP5328A universal counter
- (4) HP3437A system voltmeters
- (7) HP3495 scanners

A data acquisition system based around an HP9825A calculator is also linked via an RS232 serial link to the main computer. This satellite system includes the following:

- (1) HP3455A digital voltmeter
- (1) HP3495A scanner
- (1) HP59309A relay actuator

FIGURE 10-1

SPDE SYSTEM INSTRUMENTATION

$T_{E1,2,3}$ (expansion space)

P_{FDGS}, T_{FDGS} (forward displacer gas spring)

P_{ADGS}, T_{ADGS} (aft displacer gas spring)

x_{D2} (displacer position)

P_{BRNG} (bearing plenum)

P_{MEAN} (mean pressure)

T_{ALT} (alternator windings)

x_{P2} (piston position)

T_{PGS2} (piston gas spring)

$x_{C1,2}$ (case vibration)

P_{CS}, T_{CS} (compression space)

x_{D1} (displacer position)

P_{PGS} (piston gas spring)

T_{PGS1} (piston gas spring)

T_{PVW} (pressure vessel wall)

x_{P1} (piston position)

FIGURE 10-2

MTI FREE-PISTON DATA ACQUISITION SYSTEM

853498
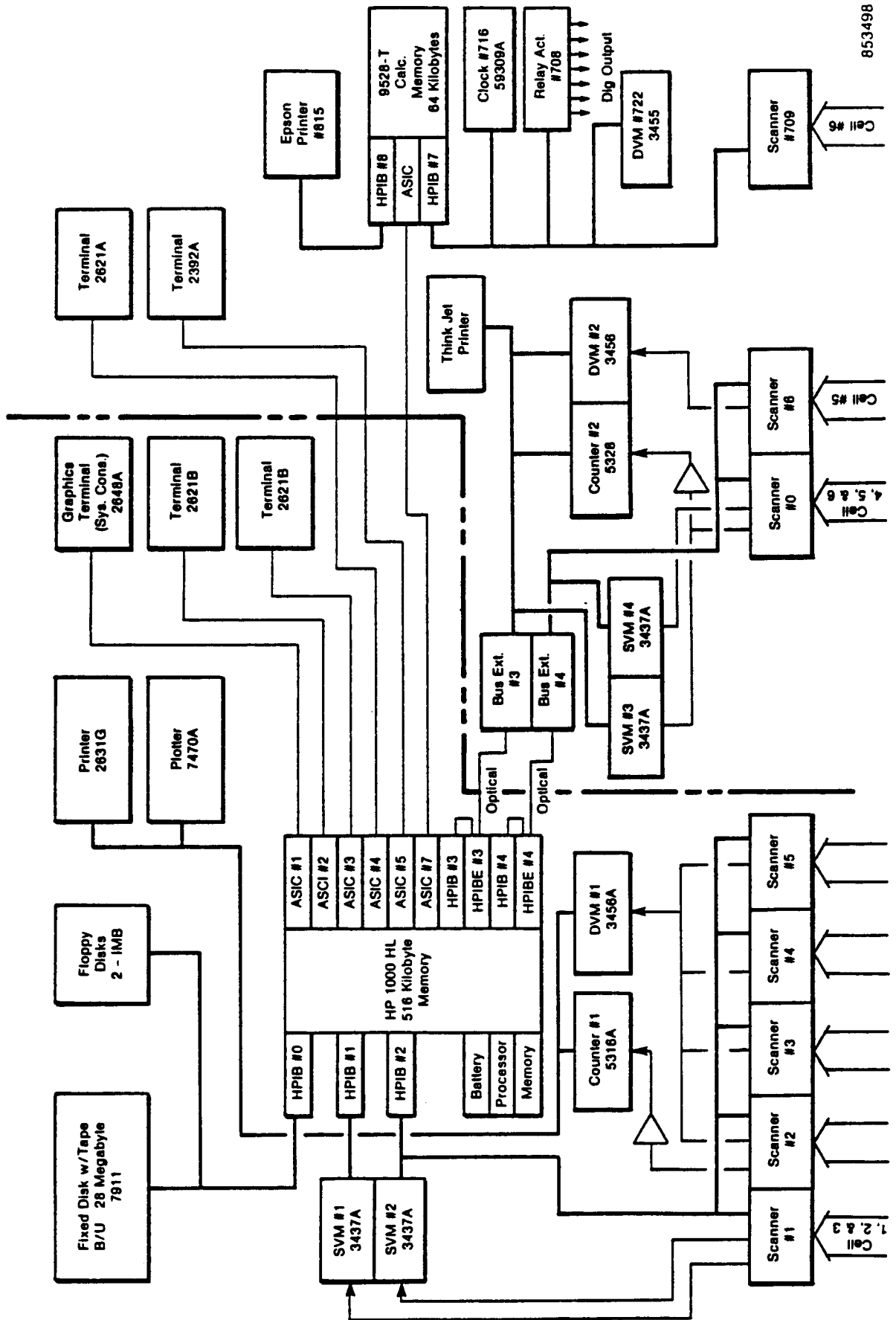
- (1) HP59309A digital clock
- (1) FX-80 Epson printer

The hard disk is divided into 11 regions. These are:

- LU14 for system files and major program modules
- LU15 for parts database programs and files
- LU16 for general storage
- LU40 for storage of latest HP software revisions, libraries
- LU41 for cell 1 programs, data
- LU42 for cell 2 programs, data
- LU43 for cell 3 programs, data
- LU44 for cell 4 programs, data
- LU45 for cell 5 programs, data
- LU46 for cell 6 programs, data
- LU47 for use by system programmer as well as a general scratch area

10.2.2 Software

The FPSE Data Acquisition System software consists of four main programs (see Figure 10-3):

1. ACQU - acquires the data from the instruments, writes the data to a file, and prints out a report.

2. PDUC - reads the data file and produces a full report, a summary report, and a data file for later plotting.

3. PLOT - generates graphic output of the raw data and/or calculated results.

4. CFIT - curve fit of data or calculated results.

ACQU: The ACQU program prompts the user for the names of two files - the current Channel Assignment File and the Data Storage File. For each sensor, the Channel Assignment File lists the scanner channel, the gain, the function and range setting for the voltmeter, and a label. This file also contains some constants

FIGURE 10-3

DATA ACQUISITION SYSTEM DATA FLOW SCHEMATIC

10-8
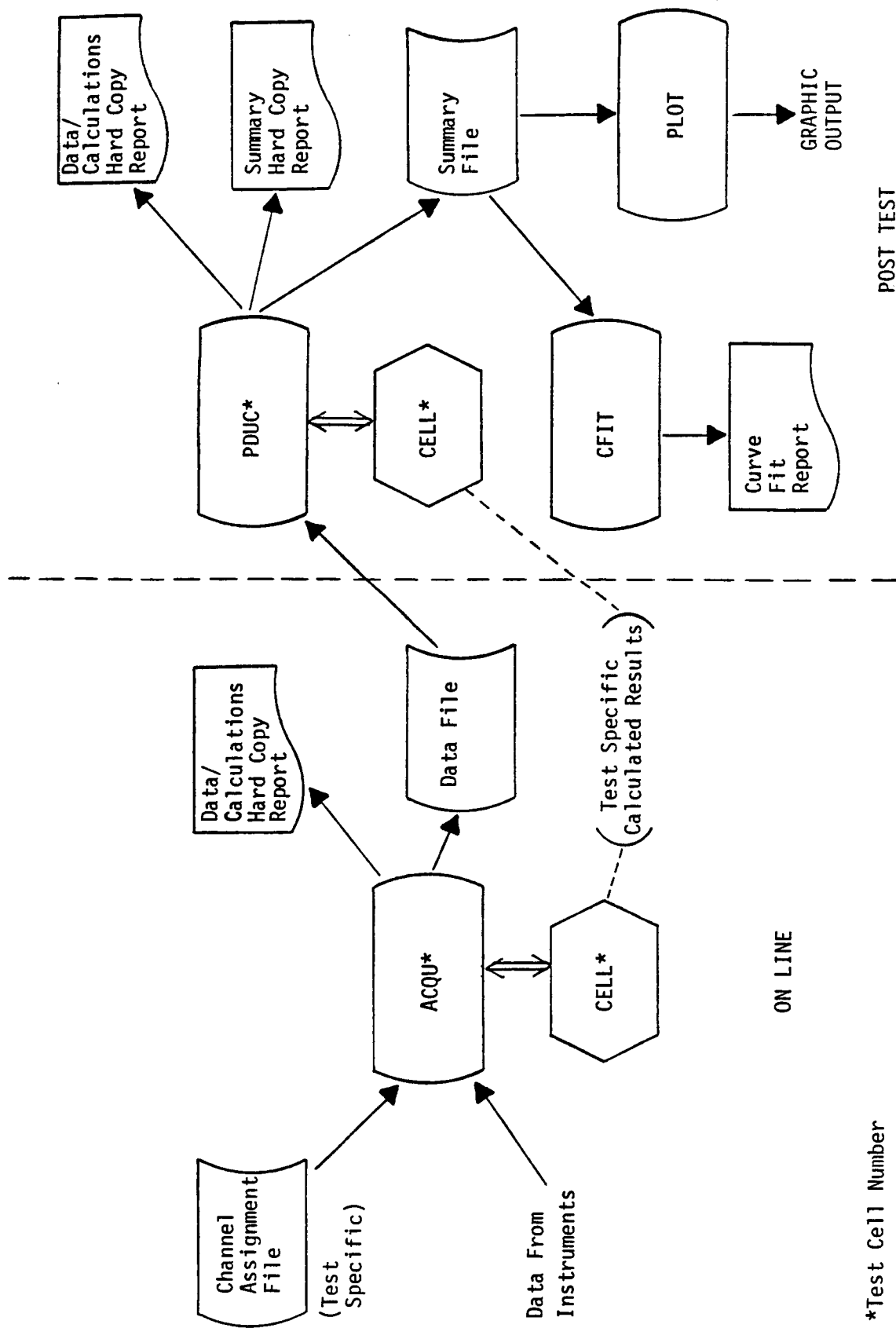
which are used in later calculations; hence, these constants can be changed without recompiling and reloading the program.

ACQU reads in this file and then takes an initial scan, reading the raw data from the voltmeters. The program converts this raw data into engineering units, performs the appropriate calculations (as specified in the subroutine CELL), and prints a report listing the converted raw data and the calculated results. The program then pauses and waits for the user to request that a scan take place and, at the user option, that the data be stored on disk in the Data Storage File.

The program takes both dynamic data and steady-state data. To take dynamic data for channel X, two HP system voltmeters are used; one connected to the reference channel (Xp1), and the other connected to channel X. The frequency is read first (from a frequency counter) and the voltmeters are each then programmed to read 99 points over four cycles. This data is stored in a system buffer and a harmonic analysis program, called HANAL, is started. This program reads the raw data, computes the amplitude of both signals, and the phase between their first harmonics. These results are then sent back to the ACQU program. This process continues through all of the dynamic channels. For steady-state channels, the voltage is read and then multiplied by gain or put through the appropriate algorithm to convert to engineering units.

PDUC: The data reduction program asks the user for the name of the Data Storage File which contains the data in questions. Then the user is asked which scans are to be summarized and what form the summary is to take. All of the data can be printed or selected variables can be summarized in column fashion. In addition, summary files can be created for later plotting. For each scan requested, the program reads the raw data from the Data Storage File and performs the calculations which appear in the CELL subroutine. The appropriate reports are then printed at the printer or terminal which was specified by the user.

PLOT: The plotting program asks the user for the name of the plot file containing the data. The labels, linetypes, data markers, etc. are then specified by the user. Multiple data sets can be placed on the same plot specified by different markers and, of course, the scale can be set by the user or computed automatically. A curve fit option is available as well.

CFIT: The curve fitting program uses a standard least squares algorithm to perform a polynomial curve fit. In addition, an exponential curve fit can be chosen, which uses a linear fit on the natural logarithms of the data.

A key issue in the data acquisition of dynamic data is the accuracy of phase measurements. A test has been performed (see Figure 10-4) to verify the accuracy of these phase readings. A 60 Hz signal with a peak amplitude of .25 volts was input into two channels connected to two different system voltmeters. With one signal being the reference, dynamic data was acquired and a harmonic analysis was performed to compute the phase between the two signals. Twenty data points were taken with this input voltage. The test was repeated for input values of .1, 1, 1.5, and 1.75 volts. The resulting plot of the phase difference between the two signals versus input voltage appears in Figure 10-5. Note that when taking engine data, most dynamic signals are above .5 volts into the system voltmeters.

FIGURE 10-4

SCHEMATIC FOR CHECKOUT OF HIGH SPEED SVM PHASE MEASUREMENT
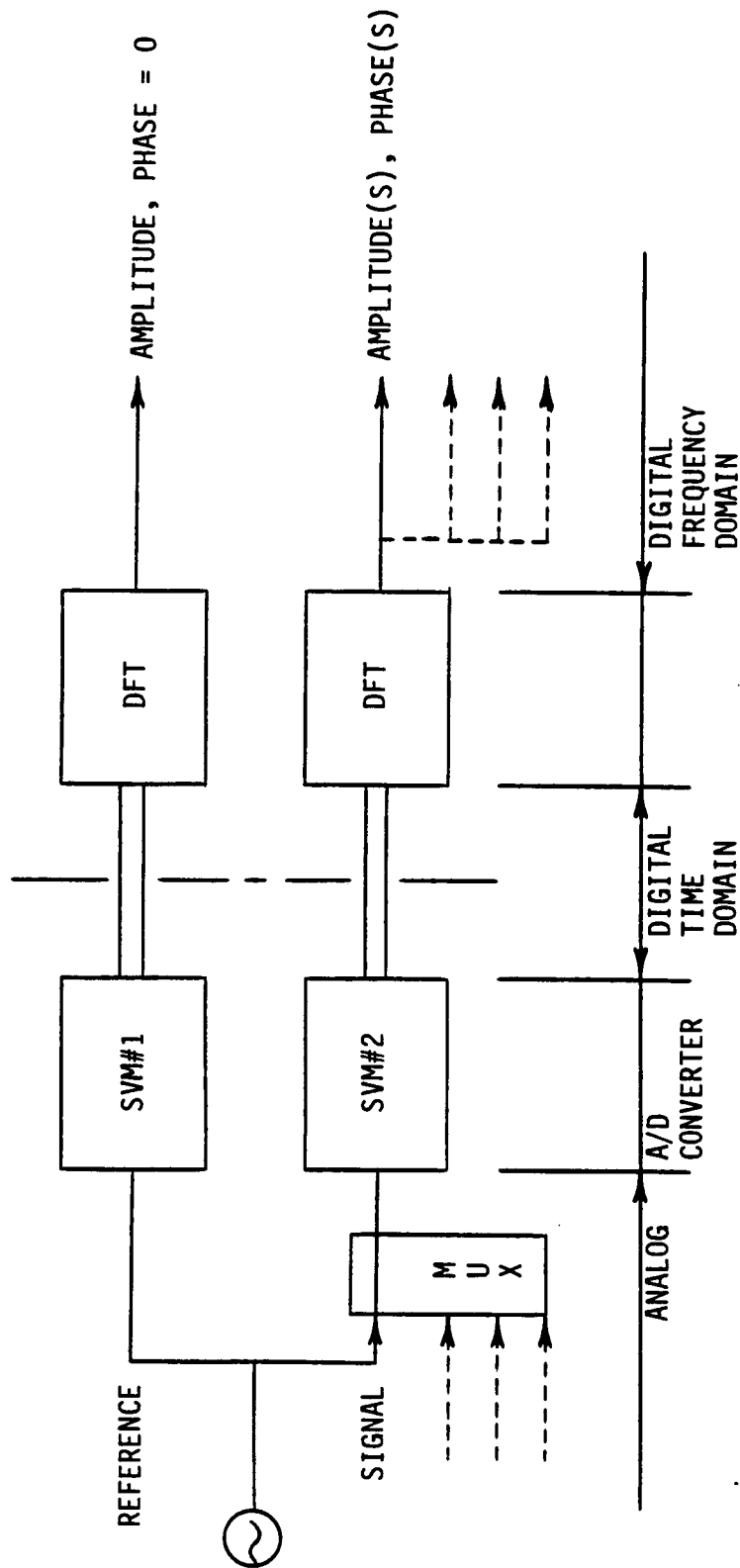
SVM - SYSTEM VOLTMETER

DFT - DESCRETE FOURIER TRANSFORM

MUX - MULTIPLEXER

FIGURE 10-5

PHASE MEASUREMENT SYSTEM CHECK
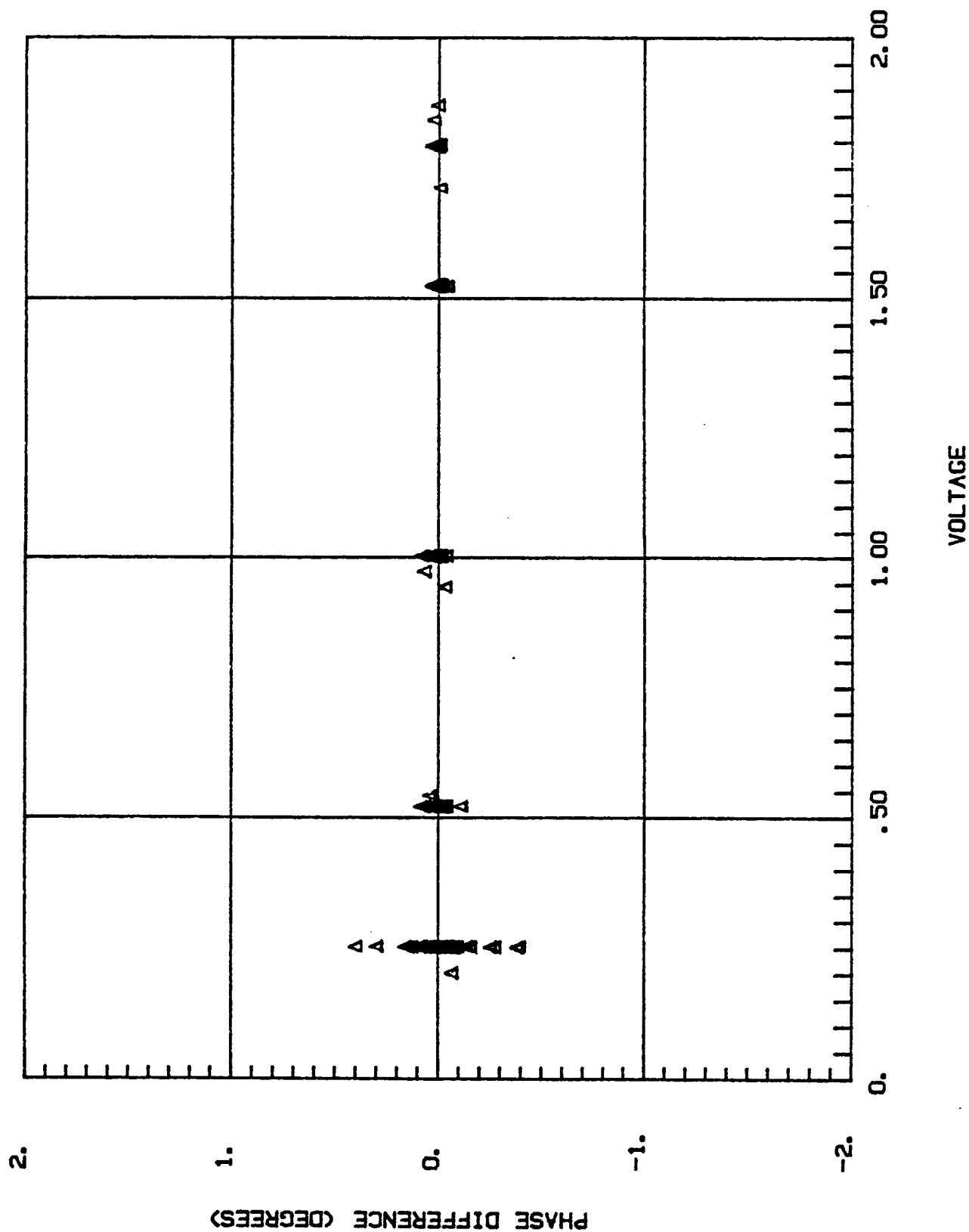
11.0 TEST RESULTS

11.1 Introduction

The objective of the SPDE test program is to demonstrate engine performance at the design point operating conditions of:

$$\text{Temperature Ratio} = 2.0$$
$$\text{Piston Stroke} = 20\text{mm} \ (X_p = 10\text{mm})$$
$$\text{Mean Pressure} = 150 \ \text{Bar}$$

The design performance goals at the above conditions are:

$$\text{Electrical Power} = 25\text{kW}$$
$$\text{Engine Efficiency} = 25\%$$

While the design temperature ratio and strokes have been achieved during checkout testing, the pressure has been limited to 75 Bar. This is because a decision was made to limit the first hydrotest to half pressure to avoid any risk of damage to the hardware during initial tests. Following a full pressure hydrotest, the operating pressure will be increased in 25 Bar increments to the design pressure. At each pressure, the operating conditions will be varied to obtain limited performance maps. These operating conditions will be a subset of the test matrix planned for sensitivity tests following the completion of a test at design conditions.

The complete sensitivity test matrix, Figure 11-1, consists of six stroke levels, six temperature levels, and four pressure levels (a total of 144 points) and will be used as a guide during the acceptance test. The data points for this test will include six stroke levels at a constant temperature ratio of 2.0 for each of four pressure levels; i.e., 75, 100, 125, and 150 Bar. The lower pressure points will be obtained before proceeding to higher pressures. A minimum of three engine data scans will be recorded by the DAS at each operating point.

The engine will be operated at a low power point (TH/TC = 1.6, X_p = 10mm, and Pm = 75 Bar) at the start and conclusion of each test run. The operating and perform-

FIGURE 11-1

SPDE TEST MATRIX

(Mean Pressure - 75, 100, 125, 150 Bar)

11-2
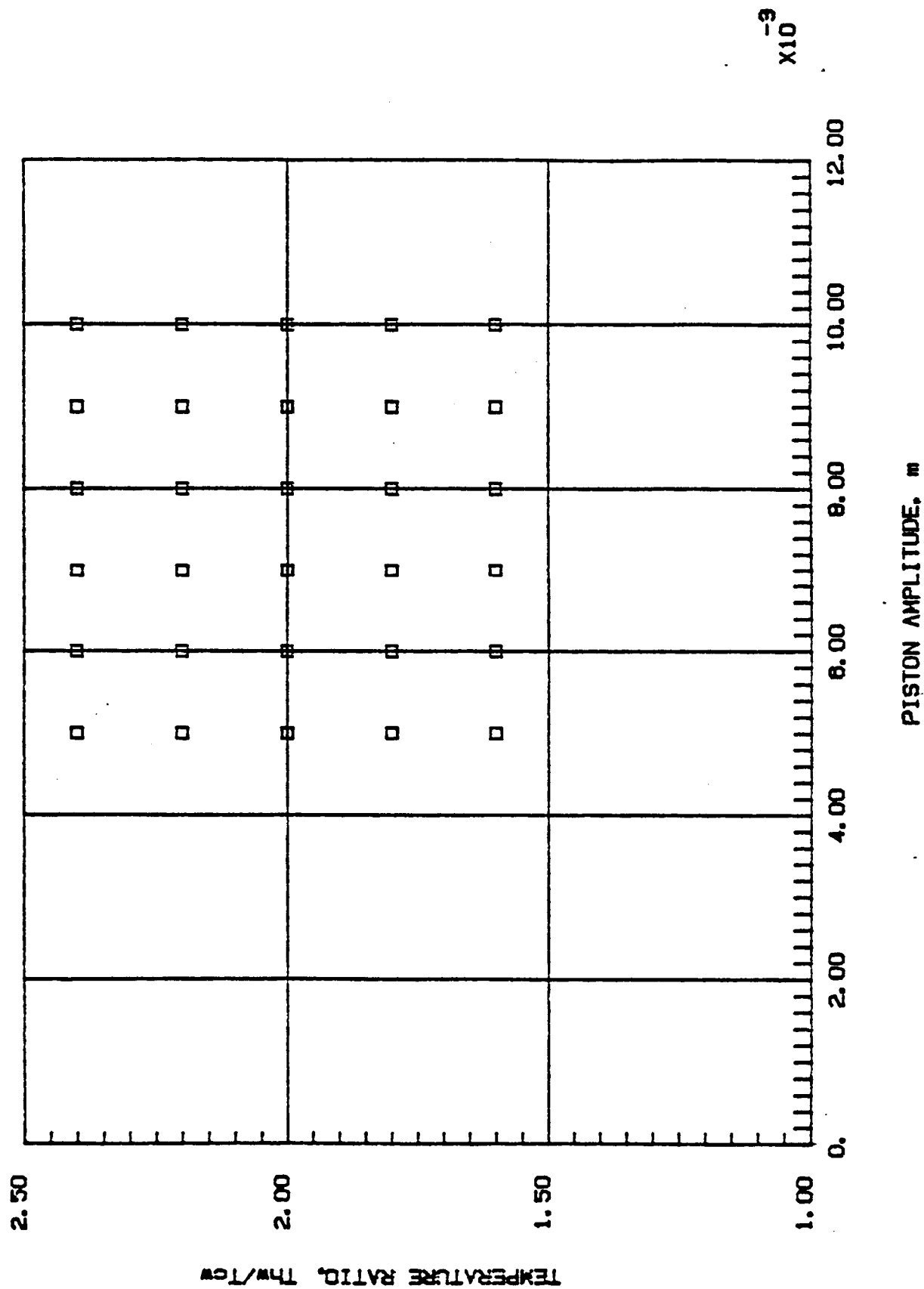
ance conditions for this point will be recorded to permit evaluation of run-to-run and beginning-to-end performance changes.

The engine performance is expected to change as the pressure is increased. Figures 11-2 to 11-5 show the effect of pressure on frequency, displacer dynamics, and power for constant piston amplitude and temperature ratio. The frequency change, which increases in proportion to $Pm^{**}1/2$, has a second order effect on the engine dynamics. However, the alternator inductive reactance, which increases in proportion to frequency, will not be compensated by the capacitive reactance of the AC capacitor. Therefore, it must be changed manually as the pressure and frequency increase. The required capacitance is plotted versus frequency in Figure 11-6.

Further, at frequencies greater than 90 Hz, the full stroke voltage across the tuning capacitor exceeds the rating of single capacitors; therefore, the capacitors will be installed in series-parallel sets to achieve the required capacitance and stay within the voltage limit (600 Vrms) of the capacitors (Figure 11-7). The tuning capacitance will be changed in steps which will cause some detuning at intermediate pressures. However, this is not expected to cause an operational problem.

11.2 Experimental Data

Table 11-1 lists the tests conducted between startup and September 30, 1985. The engine assembly and test procedures are presented in Appendix 11.1.

Each test listed in Table 11-1 was terminated due to a mechanical problem which required engine disassembly and rework. The displacer assembly on the left side of the engine has been prone to rubs between the rod and the bore of the post and flange. The test data of the September 17, 1985 run is the most comprehensive taken to date. The results from this series are shown in Figures 11-8 through 11-15.

Figure 11-8 shows alternator power versus piston amplitude (i.e., half stroke). The amplitude was limited to 8mm since the pistons were not oscillating about the design midstroke position but were biased in (toward the displacer) as shown in Figure 11-14. The power output at 8mm amplitude was 6.5kW, which is approximate-

FIGURE 11-2
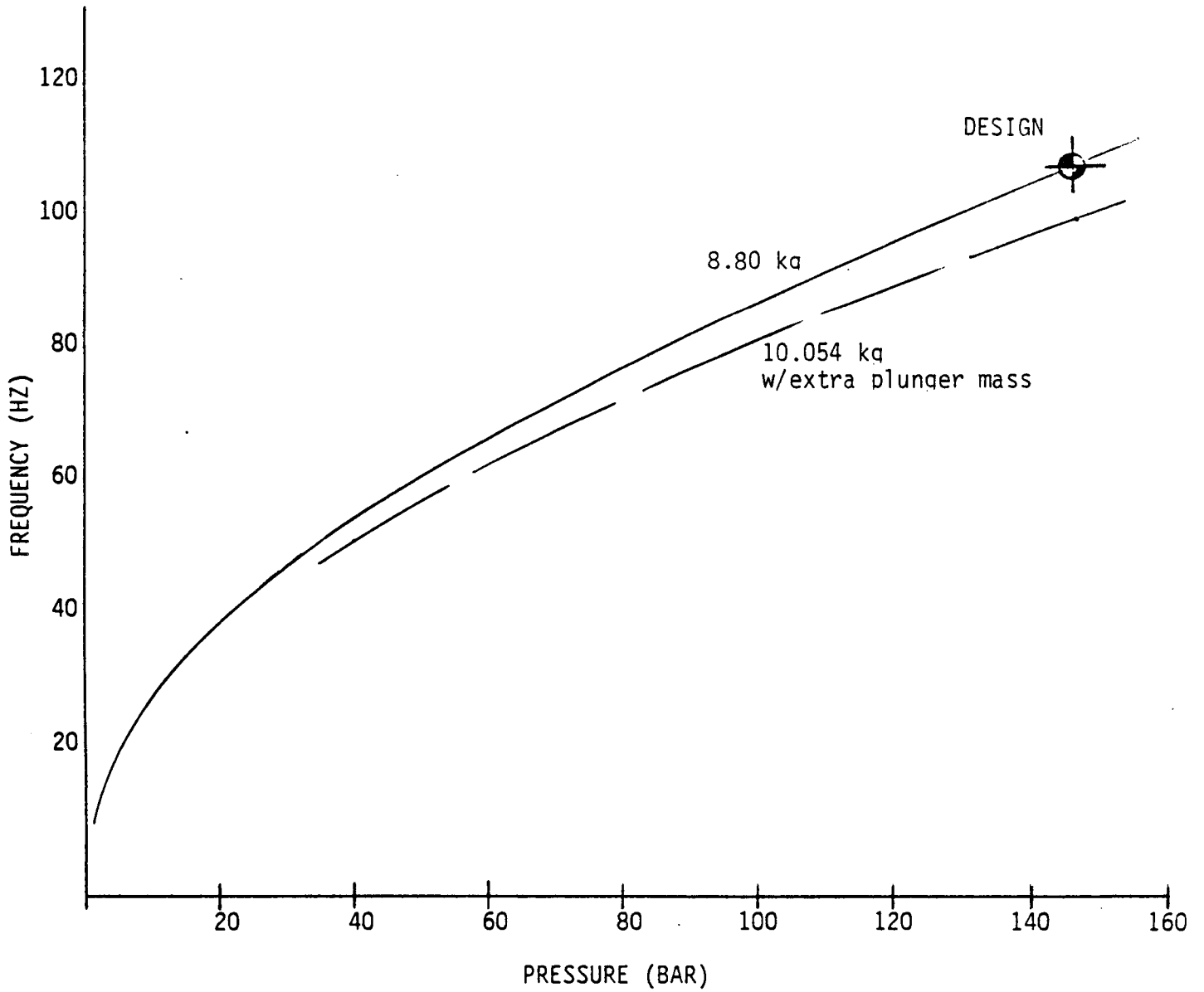
FREQUENCY VERSUS PRESSURE
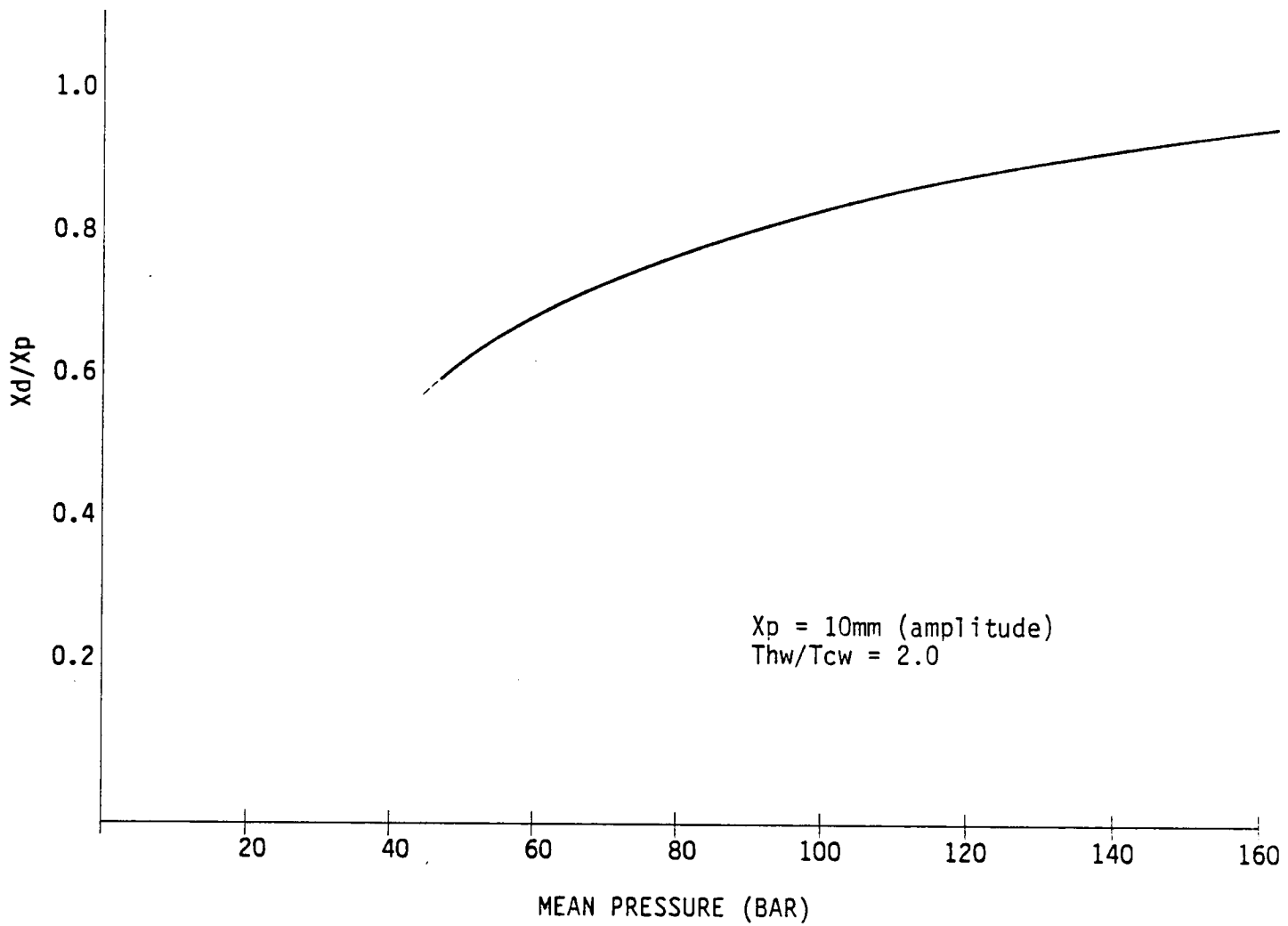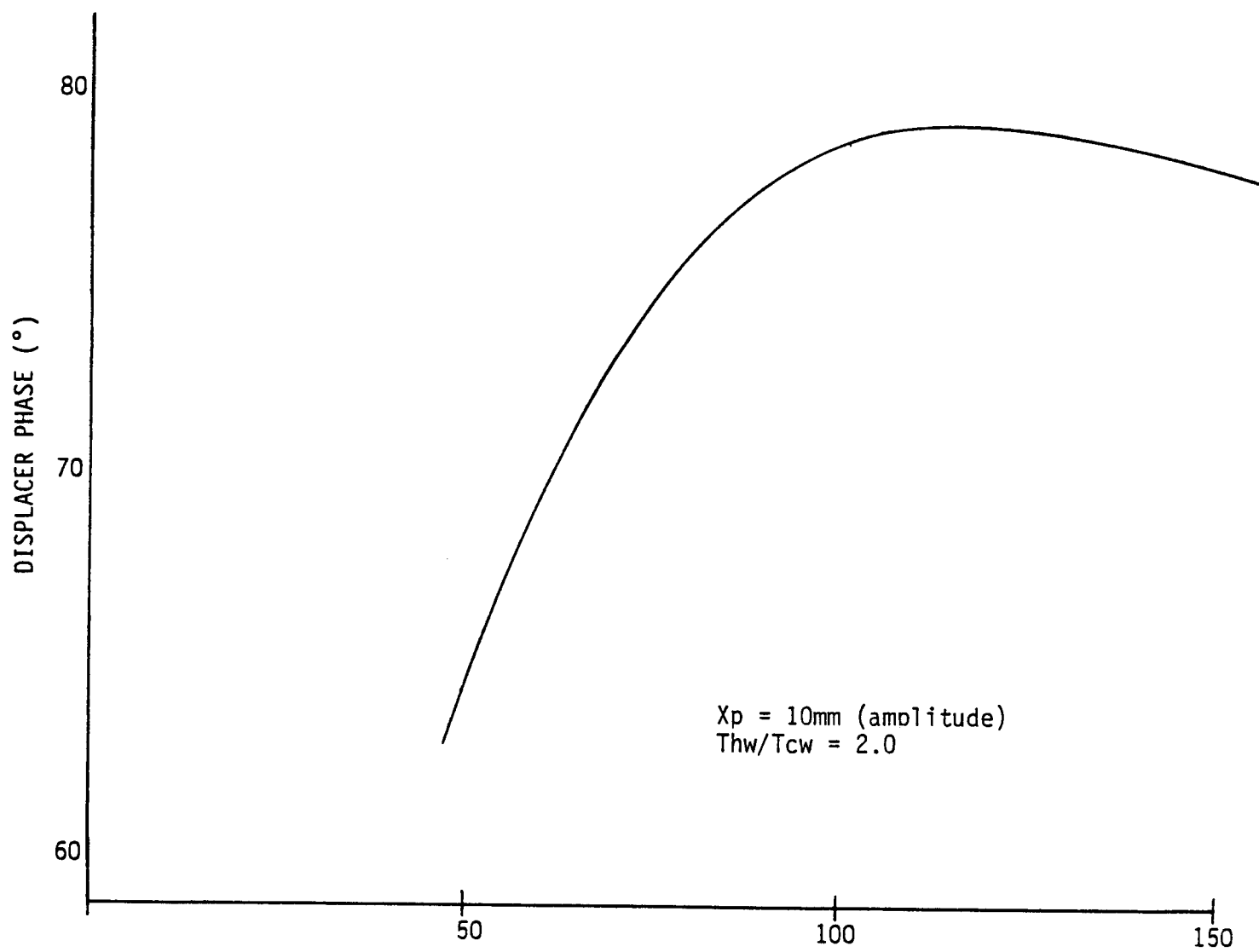
FIGURE 11-3

DISPLACER AMPLITUDE RATIO

Xp = 10mm (amplitude)
Thw/Tcw = 2.0

MEAN PRESSURE (BAR)

FIGURE 11-4

DISPLACER PHASE

Xp = 10mm (amplitude)
Thw/Tcw = 2.0

11-6

FIGURE 11-5

POWER OUTPUT

Xp = 10mm (amplitude)
Thw/Tcw = 2.0
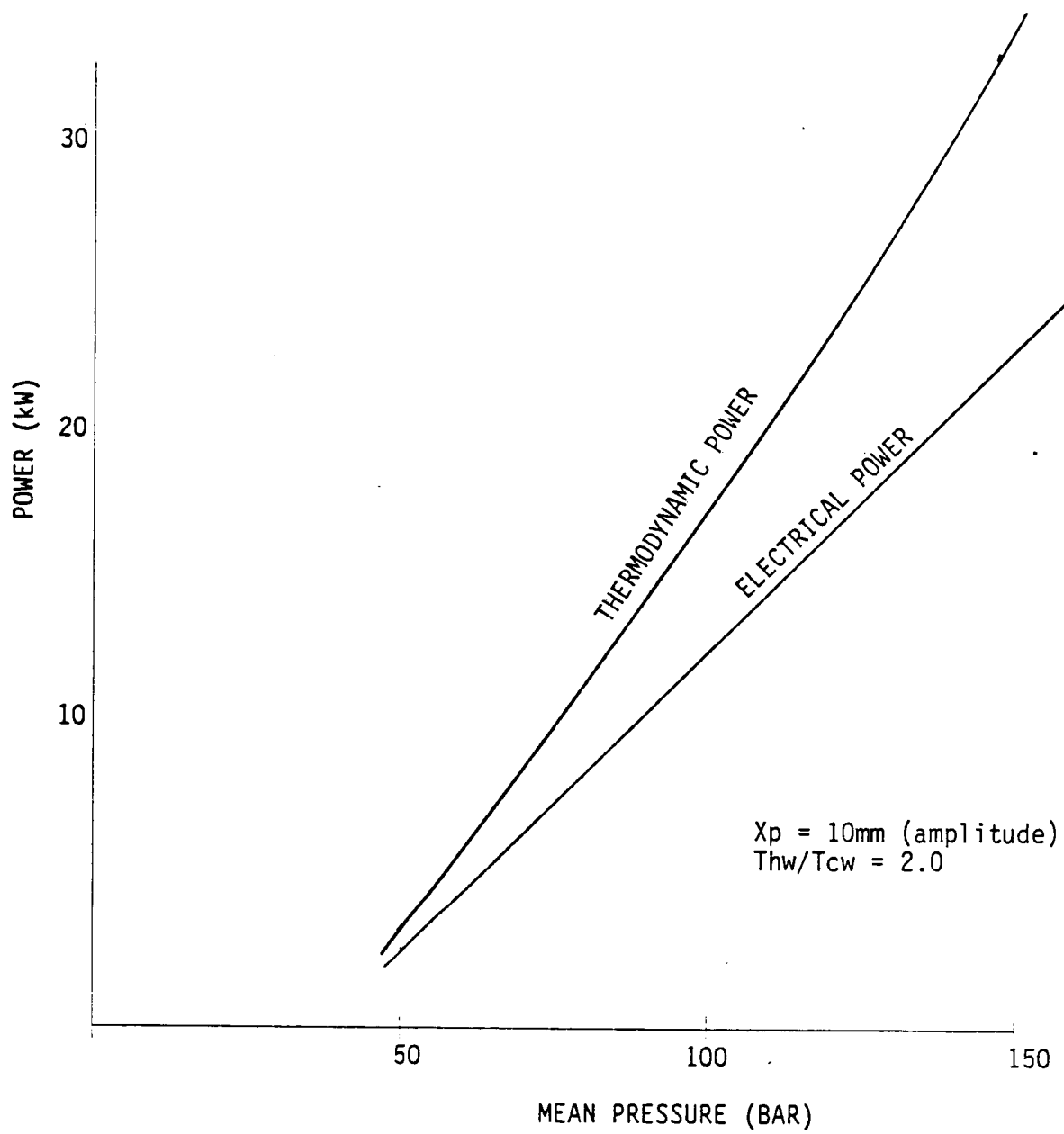
MEAN PRESSURE (BAR)

FIGURE 11-6

CAPACITANCE VERSUS FREQUENCY
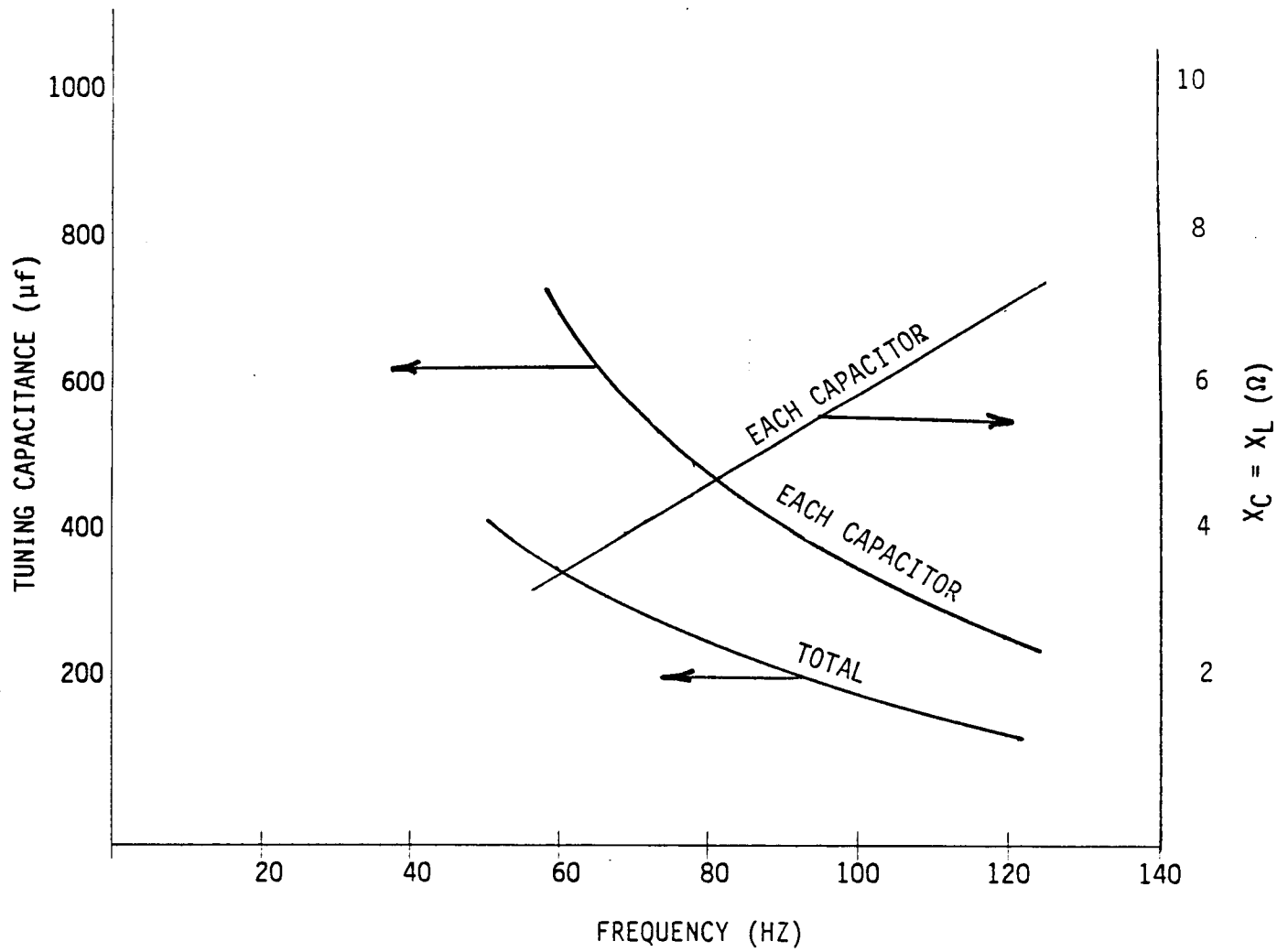
FIGURE 11-7

AC TUNING CAPACITOR

119.4 μf

① 24.7 μf

② 35.1 μf

③ 59.3 μf

150 BAR

125 BAR

100 BAR

75 BAR
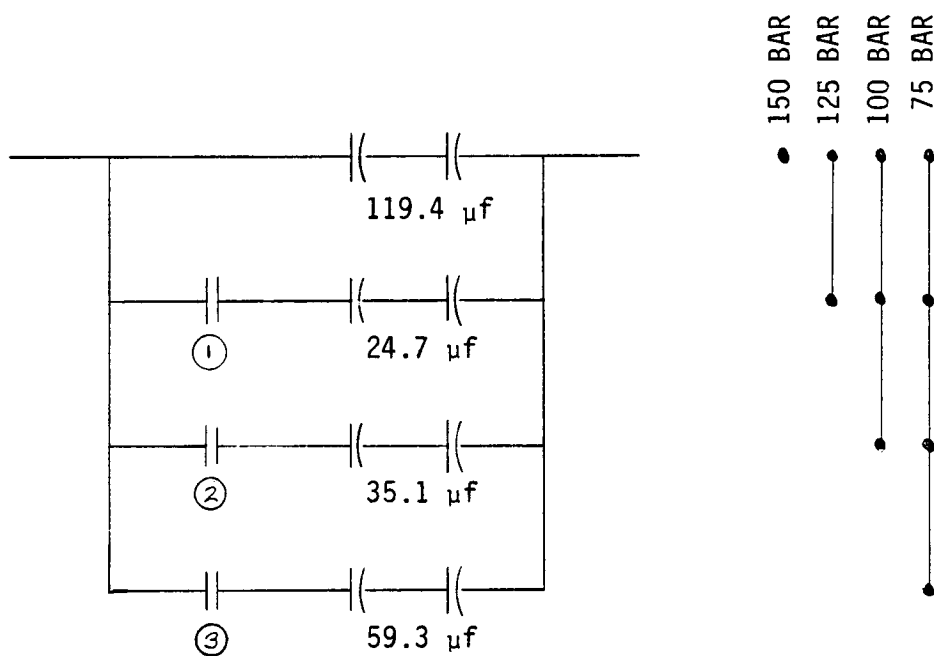
TABLE 11-1

TEST SERIES SPECIFICATIONS

DATE	PRESSURE (Bar)	TEMPERATURE RATIO	PISTON STROKE (mm)	MAXIMUM ELECTRIC POWER (kW)
7-25-85	75	1.6 - 1.8	10.0 - 16.0	2.8
8-7-85	75	1.6 - 1.77	10.0 - 19.2	3.9
8-13-85	75	1.6 - 2.0	10.0 - 18.4	6.6
9-17-85	75	1.6 - 2.0	10.0 - 16.4	7.1

FIGURE 11-8

ALTERNATOR POWER VERSUS PISTON AMPLITUDE
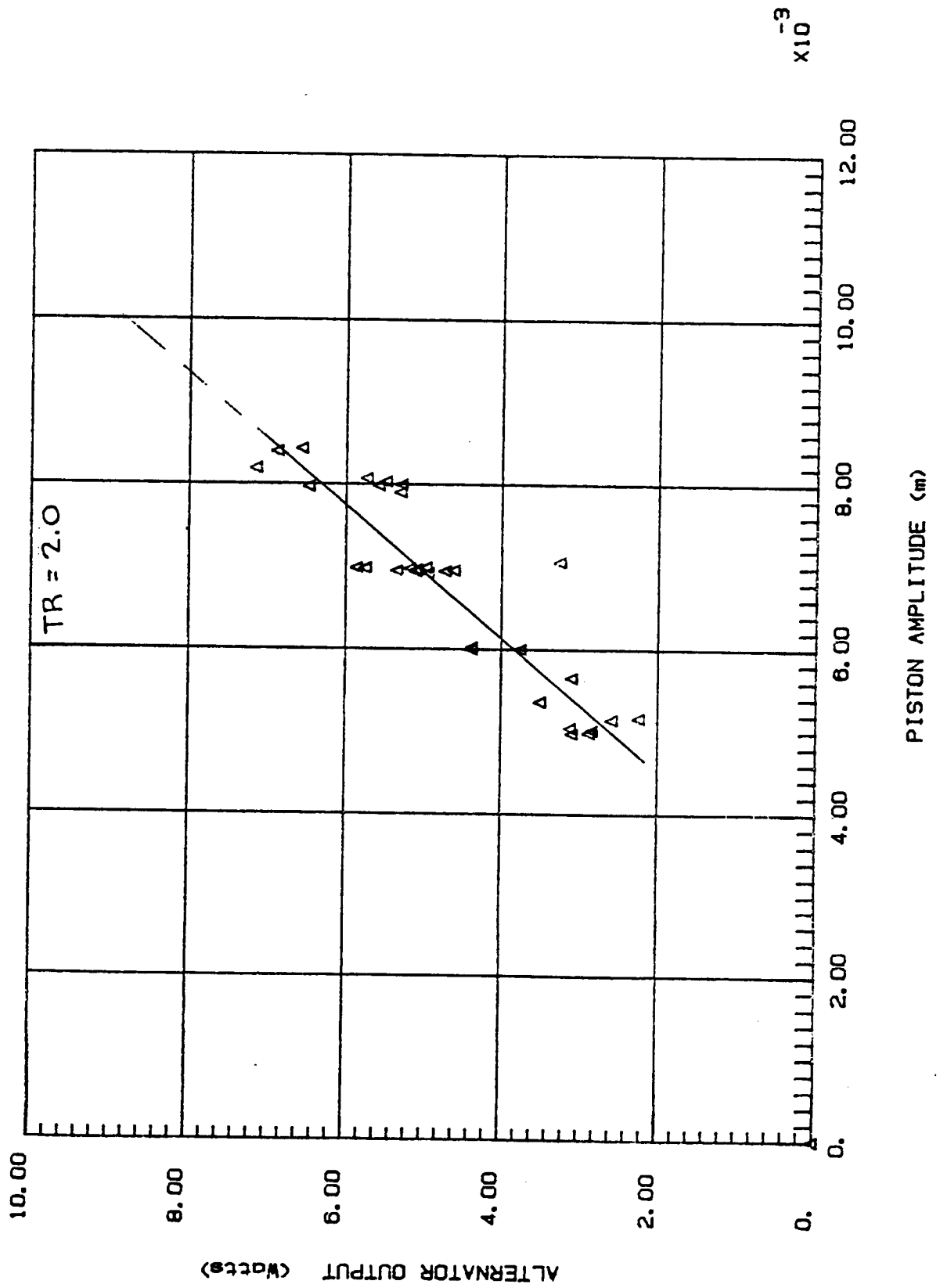
FIGURE 11-9

ALTERNATOR POWER VERSUS DISPLACER AMPLITUDE

TR=2.0

X10^3

ALTERNATOR OUTPUT (Watts)

DISPLACER AMPLITUDE (m)

X10^{-3}
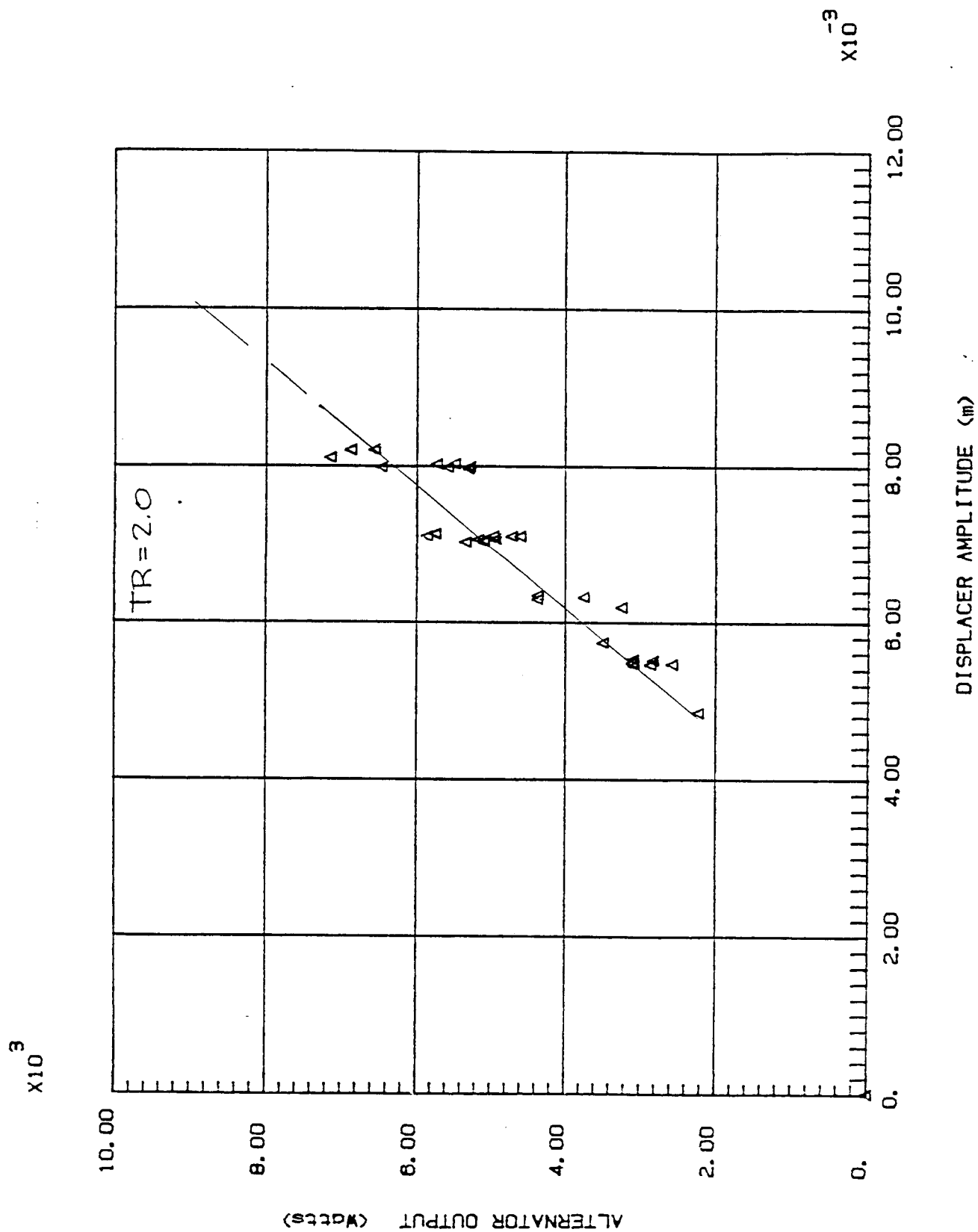
FIGURE 11-10

DISPLACER AMPLITUDE VERSUS PISTON AMPLITUDE
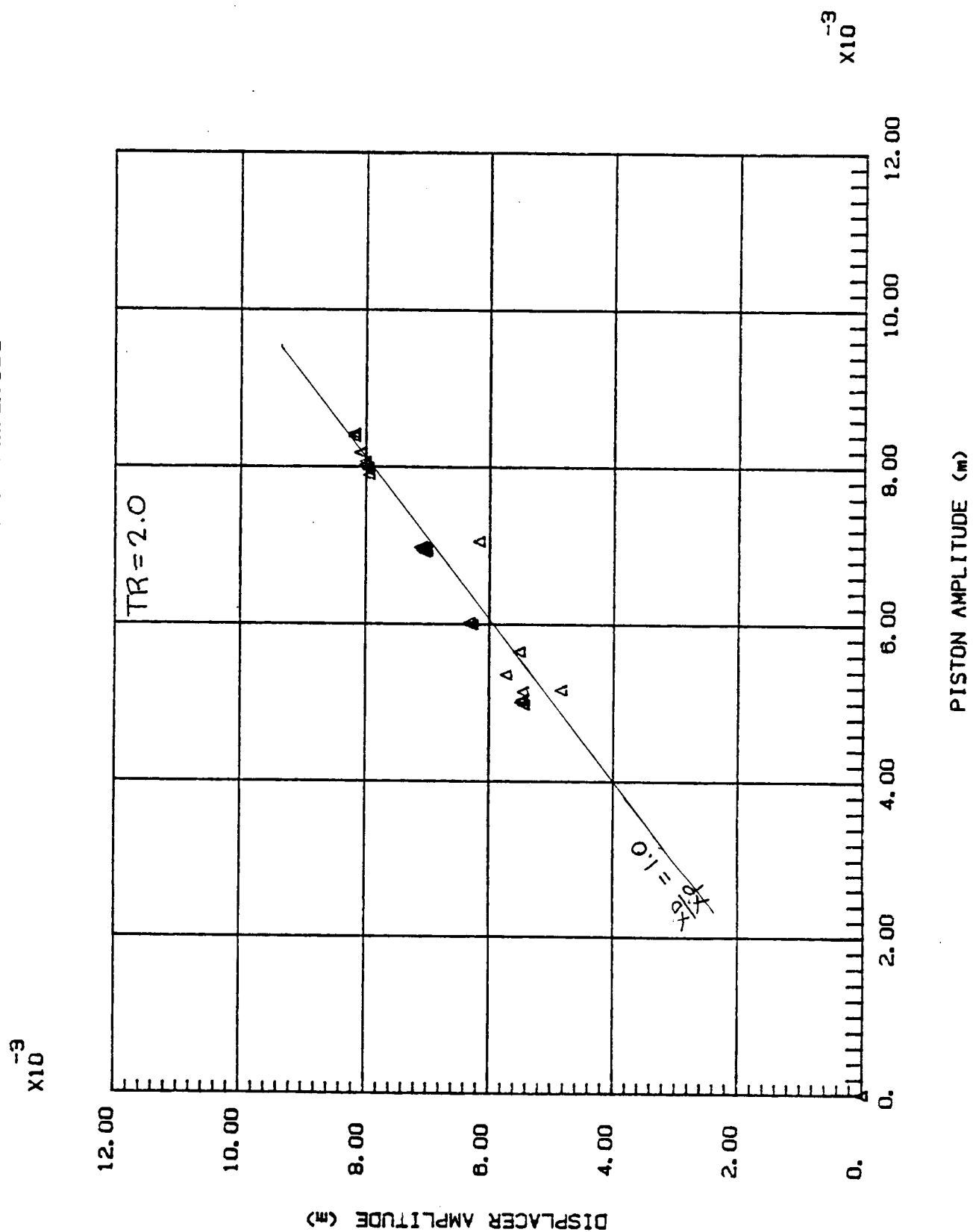
FIGURE 11-11

PV POWER VERSUS PISTON AMPLITUDE
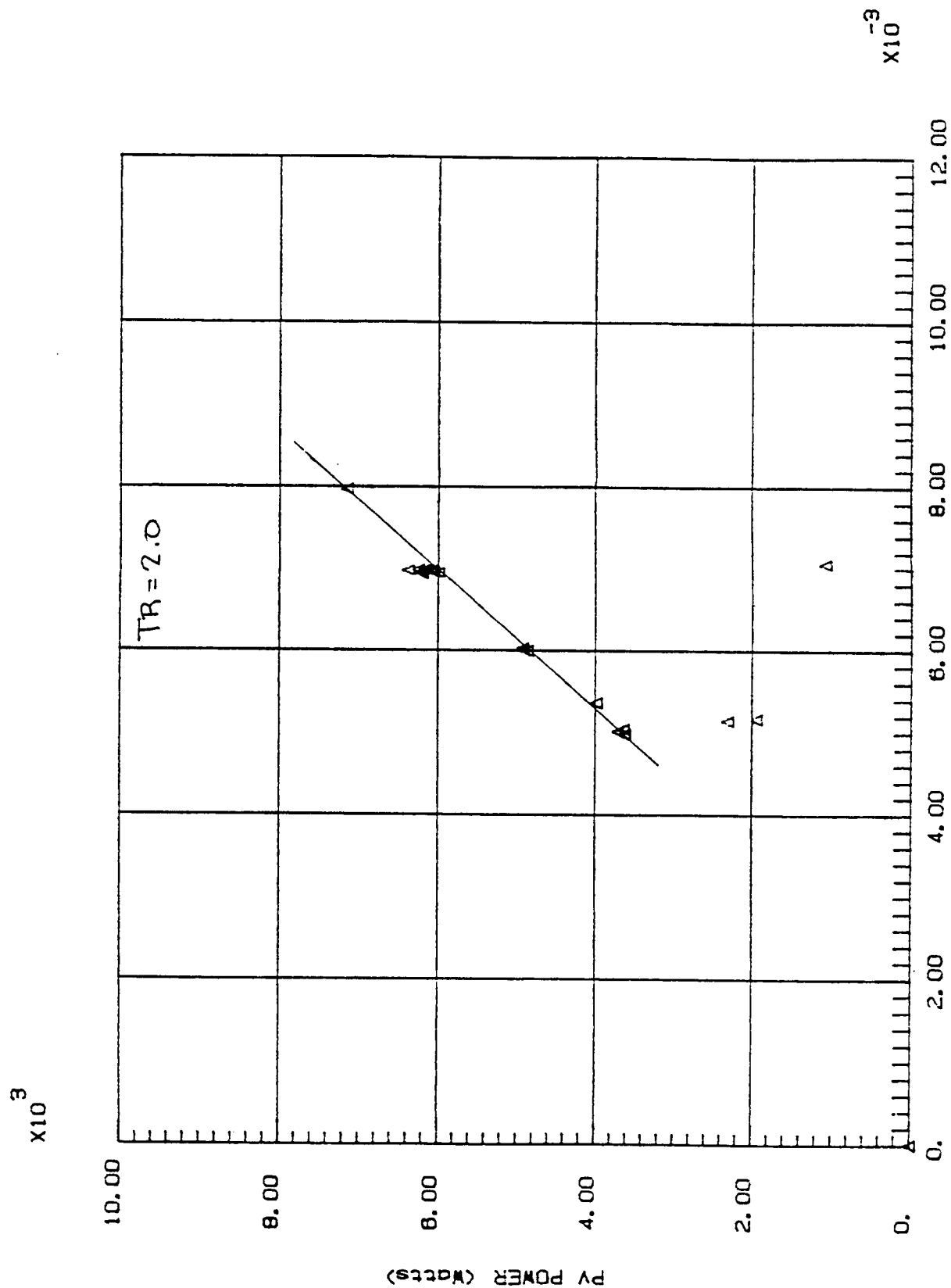
FIGURE 11-12

PV POWER VERSUS DISPLACER AMPLITUDE
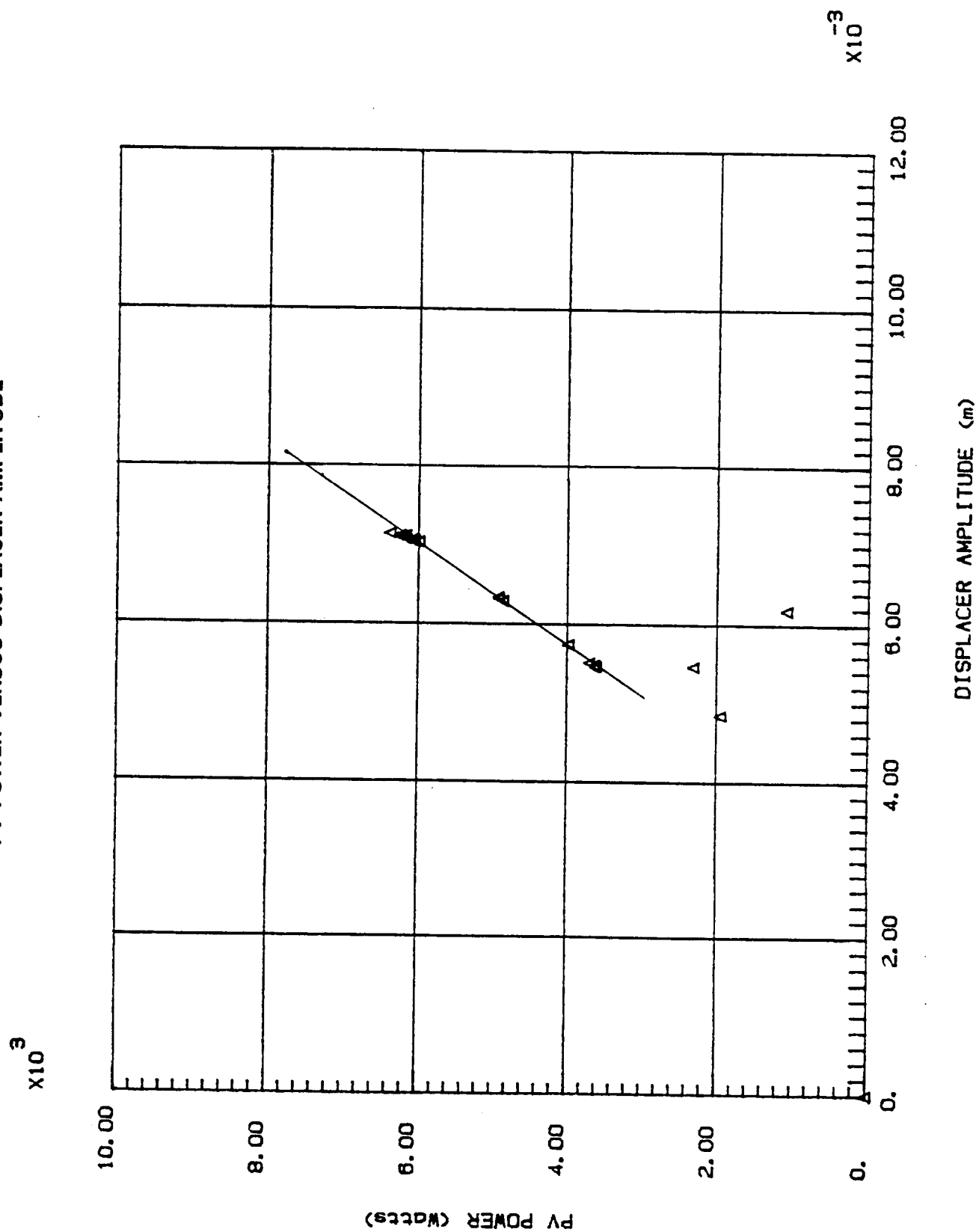
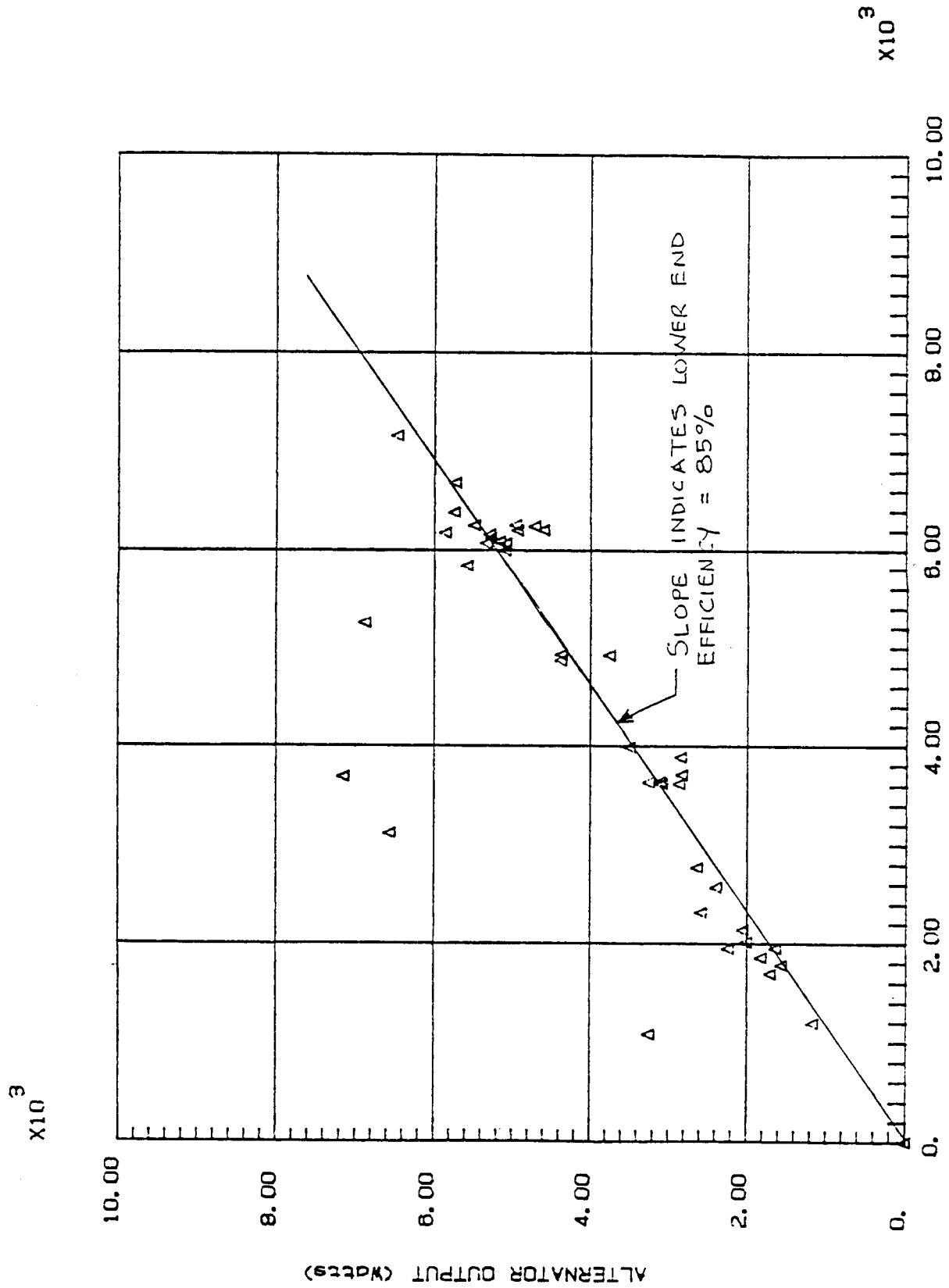FIGURE 11-13

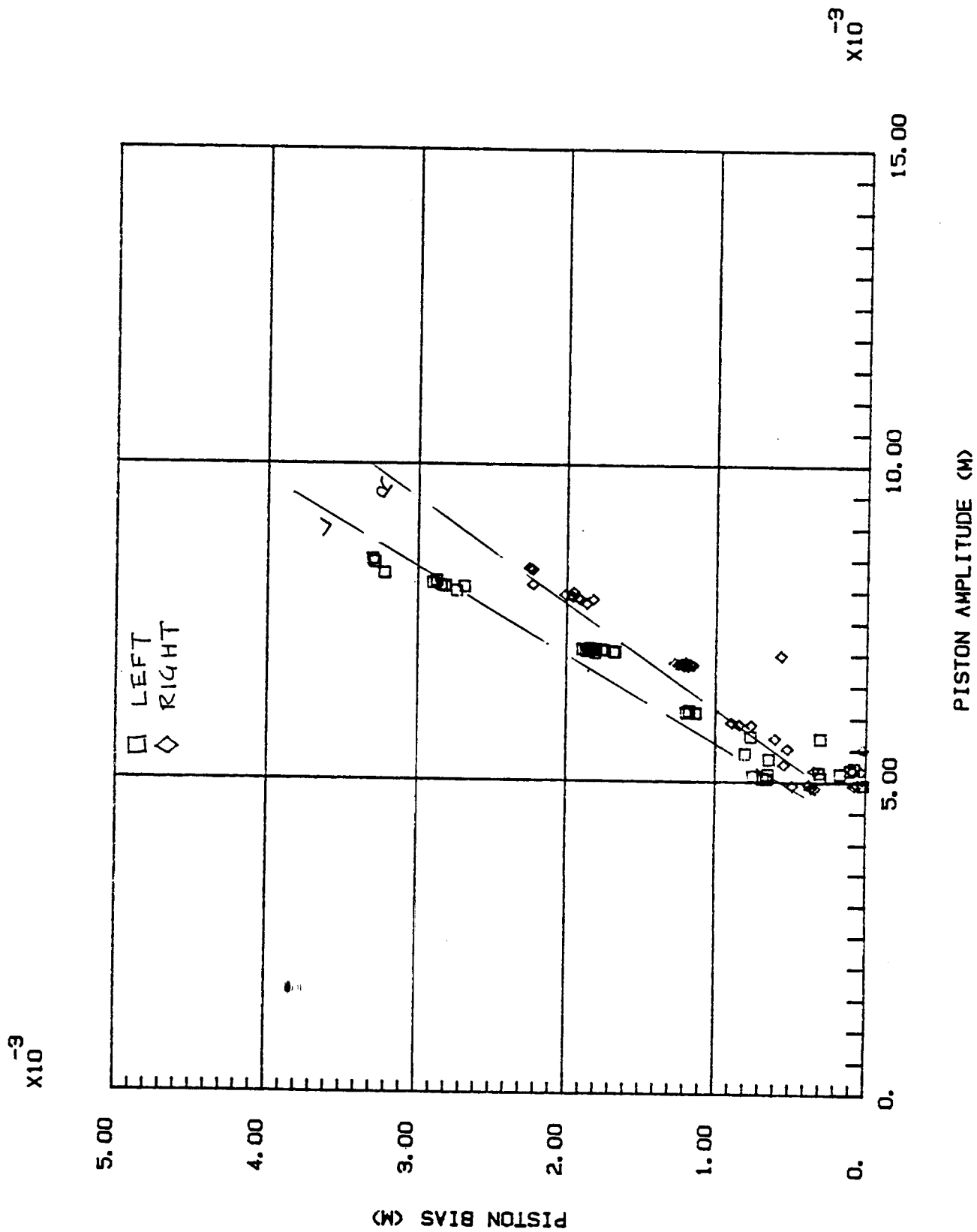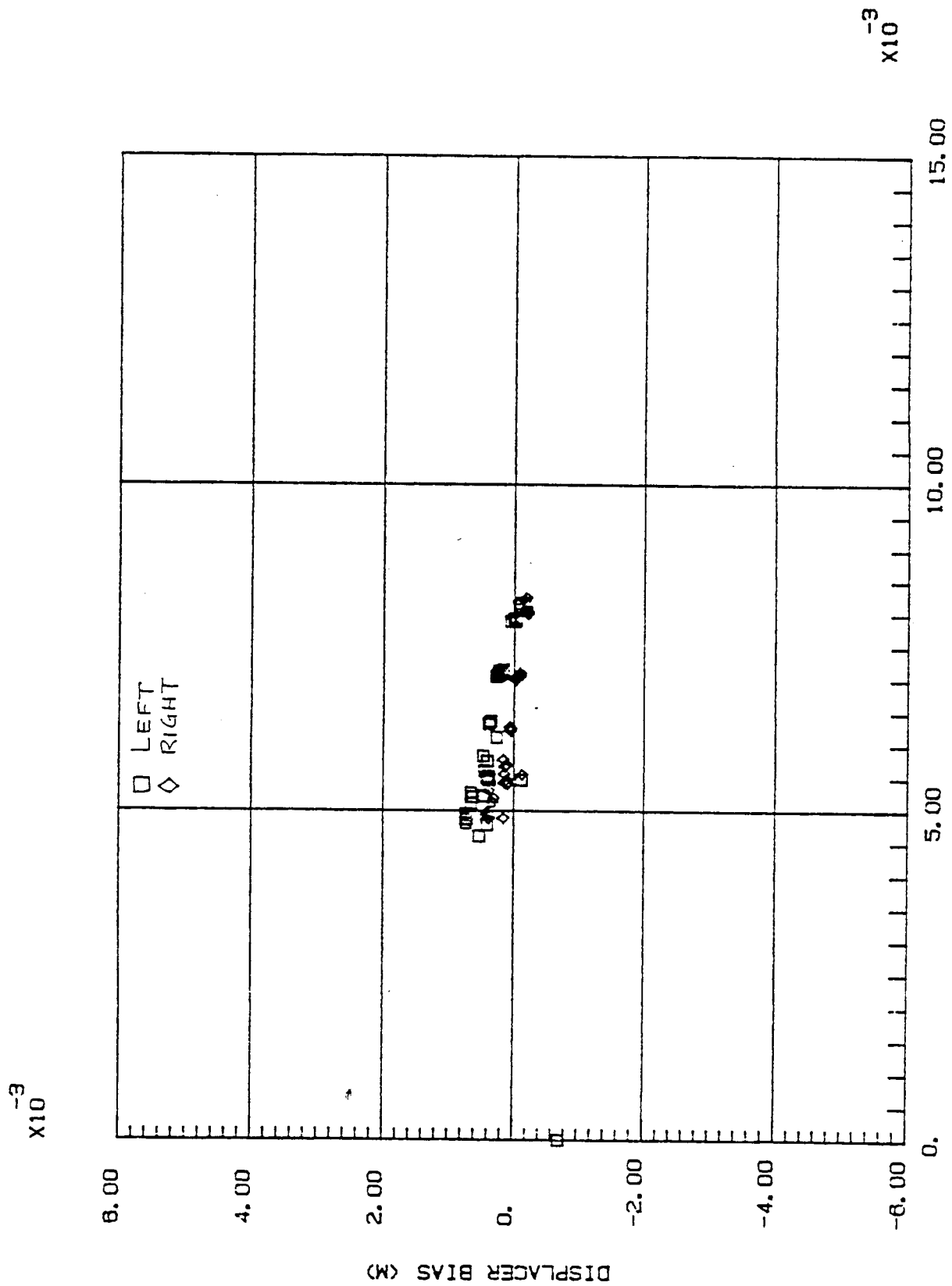## ALTERNATOR POWER VERSUS PV POWER

FIGURE 11-14

PISTON BIAS

FIGURE 11-15

DISPLACER BIAS

DISPLACER AMPLITUDE (M)

DISPLACER BIAS (M)

ly 90% of the power level predicted by theoretical analysis using the FASTIE code.

Figure 11-9 shows the alternator power versus displacer amplitude. Since Xd/Xp was approximately equal to 1.0 as shown in Figure 10, the plots in Figures 11-8 and 11-9 are virtually identical.

Figures 11-11 and 11-12 show the PV power delivered to the pistons by the working gas as a function of the piston and displacer amplitudes. These are approximately 90% of the predicted piston power at 8mm.

Figure 11-13 shows the alternator power versus piston power. The slope of the line through the data indicates the efficiency of the lower ends, which includes piston gas spring losses as well as alternator losses, is about 85%. Again, this is very close to analytical predictions. Figure 11-15 shows that unlike the pistons, the displacers operate with an almost zero bias of their midstroke positions.

The above interpretations have been made from one test series only. To date, an energy balance has not been attained to provide an overall check on the power predictions. Repeat tests at half pressure and, of course, tests at higher pressures are required to fully characterize the performance of the engine.

12.0 FUTURE WORK

Future work will depend, to a large extent, on the results of basic engine characterization tests yet to be performed. The following list identifies elements which should be covered during FY86. Longer range efforts to refine engine performance and design and/or test activities to support the development of high temperature, liquid metal compatible engines have not been included.

1. Repeat 75 Bar tests to confirm performance measurements obtained to date.

2. Perform tests on current engine at pressures up to 150 Bar, strokes up to 20 mm, and at temperature ratios up to 2.0.

3. Demonstrate engine operation on internal bearings.

4. Evaluate the effect of reduced volume in the expansion and compression space.

5. Evaluate the effect of reduced volume, flow area, and surface area in the engine heaters.

6. Evaluate the effect of alternate regenerator characteristics.

APPENDICES

APPENDIX 4.1

FREE-PISTON STIRLING ENGINE OPERATING MODES

FREE-PISTON STIRLING ENGINE OPERATING MODES

Introduction

The free-piston Stirling engine can be operated in two basic modes: as a thermal oscillator ('free' operation); or as a thermal amplifier. The SPDE is operated as a thermal oscillator.

Thermal Oscillator Engine

A simple free-piston engine consists of two moving parts: a displacer piston, and a power piston. Each piston is acted on by dynamic elements such as springs and dampers. The displacer is acted upon by the springs and dampers of its support and drive system. The power piston is acted upon by the springs and dampers associated with its support system and the engine load. In addition, the two pistons dynamically interact with each other through the engine working gas. Motion of the pistons affects the pressure of the working gas, and changes in pressure of the working gas exert forces on the pistons. In general, the pistons affect the pressure in the working gas by three different mechanisms:

- Compression or expansion caused by changes in displaced volume;
- Compression or expansion caused by transfer of gas from cold to hot or hot to cold regions of the engine; and,
- Pressure differences caused by motion of the working gas through the engine heat exchangers.

Under normal operating conditions, motion of the displacer causes power to be transferred from the working gas to the power piston. This occurs primarily through the second mechanism described above. Simultaneously, motion of the power piston causes power to be transferred from the power piston to the displacer piston primarily through the first mechanism. The power transfer to the displacer piston occurs primarily through its rod area. The term 'rod area' actually refers to the difference between the effective expansion space displacer face area and the effective compression space displacer face area. In early engine designs, this difference was associated with the actual area of a rod in the engine; hence the term rod area. In some later engines, such as the EM, the

rod area is not associated with a physical piece of hardware; such engines are called virtual-rod engines.

The power flow from the power piston to the displacer is the power feedback that maintains the displacer motion and allows the standard free-piston engine to self-oscillate. In both rod area and virtual rod engines, proper operation of the system (in general) requires that the oscillator be neutrally damped and stable (an exception is the under-damped relaxation oscillators such as the U of W heart pump). Neutral damping means that the active and reactive power flows to the piston and displacer are just balanced at the operating point. Stable means that the oscillator returns this operating point when operation is disturbed in any physically allowable manner. In a free-piston oscillator engine, the rod area is set to provide just enough feedback power flow to achieve neutral damping at a particular load level. The load level is called the critical load level, and the rod area is called the critical rod area. At other load levels, the engine will, in general, not be neutrally damped but under- or over-damped. If under-damped, engine amplitude will grow; and, if over-damped, the engine amplitude will decay. In order to prevent either occurrence, some means must be applied to return the engine to a neutrally damped condition when the load changes. This can be accomplished in a number of ways, such as heater head temperature control, displacer damping control, displacer spring control, piston spring control, or non-linear load damping.

The Technology Demonstrator Engine is an example of an engine that operates as a free-oscillator and maintains neutral damping by both displacer damping and displacer spring control. The SPDE engine operates as a free-oscillator and maintains neutral damping due to non-linear load characteristics (rectifier/filter load characteristics).

Thermal Amplifier Engine

An engine operated as a thermal amplifier has a rod area which is smaller than critical rod area at all anticipated load levels. As a consequence, the engine is over-damped at all load levels and will not free oscillate. Under this condition, there are two ways to cause the engine to operate - one is to 'drive' the displacer, and the other is to 'drive' the piston.

Displacer Drive Operation

The EM engine is an example of a thermal amplifier engine with displacer drive operation. The displacer is driven by a permanent-magnet motor located at the cold side of the displacer. The engine is operated by supplying an alternating voltage to the motor terminals. If the engine is driving a linear load, the following characteristics hold true (neglecting non-linearities in the engine):

- The alternator output voltage (as well as the amplitude of displacer and piston motion) is proportional to the input voltage to the motor; and,
- the output frequency (as well as the frequency of oscillation of the displacer and piston) is equal to the input frequency.

The above characteristics are those of a simple linear amplifier, in this case, a thermal amplifier. The power amplification ratio (PAR) is defined as the ratio of the power generated by the engine to power input to the motor. The PAR depends on the rod area, since the higher the power feedback through the rod, the lower the power feedback through the motor. The higher the PAR, however, the more restricted the load range over which the engine is stable. In the extreme of zero rod area, all feedback power is supplied by the motor, the power amplification is low, and the engine is stable for all load levels.

As stated earlier, the operating frequency of the engine is equal to the input frequency to the motor. This means that, unlike a free oscillator which operates at its own natural frequency, a thermal amplifier may be driven at any frequency. Unfortunately, as with any high tuned amplifier, high power output is only achieved near the amplifier's natural frequency.

The design point PAR of the EM is 15, with a stable load range from 25 percent to full power. At full load power, the displacer power flow is split evenly between the rod and the motor.

Piston Drive Operation

Operation of the displacer-driven engine is easy to visualize; power is input to the displacer, and the power is removed from the power piston. Operation of the piston-driven engine is fundamentally the same, but not as easily visualized.

This drive approach can be utilized in amplifier engines with linear alternators as in the present SPDE.

To operate the engine, alternating voltage is applied to the alternator output terminals. If the alternating voltage is in the proper frequency range, the engine will respond by supplying power to the AC voltage source. As with the displacer drive case, the following characteristics hold true:

- The amplitude of oscillation of the displacer and piston is proportional to the applied voltage; and,
- The frequency of oscillation is equal to the source frequency.

Piston-driven operation is generally limited to engine alternator systems in which the 'voltage source of proper frequency' is a utility grid. Such an installation is generally referred to as grid-connected or grid-slaved installation.

The power to drive the displacer may flow entirely through the displacer rod as in a conventional free oscillator, or may flow through the rod and displacer motor as in the displacer drive case. The field EM is a piston-driven unit, which uses a split feedback approach.

APPENDIX 8.1.

MTI PERMANENT MAGNET GENERATOR MAGNETIC ANALYSIS

MTI PERMANENT MAGNET GENERATOR MAGNETIC ANALYSIS

Summary

This report describes the magnetic analysis of a permanent magnet alternator. The analysis was performed using the finite element method. The magnetic fields in and around the device were calculated for various positions of the movable permanent magnets. From these fields, the open circuit voltage in the armature coil was computed. The value came out to be only about 65% of the designed value. The self-inductance of the alternator was also computed from the finite element results, and this value agreed well with the design calculation.

Description of the Analysis

The finite element method has been proven to be an accurate and reliable method to analyze complicated magnetic structures. The method can, with relative ease, handle problems with arbitrary shapes, different material properties, and various current distributions. The method was applied to the alternator, the cross-section of which is shown in Figure 8.1-1. The rectangular piece on top is ferromagnetic as is the U-shaped structure below it. Two permanent magnets are located in the air gaps on the right and left. The alternator is axisymmetric; the axis of rotation begins the X axis. The rectangular area below the air gap enclosed by the U-shaped bottom piece contains a coil which is also axisymmetric around the X axis. A reciprocating motion of the permanent magnets causes an alternating flux to link the coil and thus induces an emf.

The following assumptions were made for this analysis:

1. The iron does not saturate and, therefore, may be treated an a high but constant permeability material. This means that the analysis could be done in a linear fashion. The assumption was later checked with the results of the calculation and found to be valid. The flux densities found were not enough to saturate the iron.

FIGURE 8.1-1

GEOMETRY OF GENERATOR

MTI4**.FEM
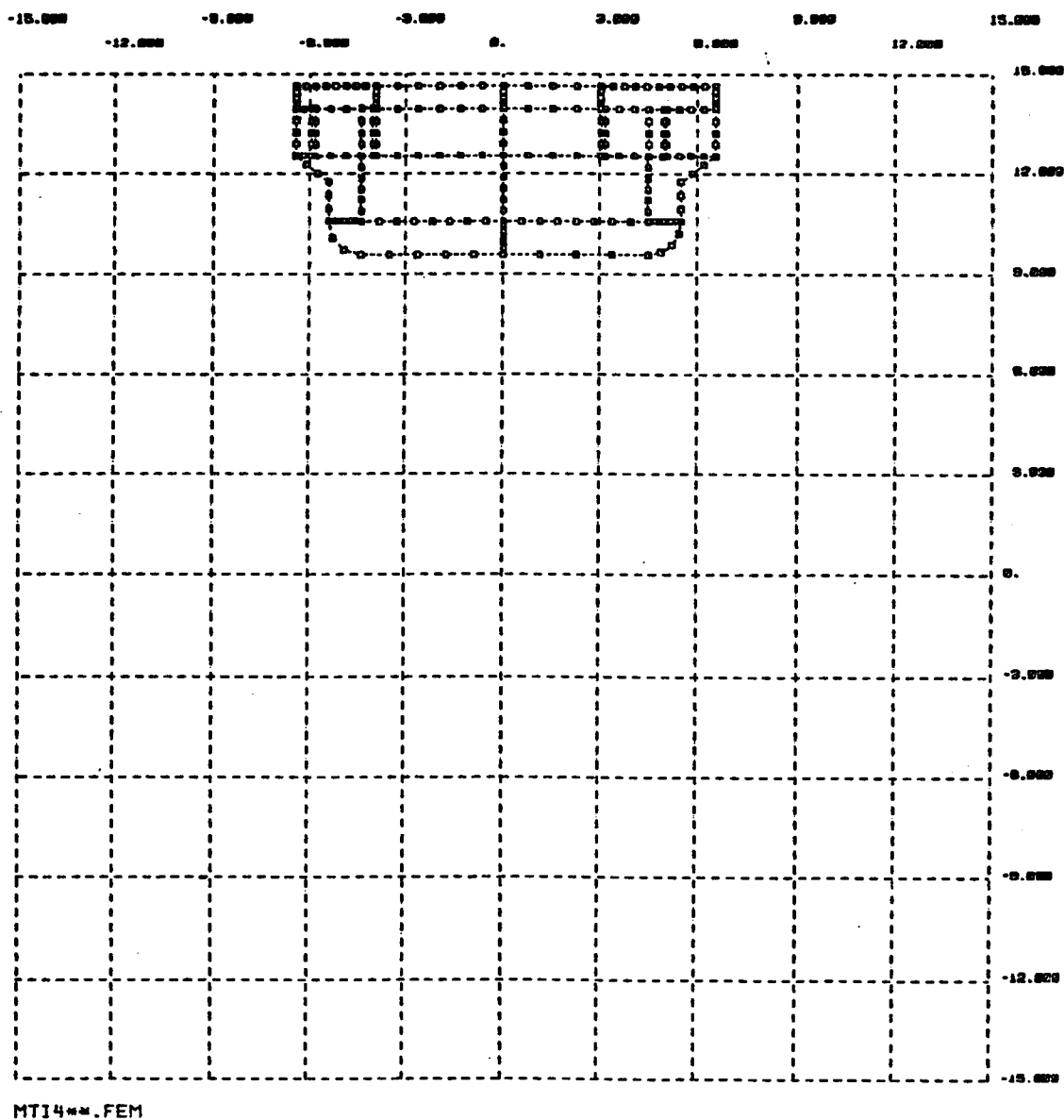
2. The problem was considered two-dimensional rather than axisymmetric. This also simplifies the analysis; and because nothing in the analysis deals with the regions close to R=0, the assumption seems valid.

3. The permanent magnets were represented by equivalent current sheets. This is common practice today and has been shown to give good results, especially in cases such as this in which the magnet has a simple shape and there is little cross flux; i.e., flux perpendicular to the N-S axis of the magnet. The calculation of the equivalent circuit is shown in Attachment A.

4. The effects of eddy currents were ignored. This seems reasonable due to the low frequency and the fact that all of the conducting structures were laminated.

The two-dimensional cross-section of the divide is shown in Figure 8.1-1. The dimensions are in centimeters. The cross-section was then divided into sub-regions as shown in Figure 8.1-2. This division aids in the input of material properties and sources and also helps facilitate the finite element grid generation. A section of the finite element grid with corresponding element numbers are shown in Figures 8.1-3 and 8.1-4. In order to represent the different positions of the permanent magnets, several different combinations of sub-regions were used, and the finite element was reconstructed for each case.

Figures 8.1-5, 8.1-6, and 8.1-7 shows the flux distribution at three different magnet positions. Figure 8.1-5 is the maximum flux linkage position, Figure 8.1-6 is an intermediate position, and Figure 8.1-7 is the minimum position. The figures are plots of equi-magnetic vector potential contours. These lines give the direction of the flux. Also, the same amount of flux is enclosed between each two lines. Therefore, the flux density, the flux per unit area, is greater in regions in which these lines are close together, and the flux density is less in regions in which the lines are far apart. The flux density is, therefore, high in the iron and low in the region of the coil. The results of Figure 8.1-5 predicted that the maximum flux linkage of the coil was less than had been expected. The magnet on the left is completely in the air gap and sends flux around the magnetic circuit (clockwise in this case). The magnet on the right sends flux in the opposite direction(counter-clockwise); but, since it is not in the air gap, it was
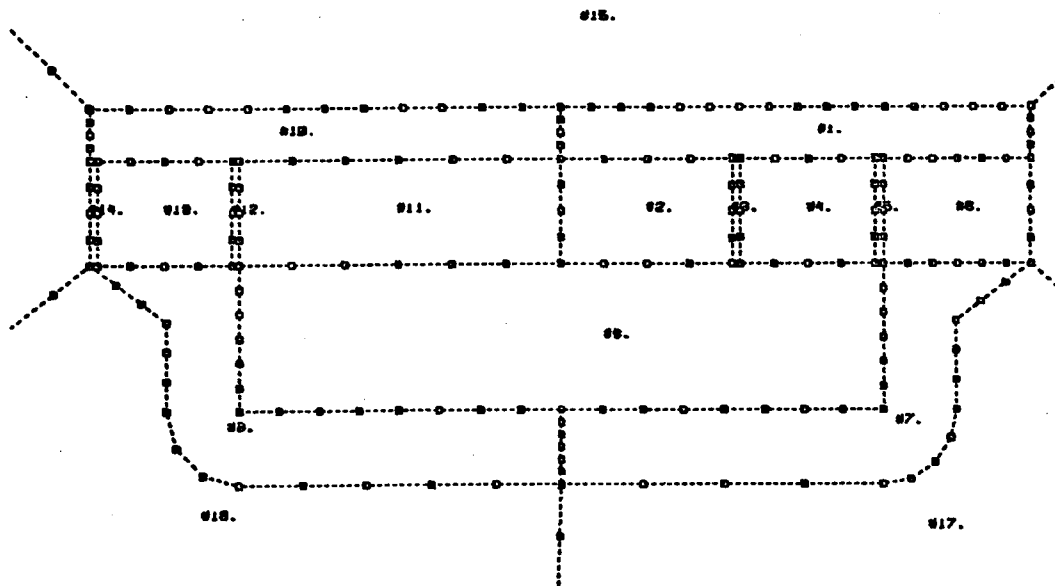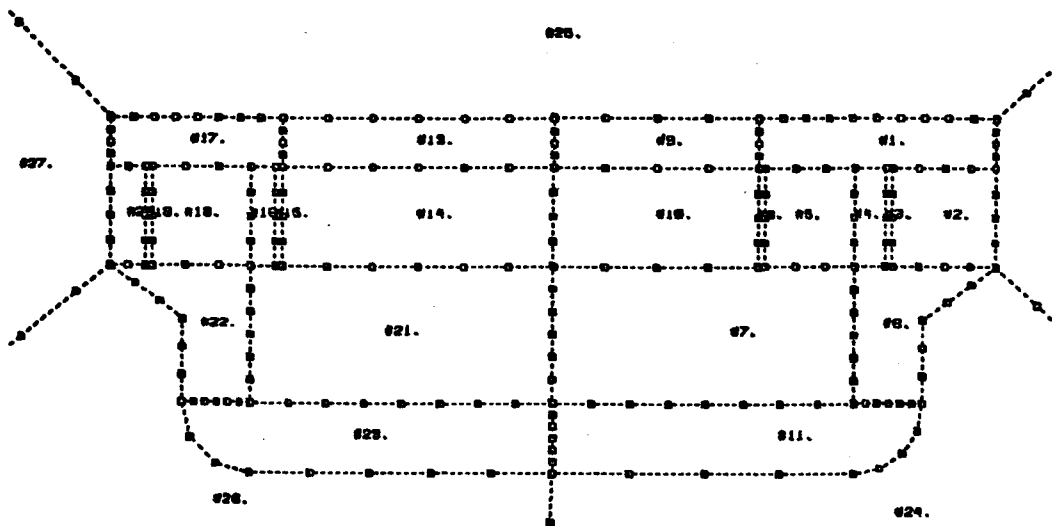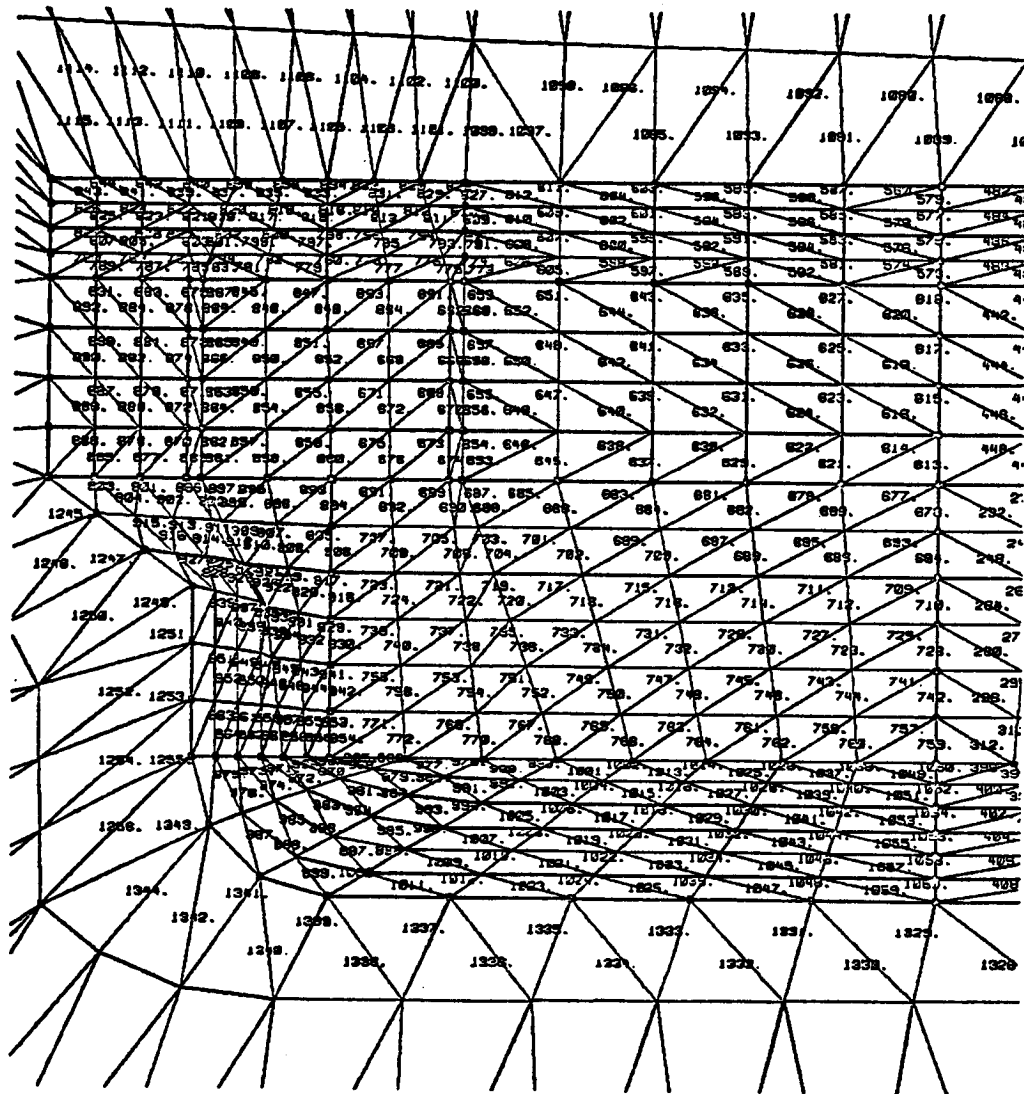
FIGURE 8.1-2a

SUBREGIONS FOR MAXIMUM FLUX POSITION

FIGURE 8.1-2b

SUBREGIONS FOR INTERMEDIATE FLUX POSITION

FIGURE 8.1-3

FINITE ELEMENTS AND NUMBERING FOR WINDING AND GAP REGIONS

MTI2**.FEM

FIGURE 8.1-4

FINITE ELEMENTS AND NUMBERING

BLOW-UP OF MAGNET AND CURRENT SHEET SUBREGIONS

MTI5**.FEM
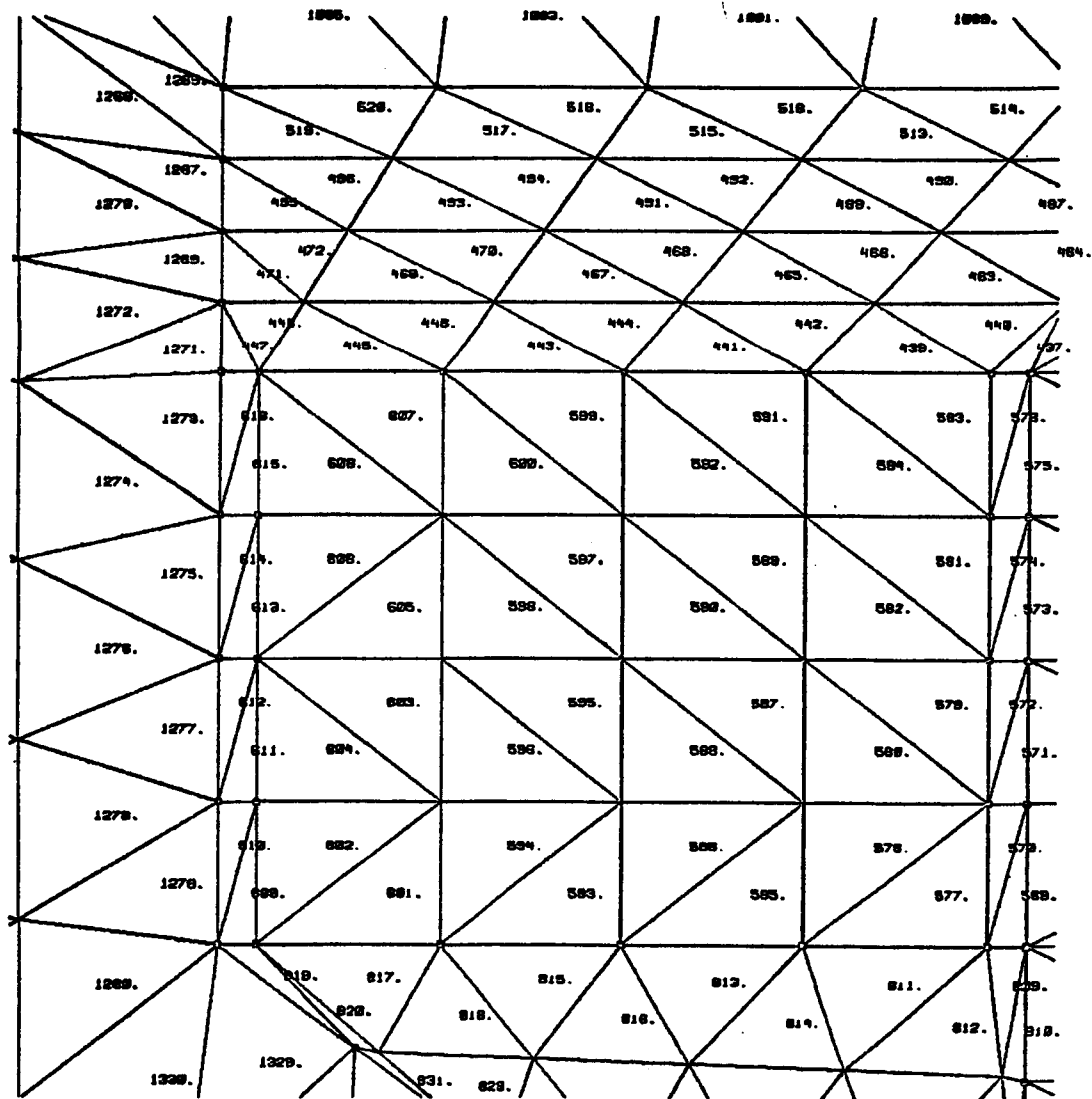
FIGURE 8.1-5

FLUX PLOT AT MAXIMUM FLUX LINKAGE
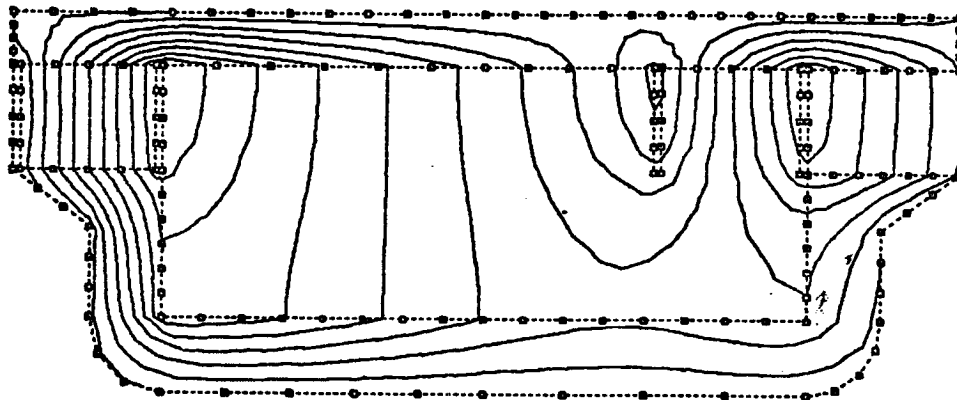
FIGURE 8.1-6

FLUX PLOT AT INTERMEDIATE FLUX LINKAGE
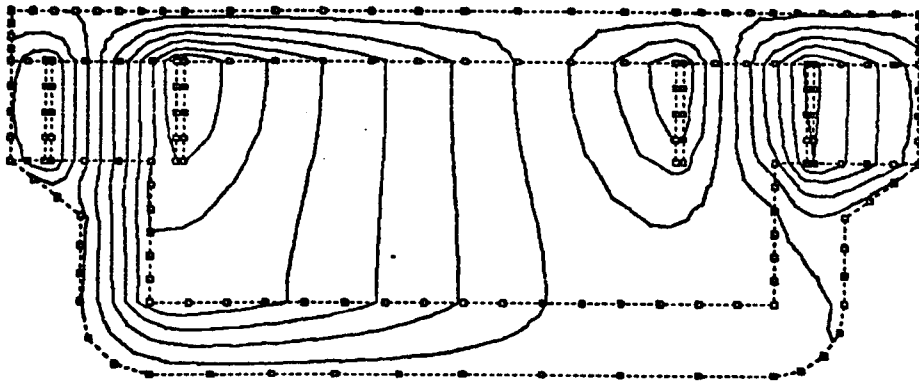
MTI3**.FEM

REAL/LINE	IMAG/LINE	SUBREGIONS
8.7804E-18	9.9999E-01	1. 2. 3. 4. 5. 6. 7. 8. 9. 10.11.12.14.15.16.17.20

FIGURE 8.1-7

FLUX PLOT AT MINIMUM FLUX LINKAGE
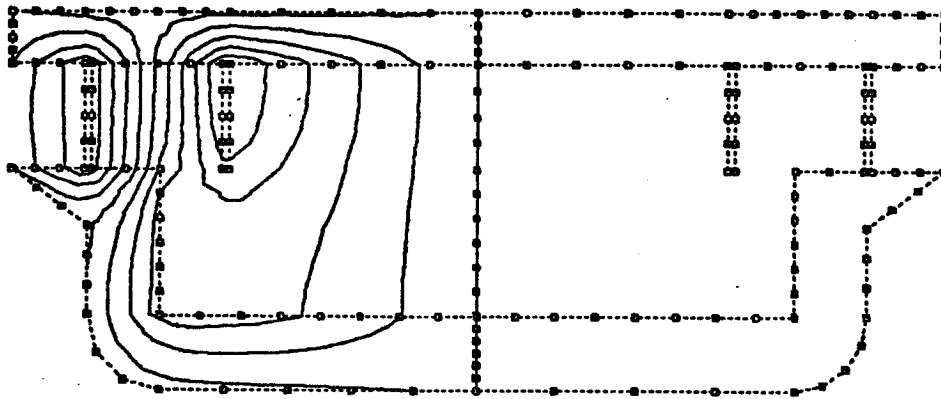
MTI2**.FEM

REAL/LINE	IMAG/LINE	SUBREGIONS
5.7300E-18	0.0000E-01	13.14.15.16.17.18.19.20.21.22.23.

not expected to have as much cancellation effect as is shown in Figure 8.1-5. It appears that only about 30% of the flux produced by the magnet on the left links the winding.
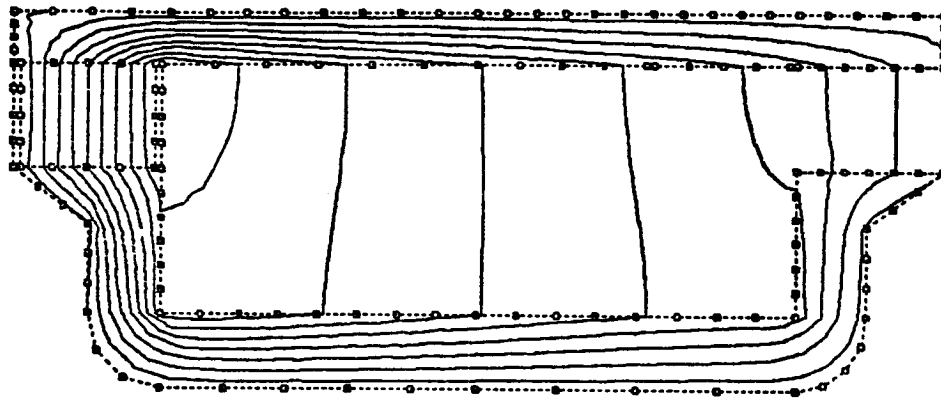
In order to check this result, the problem was divided into two separate problems which could be checked more easily and superposition was used to produce the final result. Figure 8.1-8 shows the case with only the magnet on the left in the problem, and Figure 8.1-9 shows the case with only the magnet on the right. These results were checked with Ampere's law along several paths and were found to be correct. There was, therefore, no reason to doubt their validity. Note that Figure 8.1-9 shows a great deal of this 'reverse flux'. The two solutions were added together and gave the results of Figure 8.1-5 as expected. The RMS open circuit voltage for this case was 84 volts as opposed to the 129 volt design value. This calculation is shown in Attachment B.

One further case was run in order to calculate the self-inductance of the coil. This is shown in Figure 8.1-10. The magnets were ignored and the coil was given an excitation of one ampere turn uniformly distributed through its area. The flux linkage was calculated and the inductance found. The calculation, along with an approximate check, is shown in Attachment C.

FIGURE 8.1-8

LEFT MAGNET EXCITATION ONLY

MTI5**.FEM

REAL/LINE	IMAG/LINE	SUBREGIONS
1.9119E-05	6.9696E-91	1. 2. 3. 4. 5. 6. 7. 8. 9. 10.11.13.14.17.

FIGURE 8.1-9

RIGHT MAGNET EXCITATION ONLY

MTI5**.FEM
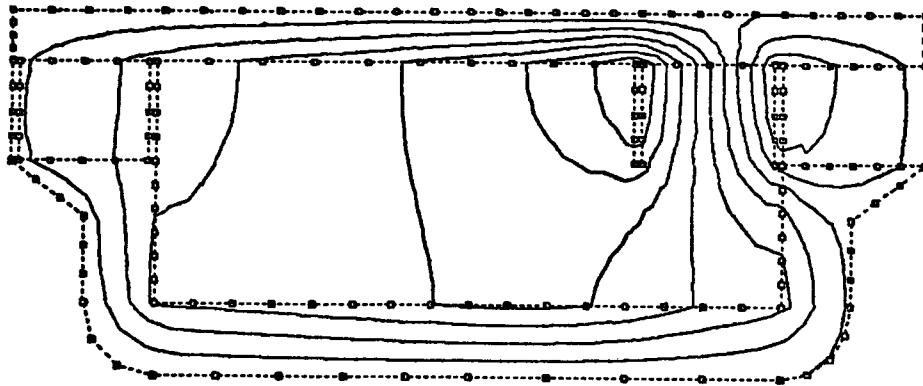
REAL LINE	IMAG LINE	SUBREGIONS
1.8363E-05	9.9206E-01	1. 2. 3. 4. 5. 6. 7. 8. 9. 10.11.12.13.14.

FIGURE 8.1-10

**FLUX PLOT WITH WINDING EXCITATION
FOR INDUCTANCE CALCULATION**
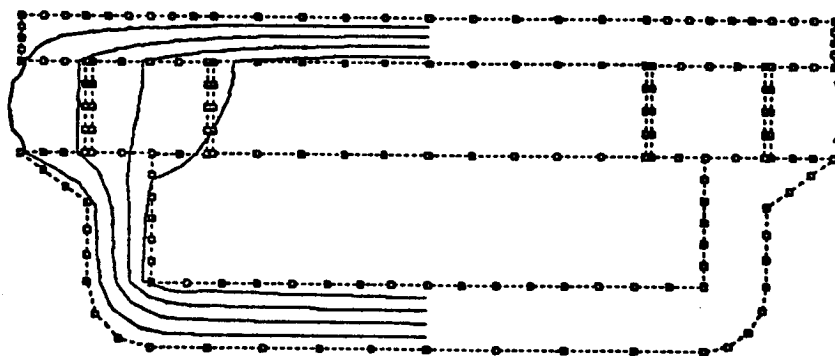
ATTACHMENT A - CURRENT SHEET CALCULATION

The calculation of the equivalent current sheet to represent the permanent magnet is based on finding the current excitation that will give the same flux density as the permanent magnet if the current sheet of the same height as the magnet were placed in an infinitely permeable magnetic core. The equation used to find these currents is:

$$I = B_r \cdot d/\mu o$$

Where: B_r = the flux density of the magnet

d   = the height of the magnet

μo = the free space permeability

For the case considered here:

$$I = \frac{9 \times 10^3 \text{ gauss} \times 10^{-4} \text{ gauss/weber} \times .14 \text{ meters}}{4 \times 10^{-7} \text{ henries/meter}}$$

= 10,026 amperes

ATTACHMENT B - CALCULATION OF THE INDUCED VOLTAGE

The induced open circuit voltage in the armature coil was calculated from the results of Figure 8.1-5. This gave the peak value of the flux linkage from which the open circuit voltage was calculated. No Fourier analysis was performed on the voltage wave shape. The RMS voltage was found by dividing the peak voltage by $\sqrt{2}$. As stated before, the plot of Figure 8.1-5 is a plot of equi-vector potential contours. The vector potential, which is calculated at each of the finite element nodes, is a measure of the 'flux level' in the system.

The difference in vector potential between any two points gives the flux (per unit depth) between those two points in a direction normal to the line connecting the two points. Using this principle, the determination of the flux linkage becomes quite straight-forward. Care must be taken, however, to account for the fact, which is apparent from the figure, that all of the flux does not link all of the turns. This partial linkage must be included and weighed by the fraction of the turns linked. The flux per unit depth was, therefore, found by finding the vector potential at 10 locations beginning at the left boundary of the winding and proceeding horizontally to the rightmost edge of the generator. The flux between each two points was found and multipled by the fraction of the coil area which the flux enclosed. The summation of these 10 values gave the flux linkage per unit depth. The voltage was calculated by using the following formula:

V = (flux/depth) x (circumference) x (# of turns) x (angular frequency) / $\sqrt{2}$

ATTACHMENT C - CALCULATION OF THE SELF-INDUCTANCE OF THE COIL

The self-inductance of the winding was found in a manner similar to the calculation of the induced voltage. The difference was that instead of the flux being generated by the permanent magnets, the flux, in this case, was due to currents in the winding itself. The flux plot for this case is shown in Figure 8.1-10. One ampere turn, uniformly distributed in the winding area, was used at the source of excitation. The flux linkage of the coil was found using the method in Attachment B. This value is the 'effective' permeance' of the coil. The inductance is found by multiplying this number by the square of the turns. The inductive reactance is found by multiplying the inductance by the angular frequency.

Observing the flux pattern of Figure 8.1-10, it can be seen that most of the flux links the winding and crosses the two air gaps. A check on the solution can, therefore, be found by a simple magnetic circuit calculation. In this case, flux density would be:

$$B = I \times \mu o \; / \; (2G)$$

and the inductance could be found by assuming that all of this flux links the winding. The value found by this approximate method was 1.38 ohms. The finite element results indicate 1.8 ohms. This difference seems reasonable due to the addition of the partial linkages in the finite element calculation.

APPENDIX 8.2

EXPERIMENTAL DETERMINATION OF THE FLUX LINKAGE FACTOR

USED IN THE DESIGN OF THE SPDE ALTERNATOR

EXPERIMENTAL DETERMINATION OF THE FLUX LINKAGE FACTOR

USED IN THE DESIGN OF THE SPDE ALTERNATOR

The magnetic circuit of the SPDE alternator has large volumes of space with relative permeability of unity (i.e., like that of air). The flux, therefore, is not mostly confined to steel paths as is normally the case of magnetic circuits with small air paths. Hence, the simpler methods of calculating the reluctances are not adequate. As part of the magnets are outside the poles and other parts have steel facing only on one side, the calculation of flux linkages of the alternator coil is particularly difficult.

This problem was resolved by two approaches. First, a finite element analysis was performed and is reported in Appendix 8.1. Second, a small laboratory model was built to simulate the geometry of the alternator to obtain an experimental determination of the flux linkages.

Figure 8.2-1 shows the sketch of the alternator simulation model. The effect of curvature was not simulated in this model. The permanent magnets are simulated by aircore rectangular coils. Figure 8.2-2 shows the simulation of the permanent magnet in more detail. The magnet simulation coils were sandwiched between two plastic sheets as shown in Figure 8.2-3. This sandwiching arrangement held the magnet simulation coils in a fixed relative position to each other. The thickness of the sandwiching plastic sheets was such as to simulate the radial air gaps between the outer stator and the magnets and between the inner stator and the magnets of the alternator.

A mechanical arrangement was provided so the coil assembly can be located as shown in Figure 8.2-1 between the simulated inner and outer stators. The mechanical arrangement also allowed the location of the coil sandwich assembly in any position relative to the stators in the X direction.

The alternator coil was simulated by a coil wound to occupy a major portion of the slot area. This coil is not shown in Figure 8.2-1 for the sake of clarity. However, the coil is shown in Figure 8.2-4, where the magnet simulation coils are not shown for the sake of clarity.

FIGURE 8.2-1

ALTERNATOR SIMULATION MODEL

VOLT METER

SIMULATED INNER STATOR

SEARCH COIL

SIMULATED OUTER STATOR

AIR CORE COILS SIMULATING PERMANENT MAGNETS
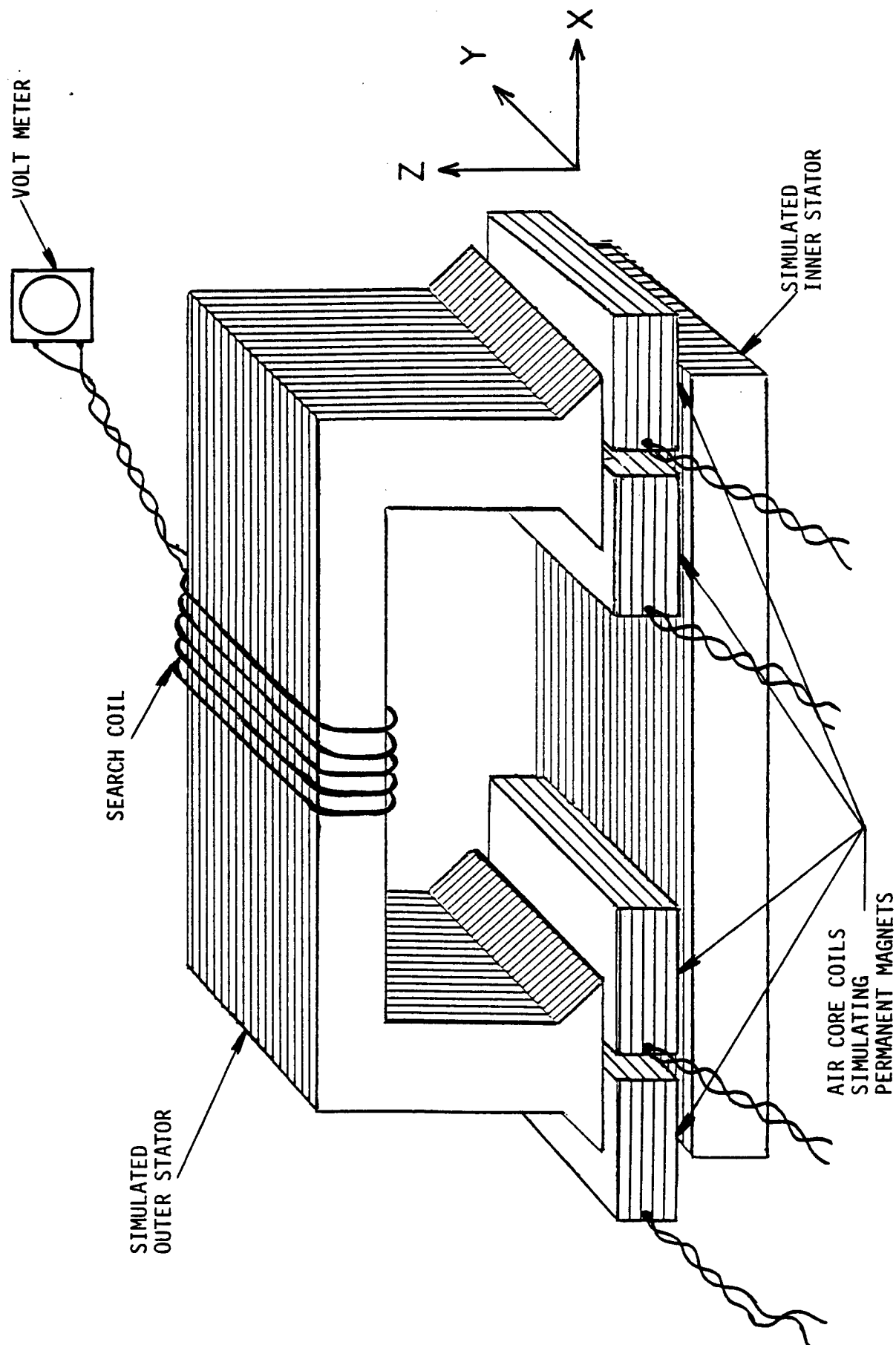
FIGURE 8.2-2

DETAILS OF PERMANENT MAGNET SIMULATION

PERMANENT MAGNET
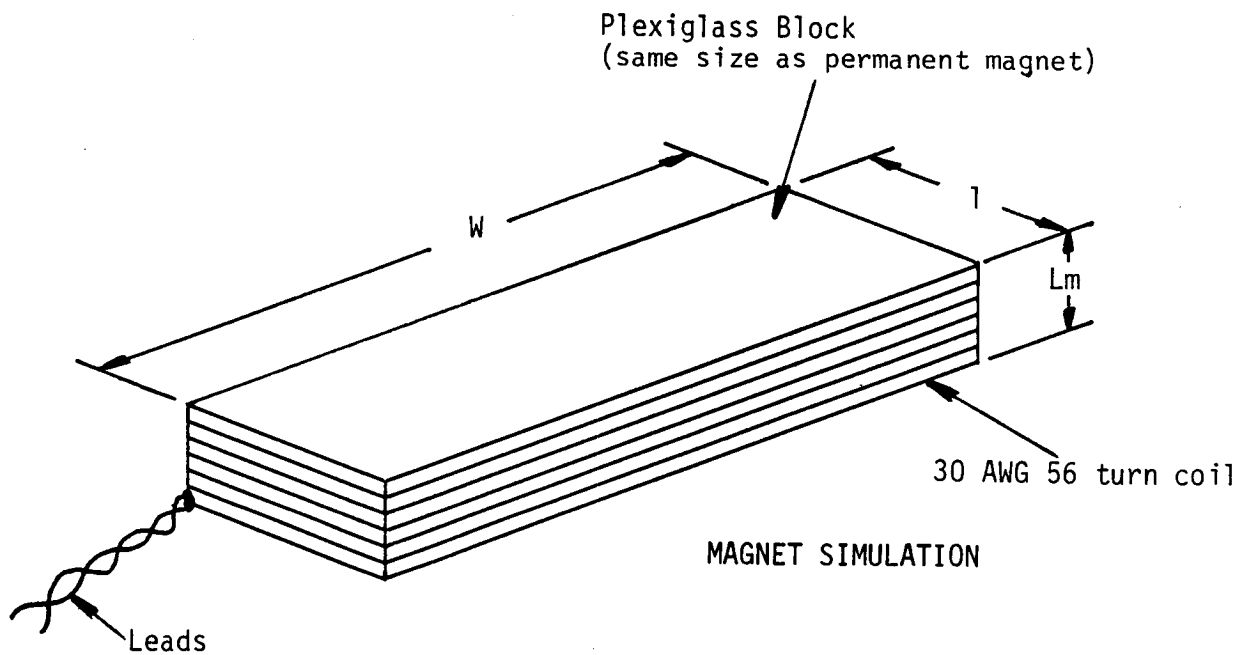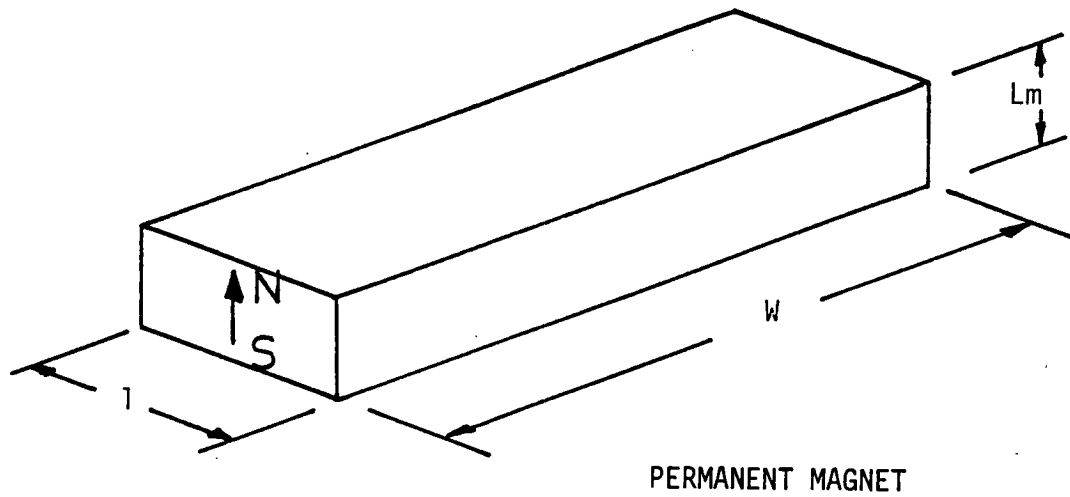
MAGNET SIMULATION

FIGURE 8.2-3

SIMULATED PLUNGER ASSEMBLY

MAGNET SIMULATION
COIL

UPPER SHEET OF
SANDWICH

LOWER SHEET OF
SANDWICH
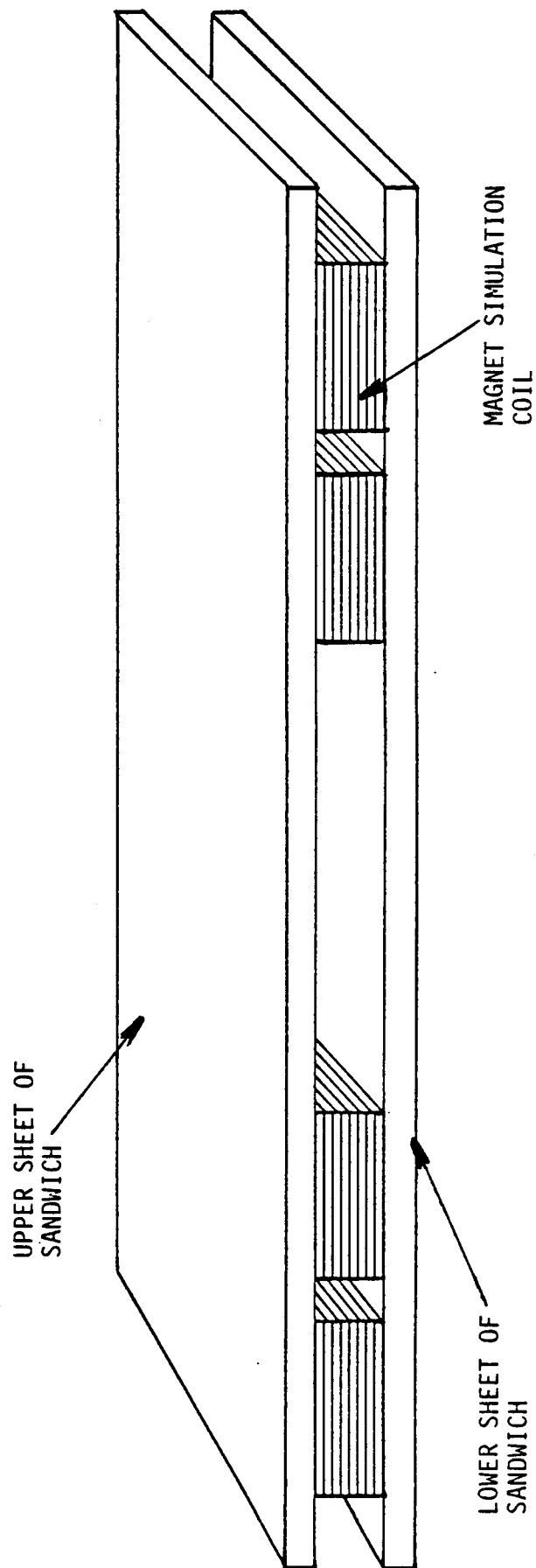
FIGURE 8.2-4

ALTERNATOR SIMULATION MODEL
SHOWING SIMULATED ALTERNATOR COIL

SIMULATED
ALTERNATOR
COIL

SIMULATED
OUTER STATOR

SIMULATED
INNER STATOR
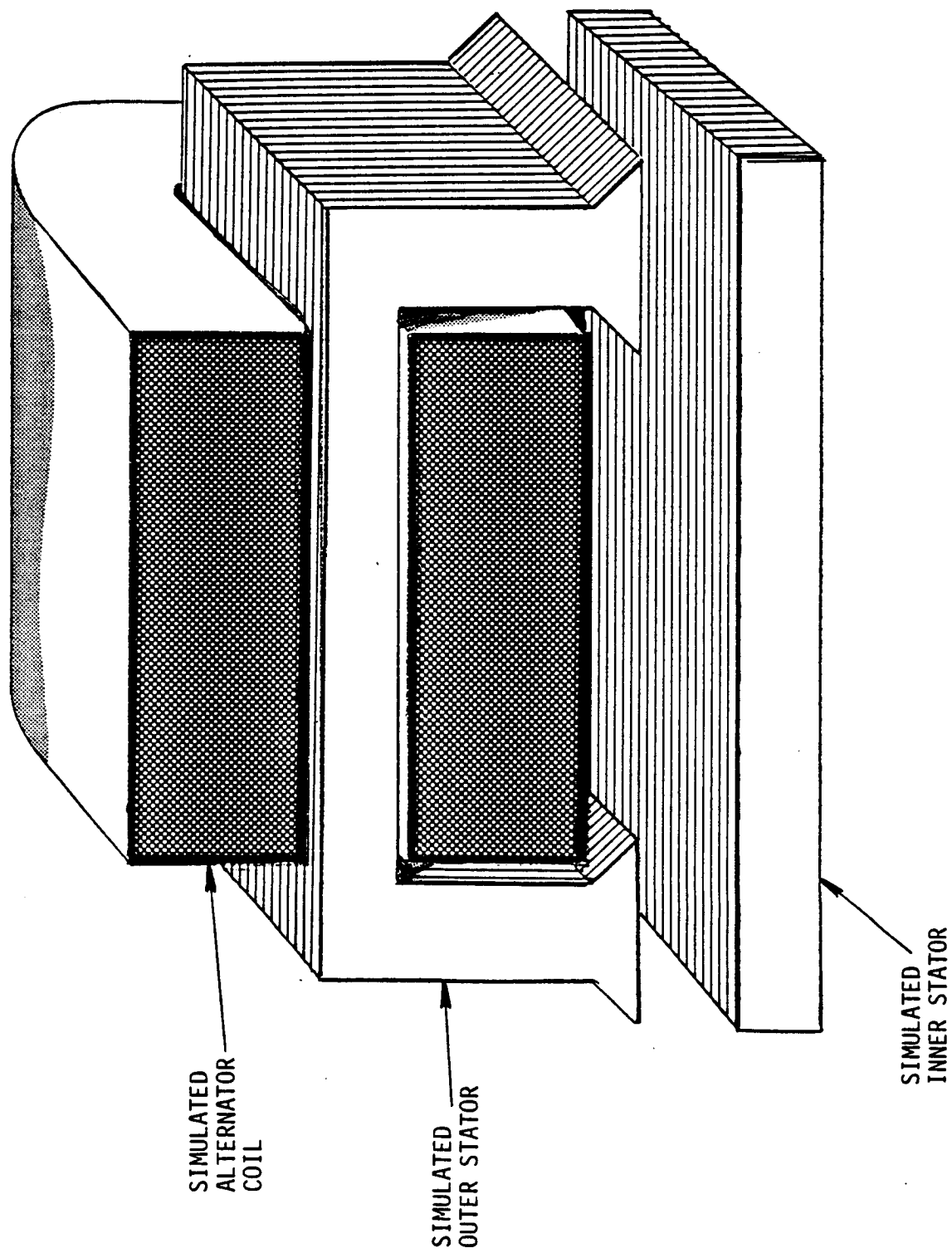
The magnet simulation coils are connected in series in such a way as to replicate the relative polarities of the magnets in the SPDE alternator. The coils were supplied with AC current. The flux linkages of the simulated alternator coil were determined by the measurement of voltage induced in that coil.

Figure 8-5 (refer to Section 8) shows the flux linkage vs. X (the relative position of the magnet simulation coil assembly with respect to the stators) as obtained by the above method. In these measurements, the excitation coil current was held constant while the position in the X direction was varied.

Subsequently, the experiment was repeated with only one of the magnet simulation coils excited. In this experiment, the magnitude of excitation current was held to be the same as in the earlier experiment.

The data from these two experiments can now be used to determine the following ratio:

Ratio = Flux Linkages with Excitation Provided by All Four Magnets
----
Flux Linkage Due to Only One Magnet

The alternator coil flux linkages with only one magnet present under one of the outer stator poles can be estimated using a relatively simple magnetic circuit. The experimentally determined ratio discussed above is used to compute the alternator coil flux linkages due to the excitation provided by all of the four magnets from the flux linkages computed for the case of only one magnet.

APPENDIX 11.1

SPDE ENGINE SHAKEDOWN AND ACCEPTANCE TEST PLAN

SPDE ENGINE SHAKEDOWN AND ACCEPTANCE TEST PLAN

Introduction

This test plan describes in general terms the assembly and inspection of the SPDE, the initial shakedown testing, and the acceptance test to be performed on the SPDE engine.

During the early stages of engine development, it is not desirable to develop very detailed test plans, as there are a large number of contingencies which would need to be considered. Therefore, this test plan will describe the philosophy guiding the engine development and the general process which will be followed if the shakedown and acceptance tests proceed smoothly. Problems identified during the shakedown testing will result in modifications to this test plan which will be verbally communicated to the NASA Program Manager for his approval.

Facility Checkout

The facility will be checked out prior to engine installation as much as possible. This checkout will include the following major items:

Instrumentation

The instruments will be calibrated following established MTI procedures. The calibrations are NBS traceable and documented.

Heating/Cooling System

The heating and cooling systems will be operationally checked out prior to engine installation. In addition, the instrumentation associated with these systems will be checked for consistency. The final test of these systems will be a calorimetric heat balance test in which the heat from the salt will be delivered directly to the cooling system. The heat delivered to the calorimeter will be calculated from the measured flow and delta temperature on the hot salt side of

11.1-1

the calorimeter. The heat extracted from the calorimeter will be calculated from the measured flow and delta temperature on the coolant side of the calorimeter. The heat in and out should balance within a few percent.

Electrical Load System

The electrical load system will be operationally checked out by supplying power from a dummy source, such as the starter power supply or the utility power grid. Also, the power measurements through the electrical system will be compared for consistency. This comparison will be limited to about 5kW (20% of design). These measurements will also be compared to the heat delivered to the cooling water by measuring the flow and delta temperature across the water cooled load.

Helium Pressure Control and External Bearing Supply

The helium system will be operationally checked out. The consistency of the various pressure transducers and gages will be evaluated.

Engine Assembly and Inspection

The first several engine assemblies will be completed with experienced technicians working under close supervision of the development engineer. The engine design engineer will also be available on an 'as needed' basis to answer questions and lend assistance where needed. This design is very similar to the EM, ADM, and HAHP engines; therefore, the assembly procedures are familiar to both engineers and technicians.

While no formal assembly procedures will be used, an outline (or checklist) of critical steps will be developed prior to and during the engine assembly so later builds can be completed with less direct supervision.

As the assembly is proceeding, the components used in each engine half will be documented on an engine build sheet.

The critical clearances, which include the bearing and seal clearances, will be documented. The measurements for this documentation will initially be taken from

vendor inspection reports. The critical dimensions will be remeasured on an 'as required' basis through the shakedown and acceptance test periods. Each engine part will be weighed to assess dynamic engine balance and power to weight. The results of the dimensional and weight measurements will be recorded on the engine build sheet.

During assembly, the displacer will be gas pressure tested; the primary purpose of this test is to identify leakage at the displacer shell to base joint.

The piston and displacer position transducer is integral with the assembly and depend on hardware geometry, the transducer, and signal conditioning hardware. These transducers are, therefore, calibrated as the final step in assembling each engine section.

Engine Shakedown Tests

The specific tests planned for the shakedown or debugging phase of the engine development are briefly described in this section. These tests are divided into three general categories:

- Bench/Static Checkout
- Initial Engine Operational Checkout
- Low Pressure Engine Operation

Bench/Static Checkout

Engine Hydrotest - The engine will be hydrotested to verify the structural integrity of the pressure wall and the high pressure bolted flanges. The test pressure will be 165% of the operating mean pressure to allow for a 10% pressure amplitude.

Bearing System Leak Check - The purpose of this test is to ensure that the bearing supply system, both inside and outside the engine, is leak tight. This is particularly important for internally pumped bearings since leaks represent a flow and power loss to the system. The supply system will be leak checked by plugging the feed holes with a dummy rod or piston. The system will

then be leak checked by pressurizing the system through a flow meter used for flow checking the bearings. The system will be acceptably leak tight if the measured flow is less than 2% of the design flow.

Bearing Flow vs. Pressure - The purpose of this test is to evaluate the as built geometry of the bearings. This test will be carried out using an available flow meter which has been set up to evaluate bearing flow at low supply pressures. The effective bearing clearance will be estimated from the flow measurement and will be a baseline measurement from which bearing degradation can be evaluated.

While no formal sidepull tests are planned during the initial shakedown tests, the displacer and piston assemblies will be qualitatively checked for freedom of movement. This is generally an indication that the engine will run without significant rubbing once it is all assembled.

Static Alternator Test - The purpose of this test is to evaluate several as built characteristics of the alternator, including:

- the effective axial stiffness of the magnets;
- the effective inductance of the AC coil;
- the flux linkage between the magnets and coil; and,
- the flux density in the stator back iron.

From this information, a reasonably accurate estimate of the dynamic performance and characteristics can be made.

This test will be performed with the alternator assembled and the power piston/plunger assembly installed and connected to a calibration fixture. The fixture will allow the plunger to be slowly moved through the normal piston/plunger stroke. A piezoelectric force link will be installed between the drive fixture and the plunger, and the piston position probes will be installed and calibrated. For the flux linkage test, an integrating flux meter will be connected to the coil, while a DC current source will be connected to the coil for the other force vs. position tests.

The flux linkage in the alternator will be tested by moving the plunger throughout the stroke range with the position and flux meter output connected to an X-Y recorder. This will be used to evaluate the voltage generated by the alternator.

The magnetic and electrical alternator force will be tested by moving the plunger throughout the stroke range with the position and force outputs connected to an X-Y recorder. This will be done for zero current in the coil to evaluate the axial centering force and 'magnetic' spring force on the piston/plunger assembly. The force vs. position will also be measured with several levels of DC current flowing through the coil. This will be used to evaluate the 'electrical' force on the piston/alternator. This data can also be used to check the results of the flux vs. position tests.

Displacer Damper Valve Operation and Characteristics - The purpose of this test is to first ensure the displacer damper valve operates properly, thus ensuring that the engine can be shut down under any of several emergency conditions. The second purpose is to measure the flow coefficient vs. valve position. The flow coefficient will determine the displacer damping which is due to the valve 'leakage'.

Initial Engine Operational Checkout

The two primary objectives of the initial engine operation are to complete the mechanical checkout of the engine and to complete the checkout of the instrumentation and data acquisition system. These two aspects of the engine operation will be carried out concurrently. For this test, the engine will be completely installed in the cell and all instruments and utility connections will be made.

For this test, the engine will initially be motored with the engine heater cold. The cooling water will be on, the load will be disconnected, and the engine will be charged to 75 Bar or less. The bearings will be supplied from the external boost pump. The engine will be motored by initially applying a low amplitude AC voltage to the alternators from the starter power supply. At this point, the power pistons should be moving through some fraction of the design stroke. The displacers will then be pneumatically centered, and the AC voltage will be slowly

11.1-5

increased to the limit of either the power supply or the piston stroke capability.

The piston and displacer strokes should increase to a reasonable level (5mm or more) and be relatively well balanced as indicated by both the transducer outputs and the overall engine vibration. The natural frequency of the engine will be determined by sweeping the power supply frequency to maximize piston stroke, which should occur at about 75 hz when the engine is at 75 Bar. The mechanical checkout will be complete when reasonable piston and displacer strokes are achieved and their motions are stable about their respective midstroke ports.

While the engine is being motored, the instrumentation and data acquisition systems will be exercised. All signals will be checked for consistency and proper operation. Low pressure operation will allow safe access to instruments and connections inside the test cell for troubleshooting measurements while the engine is operating. Access to the cell will not be permitted when the engine pressure is above 75 Bar.

Following the mechanical and instrumentation checkout, the engine will be started, again at low pressure.

Low Pressure Engine Operation

The engine operational checkout will continue with low pressure engine operation for which the heater temperature will be increased to the design temperature of 375-400°C. The heater temperature will be adjusted as necessary to obtain a temperature ratio of 2.0 (heater tube to cooler tube temperature). The engine should operate and produce net output power at this temperature ratio. Engine performance data will be obtained at 50 and 75 Bar for this test. First order code predictions will be made prior to running the low pressure tests. The engine load will be adjusted such that design piston stroke is obtained at each operating pressure. For this test, the bearings will be supplied from the external gas booster.

The engine will be operated for this and all other engine tests following the start-up/shutdown procedures established for this program.

The results of the low pressure tests will be compared to analytic predictions. The predictions will then be used to extrapolate the test results to the design pressure. On the basis of this comparison, hardware modifications to adjust the engine dynamics will be recommended for the next, Acceptance Test, phase.

Following the low pressure test, the engine will be disassembled to perform a high pressure hydrotest. At this time, the dynamic hardware will be disassembled to inspect the critical bearings and seal for wear and all other hardware for any damage.

Acceptance Test

The acceptance test goal is to obtain operating performance data at the SPDE design conditions of:

Pmean	= 150 B
Frequency	= 105 hz
Piston Stroke	= 20mm
Temperature Ratio	= 2.0
Cooler Temperature	= 50°C
Heater Temperature	= 375°C

Hardware modifications identified during low pressure testing will be implemented during the build for the acceptance test.

The engine will be assembled and installed in Cell #5. All utilities and instruments will be connected.

The engine will be started following the start-up check list and will be operated at low pressure and the design temperature ratio to repeat the low pressure test points of 50 and 75 Bar operating pressure. The results of these operating points will be compared to that obtained during the low pressure testing and predictions which include the effect of any hardware changes. The operating pressure will then be raised to 100, 125, and 150 Bar with the stroke and temperature ratio at their design values. The engine will be operated at the design point conditions for a sufficient time to obtain steady-state operating data.

All parameters necessary to obtain power, efficiency, energy balance, and internal loss performance will be measured and recorded by the data acquisition system (DAS).

The results of the acceptance test will be compared to predicted performance and the results of the low pressure tests.

LIMITED DISTRIBUTION LIST

NASA/Lewis Research Center
21000 Brookpark Road
Cleveland, OH 44135

ATT: D. Alger   MS 301-2 (50 copies)
          J. Dudenhoefer   MS 301-2
          W. Tomazic   MS 301-2
          R. Shaltens   MS 301-2
          W. Tabata   MS 301-2
          J. Slaby   MS 301-2
          D. Beremand   MS 301-2
          J. Cairelli   MS 301-2
          R. Tew   MS 301-2
          J. Schreiber   MS 301-2
          S. Geng   MS 301-2
          L. Thieme   MS 301-2
          J. Winter   MS 301-5
          R. Sovie   MS 301-5
          H. Bloomfield   MS 301-5
          M. Dustin   MS 301-3
          T. Mroz   MS 301-5
          A. Juhasz   MS 301-5
          G. Schwarze   MS 301-2
          H. Brandhorst   MS 301-3
          J. Fordyce   MS 3-5

NASA Headquarters
Washington, DC 20546
ATT: RP/E. VanLandingham
       RP/A. Schnyer

R. Wiley
OSD/SDIO
The Pentagon
Washington, DC 20301-7100

Strategic Defense Initiative Organization
OSD/SDIO/CA
ATT: Col. J.A. Ball
Washington, DC 20301-7110

Jet Propulsion Laboratory
4800 Oak Grove Drive
Pasadena, CA 91009
ATT: MS 506-432 - V. Truscello
                J. Mondt

Department of Energy
ATT: P. Sutton, MS 5-G030
Forrestal Building
Washington, DC 20585

General Electric Company
ATT: R.J. Katucki
P.O. Box 8555
Philadelphia, PA 19101

General Electric Company
ATT: W.S. Chiu
P.O. Box 8661
Philadelphia, PA 19101

McDonnell Douglas Company
ATT: R.T. Kawai, MC 36-41
3855 Lakewood Blvd.
Long Beach, CA 90846

Rockwell International
ATT: R.B. Harty
Energy Systems Group
8900 DeSoto Avenue
Canoga Park, CA 91304

Sandia National Laboratory
Albuquerque, NM 87185
ATT: J.A. Leonard
      K. Linker

Stirling Technology Company
ATT: M.A. White
2952 George Washington Way
Richland, WA 99352

Sundstrand Aviation
ATT: R.E. Niggermann
4747 Harrison Avenue
P.O. Box 7002
Rockford, IL 61125

Sunpower, Inc.
6 Byard
Athens, OH 45701
ATT: W. Beale
      B. Penswick

The Garrett Corporation
ATT: A.E. Hause
One First National Plaza
Suite 1900
Dayton, OH 45402

TRW
Space and Technology Group
One Space Park
Redondo Beach, CA 90278
ATT: A.D. Schoenfeld

Westinghouse Electric Company
ATT: J.L. Powell
P.O. Box 355
Pittsburgh, PA 15230-0355

Westinghouse Electric Company
ATT: D.L. Ayers
1310 Buelah Road
Pittsburgh, PA 15235